

DDC FILE COPY

AD A058802

Report No. ¹⁷USCG/D-54-78

Task No. 4714.22.1

LEVEL

13

⁶ A STUDY TO CONDUCT EXPERIMENTS CONCERNING
TURBULENT DISPERSION OF OIL SLICKS,

¹⁰ Jung-Tai/Lin
Mohamed/Gad-el-Hak
Heien-Ta/Liu



13148P.



¹¹ APRIL 1978

⁹ FINAL REPORT. Oct 76 - Apr 78,

¹⁴ FRC-112

¹⁵ DOT-CG-61688-A

Document is available to the U. S. public through the
National Technical Information Service,
Springfield, Virginia 22161

Prepared for
U. S. DEPARTMENT OF TRANSPORTATION
UNITED STATES COAST GUARD
Office of Research and Development
Washington, D.C. 20590

390 409
78 09 05 234

NOTICE

This document is disseminated under the sponsorship of the Department of Transportation in the interest of information exchange. The United States Government assumes no liability for its contents or use thereof.

The United States Government does not endorse products or manufacturers. Trade or manufacturers' names appear herein solely because they are considered essential to the object of this report.

The contents of this report do not necessarily reflect the official view or policy of the U. S. Coast Guard and do not constitute a standard, specification, or regulation.

Technical Report Documentation Page

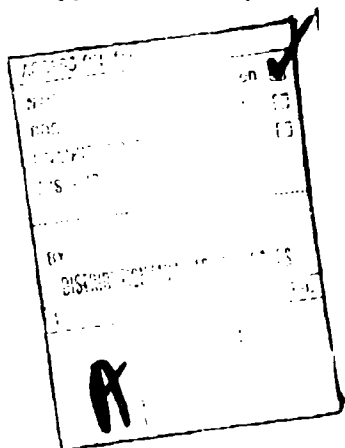
1. Report No. CG-D-54-78	2. Government Accession No.	3. Recipient's Catalog No.	
4. Title and Subtitle A STUDY TO CONDUCT EXPERIMENTS CONCERNING TURBULENT DISPERSION OF OIL SLICKS		5. Report Date April 1978	6. Performing Organization Code
		8. Performing Organization Report No. FRC Report No. 112	
7. Author(s) J. T. Lin, M. Gad-el-Hak, and H. T. Liu		10. Work Unit No. (TRAIS)	
9. Performing Organization Name and Address Flow Research Company 21414-68th Avenue South Kent, Washington 98031		11. Contract or Grant No.	
		13. Type of Report and Period Covered Final Report October 1976 to April 1978	
12. Sponsoring Agency Name and Address Office of Research and Development United States Coast Guard Washington, D.C. 20590		14. Sponsoring Agency Code USCG	
15. Supplementary Notes Deep Water Ports Program U. S. Coast Guard			
16. Abstract Laboratory experiments were conducted in a wind-wave tank to study the turbulent characteristics in the water boundary-layers under the action of wind and waves and to study the oil dispersion characteristics under the action of breaking waves. Effects of an oil slick on the wind-waves or mechanically-generated waves with wind were also investigated. The objective was to understand by means of laboratory experiments the behavior of oil dispersion in the upper ocean. Two new instruments, a laser Doppler velocimeter and a photodiode wave gauge, have been developed to measure remotely the velocity and the vertical displacement of the water surface. The two new techniques and the experimental results are described in detail. For field application, empirical formulas were derived from the laboratory results.			
17. Key Words Boundary-Layer, Breaking Waves, Dissipation, Laser Doppler Velocimeter, Mechanical Waves, Oil Concentration, Oil Dispersion, Phase Speed, (Photodiode) Wave Gauge, Sea State, Size Distribution, Surface Drift		18. Distribution Statement Document is available to the U.S. public through the National Technical Information Service, Springfield, Virginia 22161	
19. Security Classif. (of this report) Unclassified	20. Security Classif. (of this page) Unclassified	21. No. of Pages 206	22. Price

PREFACE

This report is submitted to the U.S. Coast Guard, Department of Transportation, by Flow Research Company (FRC) in completion of the research work on "A Study to Conduct Experiments Concerning Turbulent Dispersion of Oil Slicks," under Contract No. DOT-CG-61688-A. The objective of the research study was to characterize (qualitatively and quantitatively) and to identify the mechanisms behind turbulence due to wind, waves and currents operating independently and coupled, with and without an oil slick present.

This research study is a part of the integrated research program sponsored by the Deepwater Ports program and the U.S. Coast Guard to identify the sea-state threshold beyond which containment and recovery of oil are impractical because of the natural dispersion of oil slicks. Other parts of the research program include (i) a preliminary theoretical study by Arthur D. Little Inc. under Contract No. DOT-CG-61-505A (Raj, 1977), (ii) a laboratory study by Massachusetts Institute of Technology (MIT) under Contract No. DOT-CG-61-802A to investigate the effects of oil properties on oil dispersion, and (iii) a field study by the Naval Underwater Systems Center to conduct observations of surface layer turbulence associated with wind stress and breaking waves.

The research team at FRC was headed by Dr. J. T. Lin and assisted by Drs. M. Gad-el-Hak and H. T. Liu. Mr. R. Srnsky's assistance in conducting experiments is gratefully acknowledged. Technical Services, provided by M. Wallace, D. Turner, I. Smith, M. A. Kerstein and M. McKenna in drafting, typing and editing is recognized gratefully. We also acknowledge Drs. S. Veenhuizen and M. Rizk for their valuable comments on the write-up of this report. The research study was monitored by Mr. R. A. Griffiths of the Coast Guard. We gratefully acknowledge his support and cooperation throughout the course of the research study.



METRIC CONVERSION FACTORS

Approximate Conversions to Metric Measures

Symbol	When You Know	Multiply by	To find	Symbol
LENGTH				
in	inches	2.5	centimeters	cm
ft	feet	30	centimeters	cm
yd	yards	0.9	meters	m
mi	miles	1.6	kilometers	km
AREA				
in ²	square inches	6.5	square centimeters	cm ²
ft ²	square feet	0.09	square meters	m ²
yd ²	square yards	0.8	square meters	m ²
mi ²	square miles	2.6	square kilometers	km ²
	acres	0.4	hectares	ha
MASS (weight)				
oz	ounces	28	grams	g
lb	pounds	0.45	kilograms	kg
	short tons (2000 lb)	0.9	tonnes	t
VOLUME				
tblsp	tablespoons	5	milliliters	ml
teaspoon	teaspoons	5	milliliters	ml
fl oz	fluid ounces	30	milliliters	ml
c	cups	0.24	liters	l
pt	pints	0.47	liters	l
qt	quarts	0.95	liters	l
gal	gallons	3.8	liters	l
fl	cubic feet	0.03	cubic meters	m ³
yd ³	cubic yards	0.76	cubic meters	m ³
TEMPERATURE (exact)				
°F	Fahrenheit temperature	5/9 (after subtracting 32)	Celsius temperature	°C

* 1 U.S. liquid quart = 0.9463536 liters. 1 U.S. dry quart = 1.101221 liters. 1 U.S. liquid gallon = 3.785411784 liters. 1 U.S. dry gallon = 4.40488377086 liters. 1 U.S. liquid pint = 0.473176473 liters. 1 U.S. dry pint = 0.550610471 liters. 1 U.S. liquid ounce = 0.2957352956 liters. 1 U.S. dry ounce = 0.28349523125 liters. 1 U.S. liquid cup = 0.2446592593 liters. 1 U.S. dry cup = 0.2511984946 liters. 1 U.S. liquid pint = 0.473176473 liters. 1 U.S. dry pint = 0.550610471 liters. 1 U.S. liquid quart = 0.9463536 liters. 1 U.S. dry quart = 1.101221 liters. 1 U.S. liquid gallon = 3.785411784 liters. 1 U.S. dry gallon = 4.40488377086 liters.

Symbol	When You Know	Multiply by	To find	Symbol
LENGTH				
mm	millimeters	0.39	inches	in
cm	centimeters	0.4	inches	in
m	meters	3.3	feet	ft
yr	meters	1.1	yards	yd
km	kilometers	0.6	miles	mi
AREA				
cm ²	square centimeters	0.16	square inches	in ²
m ²	square meters	1.2	square yards	yd ²
km ²	square kilometers	0.4	square miles	mi ²
ha	hectares (10,000 m ²)	2.5	acres	
MASS (weight)				
g	grams	0.035	ounces	oz
kg	kilograms	2.2	pounds	lb
t	tonnes (1000 kg)	1.1	short tons	
VOLUME				
ml	milliliters	0.03	fluid ounces	fl oz
l	liters	2.1	pints	pt
l	liters	1.06	quarts	qt
l	liters	0.26	gallons	gal
m ³	cubic meters	35	cubic feet	ft ³
m ³	cubic meters	1.3	cubic yards	yd ³
TEMPERATURE (exact)				
°C	Celsius temperature	9/5 (then add 32)	Fahrenheit temperature	°F

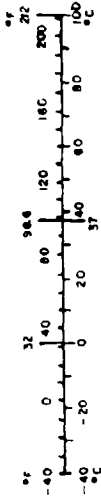


TABLE OF CONTENTS

TECHNICAL REPORT DOCUMENTATION PAGE	i
PREFACE	ii
METRIC CONVERSION FACTORS	iii
TABLE OF CONTENTS	iv
LIST OF TABLES	vi
LIST OF FIGURES	vii
LIST OF SYMBOLS	xi
1. INTRODUCTION	1
2. EXPERIMENTAL SETUP	5
2.1 Wind-Wave Tank	5
2.2 Reverse Flow Control	6
2.3 Oil Feeding System	7
2.4 Selection of Oil	8
3. EXPERIMENTAL INSTRUMENTS AND TECHNIQUES	10
3.1 Hot-Wire and Hot-Film Probes	10
3.2 Laser Doppler Velocimeter	10
3.3 Capacitance Probes	12
3.4 Photodiode Wave Gauge	13
3.5 Data Acquisition and Processing	15
4. EFFECT OF WIND ON WATER MOTION	16
4.1 Air Boundary-Layer	17
4.2 Wave Characteristics	18
4.3 Surface Drift Velocity	19
4.4 Water Boundary-Layer	20
4.5 Mean Velocity	21
4.6 RMS Velocity Fluctuations	22
4.7 Velocity Spectra	25
5. EFFECTS OF WAVES ON WATER MOTION	28
5.1 Wave Characteristics	28
5.2 Surface Drift Velocity	31
5.3 Water Boundary-Layer	34
5.4 Mean Velocity	35
5.5 RMS Velocity Fluctuations	36
5.6 Mean Square Velocity Time Derivatives	38

5.7	Velocity Spectra	38
6.	OIL DISPERSION	41
6.1	Flow Visualization	41
6.2	Oil Concentration	42
7.	CONCLUSIONS	45
7.1	Turbulence and Wave-Induced Motion	45
7.2	Wave Growth Characteristics	46
7.3	Surface Drift Velocity	46
7.4	Oil Dispersion	47
8.	RECOMMENDATIONS FOR FUTURE RESEARCH	48
8.1	Surface Drift Velocity	48
8.2	Turbulent Motion Versus Wave-Induced Motion	48
8.3	Taylor's Frozen Turbulence Hypothesis	49
8.4	Oil Concentration Flux	49
	REFERENCES	50
	Appendix A: Chronological Annotations	62
	Appendix B: Comparison of Velocity Measurements by LDV and Hot-Film Probes	71
	Appendix C: Effects of Oil Slick on Wind-Waves	72
	Appendix D: Effect of Oil Slick on Mechanically-Generated Waves With Wind	77
	TABLES	81
	FIGURES	99

LIST OF TABLES

TABLE 1. -SUMMARY OF OIL PROPERTIES, ARCO DIESEL	82
TABLE 2. -WATER SURFACE DRIFT VELOCITY FOR WIND-WAVES	83
TABLE 3. -WATER BOUNDARY-LAYER THICKNESS FOR WIND-WAVES	84
TABLE 4. -AIR AND WATER SHEAR STRESSES	85
TABLE 5. -MEASUREMENTS OF VELOCITY IN WATER BOUNDARY-LAYER	86
TABLE 6. -MEASUREMENTS OF VELOCITY IN WATER BOUNDARY-LAYER	87
TABLE 7. -MEASUREMENTS OF VELOCITY IN WATER BOUNDARY-LAYER	88
TABLE 8. -MEASUREMENTS OF VELOCITY IN WATER BOUNDARY-LAYER	89
TABLE 9. -MEASUREMENTS OF VELOCITY IN WATER BOUNDARY-LAYER	90
TABLE 10. -MEASUREMENTS OF VELOCITY IN WATER BOUNDARY-LAYER	91
TABLE 11. -MEASUREMENTS OF VELOCITY IN WATER BOUNDARY-LAYER	92
TABLE 12. -MEASUREMENTS OF VELOCITY IN WATER BOUNDARY-LAYER	93
TABLE 13. -MEASUREMENTS OF VELOCITY IN WATER BOUNDARY-LAYER	94
TABLE 14. -MEASUREMENTS OF VELOCITY IN WATER BOUNDARY-LAYER	95
TABLE 15. -MEASUREMENTS OF VELOCITY IN WATER BOUNDARY-LAYER	96
TABLE 16. -MEASUREMENTS OF VELOCITY IN WATER BOUNDARY-LAYER	97
TABLE 17. -MEASUREMENTS OF VELOCITY IN WATER BOUNDARY-LAYER	98

LIST OF FIGURES

FIGURE 1.	WIND-WAVE TANK.	100
FIGURE 2.	OIL FEEDING SYSTEM SCHEMATIC.	101
FIGURE 3.	HOT-WIRE PROBE CALIBRATION.	102
FIGURE 4.	HOT-FILM PROBE CALIBRATION.	103
FIGURE 5.	LASER DOPPLER VELOCIMETER.	104
FIGURE 6.	PLIOLITE PARTICLES PHOTOGRAPHIED WITH ELECTRONIC MICROSCOPE.	105
FIGURE 7.	BLOCK DIAGRAM FOR PROCESSING OF LDV SIGNALS.	106
FIGURE 8.	COMPARISON OF LDV OUTPUT WITH PITOT TUBE OUTPUT.	107
FIGURE 9.	CALIBRATION OF CAPACITANCE PROBE.	108
FIGURE 10.	SCHEMATIC OF PHOTODIODE WAVE GAUGE FOR WATER-WAVE MEASUREMENTS.	109
FIGURE 11.	PHOTODIODE WAVE GAUGE SETUP.	110
FIGURE 12.	OPERATIONAL PRINCIPLE OF WAVE GAUGE.	111
FIGURE 13.	PHOTODIODE WAVE GAUGE CALIBRATION.	112
FIGURE 14.	WAVE PROFILE MEASURED WITH PHOTODIODE WAVE GAUGE.	113
FIGURE 15.	WAVE PROFILE MEASURED WITH CAPACITANCE PROBE.	114
FIGURE 16.	DEFINITION SKETCH FOR OIL DISPERSION IN WIND-WAVES.	115
FIGURE 17.	PROFILES OF MEAN VELOCITY AND TURBULENCE INTENSITY IN AIR BOUNDARY-LAYER.	116
FIGURE 18.	MEAN VELOCITY PROFILE IN AIR BOUNDARY-LAYER.	117
FIGURE 19.	INSTANTANEOUS WATER SURFACE DISPLACEMENT OF WIND-WAVES.	118
FIGURE 20.	WAVE ENERGY SPECTRUM.	119
FIGURE 21.	VARIATION OF RMS WAVE HEIGHT WITH WIND SPEED.	120
FIGURE 22.	VARIATION OF DOMINANT WAVE FREQUENCY WITH WIND SPEED.	121
FIGURE 23.	FETCH EFFECTS ON DOMINANT WAVE FREQUENCY.	122
FIGURE 24.	VARIATION OF WAVE PHASE VELOCITY WITH WIND SPEED.	123
FIGURE 25.	FETCH EFFECTS ON WAVE PHASE VELOCITY.	124
FIGURE 26.	VARIATION OF DOMINANT WAVE LENGTH WITH WIND SPEED.	125
FIGURE 27.	VARIATION OF DOMINANT WAVE SLOPE WITH WIND SPEED.	126
FIGURE 28.	FETCH EFFECTS ON DOMINANT WAVE LENGTH.	127
FIGURE 29.	VARIATION OF SURFACE DRIFT VELOCITY WITH FETCH.	128
FIGURE 30.	DYED WATER BOUNDARY-LAYER.	129
FIGURE 31.	WATER BOUNDARY-LAYER THICKNESS.	132
FIGURE 32.	MEAN VELOCITY PROFILE IN WATER BOUNDARY-LAYER.	133

FIGURE 33.	MEAN VELOCITY DEFECT PROFILE IN WATER BOUNDARY-LAYER.	134
FIGURE 34.	MEAN VELOCITY PROFILES IN WATER BOUNDARY-LAYER: EFFECTS OF WIND SPEED.	135
FIGURE 35.	RMS OF LONGITUDINAL VELOCITY FLUCTUATIONS IN WATER BOUNDARY-LAYER.	136
FIGURE 36.	RMS OF LONGITUDINAL VELOCITY FLUCTUATIONS IN WATER BOUNDARY-LAYER.	137
FIGURE 37.	RMS OF VERTICAL VELOCITY FLUCTUATIONS IN WATER BOUNDARY-LAYER.	138
FIGURE 38.	RMS OF VERTICAL VELOCITY FLUCTUATIONS IN WATER BOUNDARY-LAYER.	139
FIGURE 39.	REYNOLDS STRESS PROFILES IN WATER BOUNDARY-LAYER.	140
FIGURE 40.	DISSIPATION RATE IN WATER BOUNDARY-LAYER.	141
FIGURE 41.	LONGITUDINAL VELOCITY SPECTRUM IN WATER BOUNDARY-LAYER.	142
FIGURE 42.	LONGITUDINAL VELOCITY SPECTRA IN WATER BOUNDARY-LAYER.	143
FIGURE 43.	VERTICAL VELOCITY SPECTRA IN WATER BOUNDARY-LAYER.	144
FIGURE 44.	CO- AND QUAD-SPECTRUM OF LONGITUDINAL AND VERTICAL VELOCITIES IN WATER BOUNDARY-LAYER.	145
FIGURE 45.	MAGNITUDE AND PHASE OF CROSS-SPECTRUM OF LONGITUDINAL AND VERTICAL VELOCITIES IN WATER.	146
FIGURE 46.	WATER SURFACE PHOTOGRAPH.	147
FIGURE 47.	AIR BUBBLES ENTRAINED INTO WATER UNDER WAVE CREST.	149
FIGURE 48.	WAVE ENERGY SPECTRA (CAPACITANCE PROBE).	150
FIGURE 49.	DOMINANT PHASE SPEED, C_p VERSUS WAVE STEEPNESS. H/λ	151
FIGURE 50.	VARIATION OF WAVE HEIGHT WITH FETCH.	152
FIGURE 51.	WAVE ENERGY SPECTRA AT TWO FETCHES.	153
FIGURE 52.	WAVE ENERGY SPECTRA WITH MECHANICALLY GENERATED WAVE.	154
FIGURE 53.	VARIATION OF WAVE ENERGY SPECTRUM WITH WIND SPEED.	155
FIGURE 54.	SURFACE DRIFT VELOCITY U_s VERSUS FETCH x .	156
FIGURE 55.	SURFACE DRIFT CURRENT V_s VERSUS WAVE STEEPNESS H/λ .	157
FIGURE 56.	DYED WATER BOUNDARY, $H_0 = 7.62$ cm, $U_\infty = 10$ m/sec, $x = 4$ m.	158
FIGURE 57.	THICKNESS OF WATER BOUNDARY-LAYER δ_w VERSUS FETCH x .	159
FIGURE 58.	VERTICAL PROFILES OF LONGITUDINAL MEAN VELOCITY IN BREAKING AND NON-BREAKING WAVES.	160
FIGURE 59.	VERTICAL PROFILES OF VERTICAL MEAN VELOCITY IN BREAKING AND NON-BREAKING WAVES.	161
FIGURE 60.	VERTICAL PROFILES OF RMS LONGITUDINAL VELOCITY IN BREAKING AND NON-BREAKING WAVES.	162

FIGURE 61.	VERTICAL PROFILES OF RMS VERTICAL VELOCITY IN BREAKING AND NON-BREAKING WAVES.	163
FIGURE 62.	VERTICAL PROFILES OF RMS VELOCITY FLUCTUATIONS IN BREAKING AND NON-BREAKING WAVES.	164
FIGURE 63.	VERTICAL PROFILES OF MEAN SQUARE VELOCITY TIME DERIVATIVES IN BREAKING AND NON-BREAKING WAVES.	165
FIGURE 64.	SPECTRUM OF LONGITUDINAL VELOCITY FLUCTUATIONS IN BREAKING WAVES.	166
FIGURE 65.	SPECTRUM OF VERTICAL VELOCITY FLUCTUATIONS IN BREAKING WAVES.	167
FIGURE 66.	SPECTRUM OF LONGITUDINAL VELOCITY FLUCTUATIONS IN BREAKING WAVES.	168
FIGURE 67.	SPECTRUM OF VERTICAL VELOCITY FLUCTUATIONS IN BREAKING WAVES.	169
FIGURE 68.	VERTICAL PROFILE OF INSTANTANEOUS OIL VOLUME CONCENTRATION.	170
FIGURE 69.	VERTICAL PROFILES OF MEAN AND RMS OIL VOLUME CONCENTRATION.	171
FIGURE 70.	VERTICAL PROFILE OF MEAN OIL VOLUME CONCENTRATION.	172
FIGURE 71.	SIZE DISTRIBUTION OF OIL DROPLETS.	173
FIGURE 72.	COMPARISON OF LONGITUDINAL MEAN VELOCITY PROFILE MEASURED IN WIND-WAVES BY LDV AND HOT-FILM PROBES.	174
FIGURE 73.	COMPARISON OF RMS LONGITUDINAL VELOCITY PROFILE MEASURED IN WIND-WAVES.	175
FIGURE 74.	TRANSIENT PROFILES OF WIND WAVES IN RESPONSE TO OILSLICK.	176
FIGURE 75.	WIND-WAVE PROFILES WITHOUT OIL SLICK.	177
FIGURE 76.	WIND-WAVE PROFILES WITH OIL SLICK. X = 4 m. VERTICAL SCALE 0.2 cm/div. HORIZONTAL SCALE 0.5 sec/div.	178
FIGURE 77.	VARIATION OF RMS WAVE HEIGHT WITH WIND SPEED.	179
FIGURE 78.	VARIATION OF RMS WAVE HEIGHT WITH FETCH.	181
FIGURE 79.	WAVE ENERGY SPECTRUM.	181
FIGURE 80.	WAVE ENERGY SPECTRUM VARIATION WITH WIND SPEED.	182
FIGURE 81.	WAVE ENERGY SPECTRA MEASURED WITH AND WITHOUT OIL.	183
FIGURE 82.	WAVE ENERGY SPECTRA MEASURED WITH AND WITHOUT OIL.	184
FIGURE 83.	WAVE ENERGY SPECTRA MEASURED WITH AND WITHOUT OIL.	185
FIGURE 84.	PROFILES OF MECHANICALLY GENERATED WAVES WITH WIND, VERTICAL SCALE = 2 cm/DIV., HORIZONTAL SCALE = 0.5 sec/DIV.	186
FIGURE 85.	A TYPICAL PROFILE OF NONBREAKING WAVES WITHOUT OIL.	187
FIGURE 86.	TYPICAL PROFILE OF BREAKING WAVES WITHOUT OIL.	188
FIGURE 87.	PROFILE OF MECHANICAL GENERATED WAVES WITH WIND AND OILSLICK. VERTICAL SCALE = 2 cm/div., HORIZONTAL SCALE = 0.5 sec/div.	189
FIGURE 88.	VARIATION OF WAVE HEIGHTS WITH FETCH.	190

FIGURE 89.	VARIATION OF RMS WAVE HEIGHTS WITH WIND SPEED.	191
FIGURE 90.	COMPARISON OF WAVE ENERGY SPECTRA, $H_o = 2.54$ cm.	192
FIGURE 91.	COMPARISON OF WAVE ENERGY SPECTRA, $H_o = 5.08$ cm.	193
FIGURE 92.	COMPARISON OF WAVE ENERGY SPECTRA WITH AND WITHOUT OIL SLICK.	194

SYMBOLS

<u>Symbol</u>	<u>Description</u>	<u>Dimensions*</u>
C	instantaneous oil volume concentration	-
\bar{C} , c	mean and fluctuating oil volume concentration	-
c_d	windstress coefficient	-
C_p	wave phase speed	LT^{-1}
c_w	wavedrag coefficient	-
d_f	spacing of the LDV fringes	L
$E_{11}(k_1)$	one dimensional wave number spectrum of turbulence	L^3T^{-2}
f	wave frequency (Hz)	T^{-1}
f_d	Doppler frequency	T^{-1}
f_o	dominant wave frequency	T^{-1}
Δf	frequency shift by a Bragg cell	T^{-1}
g	gravitational acceleration	LT^{-2}
H	dominant wave height	L
H_o	stroke of wave-maker	L
k_1	wave number	L^{-1}
R_λ	turbulence Reynolds number, $= \bar{u}^2 \lambda / \nu$	-
$S(f)$	wave energy spectrum	L^2T
$S_u(f), S_w(f)$	spectral density of longitudinal, vertical velocity fluctuations	L^2T^{-1}
t	time	T
\bar{U}	mean longitudinal velocity	LT^{-1}
U_d	Stokes' surface drift velocity	LT^{-1}
U_p	particle velocity	LT^{-1}
U_s	surface drift velocity	LT^{-1}
U_∞	wind speed in the free-stream	LT^{-1}
u, v, w	Cartesian velocity fluctuating components	LT^{-1}
u_*	water friction velocity	LT^{-1}
u_{*g}	air friction velocity	LT^{-1}

* L = length, T = time, M = mass

$\sqrt{u^2}$	root-mean-square longitudinal velocity fluctuations	Lt^{-1}
$\frac{uw}{w^2}$	Reynolds stress	L^2T^{-2}
	root-mean-square vertical velocity fluctuations	Lt^{-1}
x, y, z	Cartesian coordinates, x is fetch positive downwind of the shore, y is positive on the left when viewed downwind, and z is positive upwards	L
z_o	roughness height	L
α, β	numerical constants	-
γ	surface tension per unit density	L^3T^{-2}
δ_a	air boundary-layer thickness	L
δ_w	water boundary-layer thickness	L
ϵ	turbulence dissipation rate	L^2T^{-3}
$\frac{\eta}{n^2}$	vertical displacement of water surface	L
	rms of the vertical displacement of water surface	L
θ	angle	-
θ	momentum thickness of the boundary layer of surface waves	L
λ	dominant wavelength, or turbulence microscale, or wave length of light	L
ν	kinematic viscosity of the water	L^2T^{-1}
ρ_A	density of the air	ML^{-3}
ρ_w	density of the water	ML^{-3}
τ_d	Doppler period	T

1. INTRODUCTION

Because of the increasing demand for oil imports to the United States, transport facilities capable of unloading from the 200,000 to 700,000 DWT class of very large crude carriers (VLCC) are urgently required (Patton and Johnson, 1974). A direct shipment by a VLCC to a coastline, for example, the Gulf Coast, has considerable economic advantage. Unfortunately, the Gulf Coast has a gradually sloping continental shelf, which requires that deep-water ports for unloading oil directly from the VLCC must be located offshore. Severe sea and weather conditions in this area have been reported. According to the National Climatic Center, the wave height could be greater than five feet for 33 percent of the fall and winter seasons and greater than eight feet for 10 percent of the same seasons. Under these conditions, oil spills during transfer operations are very likely to occur and environmental contamination would be a serious problem. Before developing a new technology to counteract potential oil-spill problems, efforts must be directed toward identifying the sea-state threshold beyond which containment and recovery are impractical because of the natural dispersion of oil slicks. The determination of the sea-state threshold for oil spill breakup, however, requires an understanding of the turbulent motion in the upper ocean and its effect on the dispersion of oil slicks. In the following, let us review our understanding of this phenomena.

In the upper ocean, there are three important mechanisms for the generation of turbulence: (i) wave breaking, (ii) shear or current, and (iii) buoyancy-induced motion. The importance of the first mechanism, wave breaking, in generating turbulence is shown by the measurements of Grant, et al. (1963), i.e., the turbulent dissipation rate in the region near the surface has a larger value than that at some distance below the surface. Phillips (1966) estimated that the energy flux of the turbulence from breaking waves may be comparable with, or greater than, the direct energy flux of the surface current associated with wind stress. The second mechanism, dynamic instability of various shearing flows, is mainly caused by wind-induced currents. Background shearing currents,

for example, caused by the confluence of different water masses are often sources of appreciable turbulence in surface waters. The third mechanism, buoyant or convective instability, is important in regions where substantial cooling or surface evaporation appears and the surface layer tends to be statically unstable. This mechanism results in free convection characterized by an irregular cellular motion.

In addition to the three mechanisms of turbulence generation previously described, stratification in the surface water requires some consideration. In a stably stratified fluid, stratification can inhibit the development of turbulence and the downward diffusion of turbulent energy. Another aspect of the stratification effect stems from the deepening of the mixed surface layer, and thus, the thermocline below the mixed surface layer. A portion of the energy flux from the surface is used to deepen the thermocline. Hence, the dynamics of the turbulence in surface waters cannot be separated from those of the mixed layer. For the present study, a sea in a strongly excited state is of concern and thus, the stratification in surface waters, the deepening of the mixed layer, and the buoyancy-induced instabilities, are expected not to be important in the generation of turbulence. Hence, in the following paragraph we briefly review the previous works concerning breaking waves and wind-induced currents.

Breaking waves have not been investigated carefully until recently. Longuet-Higgins (1969a, 1969b, 1973, 1974) conducted theoretical studies on the mechanisms of wave breaking. Banner and Phillips (1974) investigated the incipient breaking of small-scale waves. Van Dorn and Pazan (1975) measured the velocity in breaking waves in a wave channel. The wind-induced drift currents have been investigated by many researchers. Keulegan (1951) and Plate (1970) measured the surface current in wind-wave tanks. Baines and Knapp (1965) measured the drift profiles in a shallow channel. Bye (1965), Shemdin (1973) and Wu (1975) measured the profiles of the wind-induced drift current in wind-wave tanks. Turbulence measurements in the water near the ocean surface were conducted by Shonting (1968), by Thorton, et al. (1977) and by Donelan (1977).

In order to understand the behavior of oil dispersion in the upper ocean, it is necessary to know the turbulence characteristics (for example, vertical profiles of mean velocity and turbulence intensity). These characteristics are not yet available from existing literatures. Therefore, the first objective for the present research study is to conduct laboratory measurements of the water velocity under the action of wind and waves. From these measurements, one could obtain an empirical formula so as to apply the laboratory results to the field situation.

As far as oil dispersion studies are concerned, we have found no systematic work on oil slick breakup, however, some works on oil slick drift are available and they are summarized briefly as follows. Schwartzberg (1971) conducted laboratory experiments to study oil spills under the action of wind. He measured the surface drift current with an oil spill present. Pottinger and Reisbig (1973) conducted laboratory measurements of the drift velocity of an oil lens. Reisbig et al. (1973) investigated the coupled parallel effects of wind and waves on oil spill drift. In the field, Murray (1975) observed the effect of wind and current on the drift of large-scale oil slicks. The second objective of the present study is to investigate the oil dispersion. We will determine the vertical penetration and the size distribution of the oil droplets when the oil slick is broken.

Our approach is to conduct laboratory experiments in a wind tank. First, we investigate the water turbulence under the influence of wind. Second, we add mechanically-generated waves in the tank to study the effect of waves on the water turbulence. And, third, we select experimental conditions for oil dispersion experiments.

We describe the experimental setup in Section 2 and the experimental instruments and techniques in Section 3. New instruments, such as the laser Doppler velocimeter and the photodiode wave gauge have been developed to sense remotely the velocity and the vertical displacement of the water surface. In Section 4, we present the measurements of water turbulence under the predominant influence of wind. In Section 5, the effects of waves on the water motion are presented. Vertical profiles of the mean

velocity, rms velocity fluctuations and other statistical quantities are presented. In Section 6, we present the oil concentration measurements, including the oil concentration profile and droplet size distribution. Conclusions based on our present study are given in Section 7. Experimental results are presented in tabular and/or figure form. Finally, recommendations for future research is presented in Section 8.

2. EXPERIMENTAL SETUP

2.1 Wind-Wave Tank

The wind-wave tank used in the present investigation is composed of a wave tank and a wind tunnel, each of which is 9.1 m long, 1.2 m wide and 0.91 m deep. Figures 1a and 1b show the wind tunnel and the wave tank. The description of the wind-wave tank has been presented by Veenhuizen, et al. (1975). Since the wind-wave tank has been modified for the present investigation, a brief description is given as follows.

The wind tunnel is open-ended with a blower located in the upwind end. The wind tunnel is suspended from above over the wave tank. It has an adjustable ceiling to allow for the adjustment of the pressure gradient in the wind tunnel. The maximum speed which can be obtained in this wind tunnel is 10 m/sec.

The wave tank has transparent side walls. A carriage was mounted on top of the wave tank to transport instruments and to support probes within the wave tank and the wind tunnel. A wave maker was installed at the upwind end of the water tank. The wave maker is a vertical flap, made of 20 mm plexiglas plate, which is 40 cm high and spans across the wave tank. It is driven by an electro-hydraulic servo-control and is capable of generating surface waves containing single or multiple frequency components.

The frequency response of the flap displacement is essentially constant over the frequency range of 1/2 to 10 Hz with virtually no phase shift. The maximum stroke of the flap is 10 cm. At higher frequencies, the response displacement of the flap diminishes rapidly and is limited by the mechanical response. The maximum wave height is about 8 cm. If the wave height is over 8 cm, appreciable cross waves appear.

A wave absorber was located at the downstream end of the tank to absorb surface waves generated by the wind or the wave maker. Basically, it is a rough, porous, sloping beach which dissipates the surface-wave energy by causing the waves to break as they run up on the beach and to

be drained of energy further as the fluid runs back down the beach through many small openings on the beach surface. The wave absorber (Figure 1) is constructed of a plastic grid, topped with 5 cm layers of horse hair, and covered with a layer of herring fish netting. The wave absorber extends across the width of the tank and is 1.5 m long. When the absorber is at about a 10-degree angle to the water surface in the tank, the reflection coefficient, defined as amplitude reflected/amplitude incident, is measured to be less than 5 percent. Thus, the wave absorber works effectively in damping out the upcoming waves.

2.2 Reverse Flow Control

When wind blows over the water surface, a drift layer in the surface water sets up due to the shear stress exerted on the water by the wind. Through the action of viscosity, a water boundary-layer develops which can become turbulent when the Reynolds number is sufficiently large. The boundary-layer flow entrains the fluid from below, and its thickness grows with fetch. To satisfy the continuity of the fluid and because of the finite length of the wave tank, a reverse flow results in the lower part of the tank. The drift layer and the reverse flow, together, form a very complicated flow field. On the other hand, in the ocean except the near shore region, such a reverse flow is negligible due to the large scale of the flow field. Hence, it is desirable to minimize the reverse flow effects in the laboratory experiment.

A false bottom 15 cm above the tank floor was installed and a transition plate guided the reverse flow close to the wave absorber to flow under the false bottom. In the upwind end of the false bottom, there was a spacing of about 1 m between the end wall and the end of the false bottom. The shape and dimensions of this transition plate were determined by trial and error to maximize the flow under the false bottom and minimize the reverse flow, if any, above it. For the case when wind blows over the surface, the false bottom worked quite well and the reverse flow was practically negligible above the false bottom. When mechanically-generated waves were added, the false bottom did not seem to control the reverse flow well, so it was removed. The measurement here, however,

showed that the drift layer, for the case of mechanically-generated waves with wind, is not as deep as for the case when wind blows over the surface, and thus, the reverse flow control may not be critical.

2.3 Oil Feeding System

A flow system was made to feed a steady and uniform layer of oil at the upwind end of the wave tank, and to remove the oil continuously from the downwind end to avoid build-up of oil. Figure 2 is a schematic of the oil feeding system. A Teel rotary gear pump manufactured by Dayton Electric Manufacturing Company, model 1D 767, capable of delivering 27 liter/min with no head and 25 liter/min at 7 kg/cm^2 , is used to move the oil from a 230 litre polyurethane tank to a 20 litre constant head tank that is about 1.8 m above the water surface in the wind-wave tank. Oil from the constant head tank flows through a rotameter to a specially designed oil feeder. The feeder consists of a 19 mm aluminum tube with 48 holes ranging in sizes from 3- to 6 mm and pointing upward. Outside this tube is a 30 mm plastic tube with 48 holes, 5 mm in diameter, 25 mm apart and pointing downward. Outside the plastic tube is a 32- by 32 mm square-aluminum channel with web facing downward. A teflon sheet with one end taped to the channel guides the oil flow down on the water surface. The other end of the teflon sheet floats on the water surface. This oil feeder spans the tank above the water surface and below a transition plate which guides the air flow over the water surface. The oil discharge read from the rotameter was calibrated with a container of known volume and a stop watch. It's worth mentioning that slots were made in the transition plate to allow air to enter into the space between the transition plate and the wave surface. Thus, the teflon sheet was forced to be flat on the water surface and to follow the wave motion.

The oil fed from the oil feed system floats on the water surface and drifts downwind by the current induced by wind and waves. As the oil slick reaches the downstream end, it is mixed with some water due to the turbulent mixing. The oil-water mixture is then removed from the water

surface using a two-dimensional overflow drain that connects to a second 230 liter polyurethane tank which serves as a settling tank to allow the oil to separate from the water. The recovered oil can be recycled for the next experiment, and the water is discarded. This semi-closed system permits a continuous operation for about 15 minutes, which is enough time for completion of an experimental run of oil dispersion.

2.4 Selection of Oil

For the oil dispersion equipment, it is usually best to use crude oils, e.g., Kuwait or Libyan crude. We did not use crude oils, however, because it is difficult to control their properties, since they can vary from barrel to barrel. Moreover, the purpose of the present study was to characterize and identify dispersion mechanisms acting on an oil slick of any kind. An oil was selected based on the following criteria. The density and viscosity of the oil must be close to those of the crude oils mentioned. The oil must not mix easily with the water otherwise, the oil properties could change significantly as the dispersed oil drifts along the wind-wave tank. In other words, we are not interested in the emulsification process occurring in the present experiments. The oil must separate easily from water when the mixture of oil and water returns to the oil settling tank from the overflow drain located in the downwind side of the wave absorber, thus, the oil can be recovered for re-use. The oil must be able to form a thin sheet like the oil slick in the ocean.

To examine the rate of recovery and separation from water after mixing, four kinds of oils, namely, vegetable oil, Texaco Almag oil, Diesel oil No. 2 and mineral oil were tested for selecting the oil to be used for the oil dispersion experiment. The oil sample was put in a bottle with an equal amount of water and shaken for several seconds. A general observation as to the rate of recovery into two separate fluids was made and is described as follows. For vegetable oil, the rate of recovery is slow. Foam appears on the boundary between fluids, and water droplets are formed and are suspended in the oil. For Texaco Almag oil the rate of recovery is also slow, and water droplets suspended in oil are observed. Diesel oil No. 2 has fast recovery and

clean separation. Mineral oil has slow recovery; droplets form and suspend in both fluids, and the oil clings to the bottle.

Spreading on a water surface also was tested with the above and additional oils in selecting the best-suited oil for the oil dispersion experiment. A small quantity of the oil sample was poured on a water surface. The resulting oil behavior was observed and is described as follows. Diesel Oil No. 2 forms a film over the entire surface. Diesel Oil No. 1 forms a film, but not as readily as the Diesel Oil No. 2. Mineral Oil forms lenses, and a thick film adheres to the glass. Vegetable Oil, Texaco Almag Oil and hydraulic oil No. 215 all form lenses.

Based on the tests described above, we selected Diesel oil No. 2 because it absorbs water least, separates from water quickly and can form a thin oil film over the water surface. Prior to each experiment, the physical properties of the oil, such as specific gravity and viscosity, are measured. Table 1 is the summary of the oil properties. The physical properties did not vary noticeably during the period of experiments. For example, on December 14, 1977, we measured the oil properties before use, i.e., viscosity = $18.9 \text{ cm}^2/\text{sec}$ and specific gravity = 0.84. After use during the same day, water had mixed with oil, and both viscosity and specific gravity increased accordingly. New oil of about a quarter volume of the used oil was then added to the used oil to ensure that the oil properties remained practically unchanged. For example, between December 14, 1977 when new oil was first used and January 18, 1978, viscosity and specific gravity increased by about 7- and 10 percent respectively. Whenever we found that the specific gravity and viscosity changed significantly, the recycled oil was drained and replaced by fresh oil. As noted in Table 1, new oil was supplied for future experiments on January 19, 1978. The interfacial tension at 20°C between air and water and between air and oil are about 70- and 30 dyne/cm, respectively.

3. EXPERIMENTAL INSTRUMENTS AND TECHNIQUES

3.1 Hot-Wire and Hot-Film Probes

For velocity measurements in the air, we used two hot-wire probes manufactured by Thermo Systems Inc. (TSI 1210-T1.5) operated with two constant-temperature hot-wire anemometers (TSI Model 1054B). A typical calibration curve of the hot-wire probe is plotted in Figure 3. A Pitot-static tube with a Gilmont micromanometer was used for calibration.

Twenty channels of hot-film anemometer (TSI Models 1051-10 and 1053B) were used with ten cross-film probes (TSI Model 1284) to make simultaneous measurements of the instantaneous longitudinal and vertical velocity components in the water. The hot-film probes were mounted on a probe strut which in turn was clamped on the instrument carriage. The calibration was made by towing the hot-film probes along the wave tank. The towing speed was registered with the rotational speed of the motor which drove the towing system. A slot wheel with a light-emitting-diode and a photocell was mounted on the motor shaft. As the motor turns, the photocell registers a signal which corresponds to the speed at which the slot wheel and the motor rotate. Figures 4(a) and (b) show two calibrations of a hot-film probe for high and low speed ranges.

3.2 Laser Doppler Velocimeter

The hot-film probe is an accurate and sensitive instrument for measuring velocity; however, if there exists a reverse flow, the hot-film probe is not useful because it senses speed but not the flow direction. Hence, we cannot use the hot-film probe to measure velocity in large amplitude waves, where large reverse flow results from the orbital motion of the waves. To overcome this difficulty, we use a laser Doppler velocimeter (LDV) developed at the Flow Research Company. The LDV was designed to operate in the dual-beam backscatter mode, and it has the frequency shift capability to measure velocity even when the reverse flow is present. Some specifics which are relevant to the present experiments are described briefly as follows. Detailed descriptions of the design are given by Bachalo and Lin (1977).

The LDV consists of a 4-watt Argon-ion laser (Spectra Physics Model 164-05), a set of transmitting and receiving optics, two acousto-optic modulators or Bragg cells (Isomet Corporation), a photomultiplier (RCA 7767/1C with S11 response), an amplifier (Advantek SD7-0614B), a counter-type signal processor (Macrodyne Model 2096) and a bandpass filter (Krohn-Hite Model 3103). The laser, the optics and the photomultiplier were all mounted on a 1.2- by 0.91 m optical table which was made of 0.64 cm aluminum plates sandwiched with honeycomb. The top surface of the optical table was drilled with 0.64 cm threaded holes into which optic stands can be mounted. The optical table was mounted on a steel base, which was equipped with an oil jack for adjustment of vertical displacement up to 48 cm. The surface also could be tilted in one direction about ± 30 deg. from its leveled position.

Figures 5 (a) and (b) are a photograph and a schematic of the LDV. The laser beam projected from the laser housing is reflected twice by two 45 deg. mirrors, and then split into two beams with a splitter cube. Both beams were frequency shifted with two Bragg cells and were then focused with an achromatic lens at the measuring point. Due to the interference of the two split light beams, a fringe pattern forms at the focal point, and the fringe pattern moves at a speed corresponding to the frequency shifted by the Bragg cells. The speed at which the fringe frame moves is calculated by $d_f \times \Delta f$, where d_f is the fringe spacing and Δf is net frequency shift. The fringe spacing d_f can be calculated by

$$d_f = \frac{\lambda}{2 \sin \left(\frac{\theta}{2} \right)} \quad (3-1)$$

where λ is the wavelength of the laser and θ is the beam crossing angle at the focal point.

The water was seeded with Pliolite plastic particles for scattering purposes. The particles, manufactured by Goodyear Rubber Company, were ground, sieved and filtered to remove large ones. Figure 6 shows a photograph of the particles viewed with an electronic microscope. The average

particle size is less than 40 μ . The particles had a specific gravity of about 1.03. Because of their small size, the particles can follow the flow motion very well.

A receiving lens (0.5 m focal length) imaged the focal point onto a photomultiplier through a pinhole 0.05 cm in diameter. The scattering light from a seeded particle at the focal point was therefore collected onto the photomultiplier. The photomultiplier output, which was proportional to the scattered light intensity, was amplified, band-pass filtered and fed into the Macrodyne signal processor.

The Macrodyne processor can process and validate the frequency information in the signals, and, then, provide voltage output in both analog and digital forms proportional to the Doppler shift period τ_d . Figure 7 is a block diagram showing the various stages of data recording and processing of the LDV. The particle velocity U_p can thus be calculated from the difference between the Doppler shift frequency and the frequency shift introduced by the Bragg cells,

$$U_p = d_f(f_d - \Delta f) \quad (3-2)$$

where $f_d = 1/\tau_d$ is the Doppler shift frequency. The maximum negative velocity that can be resolved by the LDV is therefore $U = -d_f \Delta f$. The setup can be slightly modified for measurements of the instantaneous vertical velocity by rotating the beam splitter cube and the two Bragg cells 90 deg. Figure 8 shows a calibration curve of the LDV system measured in an air jet. For the measurements in the air, we used water droplets as seeding particles. The LDV measurement is in good agreement with the Pitot tube result. The calibration of the LDV in water is described in Appendix B.

3.3 Capacitance Probe

For wave-height measurement, we used a capacitance gauge manufactured by Flow Research Company (Model 1204). The capacitance gauge had a bare stainless steel tube (1.6 mm o.d.) or a teflon coated wire as the sensor.

Calibration was made, before or after each run, by displacing the probe at several predetermined vertical increments. Figure 9 is a typical calibration curve of the capacitance probe. The calibration points were fitted with a second degree polynomial.

3.4 Photodiode Wave Gauge

In case an oil slick is present, the capacitance probe fails to measure surface wave height because of oil contamination. To avoid contamination, we developed a photodiode wave gauge - a remote sensor for measuring surface wave height. The photodiode wave gauge includes a Reticon camera and a controller manufactured by Reticon Corp. (Model LC 600 V and RS 605) and a 4-watt-Argon-ion laser (Spectra Physics, Model 164-05). Figure 10 shows a schematic of the photodiode wave gauge, and Figure 11 is a photograph of the experimental setup for remotely sensing surface waves. The laser beam serves as a light source to illuminate the interface between the air and the water or between the air and the oil. Fluorescent dye (Fluorescein disodium salt) was premixed uniformly in the water. The concentration was about 1 ppm. By vertically projecting the laser beam from the air to the water or to the oil slick, a bright fluorescent beam is produced in the water and a sharp dark-to-bright interface appeared on the water surface or the surface of the oil slick. This dark-to-bright interface can be detected by a vertical linear array of photodiodes mounted inside the Reticon camera.

The photodiode array has 256 elements spaced 25.4 μm center to center. The air-water interface marked with the fluorescent dye was focused on the photodiode array by optics including lenses and extension tubes. The field-of-view can vary from a fraction of a centimeter to a few meters. The spatial resolution in measuring the vertical displacement of the air-water interface can be adjusted by varying the size of the field-of-view. For example, the spatial resolution is 0.04 cm when the field-of-view is 10 cm.

The position of the image of the air-water interface or air-oil interface was determined electronically by a scanning control. The

scanning rate ranges from 0.4- to 40 μ s, and thus, it ensures the fast response of the photodiode wave gauge. Figure 12a shows a schematic of the laser beam and the corresponding light intensity profile along the beam in the vicinity of the air-water interface. Figure 12b shows a complete scan of the VIDEO output of photodiodes. The scan started from the first diode which was focused on the laser beam above the air-water interface and ended at the last diode which was focused on the laser beam below the interface. The vertical lines in Figure 12b represent the analog pulses of the individual diodes, and, at the interface there is a large jump in voltage output. When surface waves are present, the air-water interface oscillated vertically and the pattern of the analog pulses shown in Figure 12b moves accordingly. By detecting the position of the sharp slope of the analog pulse one could therefore register the vertical displacement of the water or oil surface. The registration was done by comparing a THRESHOLD output with the VIDEO output. When the voltage output of an analog pulse is less than the threshold level, the processor registers a logical "zero". When the voltage output exceeded the threshold level within one scan, the processor will register logical "ones" for the rest of the scan (Figure 12c). The registered logical signal was then electronically counted to determine the position of the "nth" diode where the "zero"-to-"one" occurred and where the air-water interface is imaged.

Calibration of the photodiode gauge was made by displacing it at several vertical positions with predetermined increments. The diode numbers are plotted versus the vertical displacement in Figure 13. The calibration points are fitted with a straight line.

The performance of the photodiode wave gauge was dynamically calibrated with a capacitance probe positioned side by side in close proximity in a mechanically-generated wave. The wave frequency was selected to be 1.6 Hz for which the meniscus effects on the performance of the capacitance probe are not important. In Figures 14 and 15, we present the wave profiles of mechanically-generated waves measured with the photodiode

wave gauge and the capacitance probe. The two wave profiles agree quite well except in the regions near wave crests and troughs. Apparently, near wave crests and troughs, the surface tension effect causes the deviation between the wave profiles measured with the capacitance probe and the photodiode wave gauge. Note that Sturm and Sorrell (1973) conducted an experiment to determine the spatial and frequency response of a capacitance gauge to surface waves. Because of meniscus effects due to surface tension, the capacitance probe has a spatial resolution of about 6 mm and a frequency response of 8 Hz.

3.5 Data Acquisition and Process

The signals measured with instruments described in previous sections are transmitted to a minicomputer system which stores and processes the data. The system consists of a Nova-800 minicomputer with a 32-K core, supported by peripheral equipment. This peripheral equipment includes: (1) two magnetic disk drives, an Iomec and a Diablo, each having a 2.5 M words capacity, (2) a Wang 9-track 800-BPI, magnetic-tape drive, (3) a Houston Instruments DPI incremental plotter, and (4) a Versatec model 1100A electrostatic printer-plotter. In addition, the computer is equipped with floating-point, integer-multiply-divide, digital-I/O, and digital-analog-conversion hardware.

Analog data from the wind-wave tank is sent through signal conditioners which adjust the voltage ranges by subtracting a d.c. level, applying an amplification factor, and then low-pass filtering the signals before analog-to-digital conversion (A/D) for the computer. Signal conditioning is provided for 48 channels of analog data. The A/D converter, Analogic Corporation Series AN5800, has a capacity of 48 data channels at 13-bit resolution, and an overall sampling rate of 44,000 samples/sec. The data are multiplexed and sent to the computer interface by the A/D converter. The computer records the digital data on a magnetic disk on-line during the progress of the experiments for playing back and processing at a later time. Data stored on the disk may be transferred to magnetic tape for long-term storage, or it may be called into the computer core for processing.

4. EFFECT OF WIND ON WATER MOTION

Measurements of velocity in the water were conducted for the case when the wind dominated the motion. As waves were generated by wind, the wave effect on the water motion was also investigated. We first measured the mean velocity and the rms longitudinal velocity in the air boundary-layer over the water surface. Based on these measurements, we could establish the wind conditions required for the present investigation. The water surface displacement was measured to obtain the wave characteristics for the experimental conditions which were of interest here. The drift velocity on the water surface was measured to determine the effect of wind speed on the surface drift velocity. The motion in the water boundary-layer was visualized with dye, and the boundary-layer thickness was determined from the visualization results. The effect of wind speed and fetch on the evolution of the boundary-layer thickness was established from the visualization results. A vertical array of hot-film probes was positioned along the centerline of the wind-wave tank at several fetches to measure the velocity field in the water boundary-layer. Vertical profiles of the mean velocity, the rms longitudinal and vertical velocity fluctuations, the Reynolds stress and the turbulence dissipation rates were obtained. Velocity spectra were calculated from the data of velocity fluctuations to estimate the contribution of the wave motion on the velocity field. From the measurements to be described in the following, we could then determine the effect of wind on the motion in the water boundary-layer under a mobile water surface.

A definition sketch for the air and water boundary-layers to be investigated here is drawn in Figure 16. The air boundary-layer is characterized by a thickness δ_a , and the water boundary-layer by a thickness δ_w . The fetch, x , is measured from the downstream end of the transition plate which guides the air flow over the water surface, and z is positive upwards measuring from the undisturbed water surface.

The dominant wavelength and height are denoted by λ and H . The freestream velocity is denoted by U_∞ .

4.1 Air Boundary-Layer

Figure 17 shows the mean velocity and turbulence intensity profiles measured in the air boundary-layer at $x = 5$ m and $U_\infty = 10$ m/sec. The profiles are similar to the ones measured by others in wind-wave tanks. The rms of longitudinal velocity fluctuations has a maximum of about 12 percent of the freestream wind speed. The boundary-layer thickness is about 18 cm. A logarithmic profile is observed when plotting the mean velocity profile on a semi-log plot, and a solid line, representing

$$\bar{U}/u_{*a} = 5.75 \log z/z_0,$$

is drawn on Figure 18 to approximate the logarithmic profile. The friction velocity estimated from best fit is $u_{*a} = 58$ cm/sec and the aerodynamic roughness is $z_0 = 0.04$ cm. The maximum rms of longitudinal velocity fluctuation is about twice that of the air friction velocity. These results show that the air turbulent boundary-layer over wind-waves is very similar to the turbulent boundary-layer over a rough flat plate, and they are consistent with previous measurements by many investigators.

For a turbulent air boundary-layer over wind-waves, Lin and Veenhuizen (1975) collected experimental results of many investigators. They correlated the growth of the air boundary-layer thickness δ_a with the freestream velocity U_∞ and the fetch by the expression

$$\frac{g\delta_a}{U_\infty^2} = (0.025 \pm 0.003) \left(\frac{gx}{U_\infty^2}\right)^{4/5}, \text{ for } 0.2 < \frac{gx}{U_\infty^2} < 17, \quad (4-1)$$

where g is the gravitational acceleration. They also found that the air friction velocity u_{*a} can be expressed in the following form

$$\frac{u_{*a}}{U_{\infty}} = (0.055 \pm 0.01) \left(\frac{Rx}{U_{\infty}^2} \right)^{-1/10}, \text{ for } 0.3 < \frac{Rx}{U_{\infty}^2} < 200. \quad (4-2)$$

The present data conform closely to these empirical formulas.

4.2 Wave Characteristics

A typical output of a capacitance probe is shown in Figure 19. The freestream wind speed was 10 m/sec and the capacitance probe was placed at 5 m fetch. The instantaneous water surface displacement η is measured from the undisturbed water surface level. In this figure, a dominant frequency is evident, and wave packets of smaller frequency are shown to be consistent with other wind-wave observations. The frequency spectrum of the water surface displacement (wave energy spectrum), part of which is shown in Figure 19, is presented in Figure 20. The dominant frequency is 3.5 Hz, and the spectrum for $4 < f < 10$ Hz follows $S(f) = \alpha g^2 f^{-5}$, where $\alpha = 5 \times 10^{-4}$, for this particular run. The value of α is larger than the value $\alpha = 7.5 \times 10^{-6}$ observed in the ocean (Phillips, 1966). Others have found that larger values of α are observed in the laboratory than in the ocean also. The spectrum for frequencies above 10 Hz should be viewed with caution since the capacitance probe is limited in its frequency response due to the meniscus effects.

The variation of the root-mean-square value of the water surface displacements with wind speed is shown in Figure 21 for two fetches, $x = 5$ - and 6 m. As expected, $\sqrt{\eta^2}$ increases with both fetch and wind speed. The effect of wind speed variation on the dominant wave frequency is shown in Figure 22 for two fetches, $x = 5$ - and 6 m. Here, the dominant wave frequency f_0 is defined as the frequency at which the frequency spectrum peaks. The dominant wave frequency decreases with both fetch and wind speed. The effect of fetch on the dominant wave frequency is shown in Figure 23 for wind speed $U_{\infty} = 10$ m/sec. End wall effects in the wave tank possibly contribute to the leveling off of the curve shown for fetch $x \geq 5$ m.

The dominant wave phase speed could be determined by correlating the signals from two capacitance probes separated by a distance Δx in the

wind direction. For a simple train of waves, the phase speed can be measured as $C_p = \frac{\Delta x}{\Delta \tau}$, where $\Delta \tau$ is the time lag at which the cross-correlation has its first maximum. For a random train of waves, as is the case with wind-waves, a more accurate determination of $\Delta \tau$ for each wave component requires computing the Fourier transform of the cross-correlation. The complex Fourier transform consists of a real part (co-spectrum) and an imaginary part (quad-spectrum). At the dominant frequency, $\Delta \tau$ is related to the phase angle ($= \tan^{-1} \frac{\text{co-spectrum}}{\text{quad-spectrum}}$) by $\Delta \tau = \frac{\text{Phase angle}}{360 \times f_o}$. Figure 24 shows the effect of wind speed variation on the wave phase speed C_p for two fetches, $x = 5$ and 6 m. The phase speed increases with increasing wind speed. Figure 25 shows fetch effects on the wave phase speed C_p . The end wall effects possibly contribute to the leveling off of the curve.

From the dominant wave frequency f_o and the dominant wave phase speed C_p , one can easily compute the dominant wavelength $\lambda = \frac{C_p}{f_o}$. Figure 26 shows the effect of wind speed variation on λ for two fetches, $x = 5$ and 6 m; λ increases with both fetch and wind speed. The dominant wave slope \sqrt{g}/λ is shown in Figure 27 and it increases with fetch and wind speed. Figure 28 shows the effects of fetch on the dominant wavelength for wind speed $U_\infty = 10$ m/sec.

4.3 Surface Drift Velocity

The drift velocity on the water surface was measured using paper disks which had been coated lightly with wax so they would float. The diameter of the disk was about 7 mm, and the trajectory of the disc floating on the water surface was recorded with a 16-mm movie camera. The time required to travel a known distance was registered with a digital clock with 0.1 second resolution. For each run, the measurements were repeated several times, and the mean and the standard deviation of the measurements were determined. Table 2 lists the measured surface drift velocity in a tabulated form. Also shown are the number of floats observed for each run as well as the standard deviation. Figure 29

shows the variation of surface drift velocity U_s with fetch for wind speeds $U_\infty = 4, 7$ and 10 m/sec. The surface drift velocity U_s has an average value of about 3.2 percent of the wind speed.

4.4 Water Boundary-Layer

The water boundary-layer that develops under the action of wind was visualized with the dye technique. A fluorescent dye was injected at the beginning of the test section using an L-shape tube 2 mm in diameter. A sheet of laser light was used to illuminate the fluorescent dye in a vertical plane parallel to the wind direction, and a movie film recorded the motion in the boundary layer. Figures 30 (a) through (f) show the photographs of the dyed boundary layer for three wind speeds $U_\infty = 4$ -, 7 - and 10 m/sec and two fetches, $x = 1.7$ - and 3.2 m. In the photographs, a bright horizontal line appears which represents the water surface. The bright line is produced when the sheet of laser light intersects the water surface. For $U_\infty = 4$ m/sec, the boundary layer appears to be laminar at $x = 1.7$ m, and it becomes turbulent at $x = 3$ m as indicated by the substantial increase in thickness. For $U_\infty = 7$ - and 10 m/sec, the flow is turbulent at both fetches as indicated by irregularity of the dye boundary and by the eddy structure in the boundary layer. From the dye visualization results, we determined the mean thickness and its standard deviation of the water boundary-layer. Table 3 contains the results, and Figure 31 shows the dependence of the water boundary-layer thickness on fetch and wind speed. The boundary-layer thickness δ_w is non-dimensionalized using the wind speed U_∞ and the acceleration of gravity g . The solid line on the figure represents the empirical correlation

$$\frac{g\delta_w}{U_\infty^2} = 0.025 \left(\frac{gx}{U_\infty^2} \right)^{4/5} \quad \text{for } 0.2 < \frac{gx}{U_\infty^2} < 3 \quad (4-3)$$

The coefficient expressed in equation 4-3 is coincidentally equal to that computed by Lin and Veenhuizen (1975) for air boundary-layers in

wind-wave tank experiments. The present data at small fetches for wind speed $U_{\infty} = 4$ m/sec deviate considerably from this formula. We observed visually that at these fetches the water boundary-layer at wind speed $U_{\infty} = 4$ m/sec did not resemble the fully-developed turbulent boundary-layers that were observed at the same fetches for higher wind speeds.

4.5 Mean Velocity

Mean velocity profiles in the water boundary-layer were obtained by averaging the signals from individual cross-element hot-film probes over a period of 40 seconds. A typical mean velocity profile is shown in Figure 32 for wind speed $U_{\infty} = 10$ m/sec and fetch, $x = 5$ m. The figure shows three different runs to check repeatability. At the water surface, the mean drift velocity determined from the floating disk measurement is plotted, and it is denoted by a cross symbol. Near the water surface, the data show a sharp velocity gradient. The drift layer determined from the mean velocity profile has a thickness of about 25 cm. Figure 33 is a replot of the mean velocity defect profile on a semi-log paper. The mean velocity is shown relative to the surface drift velocity. One could fit a straight line to the part of the profile close to the water surface by

$$\frac{U_s - \bar{U}}{u_*} = 5.75 \log \left(\frac{-z}{z_0} \right) .$$

From the plot, the friction velocity u_* is determined to be 1.81 cm/sec, and the roughness height $z_0 = 0.029$ cm. Thus, the present result shows the existence of the logarithmic profile of the mean velocity in the region near the water surface, and it is consistent with previous measurements in wind waves by Shemdin (1973) and Wu (1975). The measurement of the mean velocity defect shows that the water boundary-layer under the water surface resembles the turbulent air boundary-layer over the water surface, and the water boundary-layer is produced as the result of the wind stress exerted on the water surface.

Table 4 shows the friction velocity as determined from similar profiles for different wind speeds and fetches. Also shown is the corresponding friction velocity for the air boundary-layer as computed from the empirical formula expressed in Equation (4-2). The ratio of the water shear stress $(\rho u_{*w}^2)_w$ to the air shear stress $(\rho u_{*a}^2)_a$ at the air-water interface indicates the percentage of momentum that is extracted from the air boundary-layer by the water boundary-layer. This ratio increases as the fetch and the wind speed increases. At $U_\infty = 10$ m/sec, and $x = 6$ m, the ratio has a value of 0.9, or equivalently, the ratio of the wave drag coefficient to the total wind drag coefficient is 0.1. Based on the saturated wave energy spectrum, Phillips (1966) estimated the ratio of the wave drag coefficient to the total wind drag coefficient c_w/c_d to be about 0.1; also Lin and Veenhuizen (1975) obtained the ratio c_w/c_d for wind waves by correlating many experimental data obtained in wind-wave tanks, i.e.,

$$\frac{c_w}{c_d} = \frac{3}{8} \frac{\rho_w}{\rho_a} \frac{g \eta^2}{U_\infty^2 \theta} \quad (4-4)$$

where ρ_w and ρ_a are water density and air density and θ is the momentum thickness of the air boundary-layer. Their computed ratio was $c_w/c_d = 0.1 \pm 0.03$, for $0.3 \leq \frac{2x}{U_\infty^2} \leq 17$.

Figure 34 shows mean velocity profiles in the water boundary-layer at fetch $x = 5$ m, for three different wind speeds, $U_\infty = 4$ -, 7- and 10 m/sec. The average velocity gradient and the thickness of the boundary-layer both increase with wind speed.

4.6 RMS Velocity Fluctuations

Figure 35 shows the vertical profiles of the rms value of longitudinal velocity fluctuations in the water boundary-layer for fetch $x = 5$ m and wind speed $U_\infty = 10$ m/sec for three repeated runs. The rms values monotonically decrease with depth below the water surface. Its maximum value occurs close to the water surface and is about 20 percent of the mean surface drift velocity and about 3.5 times the frictional

velocity u_* in water. In the turbulent air boundary-layer over the water surface, previously measured by Young et al. (1973) and Yu and Lin (1975), the maximum rms longitudinal velocity fluctuations is about 15 percent of the air freestream velocity and is about three times the air friction velocity. Hence, we have more evidence supporting that the water boundary-layer under the water surface resembles the air boundary-layer over the water surface. It should be noted, however, that $\sqrt{u^2}$ contains in part the contribution from the orbital motion of the waves. It will be shown in Section 6.7 that this contribution is by no means negligible.

Figure 36 shows the vertical profiles of the longitudinal velocity fluctuations measured at fetch $x = 5$ m and for three different wind speeds $U_\infty = 4$ -, 7- and 10 m/sec. The maximum rms value is about 20 percent of the mean surface drift velocity for wind speeds 7- and 10 m/sec, and 10 percent for wind speed 4 m/sec. These results show that the water boundary-layer for $U_\infty = 4$ m/sec has not been fully developed when comparing with those for $U_\infty = 7$ - and 10 m/sec.

The vertical profiles of the rms vertical velocity fluctuations in the water boundary-layer, $\sqrt{w^2}$ at fetch $x = 5$ m and for wind speed $U_\infty = 10$ m/sec are shown in Figure 37. Data obtained in three repeated runs are included and, the repeatability is fairly good. By comparison between Figures 35 and 37, we obtain that the ratio of $\sqrt{w^2}$ to $\sqrt{u^2}$ ranges between 0.70 near the water surface and 0.50 at larger depths. The vertical velocity fluctuations again contain in part the contribution from the orbital motion of the waves. Figure 38 shows the vertical profiles of rms and the vertical velocity fluctuations $\sqrt{w^2}$ measured at fetch $x = 5$ m for three different wind speeds, $U_\infty = 4$ -, 7- and 10 m/sec. Except for the reduced magnitude, the behavior of $\sqrt{w^2}$ is similar to that of $\sqrt{u^2}$.

The Reynolds shear stress or the correlation between the longitudinal and vertical velocity components \overline{uw} is a very important quantity that determines the vertical transfer of momentum in the water boundary-layer.

This quantity directly affects the vertical dispersion of an oil slick. Figure 39 shows Reynolds stress profiles measured at fetch $x = 5$ m and for three different wind speeds, $U_{\infty} = 4$ -, 7 - and 10 m/sec. For $U_{\infty} = 10$ m/sec, the measured maximum value of $-\overline{uw}$ is $2.6 \text{ cm}^2/\text{sec}^2$ which is about 80 percent of the shear stress estimated from the mean velocity profile (Figure 33). The Reynolds stress has a negative sign over most regions of the water boundary-layer, and, therefore, the momentum is transferred downwards.

The turbulence dissipation rate ϵ was determined from the mean square of the time derivative of the longitudinal velocity fluctuations by assuming local isotropy and the validity of the Taylor's frozen turbulence hypothesis, i.e.,

$$\epsilon = 15 \nu \overline{(\partial u / \partial t)^2} / \overline{U}^2 .$$

Figure 40 shows the vertical profiles of the dissipation rate measured at fetch $x = 5$ m for three different wind speeds, $U_{\infty} = 4$ -, 7 - and 10 m/sec.

The turbulence measurements in the water boundary-layer are conveniently tabulated in Tables 5 through 17 for different wind speeds and fetches. Each table contains the variation of the important statistical quantities with depth below the water surface. The quantities shown are mean velocity in the longitudinal direction, root-mean-square velocity fluctuation in the longitudinal and vertical directions, Reynolds stress and its coefficient, dissipation rate, dissipation rate weighted by the water depth, and the non-dimensional parameter

$$\frac{\epsilon |z|}{\overline{u^2}^{3/2}}$$

that has a value of order one in the logarithmic region. It is noted that this parameter becomes larger outside the boundary layer where the signal is contaminated with instrument noise and reverse flow effects.

4.7 Velocity Spectra

An important additional statistical quantity that could be completed from the random velocity signal is the spectrum of the velocity fluctuations, or the distribution of kinetic energy for different frequency bands. For the present study, such a quantity has an additional significance in that the contribution of the wave orbital motion to the total velocity fluctuations should be more pronounced at the dominant wave frequency. A typical spectrum $S_u(f)$ of longitudinal velocity obtained in Run No. OIL-21 is shown in Figure 41 for fetch $x = 5$ m and wind speed $U_\infty = 10$ m/sec. The spectrum shown is measured at depth $z = -0.8$ cm below the undisturbed surface. The dominant frequency $f = 3.5$ Hz, corresponds exactly to that in the wave energy spectrum. It is seen from the figure that the contribution of the orbital motion to the total velocity fluctuations is by no means negligible. The second harmonic component at $f = 7.0$ Hz is noticeable. In the frequency range greater than the dominant wave frequency, the velocity spectrum is, however, wider than the wave energy spectrum, an indication of the transfer of turbulent energy from low frequency (large scale) to high frequency (small scale). The broken line shown on the figure represents the relation $S_u(f) = 25f^{-5/3}$, that is expected to be valid for an inertial subrange. The $-5/3$ law range covers about one decade of the frequency domain. By using Taylor's frozen turbulence hypothesis we can convert the frequency spectrum $S_u(f)$ into the one-dimensional wave number spectrum $E_{11}(k_1)$ as follows:

$$E_{11}(k_1) = 25 \left(\frac{\bar{U}}{2\pi} \right)^{-2/3} k_1^{-5/3}, \quad (4-5)$$

where k_1 is the wave number component in the streamwise direction. Equation (4-5) can then be used to estimate the Kolmogorov's constant α expressed in the inertial subrange spectrum (Hinze, 1959)

$$E_{11}(k_1) = \frac{18}{55} \alpha \epsilon^{2/3} k_1^{-5/3}. \quad (4-6)$$

The value of α is calculated to be 1.79 by inserting $\bar{U} = 16.16$ cm/sec and $\epsilon = 109$ cm²/sec. This value is reasonably close to the universal constant $\alpha \approx 1.44$ determined from many other turbulence measurements (Phillips 1966). Lin (1974) observed the universal constant to be $\alpha = 1.66$ by fitting experimental data to his semi-analytical spectrum in the inertial and dissipation ranges. The Kolmogorov wave number, $k_k = (\epsilon/\nu^3)^{1/4}$, is calculated to be 100 cm⁻¹ and the corresponding Kolmogorov length scale is 0.63 mm. The turbulence microscale defined as

$$\lambda^2 = \overline{U^2} / (\overline{\partial u / \partial x})^2$$

is $\lambda = 0.24$ cm, thus the turbulence Reynolds number based on the turbulence microscale, $R_\lambda = \sqrt{u^2} \lambda / \nu$, is about 150. This turbulence Reynolds number is large enough that the effects of the Reynolds number on the turbulent motions are unlikely to be important. It is worth mentioning that in laboratories, researchers have found that turbulence follows a "universal" behavior as long as R_λ is larger than 50.

Figure 42 shows the longitudinal velocity spectra measured at three different depths, $z = -0.8, -2.6$ and -7.6 cm, and at fetch $x = 5$ m, and wind speed $U_\infty = 10$ m/sec. At the frequency $f = 3.5$ Hz which corresponds to the dominant wave frequency, all these spectra show peaks. These peak values attenuate very rapidly with depth. Thus, at larger depths, the contribution from the orbital motion of the waves to the water boundary-layer becomes insignificant and the turbulent motion dominates the boundary layer flow. Here, we define turbulence as the non-organized motion in contrast to the organized orbital motion due to waves. At frequencies other than the dominant wave frequency the motion is governed by the turbulence. The turbulent energy at frequencies larger than the dominant wave frequencies attenuates rapidly with depth. The Kolmogorov frequency, defined as

$$f_k = \frac{\bar{U}}{2\pi} \left(\frac{\epsilon}{3} \right)^{1/4},$$

is calculated to be 256-, 104- and 44 Hz for $z = -0.8$, -2.6 , and -7.6 cm respectively. In other words, the viscosity cut-off frequency for the velocity spectrum decreases with the increase of depth. Figure 43 shows the spectra of vertical velocity fluctuations measured at $x = 5$ m, $U_\infty = 10$ m/sec for three depths, $z = -0.8$, -2.0 , and -7.6 cm. These spectra behave, in general, similarly to those plotted in Figure 42.

More insight into the dynamics of the water boundary-layer could be gained by computing the co- and quad-spectra of the longitudinal and vertical velocity fluctuations. These are the real and imaginary parts, respectively, of the Fourier transform of the longitudinal and vertical velocities cross-correlation. An example of these spectra is shown in Figure 44, for fetch $x = 5$ m, wind speed $U_\infty = 10$ m/sec, and depth $z = -2.6$ cm below the water surface. It is seen that both co- and quad-spectra peak at the dominant wave frequency $f_0 = 3.5$ Hz. The magnitude* and phase** of those spectra are shown on Figure 45. The magnitude peaks also at the dominant wave frequency and the phase at this frequency is -78 deg. This figure shows that the shear stress contributes not only from turbulent motion, but also from the orbital motion of waves. These results indicate the importance of the waves in transporting momentum vertically.

* Magnitude $\equiv \left[(\text{co-spectrum})^2 + (\text{quad-spectrum})^2 \right]^{1/2}$

** Phase $\equiv \tan^{-1} \left(\frac{\text{quad-spectrum}}{\text{co-spectrum}} \right)$

5. EFFECTS OF WAVES ON WATER MOTION

In this section, we present the experimental results concerning the effects of waves on the water motion. For all the experiments, the wind speed was the same, $U_{\infty} = 10$ m/sec, and waves of three different heights were generated by the wave maker. We measured the wave characteristics of these waves. The surface drift velocity under these wave conditions was measured, and the effect of wave steepness on the surface drift velocity was determined. The water boundary-layer developed under the action of wind and waves was visualized with dye, and the thickness of the water boundary-layer was determined from the visualization results. Vertical profiles of mean velocity and rms velocity fluctuations were measured using the LDV. The velocity spectra were calculated from the velocity fluctuations to determine the wave effect on the velocity field and the basic turbulent characteristics.

5.1 Wave Characteristics

The wave maker described in Section 2 was used to generate surface waves. The oscillatory motion of the wave plunger was controlled by an electronic wave generator operating at a frequency of about 1.6 Hz. The voltages of the wave generator were selected to produce three different strokes of the wave plunger, namely, $H_0 = 2.54$ -, 5.08 - and 7.62 cm. Figure 46 (a) through (d) shows the photographs of the water surface for $H_0 = 0$ -, 2.54 -, 5.08 - and 7.62 cm. All waves propagate from the left to the right. The photographs were taken at a fetch of about $x = 4$ m. For $H_0 = 0$ cm, there are no mechanically-generated waves. The waves are generated by wind. For $H_0 = 7.62$ cm, the photograph shows the spilling break up at the wave crest. In the photograph, the breaking region is shown as a bright region across the tank. The motion in the breaking wave region was so violent that we observed the entrainment of air into the water. Figure 47 shows the breaking wave region viewed from below the wave crest. In this figure, the direction of the wave propagation is from the left to the right. Under the wave crest, there appeared bright spots which indicated air bubbles. These air bubbles penetrated to a depth of about one wave height.

Figure 48 shows the wave energy spectra $S(f)$ measured with a capacitance probe at fetch $x = 2$ m and wind speed $U_{\infty} = 10$ m/sec. The spectra peak at the dominant frequency $f_0 = 1.6$ Hz and subsequent higher harmonics. The strength of higher harmonic wave components increases with H_0 . For $H_0 = 7.62$ cm, the spectral peaks at the dominant wave frequency and higher harmonics have an envelope expressed by $S(f) = 1.46 \times 10^{-4} g^2 f^{-5}$ for $f_0 < f < 10$ Hz.

The phase speed, C_p , of the dominant waves was measured with two capacitance probes separated by a distance $\Delta x = 1.02$ cm apart. These two capacitance probes were made of a thin copper wire coated with teflon. We selected the teflon coated wire probe instead of the bare stainless steel probe in order to minimize the possible cross talk between two adjacent probes. To determine the value of C_p , we calculated the cross correlation of the surface displacements measured with the two capacitance probes. The time lag of the maximum correlation, $\Delta \tau$, can therefore be determined, and it should correspond to the time required for the waves traveling over a distance Δx . Hence, the dominant phase speed can be estimated as $C_p = \Delta x / \Delta \tau$. The dominant wave speeds are 108.4-, 108.4- and 121.1 cm/sec for $H_0 = 2.54$ -, 5.08- and 7.62 cm respectively. Based on the measurements of C_0 and f_0 , we can estimate the dominant wavelength $\lambda = C_p / f_0$ as 65.3-, 65.3- and 73.0 cm for the three respective values of H_0 .

Based on the measurements of λ , one can estimate the wave phase speed by the linear wave theory. Comparison between the direct measurement and the linear wave prediction could then indicate the nonlinear effects on the wave propagation. Figure 49 shows the plot of $C_p / \sqrt{g\lambda/2\pi}$ versus the wave steepness H/λ . Here H is the wave height which can be estimated from the rms wave amplitude by $H \approx 2\sqrt{2}\sqrt{\eta^2}$. For comparison, a solid line representing

$$\frac{C_p}{\sqrt{g\lambda/2\pi}} = 1 + \pi^2 \left(\frac{H}{\lambda}\right)^2 + \frac{\pi^4}{2} \left(\frac{H}{\lambda}\right)^4 \quad (5-1)$$

is plotted (Kinsman, 1965). The last two terms in equation (5-1) represent the nonlinear effect on the phase speed. The deviation of the measurement points from the solid curve could partly be attributed to the wind induced-surface drift. Figure 50 shows the variation of rms wave amplitude $\sqrt{\eta^2}$ with fetch for three values of H_0 . We used the photo-diode wave gauge to measure the vertical displacement of the water surface because the wave height measurement by the capacitance probe becomes inaccurate when the wave breaking occurs. Each data point was calculated from a record of about 60 sec. The overall statistical error is estimated to be about 10 percent. This error is mainly contributed by a low-frequency modulation (having a period of about 20 sec) of the wave field which is possibly caused by the return flow in the wave tank.

For $H_0 = 2.54$ - and 5.08 cm, the rms wave amplitude increases with increasing fetch. For example, the wave energy per unit density, $g\eta^2$, increases from $980 \text{ cm}^3/\text{sec}^2$ at $x = 2 \text{ m}$ to $2509 \text{ cm}^3/\text{sec}^2$ at $x = 5 \text{ m}$ for $H_0 = 2.54 \text{ cm}$. In section 4.2, we have presented the measurement of rms wave amplitude for the case without mechanically-generated waves, but with wind only; the wave energy per unit density increases from practically zero at $x = 2 \text{ m}$ to $134 \text{ cm}^3/\text{sec}^2$ at $x = 5 \text{ m}$. This example shows that when mechanically-generated waves are present, the energy transfer from wind to waves appears to be more efficient than when mechanically-generated waves are not present. This observation also applies to the case of $H_0 = 5.08 \text{ cm}$. For $H_0 = 7.62 \text{ cm}$, however, the wave energy decreases with fetch. Apparently, the wave breaking causes significant energy dissipation by turbulence which overwhelms the energy transfer from wind.

Figure 51 shows the wave energy spectra measured at two fetches for $H_0 = 7.62 \text{ cm}$ and $U_\infty = 10 \text{ m/sec}$. The wave breaking reduces the energy content at the dominant wave frequency and increases the energy at higher frequencies. For $6 \text{ Hz} < f < 40 \text{ Hz}$, the wave energy spectrum follows $S(f) = 0.054 \gamma^{2/3} f^{-7/3}$. The energy gaps between higher harmonics are filled in when wave breaking occurs. Figure 52 shows the wave

energy spectra measured at $x = 5$ m for $U_{\infty} = 10$ m/sec and for various conditions of mechanically-generated waves. In the capillary wave regime, the energy increases with the value of H_0 . In the gravity wave regime, there exists an envelope expressed by $S(f) = 1.45 \times 10^{-4} g^2 f^{-5}$ for the dominant waves and their higher harmonics. This envelope could, therefore, represent the saturated wave spectrum in the present investigation. Figure 53 shows the wave energy spectra measured at $x = 5$ m for $H_0 = 7.62$ cm and for three wind speeds. In the capillary wave regime, the wave energy increases with wind speed. In the gravity wave regime, wave energy does not change appreciably, and the energy gaps between higher harmonics fill in as wind speed increases.

5.2 Surface Drift Velocity

The surface drift velocity was measured using a small paper disc floating on the water surface. The paper discs were made the same way as for the surface drift measurement described in Section 4.3. The drift of the paper discs was recorded with a 16-mm movie camera. The standard deviation of the drift velocity measurements was typically about 10 to 20 percent of the mean surface drift velocity. If breaking waves appear, paper discs may not float well on the water surface. Frequently, we did observe that paper discs were entrained into the breaking wave region below the water surface. Consequently, these paper discs were discarded when making the drift velocity measurement. On the other hand, we also observed that the standard deviation in measuring the surface drift velocity is large when breaking waves are present.

Figure 54 shows the mean surface drift velocity U_g plotted versus fetch x . The mean surface drift velocity measured at $x = 2$ m are plotted versus the wave steepness, H/λ , in Figure 55. Also plotted is the surface drift velocity measured in the wind waves at $U_{\infty} = 10$ m/sec. This is a limiting case when the height of the mechanically-generated waves approaches zero. The measurement points show that at $H/\lambda = 0.05$, the surface drift velocity is lower than that for the case when the mechanically-generated waves are not present. For $H/\lambda > 0.05$, the surface drift velocity increases with the increase of the wave steepness.

The effect of wave steepness on the surface drift has been investigated by Reisbig et al., (1973). In their laboratory experiments, the wind speed ranged from 0- to 7 m/sec and the wave steepness varied from 0- to 0.069. Their experimental results show that the drift mechanisms caused by wind and waves are not simply additive. At low wind speeds, the wave drift provides an augmentation to the wind drift, but at higher wind speeds, the waves cause a net decrease in the coupled drift velocity. This wave-induced diminishment increases as the wind speed increases. In the present investigation, we covered a wider range of H/λ . Our data show a similar wave-induced decrease when H/λ increases from 0 to 0.05. For $H/\lambda > 0.05$ the surface drift velocity increases with wave steepness. In the following paragraphs, we will try to explain the possible mechanisms which contribute to the complex behavior of the surface drift due to the coupled wind and waves.

Jeffreys (1925) hypothesized the separation mechanism for energy transfer from wind to waves. Recently, Chang et al., (1969) conducted a series of laboratory measurements of mean and turbulent velocity in the air flow region above wind-generated waves and their experimental results tend to support the separation mechanism. Banner and Melville (1976) conducted a flow visualization experiment to demonstrate that the air-flow could separate from the water surface in the lee side of mechanically-generated waves. Based on kinematic arguments, they hypothesized that the separating flow would occur when waves break. More recently, Weissman (1978) conducted laboratory experiments in the airflow over mechanically-generated waves. His experimental results, both from smoke visualization and from probe measurements, showed that the separating flow in the air could occur even though wave breaking was not apparent.

In view of the separation mechanism described above, we expect that in our experiment conducted for a wind speed of $U_{\infty} = 10$ m/sec over mechanically-generated waves, the airflow could separate from the water surface in the lee side of the waves. Although the presence of the air separation could enhance the energy transfer from wind to waves, the

effective shear stress exerted on the water by the wind is reduced. This reduction is not difficult to imagine if we realize that the separated flow would introduce a reverse flow region in which the shear stress is exerted in a direction opposite to the wind. Now, if we assume that the surface drift due to the wind should correspond to the effective shear stress exerted on the water surface, we would therefore expect that, for the case when mechanically-generated waves are present and the separation exists in the lee side of the waves, the surface drift velocity would be lower than for the case without mechanically-generated waves.

When the wave steepness increases further, additional mechanisms other than the separation mechanism could influence the surface drift. For example, the Stokes' drift (1847) on the water surface is expressed by Phillips (1966) as

$$U_d = \pi^2 \left(\frac{H}{\lambda}\right)^2 C \quad (5-2)$$

where C is the wave speed and λ is the wavelength. The Stokes' drift would become important as the wave steepness and the wave speed increase. Pottinger and Reibsig (1973) conducted an experiment to determine the effect of waves on the drift of an oil slick. The waves were generated mechanically by a wave maker. The wavelength ranged from 25- to 50 cm and the wave steepness from 0.01 to 0.07. The oil slick was, in essence, an oil lens of diameter 4.6- and 7.5 cm and thickness varying from 10^{-4} to 10^{-5} of the wavelength. Their data indicate that the oil slick drifted faster than that predicted by the Stokes' drift. They obtained an empirical relation to correlate their experimental results.

$$\begin{aligned} U_s &= U_d + U_c \\ &= \pi^2 \left(\frac{H}{\lambda}\right)^2 C + 0.445 \left(\frac{H}{\lambda}\right) C, \text{ for } 0.01 < H/\lambda < 0.07 \end{aligned} \quad (5-3)$$

$$\text{and } 25 \leq \lambda < 50 \text{ cm},$$

where U_c is the correction term of the surface drift velocity.

In the following, we will utilize the empirical result expressed in equation (5-3) to help us understand our observation of the surface drift caused by wind and waves. In Figure 55, we replot our data by subtracting the surface drift velocity by the corresponding Stokes' drift velocity, i.e., $U_s - U_d$, and subsequently by the correction term U_c , i.e., $U_s - U_d - U_c$. It is interesting to point out that the data points of $U_s - U_d - U_c$ does not show significant variation with wave steepness and they have an average value of about $0.02 U_\infty$ which corresponds to wind-induced current. This value is apparently lower than that observed for the case when mechanically-generated waves are not present. Therefore, we introduce an empirical formula for the surface drift caused by wind and waves:

$$\frac{U_s}{U_\infty} = 0.02 + \left[\pi^2 \left(\frac{H}{\lambda} \right)^2 + 0.445 \left(\frac{H}{\lambda} \right) \right] \frac{C}{U_\infty} \quad (5-4)$$

for $0.05 < H/\lambda < 0.10$, $U_\infty = 10$ m/sec and $65 \text{ cm} < \lambda < 73 \text{ cm}$.

A solid line is drawn in Figure 55 to represent equation (5-4) for $C/U_\infty = 0.12$, and it can fairly approximate our measurements.

5.3 Water Boundary-Layer

The water boundary-layer was visualized with dye techniques. The dye was introduced into the water by a vertical string 0.3 cm in diameter. The string was located along the centerline of the tank. The string was made of cotton and formed a closed loop with three point supports. Part of the string was stretched vertically in the water and part of it was exposed in the air. The part of string exposed in the air was dyed with a fluorescent dye, and it was then lowered below the water by sliding the string loop. The dye, washed away from the string, was initially vertical, and this vertical dye line was deformed and dispersed by the motion in the water. Figure 56 is a photograph showing the dye dispersion in the water for $H_0 = 7.62 \text{ cm}$ and $U_\infty = 10 \text{ m/sec}$. Two flow regions are distinctly visible. In the top region about 15 cm

below the water surface, the dye disperses in the wind direction, and in the bottom region below 15 cm from the water surface the dye disperses in the reverse direction. The top region is apparently the boundary layer of flow set up by wind and waves, and the bottom region corresponds to the return flow due to the finite length of the tank. For the case when waves are generated by wind only, we used a false bottom to channel the return flow in-between the tank bottom and the false bottom, and therefore we were able to control and minimize the reverse flow in the region between the water surface and the false bottom. We tried to use the same setup of the false bottom for the case when both wind and mechanically-generated waves were present, but the reverse flow could not be controlled as well as when only wind-generated waves were present. For lack of time to try to find a better way to control the reverse flow, we decided not to use the false bottom for the case when both wind and mechanically-generated waves were present.

The presence of the reverse flow could affect the water boundary-layer. We are not in a position to estimate these effects due to the reverse flow quantitatively, but, on the other hand, we expect that in the region near the water surface and away from the reverse flow, the flow characteristics should be most dominated by the local flow conditions such as the break up of waves and the presence of strong shear. Figure 57 presents the thickness of the water boundary-layer measured from the movie record of the dye dispersion in the water boundary-layer. We define the thickness of the water boundary-layer as the depth measured between the undisturbed water surface and the vertical position where the local mean velocity was approximately zero. The data do not show any consistent variation with fetch and wave height.

5.4 Mean Velocity

Figures 58 and 59 present the vertical profiles of longitudinal and vertical mean velocities for $H_0 = 7.62$ - and 2.54 cm. In general, we experienced some difficulties in measuring mean velocity components because of the unsteady nature of the return flow set up in the tank.

This unsteady flow apparently does not affect the measurement of velocity fluctuations (Section 5.6), but it does affect the mean velocity component. This unsteady phenomenon has a typical period of about 20 sec, but our measurement period was about 40 sec. Thus, we do experience some statistical uncertainty in measuring the mean velocity. Figure 58 shows that the mean velocity profile has a drift layer in the region about 15 cm below the undisturbed water surface, and a reverse flow between the depths of 15- and 25 cm. The drift layer does not appear as strong as when the mechanically-generated waves are absent (Figure 32). This result shows that in the presence of mechanically-generated waves, wind is no longer as effective in transferring energy into current as when the mechanically-generated waves are absent. On the other hand, we have observed that when mechanically-generated waves are present the energy transfer from wind to waves appears to be more efficient than when mechanically-generated waves are absent (Section 5.1). A systematic measurement of both energetics in the air, water and wave fields is needed to clarify how the energy is transferred from the air to the drift current and to waves.

Figure 59 shows that in the top drift layer the vertical mean velocity is small, while in the reverse flow region the vertical velocity becomes significant when compared with the longitudinal velocity.

5.5 RMS Velocity Fluctuations

Figure 60 shows the vertical profile of rms longitudinal velocity fluctuations, $\sqrt{u^2}$ measured for $H_0 = 7.62$ - and 2.54 cm. For $H_0 = 7.62$ cm, the data points are denoted by circles. At several depths, repeated measurements were made to examine the repeatability in the measurement of rms velocity fluctuations. For $H_0 = 2.54$ cm, repeated measurements were also made in two series of experiments. This good repeatability shows that the measurement of rms velocity fluctuations does not appear to be significantly affected by the return flow. Especially in the drift layer, the reverse flow should not appreciably influence the velocity field. Comparison between Figures 58 and 60

shows that the rms velocity fluctuations are much larger than the mean velocity components. This situation is in contrast with the case when the mechanically-generated waves were not present; the mean velocity components are larger than the corresponding rms velocity fluctuations (Figures 32 and 35). Therefore, we have established the experimental condition under which waves dominate wind in the generation of water motion.

The vertical profiles of rms vertical velocity fluctuations are plotted in Figure 61. The rms vertical velocity fluctuations behave in a similar manner as the rms longitudinal velocity fluctuations, and their magnitudes are about the same. Figure 62 is the replot of Figures 60 and 61 on a semi-logarithmic paper. The measurements can be approximated by

$$\sqrt{\overline{w^2}} = 33 \exp(-|z|/10.9), \text{ for } H_0 = 7.62 \text{ cm and } 3.5 < -z < 17 \text{ cm} \quad (5-5)$$

and

$$\sqrt{\overline{w^2}} = 15 \exp(-|z|/10.9), \text{ for } H_0 = 2.54 \text{ cm, } 2.5 < -z < 20 \text{ cm.} \quad (5-6)$$

This exponential attenuation of the velocity fluctuations demonstrates clearly that the velocity field is dominated by wave motion. The constant 10.9 expressed in equations (5-5) and (5-6) represents the characteristic depth of the velocity attenuation and it is about 1/6 of the dominant wave length. At depths larger than about 20 cm or about 1/4 to 1/3 of the dominant wavelength, the rms values attenuate at a rate slower than the exponential rate.

5.6 Mean Square Velocity Time Derivatives

Figure 63 shows vertical profiles of the mean square velocity time derivatives. In a stationary flow in which the mean velocity is much larger than the fluctuating velocity, the mean square velocity time derivatives $\overline{(\partial u/\partial t)^2}$ can be related to $\overline{(\partial u/\partial x)^2}$ according to Taylor's frozen turbulence hypothesis, i.e., $\overline{(\partial u/\partial t)^2} = \overline{U^2 (\partial u/\partial x)^2}$. Hence, by further assuming local isotropy, we can estimate the turbulent dissipation rate. For the present flow condition, the rms velocity fluctuation is larger than the mean velocity, therefore the application of the Taylor's hypothesis is questionable. It is our belief, however, that the measurement of $\overline{(\partial u/\partial t)^2}$ or $\overline{(\partial w/\partial t)^2}$ could still indicate small scale turbulence motion. Especially for the present situation, the velocity fluctuation is dominated by the wave motion, thus the rms values of velocity fluctuation cannot be used to indicate turbulent motion. Although $\overline{(\partial u/\partial t)^2}$ or $\overline{(\partial w/\partial t)^2}$ cannot directly relate to the dissipation rate, its measurement can give the local fluid acceleration. In case $H_0 = 2.54$ cm, the maximum $\sqrt{\overline{(\partial w/\partial t)^2}}$ is about 141 cm/sec² which is about 0.14 times the gravitational acceleration. But, for $H_0 = 7.62$ cm, the maximum $\sqrt{\overline{(\partial w/\partial t)^2}}$ becomes as high as 1680 cm/sec² which is about twice the gravitational acceleration. In general, we observed that when wave breaking occurs, extremely high dissipation rate or large local fluid acceleration appear.

5.7 Velocity Spectra

Figure 64 shows the spectrum of longitudinal velocity fluctuations measured at $z = -3.5$ cm. Two distinct spectral regions exist. Near the dominant wave frequency $f_0 = 1.6$ Hz, the spectrum peaks and is dominated by the wave motion. At frequencies higher than the dominant wave frequency, the spectrum is distributed over a wide frequency range therefore, it represents a turbulence motion. In particular, the $-5/3$ power law can be fitted as

$$S_u(f) = 48 f^{-5/3}, \text{ for } 10 < f < 100 \text{ Hz.} \quad (5-7)$$

In Figure 65, the spectrum of vertical velocity fluctuations is shown. It has a dominant peak and a second harmonic component which does not appear in the spectrum of longitudinal velocity fluctuations. For $2 < f < 10$, the spectral density of the vertical velocity fluctuations is higher than that of the horizontal velocity fluctuations. At high frequencies, the spectrum in Figure 65 is fitted by

$$S_w(f) = 66 f^{-5/3}, \text{ for } 4 < f < 100 \text{ Hz} . \quad (5-8)$$

Comparison between Figures 64 and 65 indicates a possible generation mechanism of turbulence in breaking waves. As will be shown in Section 6, the wave breaking introduces very strong vertical motion as a plume injected downwards from the point where the wave breaking occurs. The spectrum of this vertical motion corresponds to the energy excess in the spectrum of vertical velocity fluctuations for $2 < f < 10$. The spectrum shown in Figure 65 is identical to that shown in Figure 64 for the frequency range $1 \leq f \leq 2 \text{ Hz}$. The identical spectra for $S_u(f)$ and $S_w(f)$ shows unmistakably that in the frequency range $1 \leq f \leq 2 \text{ Hz}$ the motion is caused by waves.

In the frequency range $2 \leq f \leq 4 \text{ Hz}$, $S_u(f)$ is lower than $S_w(f)$, and the slope of $S_u(f)$ is smaller than that of $S_w(f)$. Based on these observations, we speculate that strong energy transfers from the vertical velocity component to the longitudinal velocity component. This speculation can readily be proven or disproven if the co- and quad-spectrum of longitudinal and vertical velocity fluctuations can simultaneously be measured.

From equations (5-7) and (5-8), the ratio $S_w(f)/S_u(f)$ is estimated to be about 1.38. This value is very close to the value of $4/3$ when the turbulence is locally isotropic. Although we question the applicability of Taylor's hypothesis to the turbulence in breaking waves, it is still

very convenient to use this hypothesis so that we can estimate the dissipation rate. Two methods are suggested:

- (i) By fitting the measured $S_u(f)$ to the Kolmogorov spectrum (Equation 4-6). Let $\bar{U} = 7.4$ cm/sec, $\alpha = 1.66$, then $\epsilon \approx 738$ cm²/sec³.

- (ii) By using the formula

$$\epsilon = 15\nu \frac{1}{\bar{U}^2} \overline{\left(\frac{\partial u}{\partial t}\right)^2}, \text{ then } \epsilon \approx 4629 \text{ cm}^2/\text{sec}^3.$$

In view of the uncertainties in the applicability of Taylor's hypothesis, the values of ϵ estimated by these two methods are reasonably accepted. From the above estimates of ϵ , one can calculate the Kolmogorov length scale to be 0.06 or 0.04 mm, respectively.

The Taylor microscale is estimated to be about 0.1 cm and the corresponding turbulent Reynolds number, R_λ , is about 200. This value of R_λ is so high that the viscosity dissipation is negligible when compared with turbulent dissipation. Hence, the effect of Reynolds number is not important in the present investigation.

Figures 66 and 67 present the spectra of longitudinal and vertical velocity fluctuations measured at $z = -10$ cm. Both spectra peak at the dominant wave frequency and have turbulence spectra $\propto f^{-5/3}$.

6. OIL DISPERSION

Based on the measurements of wave characteristics, surface drift velocity, and velocity in the water boundary-layer for the case when both wind and mechanically-generated waves are present we selected the experimental conditions $U_{\infty} = 10$ m/sec and $H_0 = 7.62$ cm for the oil dispersion experiments. Diesel oil No. 2 was used for the experiments. The oil discharge was about 50 cc/sec. The specific gravity was 0.84, the kinematic viscosity was $0.19 \text{ cm}^2/\text{sec}$. The thickness of the oil slick at the discharge point was not measured, but it was estimated as follows. By assuming that the oil slick drifts at the surface drift velocity (Figure 54) and that the slick is uniform across the tank, we estimate the slick thickness to be about 0.1 mm. In reality, the oil slick thickness was not distributed uniformly because of the presence of the boundary layer of the oil slick by the side walls. We also observed that the oil slick drifts in the form of streaks which resemble the wind rows observed in wind-generated waves.

6.1 Flow Visualization

Flow visualization experiments were conducted to investigate the evolution of the oil dispersion as the oil slick drifted downwind. The visualization results were recorded using a 35-mm camera and a 16-mm movie camera. Initially, the oil slick was in sheet form. As the oil slick drifted downwind under the action of wind and breaking waves, the oil slicks were broken into patches and lenses. Because of the combined effects of gravity and surface tension, the shape of the oil lenses was approximately elliptical with larger horizontal dimension than vertical dimension. Further downstream, oil droplets of smaller sizes were formed either by the break up of the oil lenses or by the break up of the thin oil patches (sheet-like). These droplets were spherical and they were present in bursts at a frequency corresponding to the dominant frequency of the breaking waves. The burst of oil droplets appeared as a plume plunging downwards below the water surface. The horizontal extent of the oil droplet burst decreased with depth. Most of the oil

droplets resurfaced very rapidly, and oil droplets of small sizes stayed in the water boundary-layer and convected downwind by the drift currents.

From time to time, we observed droplets having sizes of about 0.5- to 1 cm drifting very freely in the water as if they were nearly neutrally buoyant. We speculated that these droplets were, in essence, a water droplet coated with a thin oil film. We further observed that the oil film on the water droplet was not uniform in thickness. Near the top of the droplet, the oil film appeared thicker than that near the bottom due to the buoyancy of the oil in water. We called these droplets "oil bubbles" because of their resemblance to soap bubbles in the air. It must be reminded that the soap bubble has a thicker film near the bottom of the bubble. Sometimes we observed that these "oil bubbles" were attached to one or several air bubbles. These air bubbles were entrained into water by the breaking waves. The conglomerate of the oil and air bubble resurfaces very rapidly because of the additional buoyancy of the air bubble.

6.2 Oil Concentration

We used the photographic technique to measure the vertical profile of oil concentration in the water boundary-layer. The sample volume for oil concentration measurements was selected at fetch $x = 4$ m. The sample volume was defined between the side (glass) wall and a black colored vertical plate. The plate was about 30 cm high, 2 cm long and 0.2 cm thick and was positioned 1.65 cm away from and parallel to the side wall. The total sample volume was a rectangular column, 30 cm high, 2 cm long and 1.65 cm thick. Flood lamps projected light from above for illumination. The oil droplets existing in this sample volume were recorded by a polaroid camera standing about 30 cm away from the side of the tank. To determine the volume occupied by the oil droplets, their size was measured and their number was counted under a microscope. The volume measurements were made at vertical increments of 1.25 cm. At each increment, the oil concentration was determined by dividing the oil

volume to the total volume of the increment, 4.1 cm^3 . The oil droplets observed in this figure are approximately spherical in shape, thus by measuring the diameters (size) of the oil droplets, one can calculate the volume accordingly. Identifying the oil droplets in this figure is by no means a trivial task. Under these light conditions, an oil droplet is accompanied by two bright spots, one on the top and one on the bottom of the droplet. The top bright spot results from the light reflection from the top surface of the oil droplet, and the bottom bright spot results from the light passing through and refracting out of the oil droplet.

The vertical profile of instantaneous concentration is plotted in Figure 68. This vertical profile shows that the maximum volume concentration is about 0.009 and that the oil can penetrate as deep as about 20 cm ($2.6 H_0$). To obtain statistics of oil concentration, such as mean and rms, we used seven vertical profiles of instantaneous oil concentration. These profiles were measured from photographs which were sequentially taken at time increments of about 10 sec. Hence, each photograph could be treated as an independent observation. Figure 69 shows the vertical profiles of mean and rms oil volume concentration, \bar{C} and $\sqrt{c^2}$. The rms oil concentration was measured by calculating the standard deviation of the seven instantaneous concentration profiles, thus it includes both wave-induced and turbulent fluctuations. The rms oil concentration is comparable to the mean value.

The vertical profile of the mean oil concentration is replotted on a semi-logarithmic graph in Figure 70. The profile can be approximated by

$$\bar{C} = 0.015 \exp(-|z|/7.9), \text{ for } 5 \text{ cm} < -z < 20 \text{ cm.} \quad (6-1)$$

The constant in the exponent of equation (6-1) is a characteristic depth 7.9 cm for the oil concentration. This characteristic depth is comparable to that observed from the vertical profile of rms velocity fluctuations (Section 5.5).

From the seven photographs aforementioned, we obtained the size distribution of oil droplets for $U_{\infty} = 10$ m/sec and $x = 4$ m. For each photograph, we counted the total number of oil droplets. The oil droplets were thus grouped according to their sizes. The smallest size of oil droplets which could be resolved photographically was 0.5 mm, and the size increment was 0.25 mm. For each size group, we obtained the number of oil droplets. By dividing this number by the total number of oil droplets, we can then obtain the percentage frequency for that size of oil droplets; therefore, the size distribution of oil droplets for this photograph is determined. From the seven photographs, we can further obtain the average percentage frequency for a specific size. Figure 71 is the size distribution of oil droplets. The average oil droplet size is about 1.1 mm and the most frequently observed size is 0.75 mm for the present investigation.

7. CONCLUSIONS

7.1 Turbulence and Wave-Induced Motion

Based on the experimental data obtained in the present research study, we conclude that the turbulence structure in surface waters depends strongly on its generating mechanisms. For the present interest, two mechanisms, namely wind and waves, were considered. The important findings are summarized in the following:

- (i) When wind dominates the turbulence generation, the water boundary-layer behaves very similar to the turbulent boundary-layer over a rough surface. The mean velocity has a logarithmic region. The water boundary-layer thickness δ_w grows with fetch and is approximated by

$$\frac{g\delta_w}{U_\infty^2} = 0.025 \left(\frac{gx}{U_\infty^2} \right)^{4/5}, \text{ for } 0.2 < \frac{gx}{U_\infty^2} < 3.$$

The profile of turbulence intensity also resembles that which has been observed in the turbulent boundary-layer over a rough surface. The maximum turbulence intensity is about 0.7 percent of wind speed or 20 percent of the surface drift velocity. The contribution of wave motion to the turbulence intensity measurement is not negligible. The velocity spectrum shows a peak at the dominant wave period and a modest range of $f^{-5/3}$ law.

- (ii) When waves dominate the turbulence generation, the water flow does not resemble the boundary-layer flow. The water motion is mainly governed by waves. The wave induced motion, such as the rms velocity fluctuation attenuates exponentially with depth. The turbulent motion is predominately introduced by the wave breaking. The wave breaking introduces a strong vertical burst motion like a plume plunging downwards below the water surface. The penetration of this burst motion is about one wave height. The spectrum show a dominant peak representing the wave-induced motion and an extensive Kolmogorov spectrum $f^{-5/3}$ for almost two decades of frequencies.

The mean-square velocity time derivatives indicate significant turbulence generation near the water surface when breaking waves occur.

7.2 Wave Growth Characteristics

The wave growth characteristics have been investigated by measuring the variation of the rms wave height with fetch for various wind and wave conditions. The important findings are summarized:

- (i) For wind waves, the present results are consistent with previous measurements.
- (ii) For mechanically-generated waves with wind, the waves grow at a faster rate than without mechanically-generated waves but with wind. In other words, in the presence of mechanically-generated waves, the energy is more effectively transferred from wind to waves. When wave breaking occurs, we observe a decrease of wave energy with fetch. Apparently, the dissipation mechanism due to wave breaking overwhelms the energy transferred from wind to waves.

7.3 Surface Drift Velocity

Paper discs were used as floats to measure the surface drift velocity. The important findings are summarized:

- (i) For wind waves case, the present result is consistent with previous results, namely, the surface drift velocity is about 3.2 percent of the wind speed.
- (ii) For mechanically-generated waves with wind, the surface drift velocity not only varies with wind speed, but also with wave steepness. We obtain an empirical formula under the present experimental conditions, i.e.,

$$\frac{U_s}{U_\infty} = 0.02 + \left[\pi^2 \left(\frac{H}{\lambda} \right)^2 + 0.445 \left(\frac{H}{\lambda} \right) \right] \frac{C}{U_\infty}$$

for $0.05 < H/\lambda < 0.10$, $U_\infty = 10$ m/sec and $65 \text{ cm} < \lambda < 73 \text{ cm}$.

7.4 Oil Dispersion

Oil dispersion was investigated under conditions when breaking waves occur. As the waves break, strong vertical motion is introduced and the oil slick is broken into oil droplets. We measured the oil concentration by using the photographic technique. For the particular parameters used in the present experiment, the mean oil concentration decreases exponentially as

$$\bar{C} = 0.015 \exp (-|z|/7.9), \text{ for } 5 \text{ cm} < -z < 20 \text{ cm},$$

$$U_{\infty} = 10 \text{ m/sec and } H_0 = 7.62 \text{ cm}.$$

The rms oil concentration has values comparable to the mean oil concentration. The size distribution of oil droplets was determined photographically. The average size is about 1.1 mm.

8. RECOMMENDATIONS FOR FUTURE RESEARCH

Before we initiated this research study, very little was known concerning the turbulent motion in surface waters and the effect of turbulence on oil dispersion. The present study provides some important information necessary for understanding the turbulent dispersion of oil slicks, and it also calls for additional research effort.

8.1 Surface Drift Velocity

In Section 5.3, we have shown the complicated coupling effects of wind and waves on the surface drift velocity. Also, we have shown that it is possible, empirically, to separate the effects of wind and waves as expressed in equation (5-4). But, the expression is only for a modest range of wave steepness under given wind speed and wavelength. It would, therefore, be interesting to obtain, if possible, a similar empirical formula for a variety of wind and wave conditions. This formula could be used in numerical modeling for predicting the horizontal spread of an oil slick due to the surface drift.

8.2 Turbulent Motion Versus Wave-Induced Motion

Measurements of both longitudinal and vertical velocity components in wind waves and in mechanically-generated waves with wind show two basic motions, namely, turbulent motion and wave-induced motion. The interaction between the turbulent motion and the wave-induced motion is not well understood. On the other hand, the updated turbulent theory cannot include the wave-induced motion. The following approaches are suggested:

- (1) Separate the turbulent motion from the wave-induced motion by the phase-averaging technique, and then investigate the characteristics separately for either type of motion.
- (11) extend the present turbulence theory by including the wave-induced motion. For the study of oil dispersion, we do not recommend a complicated turbulent theory; instead, a theory equivalent to the eddy viscosity approximation could be considered.

8.3 Taylor's Frozen Turbulence Hypothesis

Most of turbulence measurements was done in time series. Taylor's frozen turbulence hypothesis is frequently used to convert statistics measured in the time domain into the spatial domain. For the case when the mean velocity is much larger than the fluctuating component, Taylor's hypothesis is valid. But, when the fluctuating velocity component is larger than the mean velocity component, the validity of Taylor's hypothesis is subject to doubt. Theoretical and experimental studies are needed to investigate the validity of Taylor's hypothesis.

8.4 Oil Concentration Flux

Visualization techniques have been used to measure oil concentration. The technique can further be used to determine the oil concentration fluxes simply by multiplying the volume of the oil droplet by its corresponding velocity components. The oil concentration fluxes could yield the important information such as eddy diffusivity of oil dispersion.

REFERENCES

- Aitken, J. (1884) "On the Effect of Oil on a Stormy Sea," Proc. Roy. Soc., Edin. 12, pp. 56-75.
- Baines, W. D. and Knapp, D. J. (1965) "Wind Driven Water Currents," J. Hyd. Div. A.S.C.E. 91, pp. 205-221.
- Banke, E. G. and Smith, S. D. (1971) "Wind Stress Over Ice and Over Water in the Beaufort Sea," J. Geophys. Res. 76, 7368.
- Banner, M. L. and Phillips, O. M. (1974) "On the Incipient Breaking of Small Scale Waves," J. Fluid Mech. 65, pp. 647-656.
- Banner, M. L. and Melville, W.K. (1976) "On the Separation of Air Flow over Water Waves," J. Fluid Mech. 77, pp. 825-42.
- Beebe, P. S. (1972) "Turbulent Flow Over a Wave Boundary," Ph.D. Thesis, Colorado State University.
- Boardman, G. and Dawson, F. (1972) "Process of Dispersing Oil Slicks," Official Gazette, U.S. Patent Office 895, no. 1, 255.
- Bole, J. B. and Hsu, E. Y. (1967) "Response of Gravity Water Waves to Wind Excitation," Dept. of Civil Engr. Tech. Rept. 79, Stanford University.
- Bye, J. A. T. (1965) "Wind-Driven Circulation in Unstratified Lakes," Limnol. Oceanogr. 10, pp. 451-458.
- Canevari, G. P. (1969) "General Dispersant Theory," Proc. Jt. Conf. on Prevention and Control of Oil Spills, New York City, pp. 171-177.

- Chang, P. C. (1969) "Laboratory Measurements of Air Flow Over Wind Waves Following the Moving Water Surface," Ph.D. Thesis, Department of Civil Engineering, Colorado State University.
- Chang, P. C., Gorove, A., Atchley, B., and Plate, E. J. (1970) "A Self-Adjusting Probe Positioner For Measuring Flow Fields in the Vicinity of Wind-Generated Water Surface Waves," Rev. Sci. Instrum. 41, 1544.
- Chang, P. C. and Cheng, I. M. (1972) "Interaction Subrange Spectra of Turbulent Wind Over the Air-Water Interface," J. Physical Ocean. 2, p. 273.
- Colonell, J. M. (1966) "Laboratory Simulation of Sea Waves," Dept. of Civil Engr. Tech. Report 65, Stanford University.
- Davies, J. T., Qudwai, A. and Hansed, A. (1968) "Surface Stresses in Ripple Formation Due to Low Velocity Air Passing Over a Water Surface," Chem. Engng. Sci. 23, pp. 331-337.
- Donelan, M. A. (1977) "White Caps and Momentum Transfer," NATO Symposium on Turbulent Fluxes through the Sea Surface Wave Dynamics and Prediction Marseille, France, Sept. 12-16.
- Dreyer, A. A. (1973) "Study of Wind-Generated Seawaves in Shallow Sea," Thesis, USSR Academy of Sci., Shirshov Institute of Oceanography.
- Eloubaidy, A. F. (1969) "Wind Waves and Reaeration Coefficient in Open Channel Flow," Ph.D. Dissertation, Colorado State University.
- Faller, A. (1963) "An Experimental Study of the Instability of the Laminar Ekman Boundary Layer," J. Fluid Mech. 15, pp. 560-576.

- Fannelop, T. K. and Waldman, G. D. (1972) "Dynamics of Oil Slicks,"
AIAA Journal 10, No. 4, pp. 506-510.
- Fay, J. A. (1969) "In Oil on the Sea," edited by D. P. Hoult, New York,
Plenum, pp. 53-63.
- Fay, J. A. (1971) "Physical Processes in the Spread of Oil on a Water
Surface," Conference on Prevention and Control of Oil Spills,
Washington, D.C.
- Fischer, H. B. (1967) "The Mechanics of Dispersion in Natural Streams,"
Proc. ASCE, J. of Hyd. Div. 93, No. HY6, pp. 187-216.
- Fischer, H. B. (1969) "The Effect of Bends on Dispersion in Streams,"
Water Resources Research 5, No. 2, pp. 496-506.
- Gad-el-Hak, M. and Lin, J. T. (1977) "Literature Survey of Turbulence
and Oil Dispersion in Surface Waters," Flow Research Note No. 111,
February.
- Glover, R. E. (1964) "Dispersion of Dissolved or Suspended Materials in
Flowing Streams," U.S. Geol. Survey, Prof. Paper 433-B.
- Grant, H. L., Moilliet, A., and Vogel, W. M. (1963) "Turbulent Mixing in
the Thermocline," Pacific Naval Lab. preprint, Esquimalt, B.C.,
Canada.
- Hoult, D. P. (1972) "Oil Spreading on the Sea," Annual Review of Fluid
Mech. 4, pp. 341-368.
- Hidy, G. M. and Plate, E. J. (1966) "Wind Action on Water Standing in
a Laboratory Channel," J. Fluid Mech. 26, pp. 651-687.

- Ichiye, T. (1967) "Upper Ocean Boundary-Layer Flow Determined by Dye Diffusion," Phys. Fluids Suppl. S270-7.
- Jeffreys, H. (1925) "On the Formation of Water Waves by Wind, I" Proc. Roy. Soc. A107, pp. 189-206.
- Jeffreys, H. (1926) "On the Formation of Water Waves by Wind," Proc. Roy. Soc. London A 110, pp. 341-347.
- Jobson, H. E. and Sayre, W. W. (1970a) "Vertical Transfer in Open Channel Flow," Proc. ASCE, J. of Hyd. Div. 96, no. HY3, pp. 703-724.
- Jobson, H. E. and Sayre, W. W. (1970b) "Predicting Concentration Profiles in Open Channel," Proc. ASCE, J. of Hyd. Div. 96, No. HY10, pp. 1983-1996.
- Karaki, S. and Hsu, E. Y. (1968) "An Experimental Investigation of the Structure of a Turbulent Wind Over Water Waves," Dept. of Civil Engr. Tech. Rept. 88, Stanford University.
- Keulegan, G. H. (1951) "Wind Tides in Small Closed Channels," J. Res. Nat. Bur. Stan. 46, pp. 358-381.
- Kinner, P., Klemas, V., Leatham, W., Maurer, D., and Treasure, W. (1974) "Dye and Drogue Studies of Spoil Disposal and Oil Dispersion," Journal of Water Pollution Control Federation 46, No. 8, 2026-2034.
- Kinsman, B. (1965) Wind Waves - Their Generation and Propagation on the Ocean Surface, Prentice-Hall, Inc. Englewood Cliffs, N.J.
- Kitaigorodskii, S. A. , Krasitskii, V. P. and Zaslavskii, M. M. (1975) "On Phillips' theory of Equilibrium Range in the Spectra of Wind-Generated Waves," J. Phys. Oceanography 5, pp. 410-20.

- Klemas, V., Davis, G., and Wang, H. (1975a) "Monitoring Estuarine Circulation and Ocean Waste Dispersion Using an Integrated Satellite-Aircraft-Drogue Approach," NASA Earth Resources Survey Program.
- Klemas, V., Davis, G., and Wang, H. (1975b) "Verification by Remote Sensing of an Oil Slick Movement Prediction Model," NASA Earth Resources Survey Program.
- Klemas, V., Davis, G., and Kupferman, S. (1976) "The Influence of Coastal Fronts on the Movement and Dispersion of Oil Slicks," NASA Earth Resources Survey Program.
- Kondo, J., Fujinawa, Y., and Naito, G. (1972) "Wave Induced Wind Fluctuations Over the Sea," J. Fluid Mech. 51, p. 751.
- Kullenberg, G. and Talbot, J. W., eds. (1974) "Physical Processes Responsible For Dispersal of Pollutants in the Sea With Special Reference to the Near-Shore Zone," Symp. on Phys. Processes Responsible For Dispersal of Pollutants in the Sea With Specific Reference to the Near-Shore Zone, Denmark.
- Langmuir, I. (1938) "Surface Motion of Water Induced by Wind," Science 87, pp. 119-123.
- Leibovich, S. (1975a) "Natural Limit to the Containment and Removal of Oil Spills at Sea," Ocean Eng. 3, No. 1, pp. 29-36.
- Leibovich, S. (1975b) "Hydrodynamics Problems in Oil Spill Control and Removal," Proc. of the 7th Annual Offshore Technology Conference, Houston, Texas, pp. 527-544.

- Lin, J. T. (1971) "Velocity Spectrum of Locally Isotropic Turbulence in the Inertial and Dissipation Ranges," Phys. Fluids, 15 pp. 205-207.
- Lin, J. T. and Veenhuizen, S. D. (1975) "The Fetch Effects on Wind Waves," Flow Research Note No. 58.
- Lin, J. T. and Gad-el-Hak, M. (1977) "A Study To Conduct Experiments Concerning the Turbulent Dispersion of Oil Slicks - A Test Program and Plan," Flow Research Note No. 110. January.
- Lissauer, I. M. (1974) "A Technique For Predicting the Movement of Oil Spills in New York Harbor," Coast Guard Research and Development Center, Report No. CGR/DC-8/74.
- Lissauer, I. M. and Welsh, J. P. (1975) "Preliminary Projections of Oil Spill Movement for Three Potential Deepwater Sites in the Gulf of Mexico," Coast Guard Research and Development Center, Report No. CGR/DC-34/75.
- Liu, H. T., Lin, J. T., Delisi, D. P. and Robben, F. A. (1977) "Application of a Fluorescence Technique to Dye Concentration Measurements in a Turbulent Jet," Flow Measurement Symposium, National Bureau of Standards, Washington, D.C.
- Long, S. R. and Hwang, N. F. (1977) "On the Variation and Growth of Wave Slope Spectra in the Capillary-Gravity Range with Increasing Wind," J. Fluid Mech.
- Longuet-Higgins, M. S. (1953) "Mass Transport in Water Waves," Trans. Camb. Phil. Soc. 245A, pp. 535-581.

Longuet-Higgins, M. S. (1969a) "A Nonlinear Mechanism for the Generation of Sea Waves," Proc. Roy. Soc. A 311, pp. 371-389.

Longuet-Higgins, M. S. (1973) "A Model of Flow Separation at a Free Surface," J. Fluid Mech. 57, pp. 1-20.

Longuet-Higgins, M. S. (1974) "An 'Entraining Plume' Model of a Spilling Breaker," J. Fluid Mech. 63, No. 1, pp. 1-20.

Manton, M. J. (1972) "On the Generation of Sea Waves by a Turbulent Wind," Boundary-Layer Meteorology 2, p. 348.

McNeely, W. J. (1951) "Oil Slick Dispersion Apparatus," Official Gazette, U.S. Patent Office 883, No. 2, p. 604.

Miles, J. W. (1957) "On the Generation of Surface Waves by Shear Flows," J. Fluid Mech. 3, p. 185.

Miles, J. W. (1959a) "On the Generation of Surface Waves by Shear Flows, Part 2," J. Fluid Mech. 6, p. 568.

Miles, J. W. (1959b) "On the Generation of Surface Waves by Shear Flows, Part 3," J. Fluid Mech. 6, p. 583.

Miles, J. W. (1962) "On the Generation of Surface Waves by Shear Flows, Part 4," J. Fluid Mech. 13, p. 433.

Miles, J. W. (1967) "On the Generation of Surface Waves by Shear Flows, Part 5," J. Fluid Mech. 30, p. 163.

Murray, S. P., Smith, W. G. and Sonu, C. J. (1970) "Oceanographic Observations and Theoretical Analysis of Oil Slicks During the Chevron Spill," Louisiana State University, Report No. TR-87.

- Murray, S. P. (1972) "Turbulent Diffusion of Oil in the Ocean," Limnology and Oceanography 17, pp. 651-660.
- Murray, S. P. (1975) "Wind and Current Effects on Large-Scale Oil Slicks," Proc. of the 7th Annual Offshore Technology Conference, Houston, Texas, pp. 523-533.
- Phillips, O. M. (1958) "On Some Properties of the Spectrum of Wind-Generated Ocean Waves: J. Mar. Res. 19, pp. 231-245.
- Phillips, O. M. (1966) The Dynamics of the Upper Ocean, Cambridge University Press.
- Phillips, O. M. and Banner, M. L. (1975) "Wave Breaking in the Presence of Wind Drift and Swell," J. Fluid Mech. 66, pp. 625-640.
- Plate, E. J., Chang, P. C. and Hidy, G. M. (1969) "Experiments on the Generation of Small Water Waves by Winds," J. Fluid Mech. 35, pp. 625-656.
- Plate, E. J. (1970) "Water Surface Velocity Induced by Wind Shear," J. Engng. Mech. Div. A.S.C.E. 96, pp. 295-312.
- Pottinger, J. M. and Reishig, R. L. (1973) "The Simulation of Deep Water Waves for Oil Drift Studies," Proc. of the Missouri Academy of Science, Columbia, Missouri, April.
- Prych, E. A. (1970) "Effects of Density Differences on Lateral Mixing in Open Channel Flows," California Institute of Technology, Report No. KH-R-21.

- Raj, P. (1977) "Theoretical Study to Determine the Sea State Limit for the Survival of Oil Slicks on the Ocean," Arthur D. Little Rept. No. 79299, February.
- Reisbig, R. L., Alofs, D. J., Shah, R. C., and Banerjee, S. K. (1973) "Measurement of Oil Spill Drift Caused by the Coupled Parallel Effects of Wind and Waves," presented at Fifth Liege Colloquium on Ocean Hydrodynamics Interactions at the Sea Boundaries, the Liege Univ., Liege, Belgium, April 3-6, Vol 75, pp. 67-71.
- Reisbig, R. L. (1973) "Oil Spill Drift Caused by the Coupled Effects of Wind and Waves," Division of Engineering Research, Missouri University at Rolla.
- Ridgway, N. M. (1972) "Direction of Drift of Surface Oil With Wind and Tide," New Zealand Journal of Marine and Freshwater Research 6, Nos. 1 & 2, pp. 178-184.
- Robben, F. (1975) "Wave Slope and Height Measurement Techniques Using a Laser and Linear Diode Arrays," Flow Research Communication No. 57.
- Robben, F. A., Lin, J. T., Delisi, D. P. and Liu, H. T. (1976) "Feasibility Study of a Dye-Fluorescence Technique For Measuring Concentrations in Fluids," Flow Research Note No. 91.
- Sayre, W. W. and Chang, F. M. (1966) "A Laboratory Investigation of Open Channel Dispersion Process For Dissolved, Suspended and Floating Dispersants," U.S. Geol. Survey, Water Resources Div., Open File Report.
- Schwartzberg, H. G. (1970) "Spreading and Movement of Oil Spills," U.S. Government Research and Development Reports 70, No. 17, p. 134.

- Schwartzberg, H. G. (1971) "The Movement of Oil Spills," Joint Conference on Prevention and Control of Oil Spills, Washington, D.C.
- Shemdin, O. H. (1972) "Wind-Generated Current and Phase Speed of Wind Waves," J. Phys. Oceanogr. 2, pp. 411-419.
- Shonting, D. H. (1968) "Autospectra of Observed Particle Motions in Wind Waves," J. Marine Research, 26, pp. 43-65.
- Spencer, E. B. and Sorenson, R. M. (1970) "Set-up of Oil on Water by Wind," Texas A&M University, Report No. 128-C.O.E.
- Stewart, R. H. (1970) "Laboratory Studies of the Velocity Field Over Deep-Water Waves," J. Fluid Mech. 42, p. 733.
- Stewart, R. J. (1976) "The Interaction of Waves and Oil Spills," Massachusetts Institute of Technology, Report No. MITSG-75-22.
- Stokes, G. G. (1847) "On the Theory of Oscillatory Waves," Trans. Camb. Phil. Soc. 8, pp. 441-55; represented in Math. Phys. Pap. I, 314-26.
- Sturm, G. V. And Sorrell, F. Y. (1973) "Optical Wave Measurement Technique and Experimental Comparison with Conventional Wave Height Probe," Appl. Optics, 12, pp. 1928-33.
- Su, K. S. (1972) "Wind Waves and Diffusion in Open Channels," Ph.D. Dissertation, Colorado State University.
- Takeuchi, K. (1976) private communication, University of Stanford.
- Thorton, E. B. and Krapohl, R. F. (1974) "Water Particle Velocities Measured under Ocean Waves" J. Geophy. Res. 79, pp. 847-52.

- Thornton, E. B., Galvin, J. J., Bub, F. L., and Richardson, D. P. (1976) "Kinematics of Breaking Waves," Proc. 15th Coastal Eng. Conf., Honolulu, Hawaii, July, pp. 461-476.
- Thornton, E. B. (1977) "Rederivation of the Saturation Range in the Frequency Spectrum of Wind-Generated Gravity Waves" J. Phys. Oceans. 7, 137-140.
- Van Dorn, W. G. and Pazan, S. E. (1975) "Laboratory Investigation of Wave Breaking, Part II: Deepwater Waves," Scripps Institute of Oceanography University of California, San Diego.
- Veenhuizen, S. D. and Karaki, S. (1973) "Turbulent Air Flow Over Wind Excited Laboratory Water Waves," Department of Civil Engineering, Colorado State University.
- Veenhuizen, S. D., Yu, H. Y., Lin, J. T., and Pao, Y. H. (1975) "The Design and Construction of a Wind-Wave Towing-Tank System," Flow Research Report No. 38.
- Waldman, G. D., Fannelop, T. K. and Johnson, R. A. (1972) "Spreading and Transport of Oil Slicks on the Open Ocean," 4th Annual Offshore Technology Conference, Houston, Texas, pp. 352-364.
- Waldman, G. A., Johnson, R. A. and Smith, P. L. (1973) "The Spreading and Transport of Oil Slicks on the Open Ocean in the Presence of Wind, Waves, and Currents," AVCO Systems Division, Report No. AVSD-0068-72-RR.
- Wang, S. and Hwang, L. (1974) "A Numerical Model For Simulation of Oil Spreading and Transport and Its Application For Predicting Oil Slick Movement in Bays," Tetra Tech, Inc., Report No. TT-P-345-74-1.
- Weissman, M. (1978) Private communication.

- Wu, J. (1968) "Laboratory Studies of Wind-Wave Interactions," J. Fluid Mech. 34, pp. 91-112.
- Wu, J. (1969) "An Estimation of Wind Effects on Dispersion in Wide Channels," Water Resources Research 5, pp. 1097-1104.
- Wu, J. (1975) "Wind Induced Drift Currents," J. Fluid Mech. 68, pp. 49-70.
- Young, M. B. O., Hau, E. Y., and Street, R. L. (1973) "Air-Water Interaction: The Nature of Turbulent Heat, Mass and Momentum Transfer Mechanism in the Air Boundary-Layer," Technical Report No. 163, Dept. of Civil Engineering, Stanford University.
- Yu, H. Y. and Lin, J. T. (1975) "A Technique For Generating a Turbulent Boundary Layer in a Wind-Wave Tank," Second U.S. National Conference on Wind Engineering Research, Colorado State University.

APPENDIX A. ANNOTATIONS

Aitken (1884) studied the effect of an oil film on the waves of the sea. He was motivated by an earlier experiment, conducted in the Aberdeen Harbour, which showed the smoothing effects of oil in preventing the formation of dangerous crests.

Jeffreys (1925, 1926) studied the mechanisms of air-water interaction. He attempted to explain the physical process involved in the generation of waves by wind by using the separation mechanism hypothesis.

Keulegan (1951) measured the surface drift current in a wind-wave tank.

Longuet-Higgins (1953), in his experiments, indicated that the mass-transport velocity can be very different from that determined by Stokes on the assumption of a perfect fluid. Taking into account the viscosity and boundary conditions, he derived a formula for calculating the mass transport velocity both for standing and progressive sinusoidal waves.

Miles (1957, 1959a, 1959b, 1962, 1967) theoretically examined the momentum transfer and wave growth for a sheared airflow. He posed the problem as a hydrodynamic instability with small perturbations and he obtained a prediction of the pressure field influencing the water surface.

Grant, et al. (1963) studied the important mechanisms for the generation of turbulence in surface water. He indicated that the turbulent dissipation rate in the region near the surface is larger than that some distance below the surface.

Glover (1964) presented a solution for the diffusion equation in open channels with the initial condition of an instantaneous point source at the origin.

Baines and Knapp (1965) measured the mean drift currents induced by wind in a shallow channel.

Bye (1965) studied wind-driven circulation in unstratified lakes.

Colonell (1966) showed experimentally that Miles's theory for the momentum transfer and wave growth of a sheared airflow under-predicts the growth rates of the waves.

Hidy and Plate (1966) observed the effects of wind on water standing in a laboratory channel.

Phillips (1966) reviewed state-of-the-art knowledge on wind waves and the dynamics of the upper ocean.

Sayre and Chang (1966) reported a laboratory experiment on the dispersion process for dissolved, suspended, and floating dispersants in an open channel. They adopted Aris's moment distribution method to solve the diffusion equation numerically.

Bole and Hsu (1967) conducted a laboratory experiment to determine the response of waves to wind excitation. They observed higher growth rates for the waves than those predicted by Miles's theory.

Fischer (1967, 1969) studied the mechanics of dispersion in natural streams and the effect of bends on dispersion. He estimated the depth-averaged lateral diffusion coefficient in curved channels, and he derived an equation for predicting the longitudinal dispersion coefficient in wide open channels by adopting Taylor's convective dispersion theory.

Davies, et al. (1968) studied the ripple formation caused by low-velocity air flowing over water.

Karaki and Hsu (1968) conducted an experiment to investigate the structure of a turbulent-wind boundary-layer over a water surface.

Shonting (1968) measured the vertical velocity fluctuations in wind waves. The rms value of the vertical velocity fluctuations decreases exponentially with depth for the water region having depth less than 6 m. The autospectrum of the vertical velocity fluctuations had a dominant peak at a frequency corresponding to the spectral peak of the wave energy spectrum.

Wu (1968, 1969, 1975) in a series of reports studied wind-wave interaction in a wind-wave tank. He measured the profile of the drift current induced by wind and estimated the effect of the wind on dispersion. He pointed out that waves do have a strong effect on the diffusion process.

Canevari (1969) studied the mechanisms of and the basis for dispersing oil slicks with chemical dispersants.

Chang (1969) investigated the detailed structure of airflow above and between crests of progressing wind waves.

Eloubaidy (1969) studied the diffusion process in open channels. He noted that waves have a significant effect on the diffusion process.

Fay (1969, 1971) presented, for the first time, a systematic way to predict how oil spreads in calm water.

Longuet-Higgins (1969a, 1969b, 1973, 1974) published a series of papers on the mechanisms of wave breaking. He proposed a nonlinear mechanism for the generation of sea waves and a model for flow separation at the free surface.

Plate, et al. (1969) and Plate (1970) measured the drift velocity at the water surface for two different wind friction velocities. They observed that, over short fetches, the drift velocity increases according to a power law, while, at fetches exceeding one meter, the drift velocity maintains a constant ratio to the wind velocity.

Chang, et al. (1970, 1972) developed a self-adjusting probe positioner (wave follower) to position a crossed-film sensor above the instantaneous water surface and, thus, were able to measure the wind velocity field as near the instantaneous water surface as possible.

Jobson and Sayre (1970a, 1970b) conducted a series of experiments in a large open channel by using a continuous line of dissolved dye across the width of the channel. They measured the vertical diffusion coefficient.

Murray, et al. (1970) and Murray (1972, 1975) discussed oceanographic observations near the Chevron spilling well off the Mississippi Delta and the relative roles of the various physical factors in the behavior of oil slicks. They evaluated the role of large-scale turbulence and the effects of surface tension in the control of oil diffusion. They showed that the size and shape of a given oil slick can be predicted with knowledge of the surface current, eddy diffusivity, and the rate of oil discharge. Murray determined the relative effect of local winds and near-surface currents on determining the movement of oil slicks in coastal and shelf waters.

Prych (1970) examined the effect of density differences on lateral mixing in open channels.

Schwartzberg (1970, 1971) investigated the movement and spreading of oil spills on water. Spreading rates for small spills were measured and correlated with spill volume, oil density, and water viscosity. Field data indicated that these aspects of small spills cannot be scaled up to large spill volumes.

Spencer and Soranson (1970) analytically and experimentally studied the setup of oils having various densities and viscosities on a water surface when subjected to wind. They showed that the setup of oil is a function of wind stress and wind-generated wave action.

Stewart (1970) measured the velocity field over deep-water waves. His measured spectra showed the presence of peaks caused by water waves.

Banke and Smith (1971) presented spectra of all three wind components and co-spectra for the Reynolds stress and sensible heat flux over water in the Beaufort Sea, in which wave effects were present.

McNeely (1971) described an apparatus for measuring oil slick dispersion.

Beebe (1972) measured the turbulent flow over a wave boundary.

Boardman and Dawson (1972) presented a new process for dispersing an oil slick.

Fannelop and Waldman (1972) considered the spread of an oil slick over calm water from a theoretical viewpoint. They presented a general picture of the slick development.

Hoult (1972) wrote, from an analytical viewpoint, an excellent review article on oil spreading on the sea.

Kondo, et al. (1972) presented a spectrum for longitudinal fluctuations near the air-sea interface which indicated that an influence of the sea swell was present.

Manton (1972) modified Miles's wave theory to include the effects of the turbulence present in the airflow. A particularly interesting result was that the pressure leads the water surface elevation in space, and the phase difference remains almost constant at 75 degrees.

Ridgway (1972) presented a mathematical analysis for predicting the direction the surface oil drifts with the wind and the tide.

Shemdin (1972) measured the wind-induced current and the phase speed of wind waves.

Su (1972) described a theoretical and experimental investigation of the vertical and lateral mixing of tracer fluids in a straight, wide open channel, with and without wind on the water surface. Vertical mixing rates significantly increased when waves appeared on the water surface.

Waldman, et al. (1972, 1973) presented an analysis of the spreading and transport of oil slicks on the open ocean. They assessed the role of turbulent diffusion as a transport mechanism and presented conclusions regarding the applicability of the various analytical models.

Pottinger and Reisbig (1973) conducted laboratory experiments to determine the effect of waves on oil spill drift. The data showed that the drift velocity was greater than that predicted by Stoke's mass transport theory.

Reisbig (1973) studied the effects of the wind and waves on oil spill drift so that he could evaluate the importance of coupled wind and wave drift mechanisms in computer simulations of the total drift.

Reisbig, et al. (1973) conducted laboratory experiments to determine the surface drift speeds of an oil lens which was subjected to the separated and coupled effects of wind waves. The results show that the wind drift and wave drift mechanisms are not simply additive over all

regimes of wind speed. At low wind speeds the wave drift provides an augmentation to the wind drift. At higher wind speeds, however, the waves cause a net decrease in the coupled drift velocity.

Sturm and Sorrell (1973) developed an optical system to measure wave slope. The measured slope was integrated to obtain wave height. Wave height results obtained from this optical system were compared with those from a capacitance wave height. The meniscus effect on the performance of the capacitance wave probe was determined.

Veenhuizen and Karaki (1973) conducted an experimental study of turbulent airflow over water waves. They found an organized wave motion corresponding to the water wave in the turbulent airflow. This wave-induced motion was apparent up to four or five wave heights above the mean water level.

Young, et al. (1973) measured the turbulent heat, mass and momentum transfer mechanisms in the air boundary-layer over wind waves.

Banner and Phillips (1974) investigated the incipient breaking of small-scale waves. They presented a heuristic picture of the turbulent motion in a breaking wave.

Kinner, et al. (1974) studied spoil disposal and oil dispersion experimentally with dye.

Kullenberg and Talbot (1974) edited 31 papers on near-shore mixing caused by waves and currents, dispersion over the continental shelf, wind effects, oil slicks, and many other topics related to the physical processes responsible for the dispersal of pollutants in the sea.

Lissauer (1974, 1975) projected the movement of oil slicks and their impact locations along the shorelines of different states from three potential deep-water port sites. He used average monthly wind speeds and directions, and average monthly current patterns to predict oil slick movement.

Thorton and Krapohl (1974) measured wave height and water particle velocities in ocean waves. The measured wave-induced velocities were comparable to those calculated by linear wave theory. At low frequencies, the motion was almost totally wave induced. At higher frequencies, however, it was apparent that the motion was primarily turbulence.

Wang and Hwang (1974) developed a computer model for simulating oil spreading and transport.

Klemas, et al. (1975a, 1975b, 1976) conducted oil-slick tracking experiments to verify a predictive model for oil dispersion and movement. They found that, during certain parts of the total cycle, oil slicks tend to line up along estuarine and coastal fronts or boundaries.

Leibovich (1975a, 1975b) developed a statistical model to investigate the effect of turbulence on removing oil from the sea surface. He emphasized the importance of vertical turbulent transport to oil spill containment and cleanup operations. He also considered, theoretically, the performance of oil spill control equipment in calm and rough water. His analysis explains the observed thickening of oil in the crests of waves.

Lin and Veenhuizen (1975) studied the effect of fetch on wind waves by correlating experimental data obtained in the laboratory and in the field. They obtained empirical formulas relating the air boundary-layer thickness, the wind stress exerted on the water surface, and the wave height to the wind speed and the fetch.

Phillips and Banner (1975) theoretically estimated the reduction in the maximum amplitude that short waves, superimposed on longer ones, attain when they are at the point of incipient breaking.

Van Dorn and Pazan (1975) reported using hot-film probes successfully near a breaking wave.

Veenhuizen, et al. (1975) developed a wind-wave towing-tank system equipped with a servo-controlled wave maker for generating random surface waves, a tripping mechanism for generating a thick air turbulent boundary-layer within a short distance, and an adjustable ceiling for controlling the pressure gradient along the tank. This system has been used to generate quasi-homogeneous wind waves that have a reduced fetch effect.

Yu and Lin (1975) developed a technique for generating a thick, turbulent, air boundary-layer, within a short fetch, in a wind-wave tank.

Banner and Melville (1976) conducted laboratory experiments to investigate the airflow separation over a mobile air-water interface. It was argued that, in a frame of reference in which the interfacial boundary assumes a steady shape, the occurrence of separation requires a stagnation point on the interface. They made flow visualization and pressure measurements to demonstrate air flow separation.

Robben, et al. (1976) developed a remote sensing technique for measuring concentrations of fluids. They used an Argon-ion-laser (1-watt) to excite a fluorescent dye, Rhodamine, and measured the fluorescence intensity as an indication of the dye concentration. Dye concentrations as low as 10^{-7} g/liter can be measured with this technique.

Stewart (1976) studied, for application to the oil spill problem, the combined effects of interfacial elasticity and multiple fluid layer geometries upon the first-order properties of surface waves.

Takeuchi (1976) was the first to use a laser Doppler velocimeter to measure the turbulence in the water region below the troughs of wind waves.

Thorton, et al. (1976) measured waves, vertical and horizontal water particle velocities in spilling, plunging and surfing breakers at sandy beaches in the vicinity of Monterey, Calif. The breaking waves are highly nonlinear. Strong harmonics appear in the spectra and cross spectra of wave and velocities. The strength of harmonics is related to the beach steepness, wave height and period.

Donelan (1977) measured the momentum transfer under breaking waves in both laboratory and field. The momentum transfer process was quite intermittent. The immediate mixing of surface waters due to turbulence produced by a white cap penetrates to a depth of the order of the wave height.

Liu, et al. (1977) applied the laser dye-fluorescence technique to measure concentrations in a turbulent jet.

Long and Hwang (1977) measured wind wave slope spectra in the capillary-gravity range. Their results indicate that an equilibrium level may exist for each wind slope and that it increases in intensity with increasing wind.

Raj (1977) performed a theoretical study to determine the sea state limit for the survival of oil slicks on the ocean.

Thornton (1977) rederived the saturation range in the frequency spectrum of wind-generated waves. Using similarity arguments, a general formulation was rederived giving Phillips' wave energy spectrum $\sim g^2 f^{-5}$ in deep water. In shallow water, he obtained wave energy spectrum $\sim ghf^{-3}$ suggested by Kitaigorodskii et al. (1975). The velocity spectrum in the saturation range is derived using linear wave theory as a spectral transfer function. In both deep and shallow water he obtained the horizontal velocity spectrum $\sim f^{-3}$.

APPENDIX B. COMPARISON OF MEASUREMENTS BY LDV AND HOT-FILM PROBES

In Sections 4.5 and 4.6, we have presented the measurements of mean velocity and rms velocity fluctuations in wind waves using an array of hot-film probes. Before we proceeded to use the LDV to measure the velocity field in mechanically-generated waves with wind, we tested the LDV performance in wind waves, and made a comparison of measurements by the LDV and hot-film probes. The experimental conditions for the comparison measurement were the same as described in Section 4 except that the LDV measurement is positioned at $x = 4.75$ m and the measurement points were 20 cm away from the side wall while the hot-film probes were positioned at $x = 5$ m along the centerline of the tank which is 58 cm from the side wall. The LDV was positioned at $x = 4.75$ m because at $x = 5$ m there was a vertical column blocking the laser light from the optics of the LDV. We set the measurement point for the LDV 20 cm away from the side wall because there is a limitation in the scattering signal required to obtain good record of velocity by the LDV. In other words, if the focal distance is too large, the scattering becomes so weak that the LDV measurement is difficult. Further optimization of the present system is feasible to increase the focal distance.

Figures 72 and 73 present the comparisons for mean velocity and rms longitudinal velocity fluctuations. The agreement between these two measurements is very good in view of the fact that they were independently made with two different instruments at different times. This comparison establishes our confidence in both instruments, the LDV and the hot-film probe.

APPENDIX C. EFFECTS OF AN OIL SLICK ON WIND WAVES

Experiments were conducted to investigate the effects of an oil slick on wind waves for various wind speeds and at several fetches. Diesel oil No. 2 was used in the experiments. It was fed onto the water surface from the upstream end of the wave tank, and the discharge was 0.35 liter/sec. The specific gravity of the oil was 0.84 and the kinematic viscosity was $0.19 \text{ cm}^2/\text{sec}$.

The photodiode wave gauge was used to measure the vertical displacement of the water surface with and without an oil slick present. The gauge was positioned along the center line of the wave tank. In case an oil slick was present, the intensity of the oil fluorescence was strong enough that the interface between the air and the oil could be detected with the photodiode wave gauge. In all the experiments reported here, fluorescein disodium dye was added to the water so that the interface of the water and the air could be detected when the oil slick was absent. For each experimental run, we first took data for the case without an oil slick. Then an oil slick was fed onto the water surface to investigate its effects on wind waves.

Figure 74 shows a record of the vertical displacement of the water or oil surface at a fetch $x = 5 \text{ m}$ for wind speed $U_\infty = 10 \text{ m/sec}$. Before the oil slick reaches the measurement point, the record shows the time variation of the vertical displacement of the water surface. As the oil slick reaches the measurement point, the mean level of the air-oil interface increases and the fluctuating vertical displacement decreases. The transient stage lasts for about three to four minutes and a steady stage reestablishes four minutes afterwards. The increase of the mean level is partly due to the thickness of the oil slick and partly due to the fact that the setup of the water surface is altered by the presence of the oil slick. After the steady stage is reached, another set of data is recorded for the case when the oil slick is present. This set of data could, therefore, be compared with data obtained without an oil slick present in order to investigate the effects of oil slick on wind waves.

C.1 Wave Profiles

Figure 75 shows wind-wave profiles without an oil slick present, which were measured at fetch $x = 4$ m for three wind speeds, $U_{\infty} = 4$ -, 7 -, and 10 m/sec. The wind-wave profiles are plotted as the time variation of the vertical displacement of the air-water interface. The amplitude and period of dominant waves increase as wind speed increases and wave packets are observed. These results are consistent with those presented in Section 4.2.

Figure 76 shows the wind wave profiles when an oil slick is present. Comparison between Figures 75 and 76 indicates that the wind waves are significantly damped by the oil slick. In Figure 76(c), small scale fluctuations appear which indicate the break up of the oil slick. Visually we have seen the formation of oil lenses floating on the water surface for $U_{\infty} = 10$ m/sec.

C.2 RMS Wave Height

The rms values of the wave displacement are plotted versus wind speed in Figure 77. When the oil slick is absent, the rms wave height increases with wind speed and fetch, which is consistent with the results presented in Section 4.2. For all wind speeds, the rms wave height for the case with an oil slick present is smaller than that for the case without an oil slick present. Thus, the damping effects of an oil slick on wind waves are evident. When an oil slick is present, however, the rms wave height increases when going from 4 - to 7 m/sec wind, but decreases when going from 7 - to 10 m/sec wind. It is worth mentioning that for the case of wind speed at 10 m/sec, oil lenses formed on the water surface. We speculate that these oil lenses could transfer energy from air to water more effectively than a continuous sheet of oil slick because the presence of oil lenses makes the water surface rougher, and the waves could be more effectively damped by them. Figure 78 shows the variation of rms wave height with fetch. For the case without an oil slick, the rms values increase with fetch, which is consistent with the results obtained in Section 2. When an oil slick is present, the rms values do not vary appreciably with fetch.

C.3 Wave Energy Spectrum

Figure 79 presents the wave energy spectrum $S(f)$ measured with the photodiode wave gauge located at fetch $x = 3.2$ m for wind speed $U_{\infty} = 10$ m/sec without an oil slick present. Two distinct frequency regimes are observed, namely, a gravity wave regime and a capillary wave regime. The gravity waves have a peak spectrum at a frequency of about 4.7 Hz. In the capillary wave regime, the wave energy spectrum follows

$$S(f) = \beta \gamma^{2/3} f^{-7/3}, \quad 7.5 \text{ Hz} < f < 100 \text{ Hz},$$

where γ is the surface tension per unit density and has a value of $70 \text{ cm}^3/\text{sec}^2$ for water, and β is a numerical constant having a value of about 7.2×10^{-3} for this particular measurement. This $-7/3$ power law was obtained based on dimensional arguments (Phillips, 1966), and it was suggested originally by Hicks (See Phillips, 1958). To the knowledge of the authors, the wave energy spectrum presented in Figure 79 is the first experimental verification of this power law. The measurement of the wave energy spectrum at high frequencies is very important in understanding the characteristics of capillary waves. Since these capillary waves act as roughness elements to wind, their characteristics would influence the wind stress exerted on the water surface and, therefore, the surface drift current. In Figure 79, there are two spectra calculated from two independent records. The shaded area provides an estimate of statistical error in measuring the wave energy spectrum.

The wave energy spectra measured at a fetch, $x = 4\text{m}$ for three wind speeds, $U_{\infty} = 4\text{, } 7\text{, and } 10$ m/sec without an oil slick present are plotted in Figure 80. Each spectrum has two distinct wave regimes as aforementioned. The value of β increases with wind speed. The dominant frequency decreases with wind speed. Also, the frequency at which two distinct wave regimes join decreases with wind speed. Thus the measurements show that as wind speed increases the wave energy in both gravity and capillary wave regimes increases. Long and Huang (1977) measured

wind-wave slope spectra in the capillary and gravity ranges. Their results indicate that an equilibrium level may exist for each wind speed, and that it increases in intensity with increasing wind speed. The present results are therefore consistent with theirs. It would be interesting to investigate whether an asymptotic nature of the wave energy spectrum exists in the capillary wave regime.

The effects of an oil slick on wind waves were also investigated from measurements of wave energy spectra. Figure 81 shows the wave energy spectra measured at fetch $x = 4$ m for wind speed $U_{\infty} = 4$ m/sec, with and without an oil slick present. The oil slick influences the wave spectrum over all wave frequencies. In particular, the dominant wave frequency for the case of an oil slick being present is higher than that for the case without an oil slick. This result indicates that the onset of the wind waves is delayed by the presence of an oil slick.

Figure 82 shows the wave energy spectra measured at $x = 4$ m for $U_{\infty} = 7$ m/sec. When an oil slick is present, the energy of the dominant waves decreases, but the dominant wave frequency remains unchanged. At higher frequencies, the effect of an oil slick is not as appreciable for $U_{\infty} = 4$ m/sec. Comparison between Figures 81 and 82 shows that the effect of an oil slick depends on wind speed. Figure 83 shows a comparison of wave energy spectra measured with and without an oil slick present for wind speed $U_{\infty} = 10$ m/sec. The spectral density at the dominant wave frequency decreases significantly when the oil slick is present. In the frequency range $6 \text{ Hz} < f < 20 \text{ Hz}$, the spectral density appears flat and it is possibly contributed by the presence of oil lenses. For frequencies $f > 20 \text{ Hz}$, the oil slick effect is not appreciable. From Figures 82 and 83, we conclude the following for the present experimental conditions. For wind speed $U_{\infty} > 7$ m/sec, the effect of an oil slick on the generation of capillary waves is not significant. These capillary waves most likely are generated locally by wind and governed by surface tension. Therefore, the evolution of

capillary waves is expected to be different from that of gravity waves.
More research is needed to explore this evolution.

APPENDIX D. EFFECTS OF AN OIL SLICK ON MECHANICALLY-GENERATED WAVES WITH

WIND

Experiments were conducted to investigate the effects of an oil slick on mechanically-generated waves with wind. The wave maker was oscillated at a frequency of 1.6 Hz, and three different strokes, $H_0 = 2.54$ -, 5.08-, and 7.62 cm, were used. The wind speed was 10 m/sec except for a few cases in which wind speeds of 4- and 7 m/sec were used. Measurements of wave displacement were made with the photodiode wave gauge at four fetches, $x = 2$ -, 3.2-, 4- and 5 m. For both the cases with and without an oil slick, the experimental procedure was the same as described in Appendix C. Experimental results of wave profiles, rms wave heights and wave energy spectra were obtained to examine the effects of oil slick.

D.1 Wave Profiles

Figure 84 is the wave profile measured at $x = 5$ m for $H_0 = 2.54$ -, 5.08-, and 7.62 cm and $U_\infty = 10$ m/sec. In this figure, the apparent propagation direction of the waves is from the right to the left. The vertical scale is exaggerated to show the details of the profiles. All three profiles have the dominant wave frequency corresponding to the oscillating frequency of the wave maker, i.e., $f_0 = 1.6$ Hz. Also, superimposed on the dominant waves are higher harmonic wave components and high frequency wave components generated by wind. When the stroke of the wave maker increases, the wave steepness increases, and, as a result, the waves become unstable and begin to break. For $H_0 = 5.08$ cm, wave breaking appeared as indicated by the small-scale waves resting on wave crests, and for $H_0 = 7.62$ cm the breaking is more violent.

In Figures 85 and 86, we replot the wave profile to scale approximately. Figure 85 shows the case for $H_0 = 2.54$ cm, and the wave profile does not appreciably deviate from a sinusoidal profile. Small-scale or high frequency wave components are generated mostly by wind and their profile is shown in the enlarged plots. Wave breaking does not occur yet. Figure 86 shows the wave profile for $H_0 = 7.62$ cm. The wave profiles are highly asymmetric because the wave slope in the downstream

(downwind) side is much larger than that in the upstream side, and the wave slope at the wave crest is steeper than that at the wave trough. Two enlarged wave profiles at wave crests are re-plotted, and they represent two realizations of wave breaking. These plots clearly show that the breaking process is quite random as these two realizations do not resemble each other at all.

Figure 87 shows the wave profiles measured at $x = 5\text{m}$ for $H_0 = 2.54\text{-}$, 5.08- , and 7.62 cm and $U_\infty = 10\text{ m/sec}$ when an oil slick is present. Direct comparisons between Figures 87 and 84 reveal the effects of an oil slick on waves. For $H_0 = 2.54\text{ cm}$, the overall wave amplitude decreases, and higher harmonic wave components disappear when an oil slick is present. For $H_0 = 5.08\text{ cm}$, the presence of an oil slick makes the wave slopes at crests steeper. The wave breaking is somehow inhibited by the oil slick. As shown in Figure 87 (b), small-scale wave components hardly exist when comparing with Figure 84 (b). For $H_0 = 7.62\text{ cm}$, wave breaking occurs at wave crests. Comparison between Figures 84c and 87c shows that the wave breaking is so violent that it is not affected significantly by the oil slick.

D.2 RMS Wave Height

The rms wave heights measured with and without an oil slick are shown in Figure 88. The data plotted in the figure include three wave conditions, $H_0 = 2.54\text{-}$, 5.08- and 7.62 cm , measured at four fetches, $x = 2\text{-}$, 3.2- , 4- and 5 m . Each rms wave height was calculated from a record of about 60 seconds.

With the oil slick present, the wave energy still grows with fetch, but at a slower rate than that without the oil slick present for $H_0 = 2.54\text{ cm}$. For $H_0 = 5.08\text{ cm}$, the effect of the oil slick on the wave growth is not significant. For $H_0 = 7.62\text{ cm}$, however, the wave energy decreases as the fetch increases from $x = 2\text{ m}$ to $x = 3.2\text{ m}$, and then increases slowly for the fetch varying from $x = 3.2\text{ m}$ to $x = 5\text{ m}$. Flow visualization results show that at small fetches, say $x \approx 2\text{ m}$, the oil slick breaks into oil lenses by the wave motion and turbulence. The oil

lenses which float on the water surface could damp waves very effectively (see Appendix C.2). Further downstream, the oil lenses are broken into oil droplets which in turn disperse into the water column by the wave motion and turbulence. Thus, the oil concentration near the water surface becomes diluted, and the effect of the oil slick is no longer as strong as at small fetches. The measurements of the rms wave height are plotted versus wind speed at $x = 5$ m for $H_0 = 7.62$ cm in Figure 89. At $U_\infty = 4$ and 7 m/sec the wave energy measured with the oil slick is smaller than that measured without the oil slick. But, at $U_\infty = 10$ m/sec, the effect of oil slick is not measureable, because under this condition most of the oil slick is transported vertically below the water surface.

D.3 Wave Energy Spectrum

In this section, the wave energy spectra measured with and without the oil slick are compared. Attempts are made to clarify further the effects of an oil slick on mechanically-generated waves with wind.

In Figure 90, comparison of two spectra measured with and without the oil slick for $H_0 = 2.54$ cm at $x = 5$ m is shown. The oil slick damps out considerably the wave components with $f < 20$ Hz.

For $H_0 = 5.08$ cm (Figure 91), the spectral density is higher at $f = f_0$, $2f_0$ and $3f_0$ with the oil slick than without. This confirms the steepening of the wave crests, which is observed in Figure 87, due to the reduction in surface tension when the oil slick is present. As a result, the rms wave height is enhanced slightly rather than damped.

With further increase of $H_0 = 7.62$ cm, no noticeable difference between the two spectra is observed in Figure 92. Note that intensive breaking is in progress in both cases. The oil slick is broken into small droplets and a great number of the droplets are transported into the water column. As a result, the effect of the oil slick in wave damping is insignificant. This result shows that for $H_0 = 7.62$ cm, and $U_\infty = 10$ m/sec, the oil slick could be treated as a passive medium as it

barely affects the wave structure. In other words, the effects of oil viscosity and surface tension are unlikely to be important in the present study.

Tables

TABLE 1. -SUMMARY OF OIL PROPERTIES, ARCO DIESEL
(ASTM Grade 2D)

DATE	VISCOSITY (CPS)	TEMP. (°C)	SPECIFIC GRAVITY	REMARK
12-12-77	18.8	20.2	0.838	
12-14-77	18.9	20.1	0.840	New Oil
12-15-77	-	19.8	0.840	
12-16-77	-	-	0.840	
12-19-77	19.6	19.3	0.842	
12-21-77	19.0	-	0.842	
12-21-77	19.5	18.9	0.844	After a Day's Use
12-22-77	19.6	19.4	0.844	
1-4-78	20.2	18.4	0.845	
1-5-78	20.0	19.4	0.845	
1-6-78	20.2	19.5	0.846	
1-9-78	20.4	19.7	0.845	
1-10-78	20.5	17.9	0.846	
1-11-78	20.3	19.4	0.846	
1-13-78	20.9	17.5	0.848	
1-16-78	20.2	19.7	0.846	
1-17-78	20.4	19.3	0.846	
1-18-78	20.3	18.4	0.848	
1-19-78	18.5	19.0	0.840	New Oil
1-19-78	-	-	0.847	After a Day's Use
1-20-78	20.0	19.7	0.846	
1-23-78	20.4	19.0	0.844	
1-24-78	18.8	19.1	0.844	
1-25-78	19.0	19.0	0.842	
1-26-78	18.9	19.1	0.840	
1-27-78	18.8	17.5	0.840	
1-30-78	18.9	18.3	0.841	
1-31-78	18.5	18.9	0.840	
2-1-78	18.8	18.2	0.842	
2-2-78	19.0	19.1	0.841	
2-3-78	19.2	19.1	0.841	

TABLE 2. -WATER SURFACE DRIFT VELOCITY FOR WIND-WAVES

RUN NUMBER	U_{∞} (m/sec)	x (m)	NO. OF FLOATS OBSERVED	U_g (cm/sec)	STANDARD DEVIATION (cm/sec)
OIL-34	4	1.75	11	12.8	0.8
35	4	2.25	6	11.5	1.2
36	4	3.21	10	13.2	1.4
37	4	4.00	8	13.2	1.5
38	4	4.00	8	13.6	0.5
44	4	1.75	11	11.9	1.0
45	4	2.25	4	10.2	0.3
47	4	1.75	31	11.6	1.3
48	4	2.25	17	10.3	1.3
49	4	3.21	14	12.2	1.0
50	4	4.00	16	12.2	1.1
51	4	4.75	13	13.3	0.8
52	4	5.25	14	12.7	1.0
53	4	6.00	14	12.9	1.4
54	7	1.75	25	20.8	1.2
55	7	2.25	23	21.8	1.1
56	7	3.21	15	22.9	1.3
57	7	4.00	15	25.0	1.9
58	7	4.75	21	24.5	2.3
59	7	5.25	21	23.5	2.1
60	7	6.00	28	23.8	5.8
61	10	1.75	20	30.8	3.1
62	10	2.25	25	33.3	2.8
63	10	3.21	36	32.5	3.5
64	10	4.00	31	35.0	5.3
65	10	4.75	24	35.2	6.8
66	10	5.25	27	32.6	3.1
67	10	6.00	21	34.1	3.4

TABLE 3. -WATER BOUNDARY-LAYER THICKNESS FOR WIND-WAVES

RUN NUMBER	U_{∞} (m/sec)	x (m)	$\frac{gx}{U_{\infty}^2}$	NO. OF OBSERVATIONS	δ_w (cm)	STANDARD DEVIATION (cm)	$\frac{g\delta_w}{U_{\infty}^2}$
OIL-68	4	1.7	1.04	4	1.24	0.17	7.6×10^{-3}
71	4	2.3	1.41	10	0.75	0.17	4.6×10^{-3}
74	4	3.2	1.97	10	0.80	0.13	4.91×10^{-3}
77	4	4.0	2.45	5	5.61	0.56	3.44×10^{-2}
80	4	4.7	2.88	10	7.11	0.58	4.36×10^{-2}
83	4	5.3	3.25	10	10.16	0.40	6.23×10^{-2}
69	7	1.7	0.34	9	4.22	0.13	8.45×10^{-3}
72	7	2.3	0.46	9	7.76	0.21	1.56×10^{-2}
75	7	3.2	0.64	10	10.63	0.34	2.13×10^{-2}
76	7	4.0	0.80	10	19.13	0.75	3.83×10^{-2}
81	7	4.7	0.94	11	9.47	0.73	1.90×10^{-2}
84	7	5.3	1.06	10	17.97	0.87	3.60×10^{-2}
70	10	1.7	0.17	7	5.93	0.25	5.82×10^{-3}
73	10	2.3	0.23	9	8.69	0.32	8.52×10^{-3}
76	10	3.2	0.32	8	19.43	0.54	1.91×10^{-2}
79	10	4.0	0.39	10	23.42	1.19	2.30×10^{-2}
82	10	4.7	0.46	10	14.11	0.89	1.38×10^{-2}
85	10	5.3	0.52	10	16.42	0.57	1.61×10^{-2}

TABLE 4. -AIR AND WATER SHEAR STRESSES

U_{∞} (m/sec)	x (m)	u_{*a} (cm/sec)	u_{*a} (cm/sec)	$\frac{(\rho u_{*a}^2)_w}{(\rho u_{*a}^2)_a}$
7	5.0	38.50	0.94	0.49
7	6.0	37.80	1.01	0.58
10	2.0	64.73	1.45	0.41
10	3.2	61.74	1.27	0.35
10	4.0	60.39	1.61	0.58
10	5.0	59.06	1.81	0.77
10	6.0	57.99	1.92	0.90

TABLE 5. -MEASUREMENTS OF VELOCITY IN WATER BOUNDARY-LAYER

Run No.: 011 - 23, $U_{\infty} = 4$ m/sec, $x = 5$ m

z (cm)	\bar{u} (cm/sec)	$\overline{u^2}$ (cm ² /sec)	$\overline{w^2}$ (cm ² /sec)	\overline{uw} (cm ² /sec ²)	$\frac{\overline{uw}}{\overline{u^2} \overline{w^2}}$	ϵ (cm ² /sec ³)	$\epsilon z $ (cm ³ /sec ³)	$\frac{\epsilon z }{(\overline{u^2})^{3/2}}$
-0.84	4.99	1.37	0.83	-0.35	-0.31	30.28	25.44	9.89
-1.70	4.51	0.75	0.45	-0.08	-0.24	1.17	19.84	4.70
-2.57	4.31	0.59	0.40	-0.07	-0.30	0.30	0.78	3.78
-4.24	3.90	0.55	0.34	-0.07	-0.37	0.10	0.42	2.52
-5.94	3.87	0.47	0.29	0.06	-0.44	0.05	0.31	3.03
-7.62	3.10	1.52	0.55	-0.46	-0.55	0.19	1.42	0.40
-10.16	2.41	0.82	0.49	-0.01	-0.02	0.25	2.46	4.46
-12.73	1.38	0.79	0.29	-0.05	-0.22	0.75	9.57	19.42
-15.27	1.17	0.76	0.34	-0.01	-0.04	3.64	55.51	126.50

TABLE 6. -MEASUREMENTS OF VELOCITY IN WATER BOUNDARY-LAYER

Run No.: 011 - 30, $U_{\infty} = 4$ m/sec, $x = 6$ m

z (cm)	\bar{U} (cm/sec)	\bar{U}^2 (cm/sec)	\bar{W}^2 (cm/sec)	\overline{UW} (cm ² /sec ²)	$\frac{\overline{UW}}{\bar{U}^2 \bar{W}^2}$	ϵ (cm ² /sec ³)	$\epsilon z $ (cm ³ /sec ³)	$\frac{\epsilon z }{\bar{U}^2}$
-0.95	16.31	2.30	1.14	-2.54	-0.97	148.30	1.41	11.58
-1.82	3.58	0.72	0.38	-0.13	-0.48	2.11	3.85	10.31
-2.63	3.41	0.63	0.23	-0.04	-0.28	0.59	1.56	6.22
-3.47	3.65	1.05	0.36	-0.06	-0.16	0.46	1.58	1.37
-5.19	3.39	0.57	0.48	0.12	0.44	0.05	0.26	1.42
-6.90	6.31	2.87	0.87	1.29	0.52	0.08	0.56	0.02
-9.41	1.39	0.61	0.40	-0.003	-0.01	0.51	4.79	21.09
-14.52	1.86	0.66	0.40	-0.04	-0.15	0.12	1.78	6.18
-19.60	7.69	0.74	0.33	-0.24	-0.98	0.57	11.09	27.38
-27.18	1.31	0.50	0.43	-0.10	-0.47	0.58	15.81	126.50

TABLE 7. MEASUREMENTS OF VELOCITY IN WATER BOUNDARY-LAYER

Run No.: 011 - 33, $U_\infty = 4$ m/sec, $x = 6$ m

z (cm)	\bar{U} (cm/sec)	$\overline{u^2}$ (cm/sec)	$\overline{w^2}$ (cm/sec)	\overline{uw} (cm ² /sec ²)	$\frac{\overline{uw}}{\overline{u^2} \overline{w^2}}$	ϵ (cm ² /sec ³)	$\frac{\epsilon z }{(\text{cm}^2/\text{sec}^3)}$	$\frac{\epsilon z }{(\overline{u^2})^{3/2}}$
-1.27	3.39	0.66	0.47	-0.07	-0.23	-6.96	8.84	30.74
-2.13	3.20	0.40	0.26	-0.06	-0.58	0.78	1.66	25.91
-2.95	3.10	0.33	0.21	-0.01	-0.14	0.25	0.74	20.71
-3.78	3.05	1.27	0.46	-0.14	-0.24	0.31	1.15	0.56
-5.51	2.36	1.37	0.42	-0.11	-0.19	0.29	1.58	0.61
-7.21	1.66	1.29	0.36	-0.15	-0.32	0.45	3.21	1.50
-9.73	1.51	1.08	0.47	-0.21	-0.41	2.95	28.73	22.81
-14.83	1.64	0.98	0.41	-0.29	-0.72	0.63	9.34	9.92
-19.91	2.96	1.46	0.61	-0.61	-0.68	0.21	4.22	1.36
-27.51	2.60	1.21	0.43	0.23	0.44	0.12	3.43	1.94

TABLE 8. -MEASUREMENTS OF VELOCITY IN WATER BOUNDARY-LAYER

Run No.: 041 - 22 , $U_{\infty} = 7$ m/sec , $x = 5$ m

z (cm)	\bar{U} (cm/sec)	\bar{u}^2 (cm/sec)	\bar{v}^2 (cm/sec)	\overline{uw} (cm ² /sec ²)	$\frac{\overline{uw}}{\bar{u}^2 \bar{v}^2}$	ϵ (cm ² /sec ³)	$\epsilon z $ (cm ³ /sec ³)	$\frac{\epsilon z }{(\bar{u}^2)^{3/2}}$
-0.84	10.45	4.35	3.04	-2.40	-0.18	49.43	41.52	0.50
-1.70	8.46	2.88	1.92	-0.23	-0.04	11.68	19.86	0.83
-2.57	7.89	2.38	1.47	-0.83	-0.24	5.54	14.23	1.06
-4.24	7.38	2.17	1.10	-0.82	-0.34	1.70	7.22	0.71
-5.94	6.67	1.87	0.99	-0.67	-0.36	0.77	4.58	0.70
-7.62	6.07	1.95	1.04	-1.00	-0.49	0.75	5.70	0.77
-10.16	5.07	1.38	0.82	-0.43	-0.38	0.53	5.40	2.05
-12.73	4.65	1.28	0.72	-0.53	-0.58	0.44	5.58	2.66
-15.27	4.27	0.96	0.68	-0.41	-0.63	0.44	6.77	7.65

TABLE 9. -MEASUREMENTS OF VELOCITY IN WATER BOUNDARY-LAYER

Run No.: 0411 - 29 , $U_{\infty} = 7$ m/sec , $x = 6$ m

z (cm)	\bar{U} (cm/sec)	\bar{u}^2 (cm/sec)	\bar{w}^2 (cm/sec)	\overline{uw} (cm ² /sec ²)	$\frac{\overline{uw}}{\bar{u}^2 \bar{w}^2}$	ϵ (cm ² /sec ³)	$\epsilon z $ (cm ³ /sec ³)	$\frac{\epsilon z }{\bar{u}^{3/2}}$
-0.95	9.41	3.83	2.52	0.87	0.09	24.15	22.94	0.41
-1.82	6.32	2.12	1.34	2.19	0.77	12.52	22.79	0.24
-2.63	6.82	2.31	1.38	-0.79	-0.25	7.49	19.70	1.60
-3.47	6.17	2.11	1.22	-0.93	-0.36	4.36	15.13	1.61
-5.19	5.62	1.83	0.89	-0.43	-0.26	1.63	8.44	1.38
-6.90	4.82	1.76	0.78	-0.57	-0.42	0.85	5.84	1.07
-9.41	3.64	0.88	0.49	0.13	0.30	0.61	5.73	7.41
-14.52	4.15	1.19	0.75	-0.45	-0.50	0.73	10.63	6.31
-19.60	7.07	0.43	0.32	0.09	0.65	1.94	37.92	476.90
-27.18	2.73	1.47	0.63	-0.42	-0.45	4.27	116.10	36.56

TABLE 10. -MEASUREMENTS OF VELOCITY IN WATER BOUNDARY-LAYER

Run No.: 041 - 25 , $U_{\infty} = 10$ m/sec , $x = 2$ m

z (cm)	\bar{u} (cm/sec)	\bar{u}^2 (cm/sec)	\bar{w}^2 (cm/sec)	\overline{uw} (cm ² /sec ²)	$\frac{\overline{uw}}{\bar{u}^2 \bar{w}^2}$	ϵ (cm ² /sec ³)	$\epsilon z $ (cm ³ /sec ³)	$\frac{\epsilon z }{(\bar{u}^2)^{3/2}}$
-0.52	13.22	4.54	3.31	-0.21	-0.01	69.27	36.02	0.39
-1.38	9.68	3.04	1.86	-0.30	-0.05	13.52	18.65	0.66
-2.25	8.31	2.64	1.48	-1.08	-0.28	6.22	13.99	0.76
-3.92	6.95	2.64	1.19	-1.19	-0.38	3.28	12.85	0.70
-5.63	5.19	1.63	0.91	-1.07	-0.72	1.90	10.72	2.48
-7.30	4.65	1.30	0.79	-0.49	-0.48	1.30	9.49	4.32
-9.84	1.98	1.52	0.55	-0.32	-0.38	3.88	38.25	10.89
-12.41	1.47	0.75	0.45	-0.08	-0.24	5.94	73.71	174.70
-14.95	2.07	0.96	0.51	-0.32	-0.65	5.59	83.62	94.51

TABLE 11. MEASUREMENTS OF VELOCITY IN WATER BOUNDARY-LAYER

Run No.: 011 - 26, $U_\infty = 10$ m/sec, $x = 3.2$ m

z (cm)	\bar{U} (cm/sec)	$\overline{u^2}$ (cm ² /sec)	$\overline{w^2}$ (cm ² /sec)	\overline{uw} (cm ² /sec ²)	$\frac{\overline{uw}}{\overline{u^2} \overline{w^2}}$	ϵ (cm ² /sec ³)	$\frac{\epsilon z }{(\text{cm}^3/\text{sec}^3)}$	$\frac{\epsilon z }{(\bar{u})^{3/2}}$
-0.84	14.19	5.22	3.59	-1.11	-0.06	30.49	25.61	0.18
-1.70	12.33	4.07	2.57	-0.19	-0.02	13.85	23.55	0.35
-2.57	10.87	3.74	2.15	-2.15	-0.27	8.41	21.61	0.41
-4.24	8.19	2.99	1.43	-0.37	-0.09	4.80	21.81	0.82
-5.94	8.02	3.12	1.54	-1.76	-0.37	2.98	17.69	0.58
-7.62	6.79	2.85	1.33	-1.64	-0.43	3.04	23.18	1.00
-10.16	5.75	2.23	1.09	-0.81	-0.33	2.23	22.66	2.04
-12.73	4.51	1.57	0.81	-0.73	-0.57	1.95	24.82	6.41
-15.27	3.14	1.78	0.71	-0.57	-0.45	1.85	28.21	5.00

TABLE 12. -MEASUREMENTS OF VELOCITY IN WATER BOUNDARY-LAYER

Run No.: Oil - 27, $U_\infty = 10$ m/sec, $x = 4$ m

z (cm)	\bar{u} (cm/sec)	\bar{u}^2 (cm/sec)	\bar{w}^2 (cm/sec)	\overline{uw} (cm ² /sec ²)	$\frac{\overline{uw}}{\bar{u}^2 \bar{w}^2}$	ϵ (cm ² /sec ³)	$\frac{\epsilon z }{(\text{cm}^3/\text{sec})^3}$	$\frac{\epsilon z }{(\bar{u}^2)^{3/2}}$
-0.84	15.06	5.37	3.78	-1.81	-0.09	34.23	28.75	0.19
-1.70	12.40	4.34	2.71	0.03	0.00	14.64	24.89	0.30
-2.57	10.60	3.71	2.12	-1.29	-0.16	9.29	23.65	0.46
-4.24	8.23	2.72	1.43	-2.60	-0.67	4.29	18.17	0.90
-5.94	7.93	2.12	0.90	-0.38	-0.20	1.25	7.42	0.78
-7.62	7.20	2.24	0.94	-0.22	-0.11	0.93	7.48	0.67
-10.16	6.68	2.32	0.91	-0.57	-0.27	0.86	8.75	0.70
-12.73	5.60	2.31	0.90	-0.71	-0.34	0.90	11.45	0.93
-15.27	4.39	2.26	0.90	-0.46	-0.23	1.69	25.82	2.24

TABLE 13. -MEASUREMENTS OF VELOCITY IN WATER BOUNDARY-LAYER

Run No.: 011 - 32, $U_{\infty} = 10$ m/sec, $x = 4$ m

z (cm)	\bar{u} (cm/sec)	\bar{u}^2 (cm ² /sec)	\bar{w}^2 (cm ² /sec)	$\frac{\bar{uw}}{\bar{u}^2 \bar{w}^2}$ (cm ² /sec ²)	ϵ (cm ² /sec ³)	$\epsilon z $ (cm ³ /sec ³)	$\frac{\epsilon z }{\bar{u}^2}^{3/2}$
-0.95	15.29	6.05	3.94	-2.42	33.53	31.85	0.14
-1.82	12.65	4.70	3.07	-1.99	17.29	31.46	0.30
-2.63	11.30	4.43	2.47	-2.24	12.80	33.67	0.39
-3.47	10.26	4.00	2.34	-2.62	8.33	28.89	0.45
-5.19	9.39	3.67	1.88	-2.58	29.82	154.80	3.13
-6.90	8.10	3.74	1.56	-2.94	4.26	29.40	0.56
-9.41	5.89	2.20	1.30	-0.70	2.91	27.42	2.58
-14.92	4.05	2.08	0.87	-0.41	1.81	26.21	2.91
-19.60	2.14	1.15	0.60	-0.10	44.00	86.24	56.70
-27.18	1.56	1.03	0.59	-0.15	10.27	279.20	255.50

TABLE 14. -MEASUREMENTS OF VELOCITY IN WATER BOUNDARY-LAYER

Run No.: 011 - 21, $U_{\infty} = 10$ m/sec, $x = 5$ m

z (cm)	\bar{u} (cm/sec)	\bar{u}^2 (cm/sec)	\bar{w}^2 (cm/sec)	\overline{uw} (cm ² /sec ²)	$\frac{\overline{uw}}{\bar{u}^2}$	ϵ (cm ² /sec ³)	$\epsilon z $ (cm ³ /sec ³)	$\frac{\epsilon z }{(\bar{u}^2)^{3/2}}$
-0.84	16.13	6.37	4.60	-2.60	-0.09	109.20	91.77	0.36
-1.70	11.95	5.27	3.25	1.07	0.06	22.36	38.02	0.26
-2.57	10.50	4.76	2.82	-0.88	-0.07	15.09	38.77	0.36
-4.24	8.21	3.85	1.96	-1.08	-0.14	9.12	38.69	0.68
-5.94	7.65	3.42	1.64	-1.91	-0.34	5.26	31.23	0.79
-7.62	6.80	3.30	1.67	-1.92	-0.35	3.89	29.61	0.82
-10.16	6.28	3.10	1.54	-2.51	-0.53	3.64	36.97	1.24
-12.73	5.60	2.67	1.27	-1.70	-0.50	2.94	37.36	1.96
-15.27	5.34	2.14	1.41	-0.97	-0.32	2.81	42.90	4.38

TABLE 15. -MEASUREMENTS OF VELOCITY IN WATER BOUNDARY-LAYER

Run No.: 011 - 24 , $U_{\infty} = 10$ m/sec , $x = 5$ m

z (cm)	\bar{u} (cm/sec)	$\overline{u^2}$ (cm/sec)	$\overline{w^2}$ (cm/sec)	\overline{uw} (cm ² /sec ²)	$\overline{\frac{uw}{u^2 w^2}}$	ϵ (cm ² /sec ³)	$\epsilon z $ (cm ³ /sec ³)	$\frac{\epsilon z }{(\overline{u^2})^{3/2}}$
-0.84	27.92	4.06	3.45	0.42	0.03	24.74	20.79	0.51
-1.70	10.90	4.29	2.58	-0.31	-0.03	20.01	34.02	0.43
-2.57	10.03	3.77	2.24	-0.74	-0.09	11.61	29.84	0.56
-4.24	8.14	3.35	1.61	-1.08	-0.20	6.41	27.19	0.72
-5.94	7.18	2.88	1.33	-1.04	-0.27	3.66	21.73	0.91
-7.62	6.69	2.68	1.27	-0.75	-0.22	2.94	22.44	1.17
-10.16	6.26	2.55	1.16	-0.59	-0.20	2.41	24.52	1.48
-12.73	6.20	2.86	1.20	-0.50	-0.15	2.16	27.53	1.18
-15.27	5.67	2.24	1.25	-0.20	-0.07	2.11	32.20	2.87

TABLE 16. - MEASUREMENTS OF VELOCITY IN WATER BOUNDARY-LAYER

Run No.: 011 - 31, $U_{\infty} = 10$ m/sec, $x = 5$ m

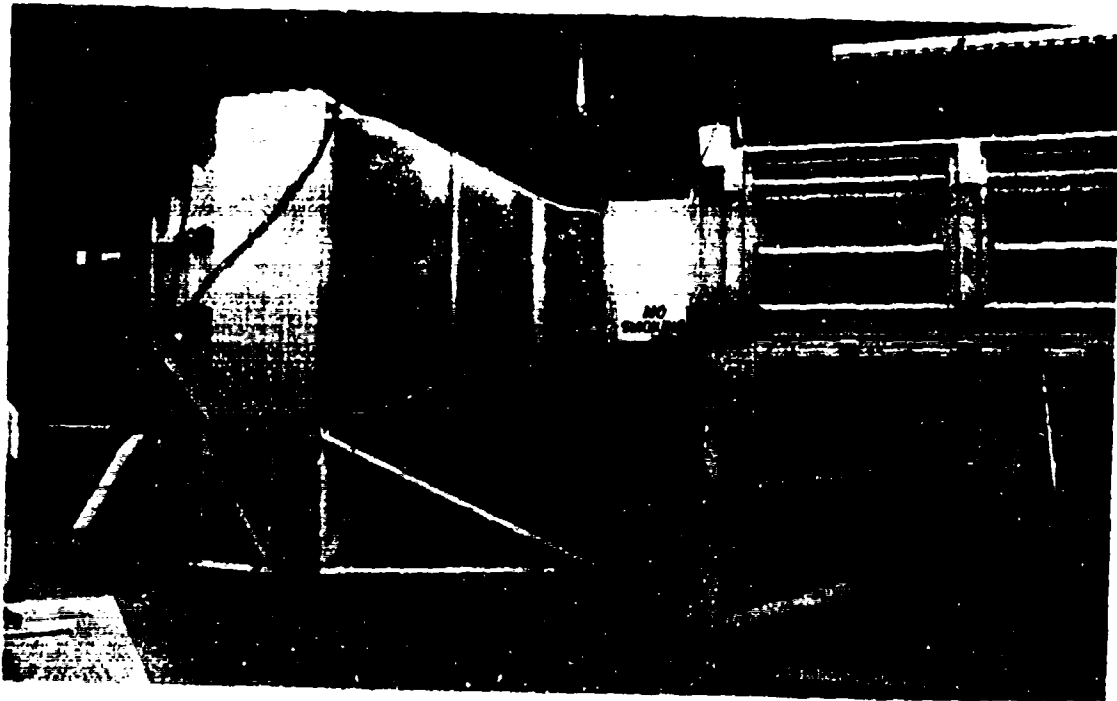
z (cm)	\bar{u} (cm/sec)	\bar{u}^2 (cm ² /sec ²)	\bar{w}^2 (cm ² /sec ²)	\overline{uw} (cm ² /sec ²)	$\frac{\overline{uw}}{\bar{u}^2}$	ϵ (cm ² /sec ³)	$\epsilon z $ (cm ³ /sec ³)	$\frac{\epsilon z }{(\bar{u})^{3/2}}$
-0.95	15.69	5.78	4.05	-2.55	-0.11	49.60	47.12	0.24
-1.82	12.75	4.72	3.21	-0.93	-0.06	17.60	32.03	0.30
-2.63	11.68	4.26	2.68	-2.44	-0.21	13.09	34.42	0.45
-3.47	11.13	3.95	2.63	-3.30	-0.32	8.50	29.51	0.48
-5.19	9.83	3.22	1.90	-2.18	-0.36	4.72	24.50	0.73
-6.90	8.11	2.83	1.48	-2.32	-0.55	2.94	20.30	0.90
-9.41	8.23	3.14	1.60	-1.79	-0.36	2.46	23.18	0.75
-14.52	4.93	1.84	1.03	-0.30	-0.16	2.44	35.38	5.68
-19.60	3.83	2.01	0.60	-0.32	-0.27	2.34	45.82	5.64
-27.18	1.79	0.89	0.60	0.07	0.13	10.83	294.30	417.50

TABLE 17. -MEASUREMENTS OF VELOCITY IN WATER BOUNDARY-LAYER

Run No.: Oil - 28, $U_{\infty} = 10$ m/sec, $x = 6$ m

z (cm)	\bar{u} (cm/sec)	\bar{u}^2 (cm ² /sec)	\bar{u}^2 (cm ² /sec)	$\frac{\overline{uw}}{u^2 \bar{u}^2}$ (cm ² /sec ²)	$\frac{\overline{uw}}{u^2 \bar{u}^2}$ (cm ² /sec ²)	ϵ (cm ² /sec ³)	$\frac{\epsilon z }{(cm^3/sec^3)}$	$\frac{\epsilon z }{(\bar{u}^2)^{3/2}}$
-0.95	14.77	5.63	3.88	-3.60	-0.17	52.23	49.62	0.28
-1.82	11.18	4.55	2.88	-0.42	-0.03	17.92	32.61	0.35
-2.63	9.29	3.97	2.31	-0.57	-0.06	14.50	38.14	0.61
-3.47	8.37	3.60	2.13	-0.93	-0.12	10.82	37.53	0.80
-5.19	6.58	2.53	1.33	1.82	0.54	5.55	28.81	1.78
-6.30	5.80	2.12	0.75	-0.19	-0.06	2.11	14.53	1.53
-9.41	5.13	2.29	0.71	0.07	0.04	1.84	17.34	1.44
-14.52	4.27	2.01	0.61	0.08	0.07	1.79	25.96	3.20
-19.60	4.22	2.45	1.27	-1.72	-0.55	10.55	206.70	14.05
-27.18	2.99	1.53	0.73	-0.11	-0.10	5.09	138.40	38.64

Figures



a. WIND TUNNEL



b. WAVE TANK

FIGURE 1. WIND-WAVE TANK

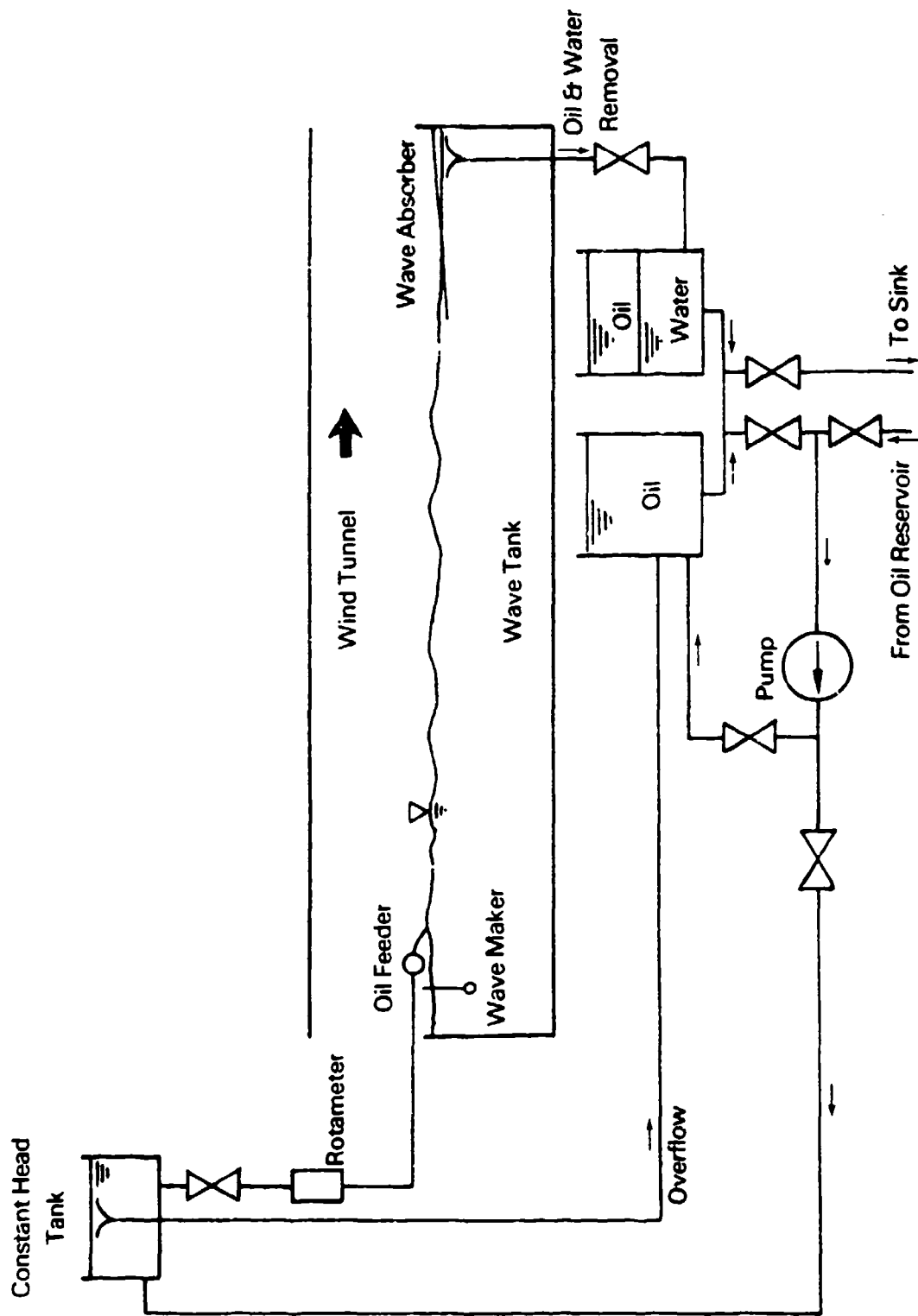


FIGURE 2. OIL FEEDING SYSTEM SCHEMATIC.

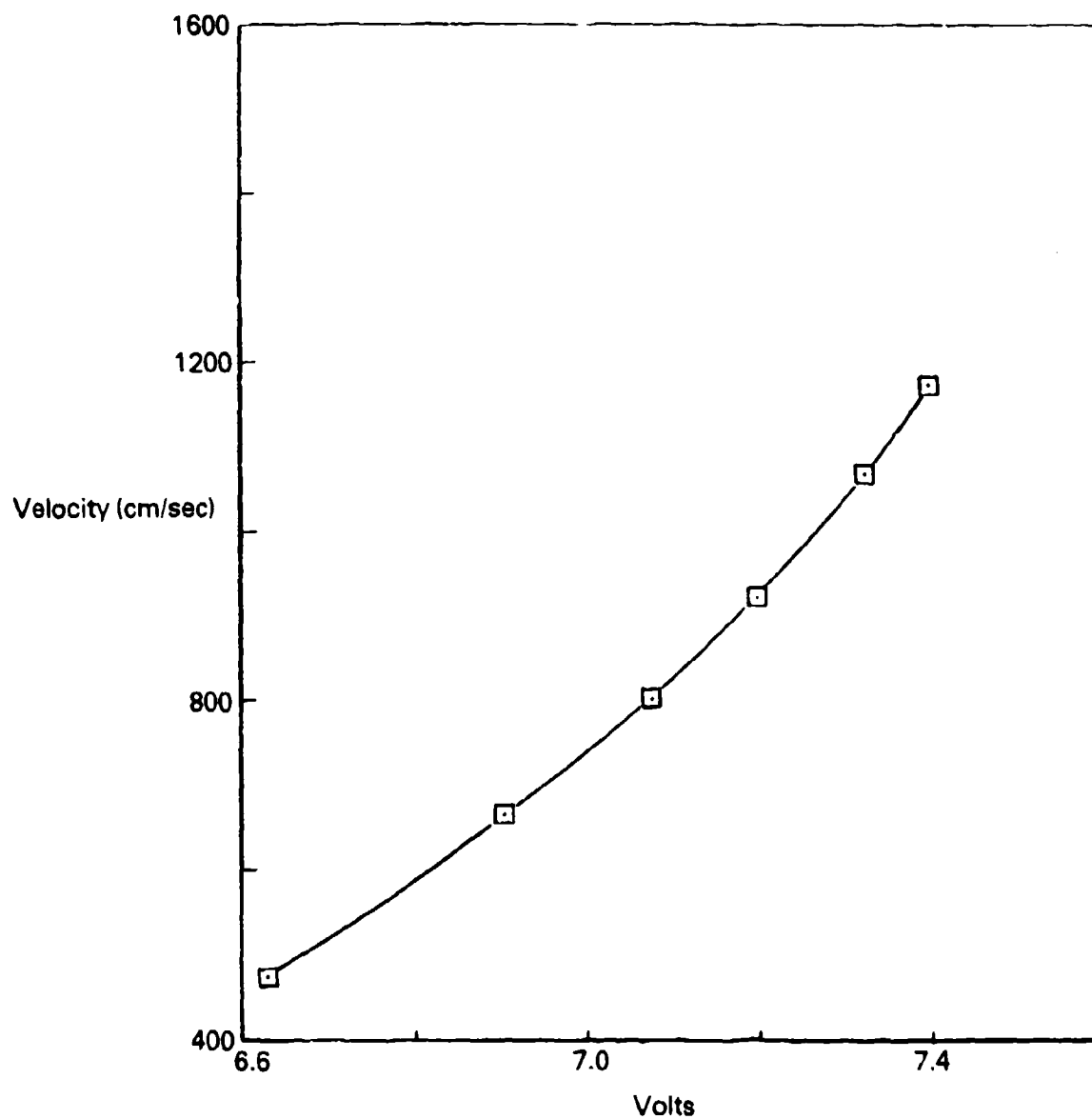


FIGURE 3. HOT-WIRE PROBE CALIBRATION.

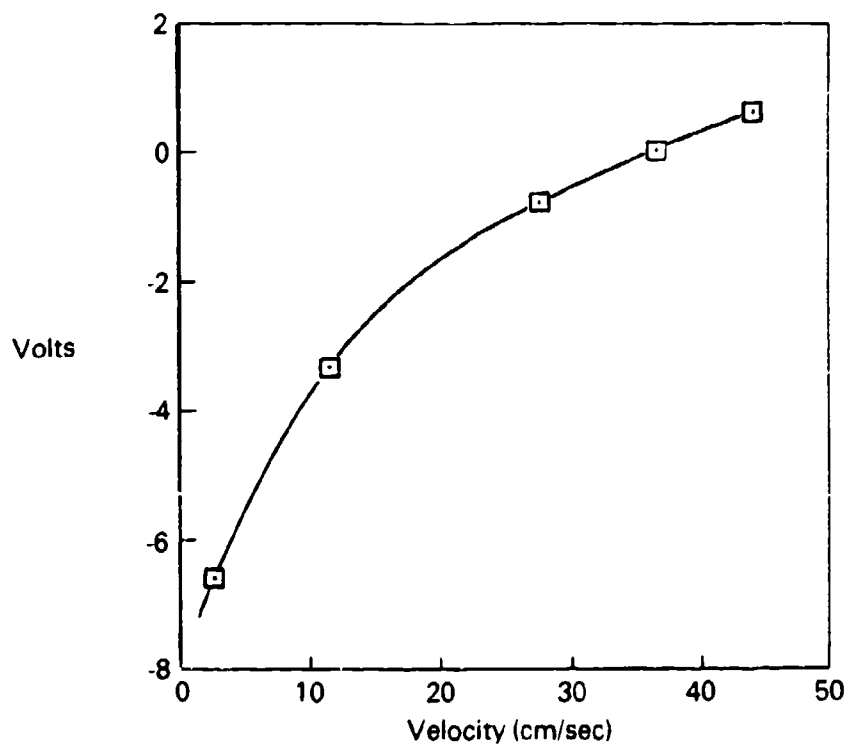
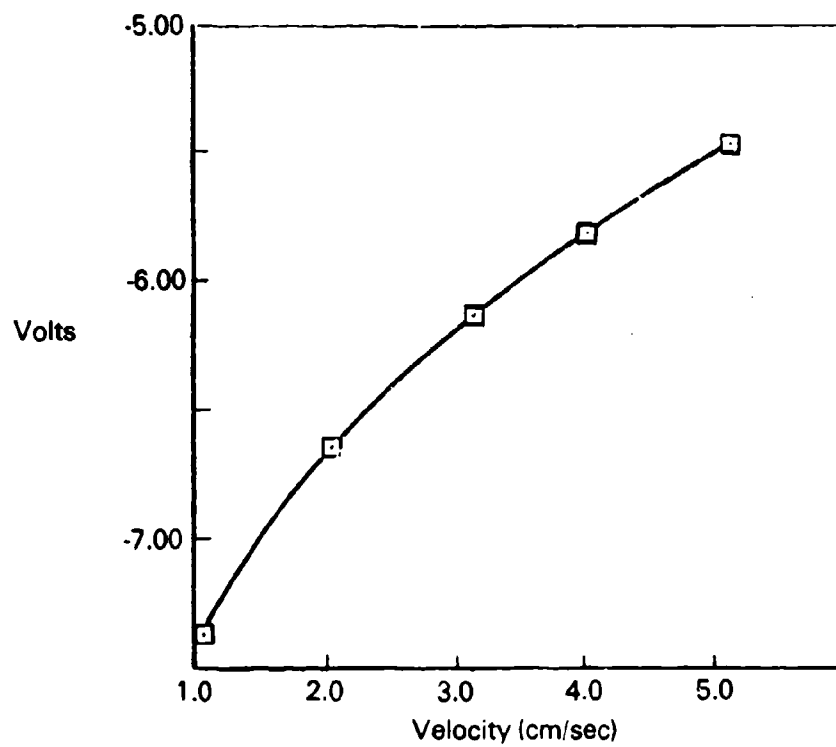


FIGURE 4. HOT-FILM PROBE CALIBRATION.

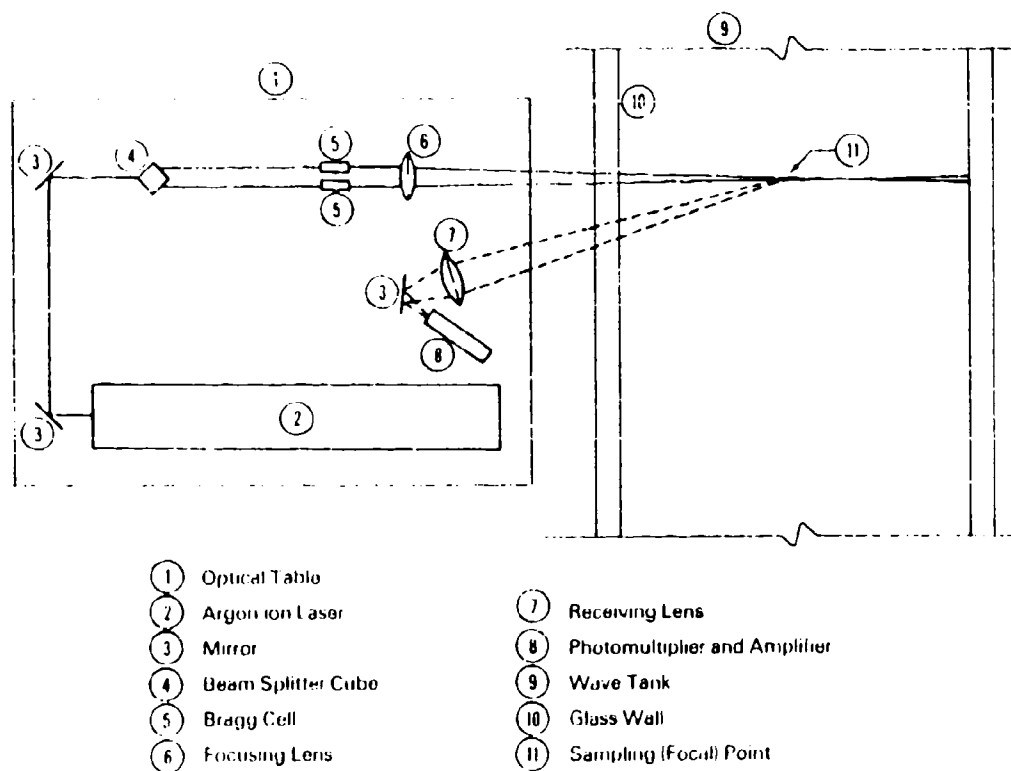
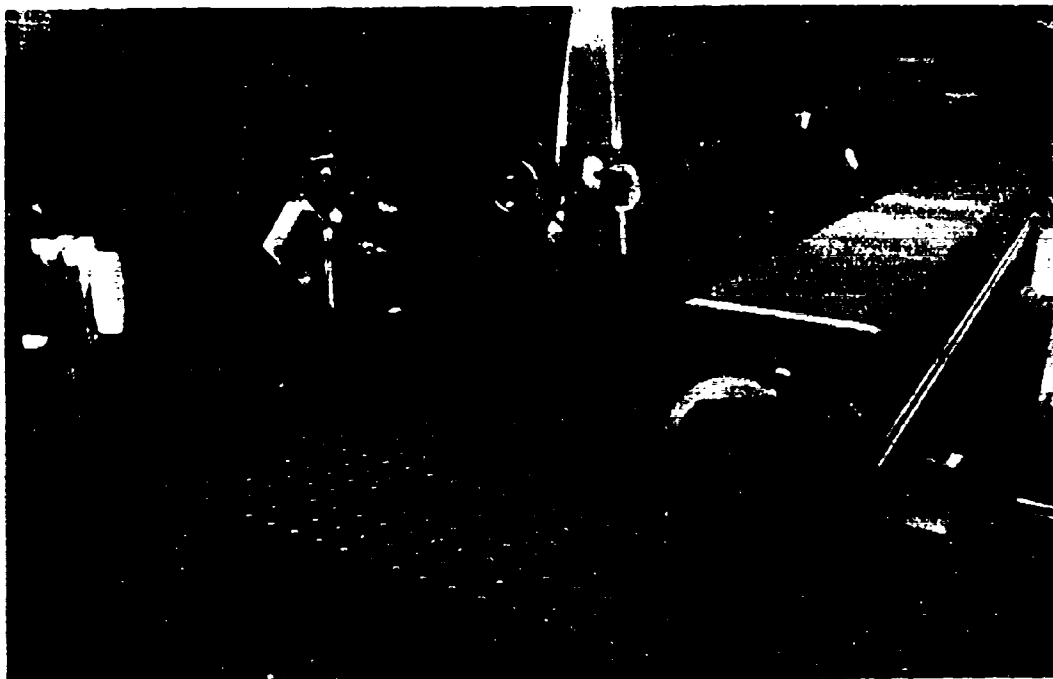


FIGURE 5. LASER DOPPLER VELOCIMETER.



0 20 40 μm

Magnification: 1000 \times
Particle Size < 40 μm
Specific Gravity: 1.03

FIGURE 6. PLIOLITE PARTICLES PHOTOGRAPHED WITH ELECTRONIC MICROSCOPE.

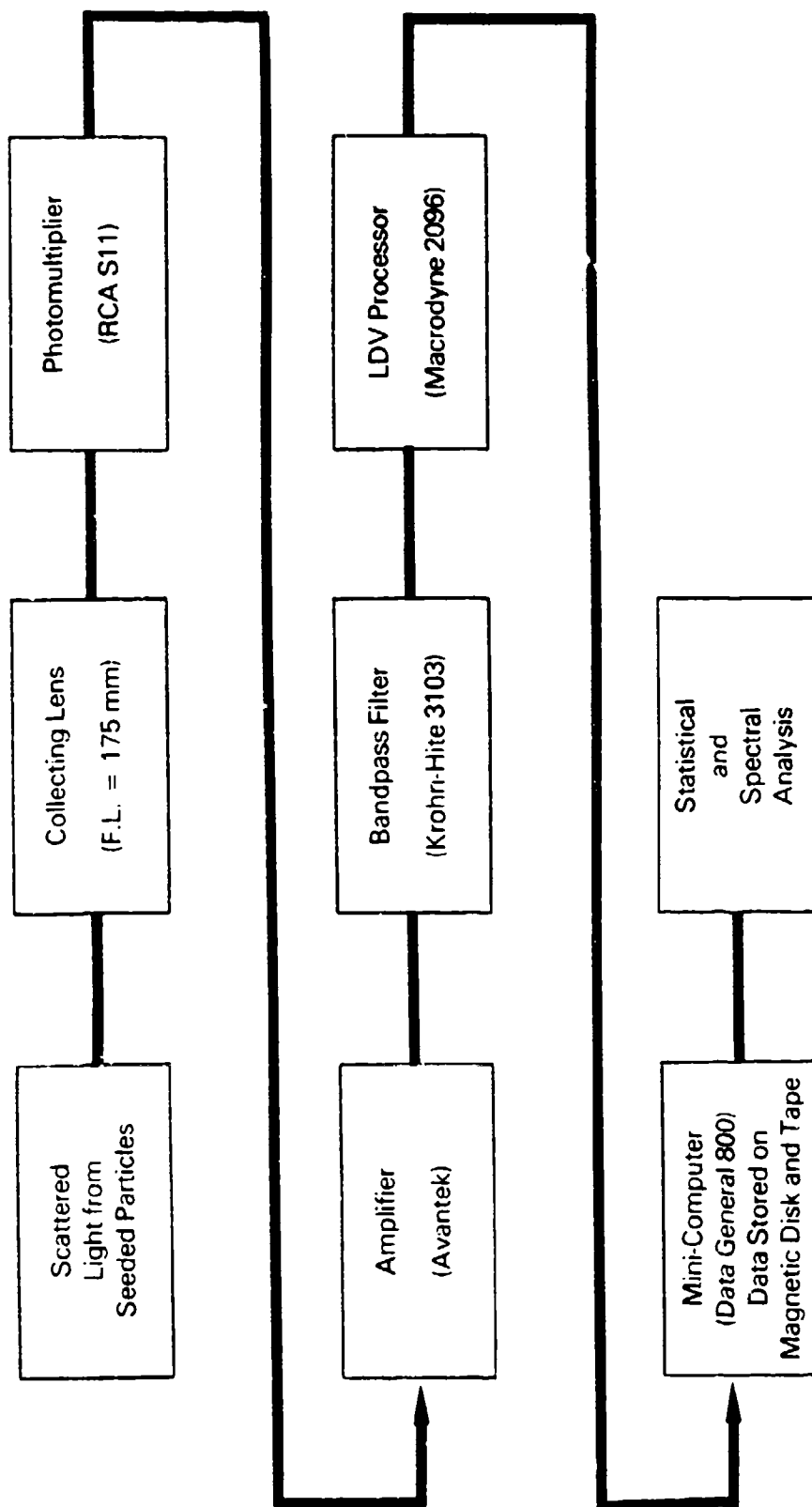


FIGURE 7. BLOCK DIAGRAM OF DATA RECORDING AND PROCESSING OF LDV.

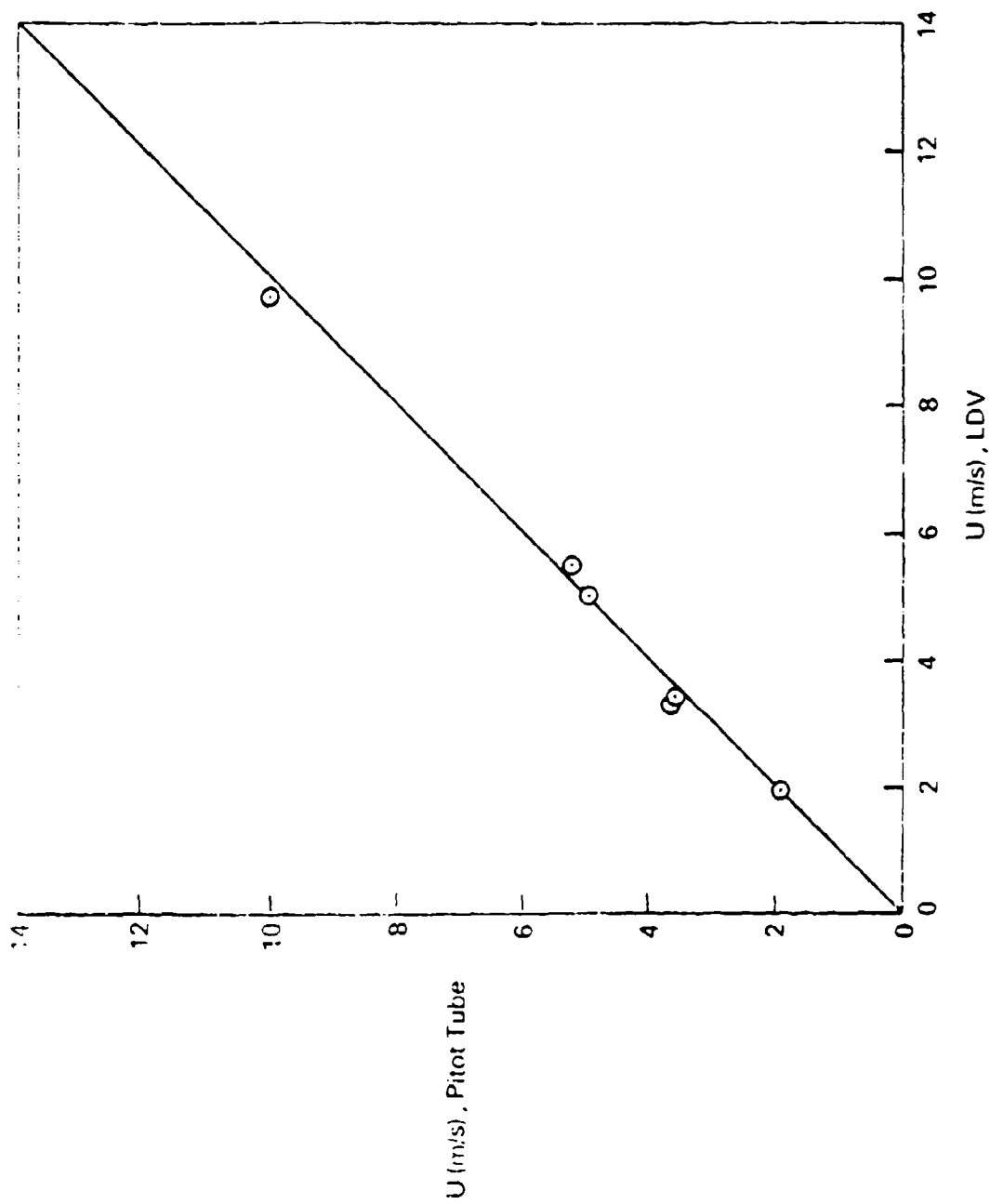


FIGURE 8. COMPARISON OF LDV OUTPUT WITH PITOT TUBE OUTPUT.

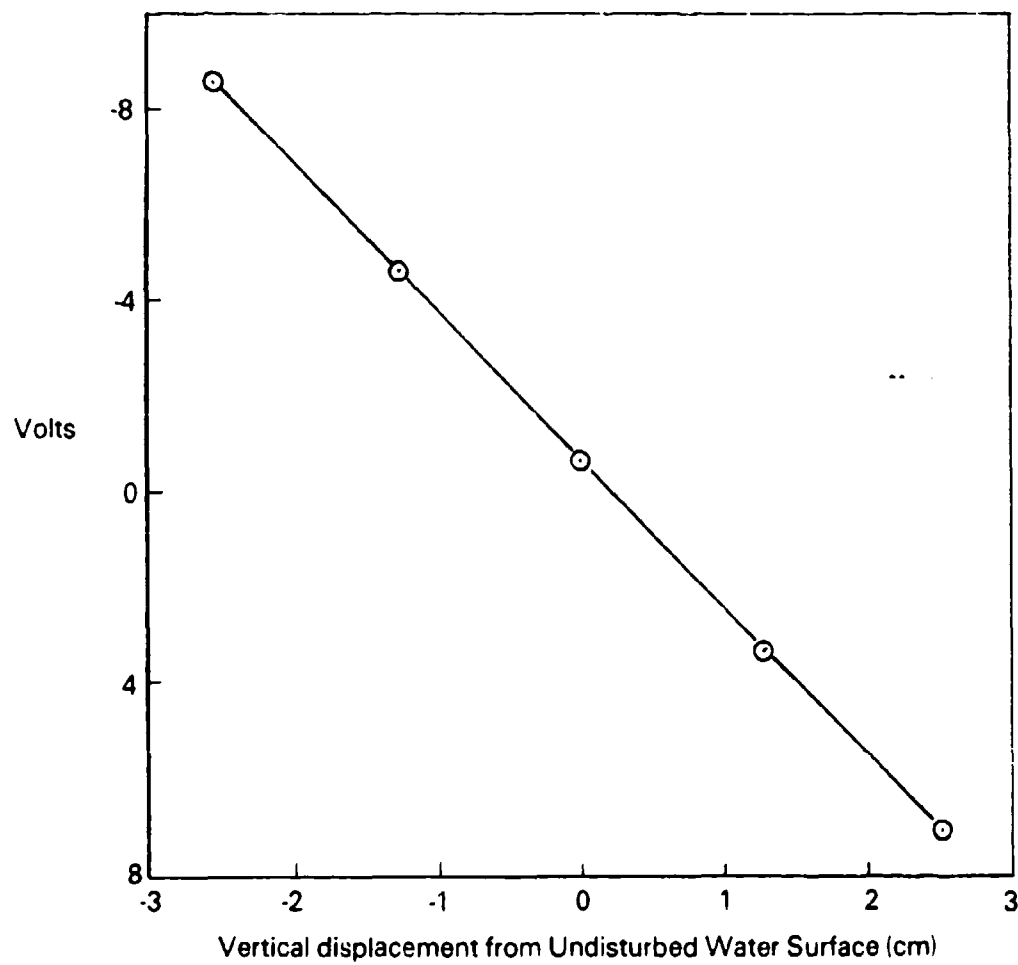


FIGURE 9. CALIBRATION OF CAPACITANCE PROBE.

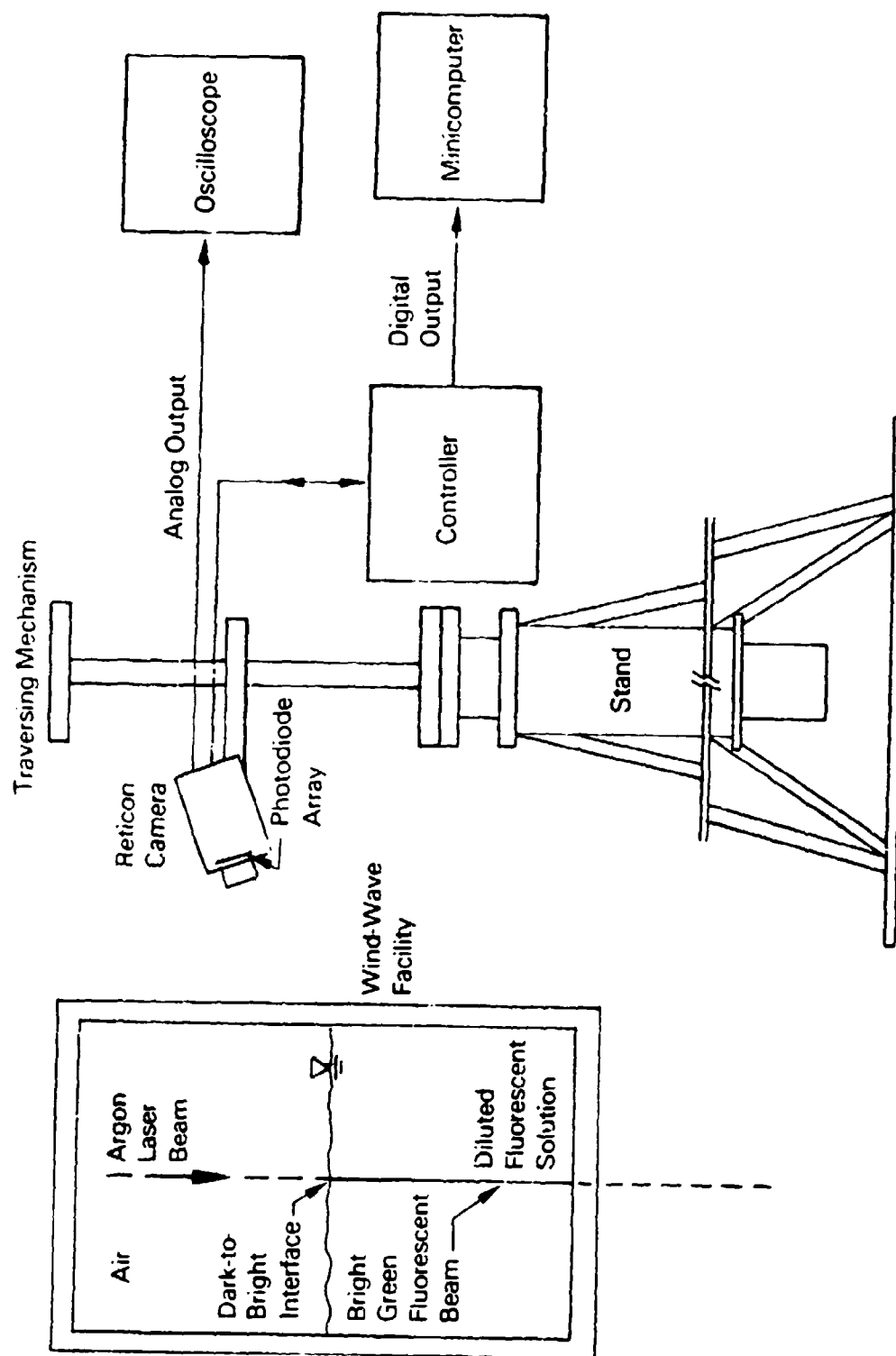


FIGURE 10. SCHEMATIC OF PHOTODIODE WAVE GAUGE FOR WATER-WAVE MEASUREMENT.

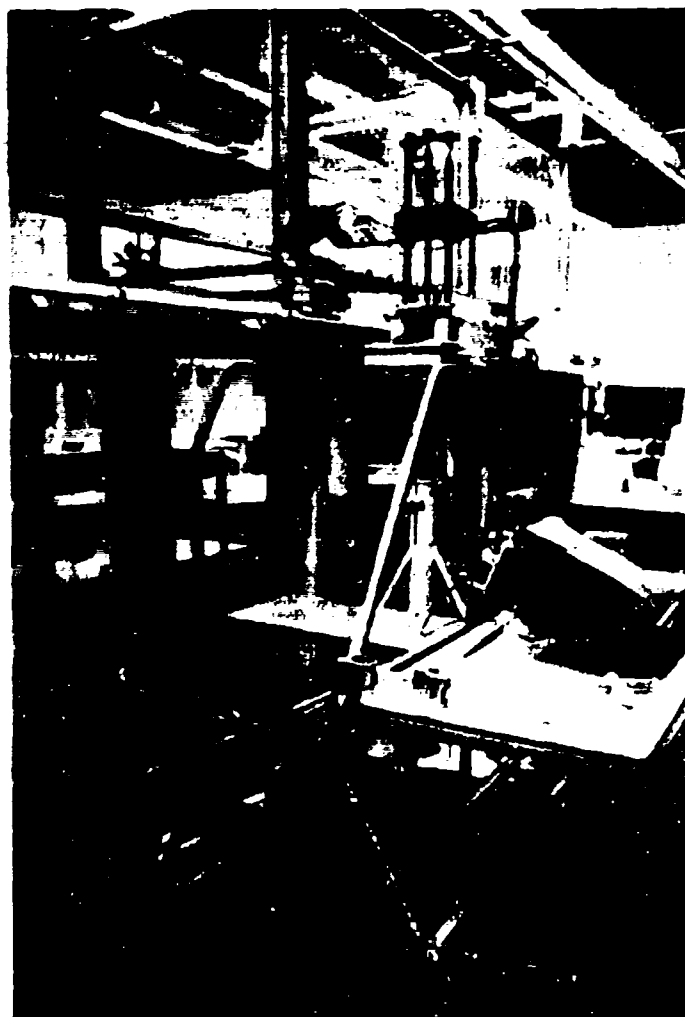
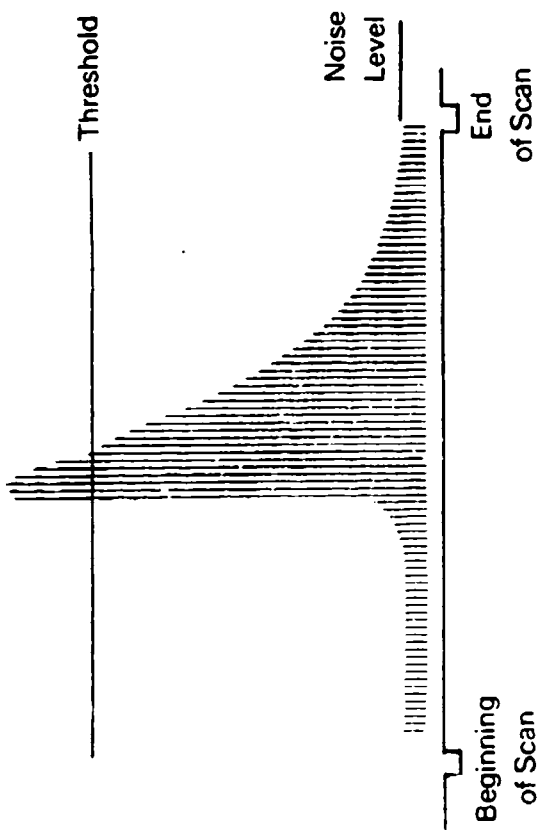
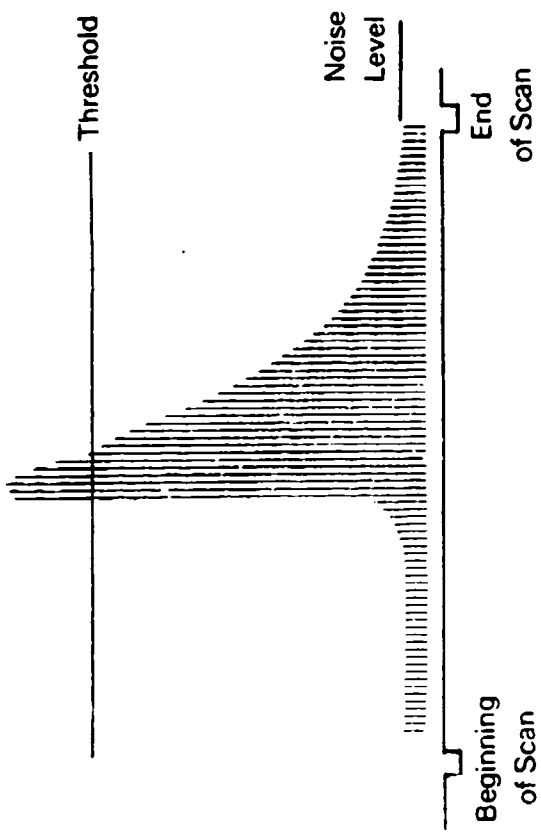


FIGURE 11. PHOTODIODE WAVE GAUGE SETUP.



111

(a) Wave "Marker"



(b) Analog Output Viewed on Oscilloscope

(c) Logical Binary Pulses



(c) Logical Binary Pulses

FIGURE 12. OPERATIONAL PRINCIPLE OF WAVE GAL'GE

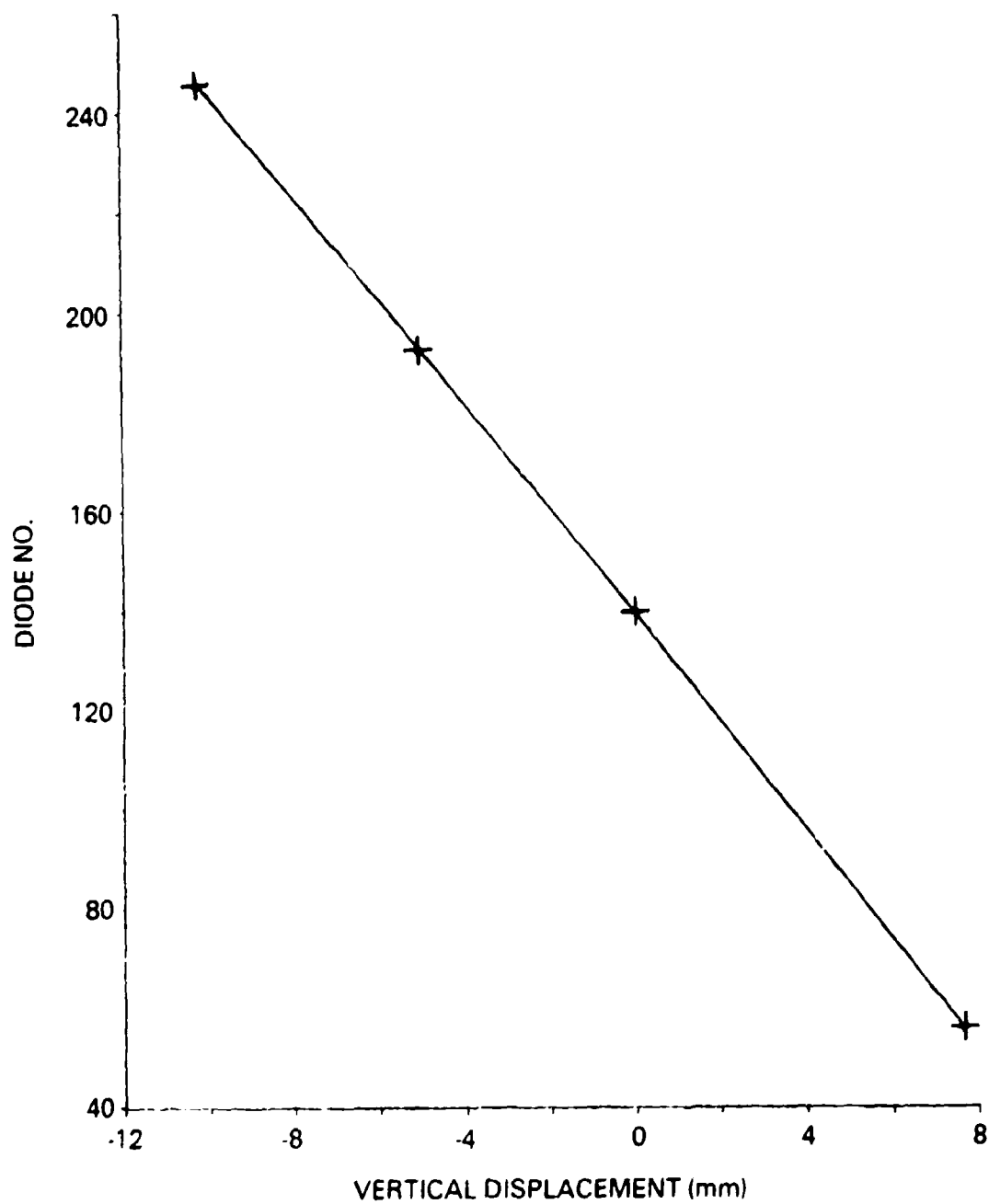


FIGURE 13. PHOTODIODE WAVE GAUGE CALIBRATION.

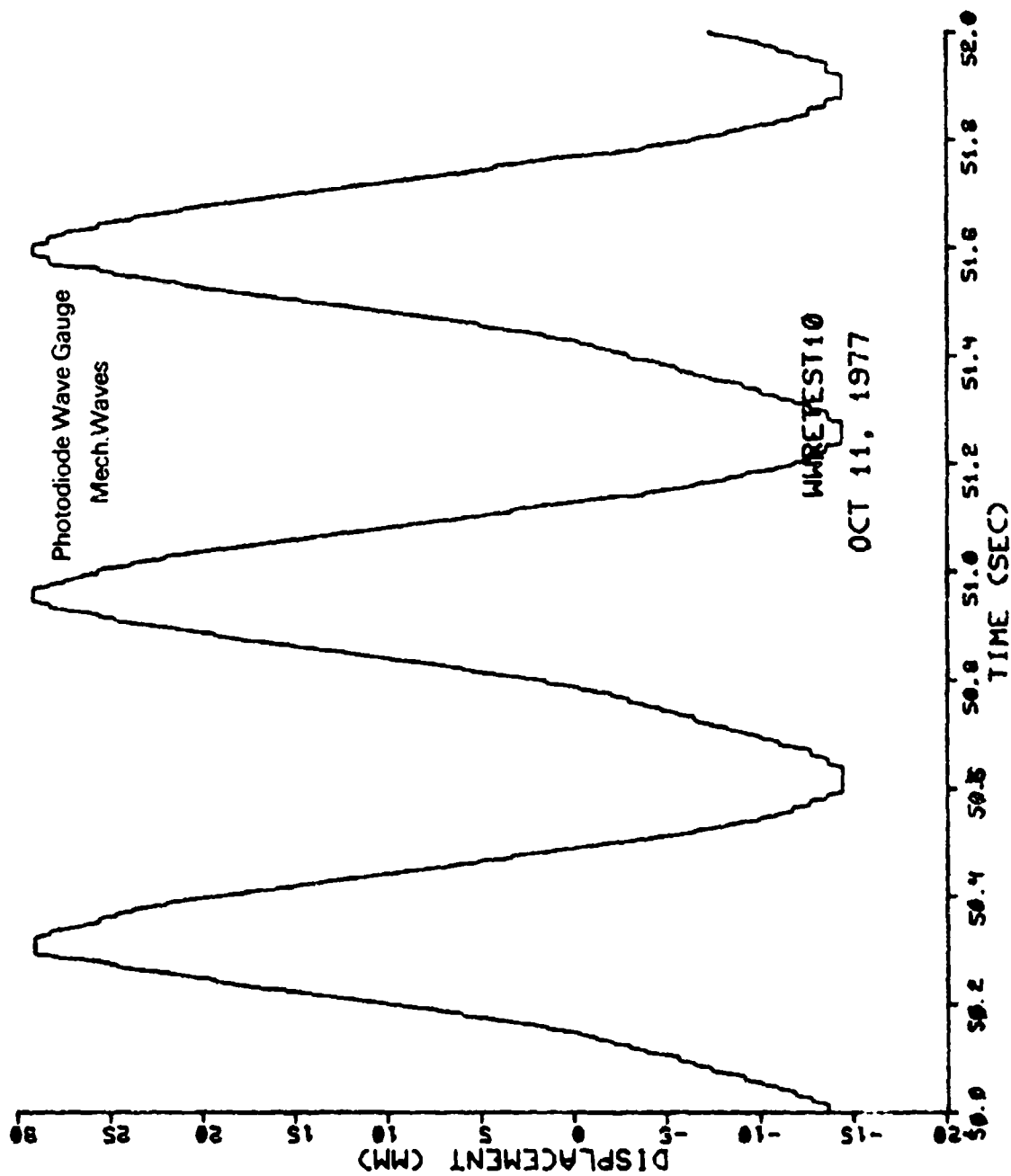


FIGURE 14. WAVE PROFILE MEASURED WITH PHOTODIODE WAVE GAUGE.

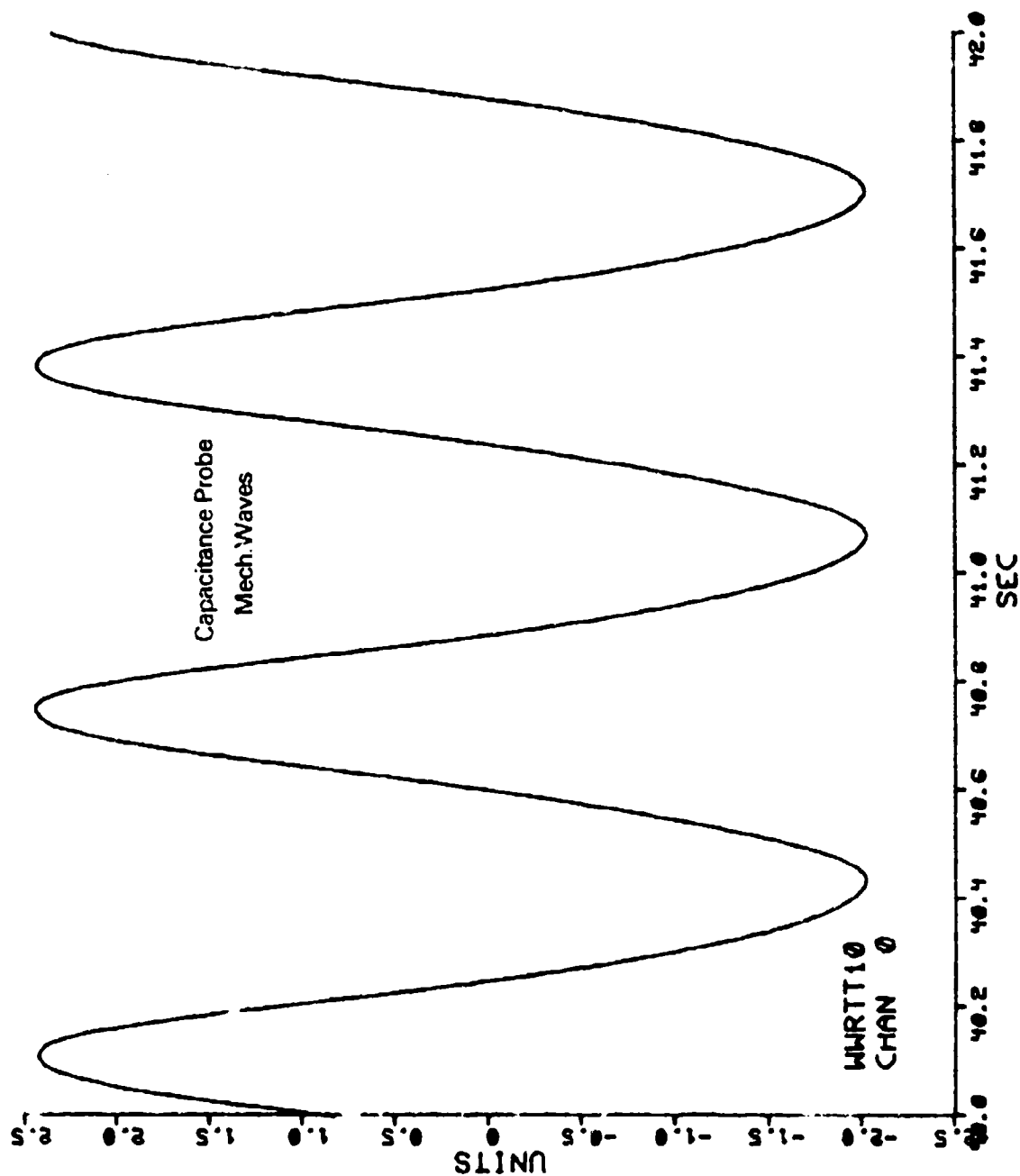


FIGURE 15. WAVE PROFILE MEASURED WITH CAPACITANCE PROBE.

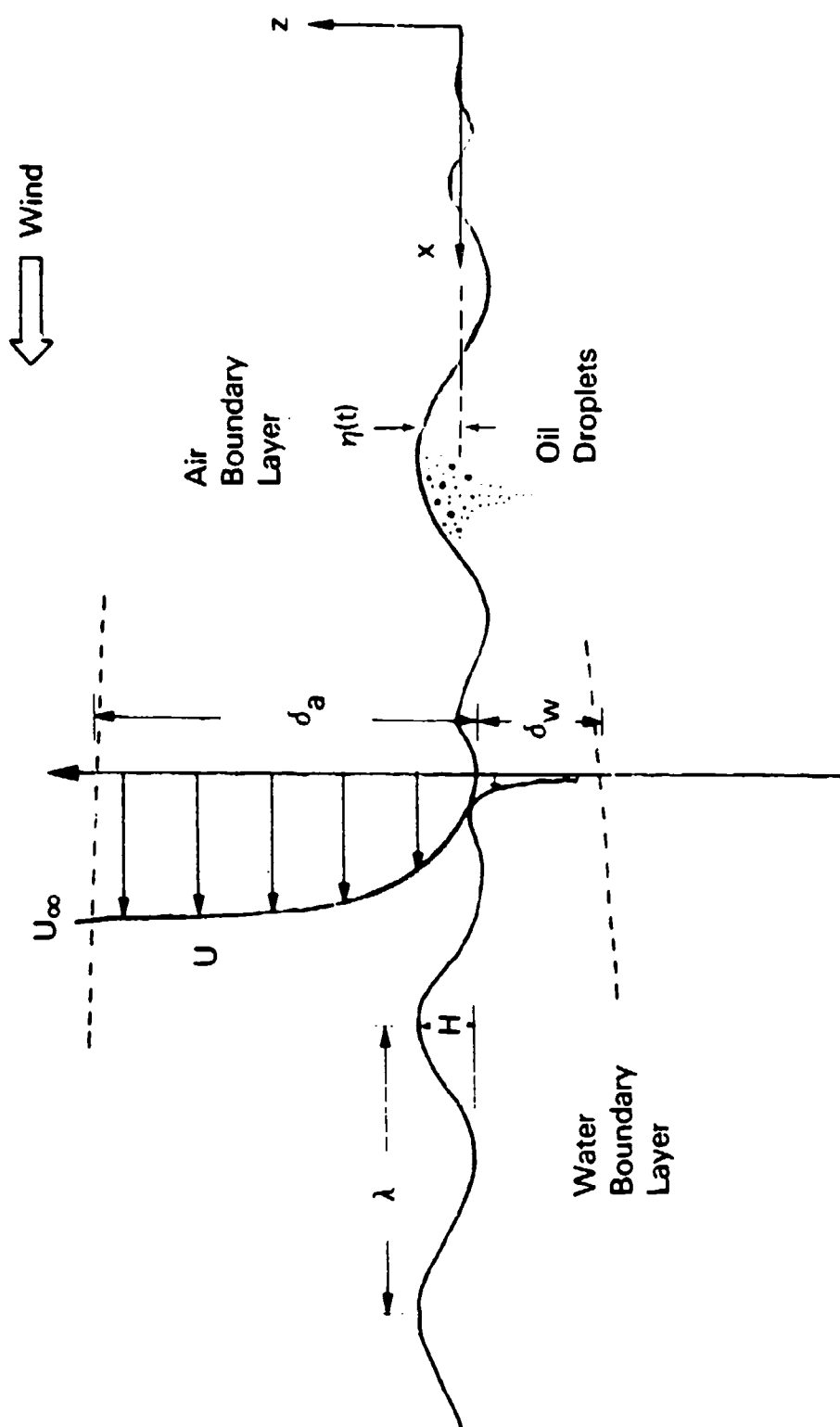


FIGURE 16. DEFINITION SKETCH FOR OIL DISPERSION IN WIND WAVES.

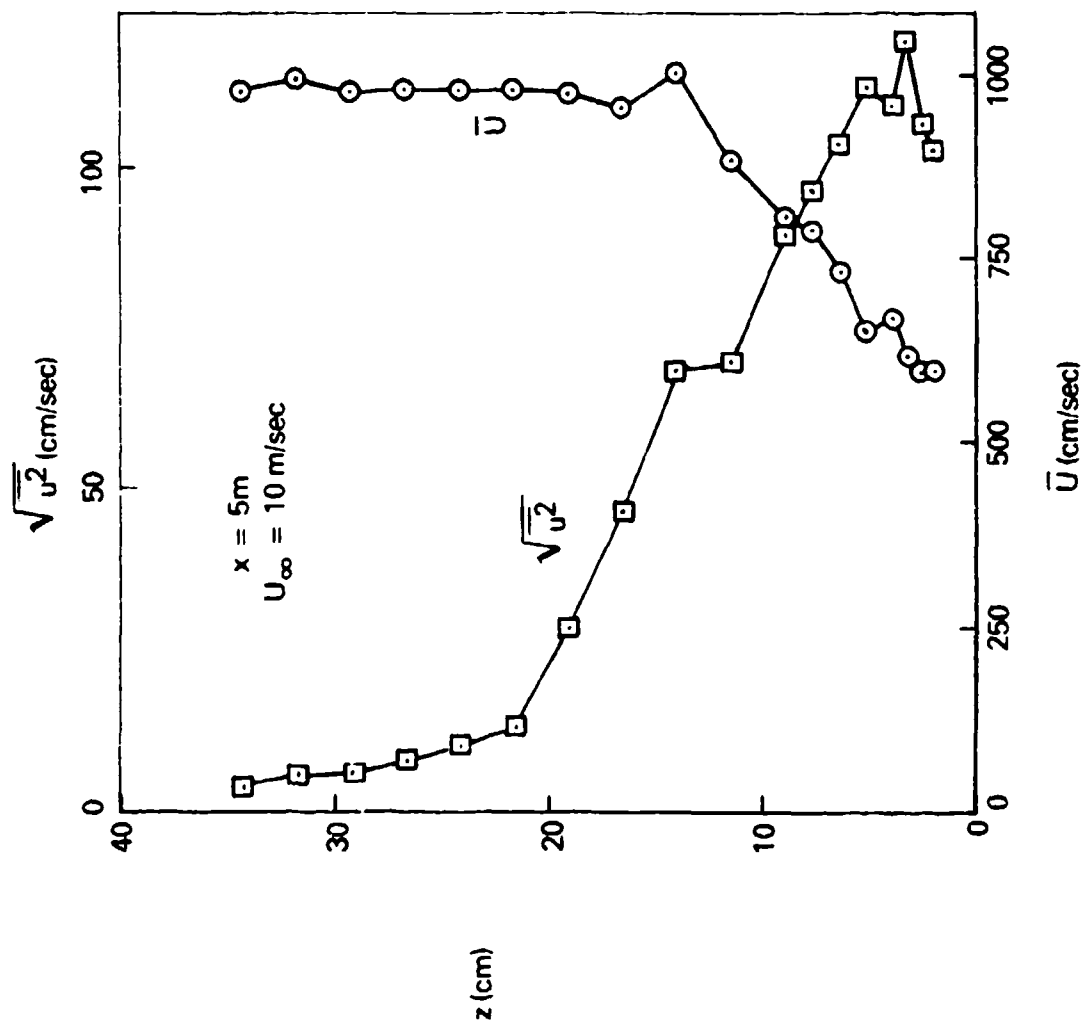


FIGURE 17. PROFILES OF MEAN VELOCITY AND TURBULENCE INTENSITY IN AIR BOUNDARY-LAYER.

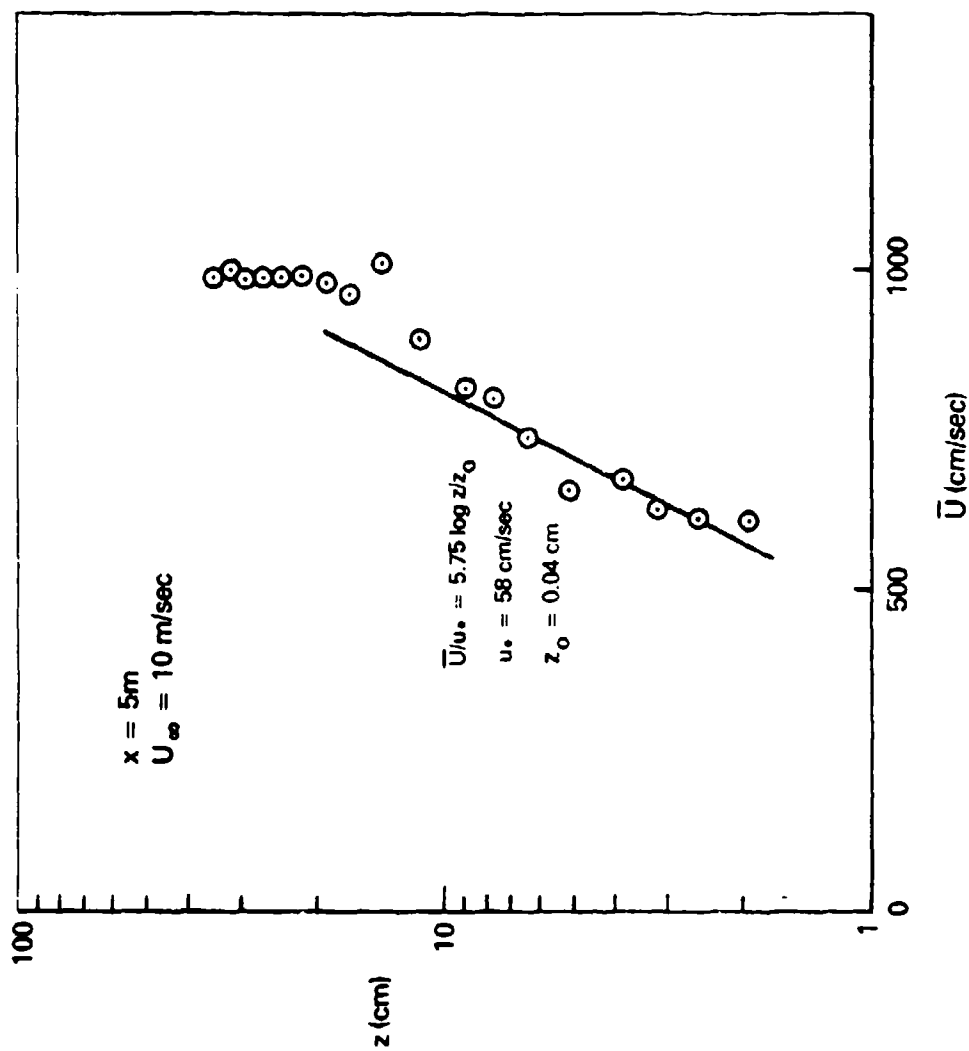


FIGURE 18. MEAN VELOCITY PROFILE IN AIR BOUNDARY-LAYER.

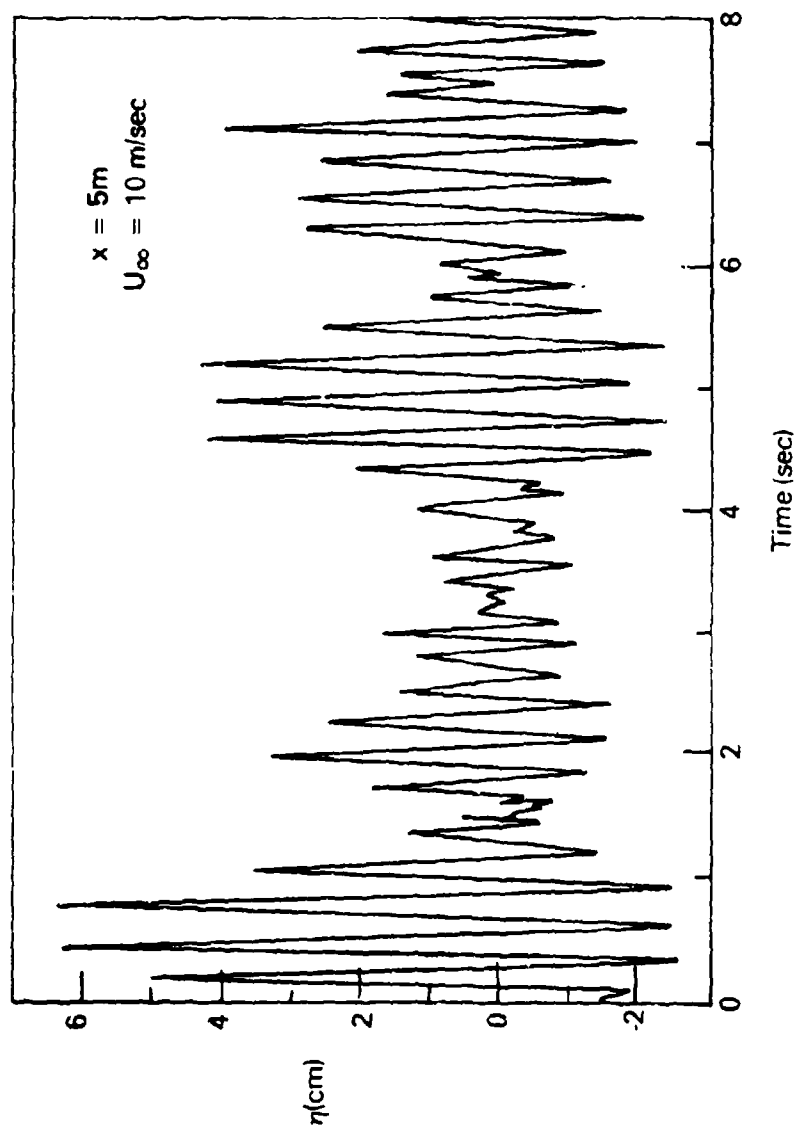


FIGURE 19. INSTANTANEOUS WATER SURFACE DISPLACEMENT OF WIND-WAVES.

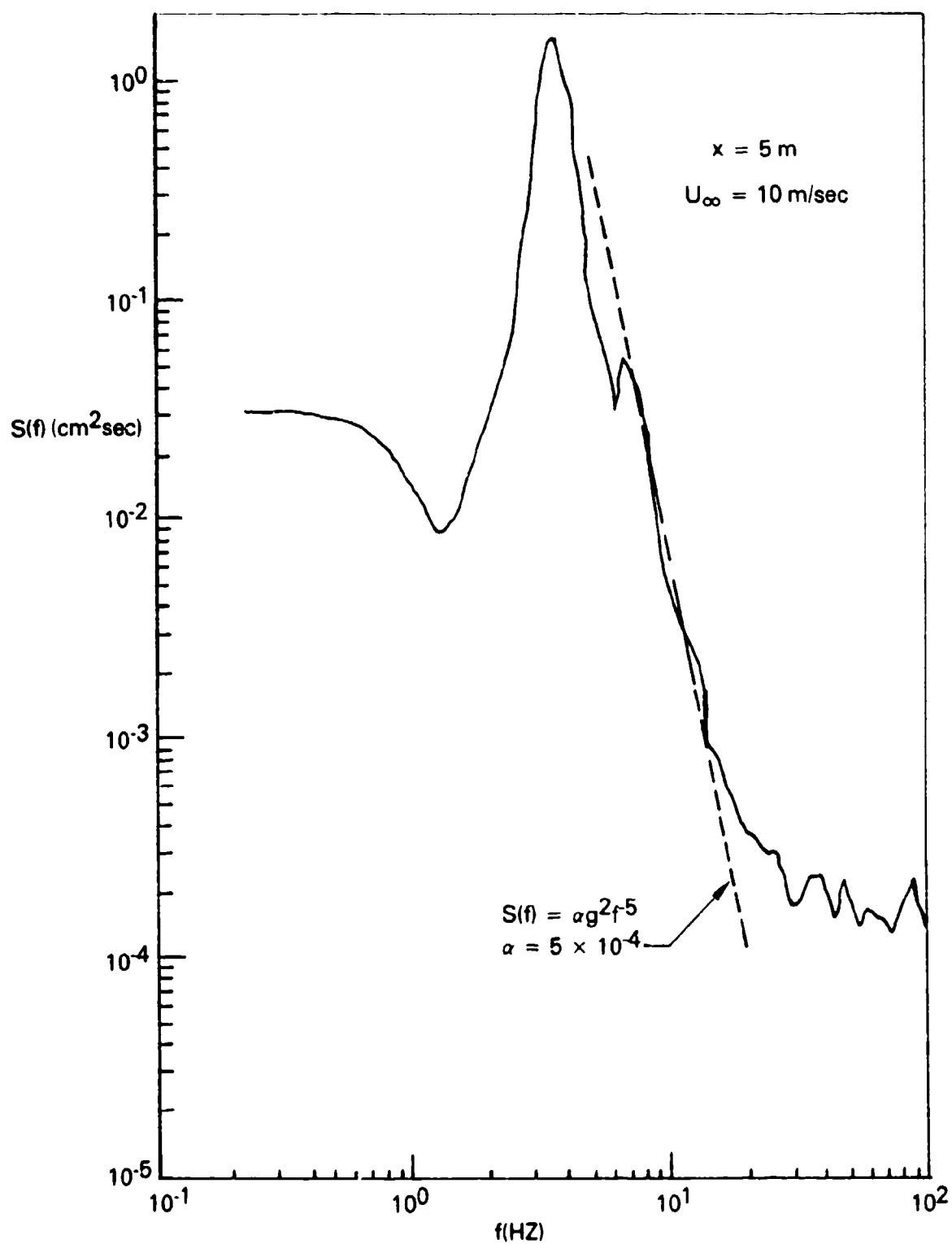


FIGURE 20. WAVE ENERGY SPECTRUM.

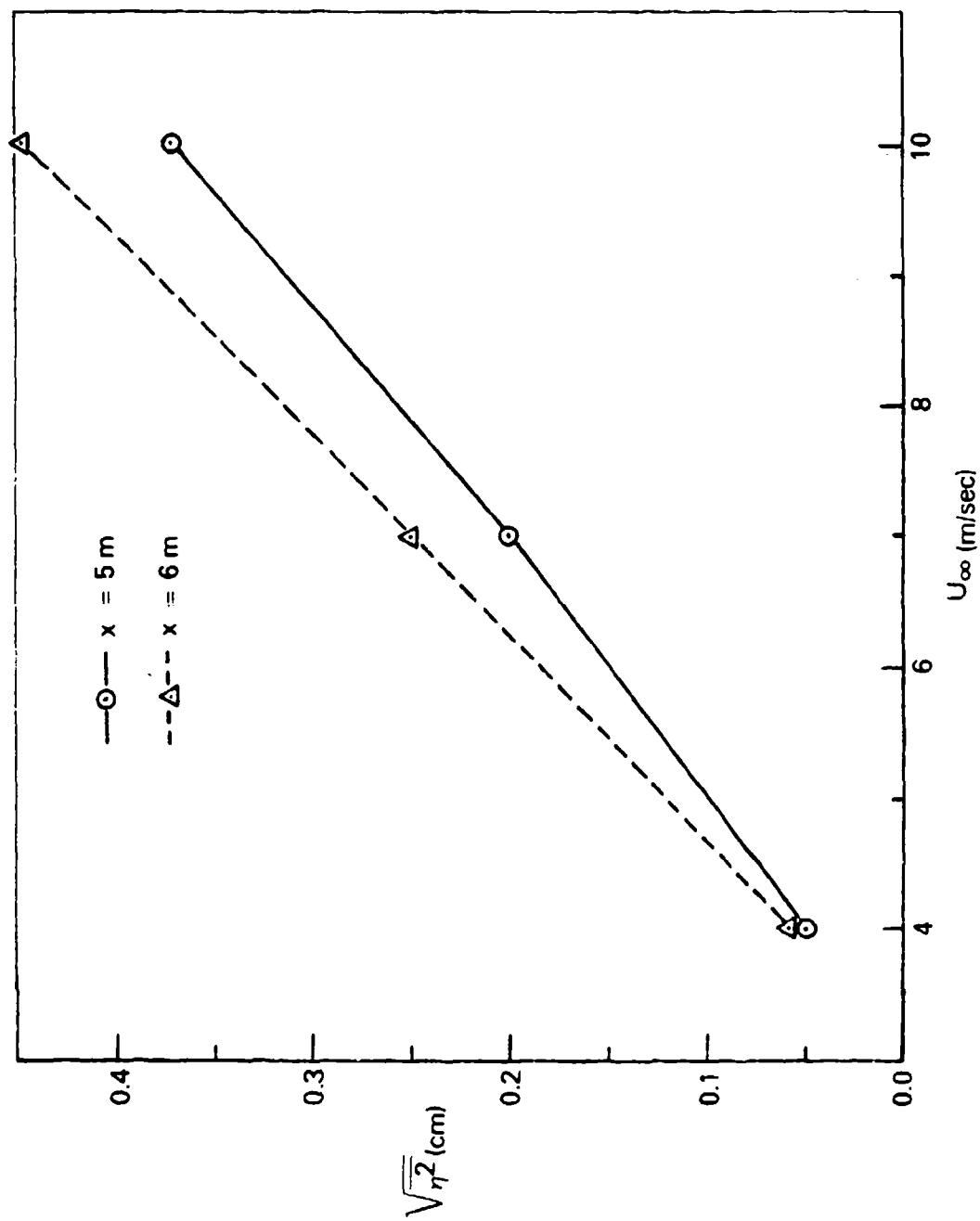


FIGURE 21. VARIATION OF RMS WAVE AMPLITUDE WITH WIND SPEED.

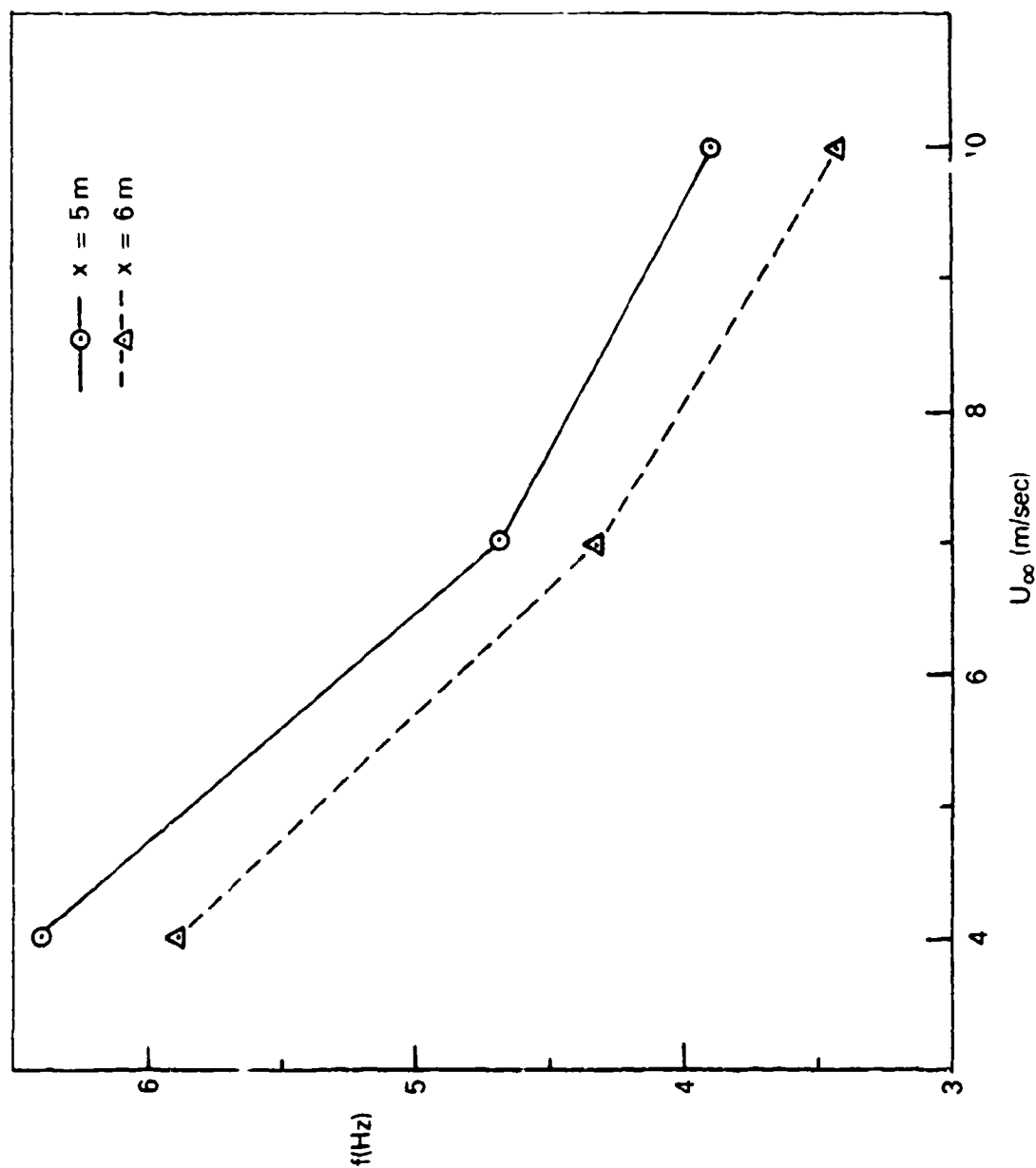


FIGURE 22. VARIATION OF DOMINANT WAVE FREQUENCY WITH WIND SPEED.

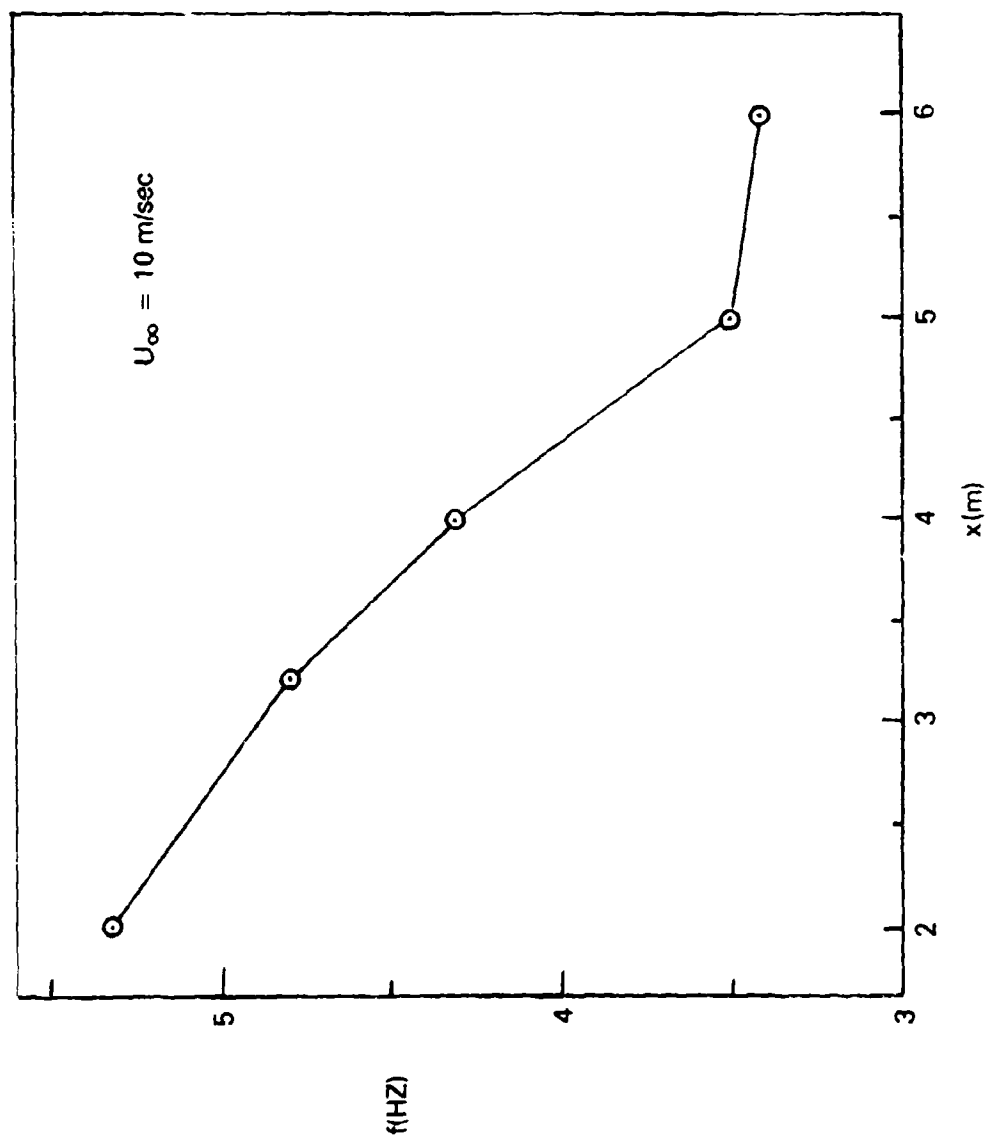


FIGURE 23. FETCH EFFECTS ON DOMINANT WAVE FREQUENCY.

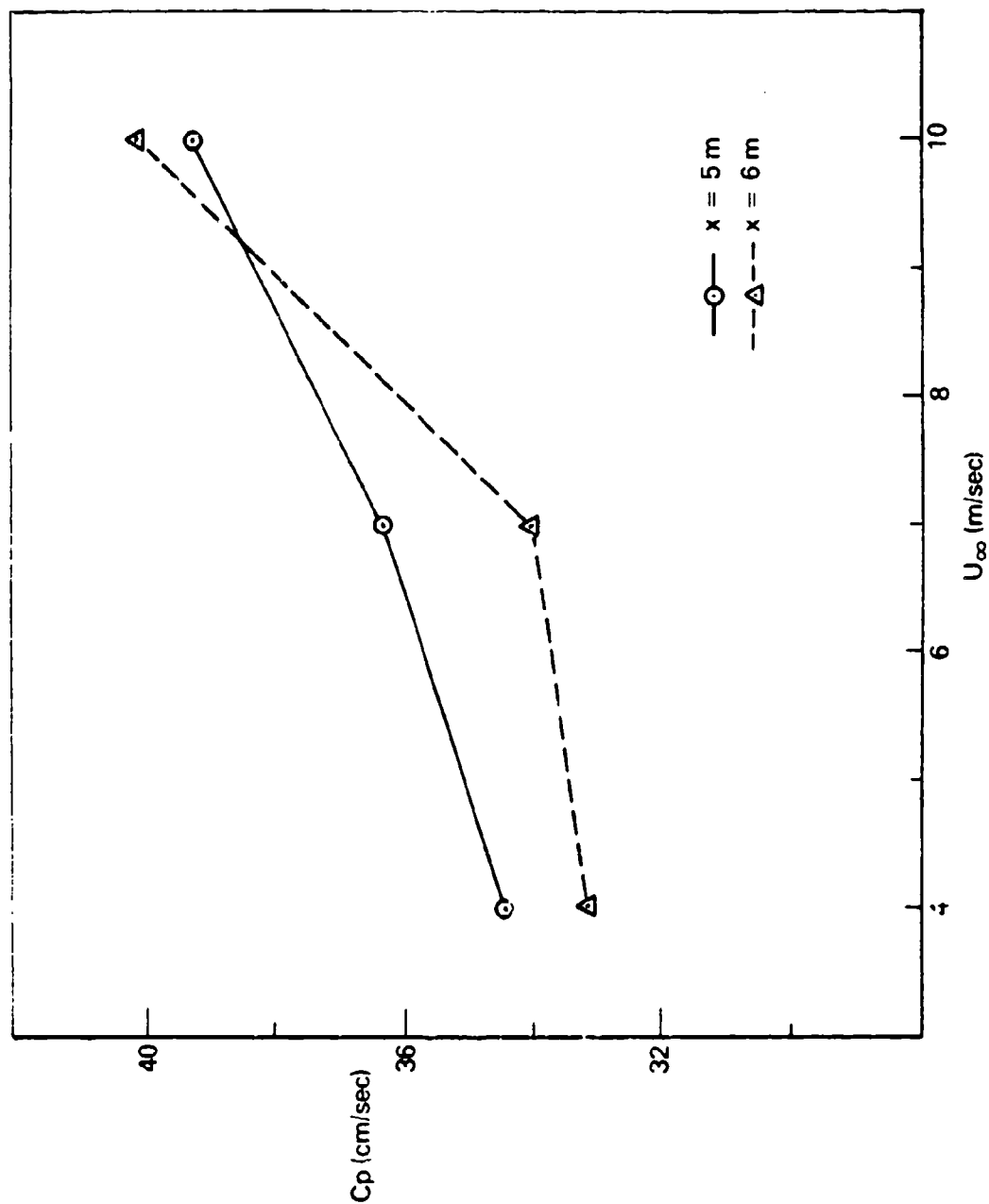


FIGURE 24. VARIATION OF WAVE PHASE SPEED WITH WIND SPEED.

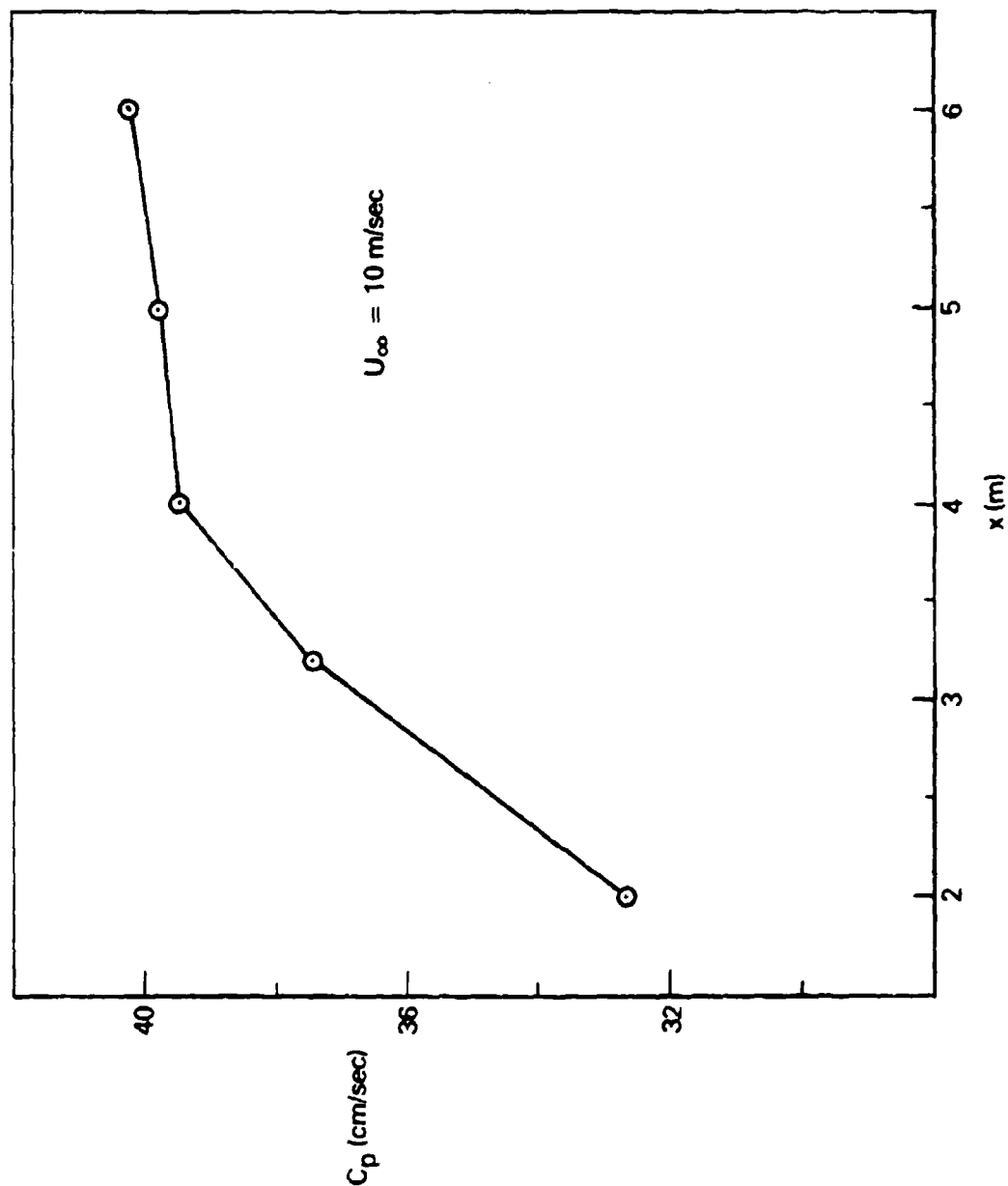


FIGURE 25. FETCH EFFECTS ON WAVE PHASE SPEED.

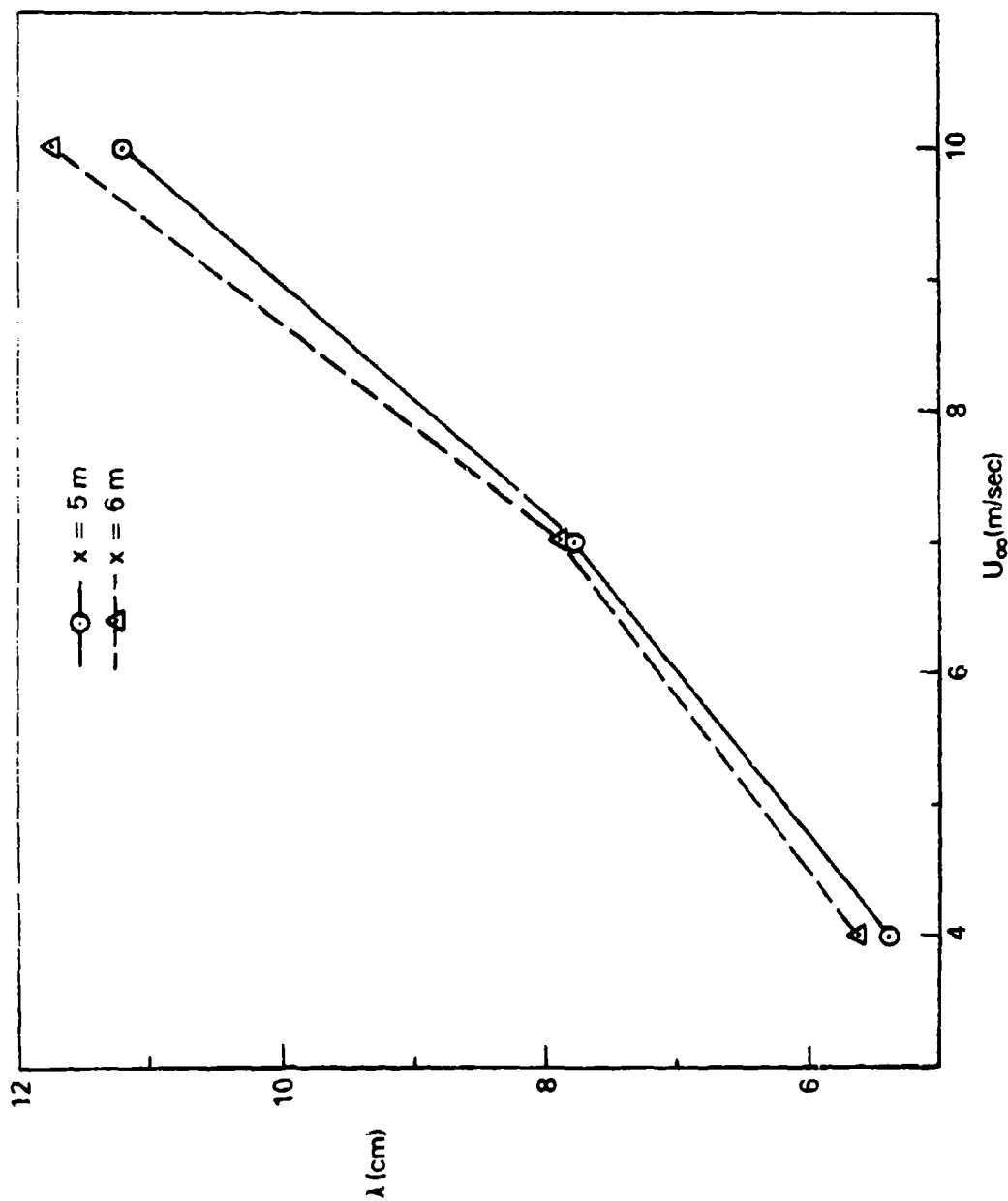


FIGURE 26. VARIATION OF DOMINANT WAVE LENGTH WITH WIND SPEED.

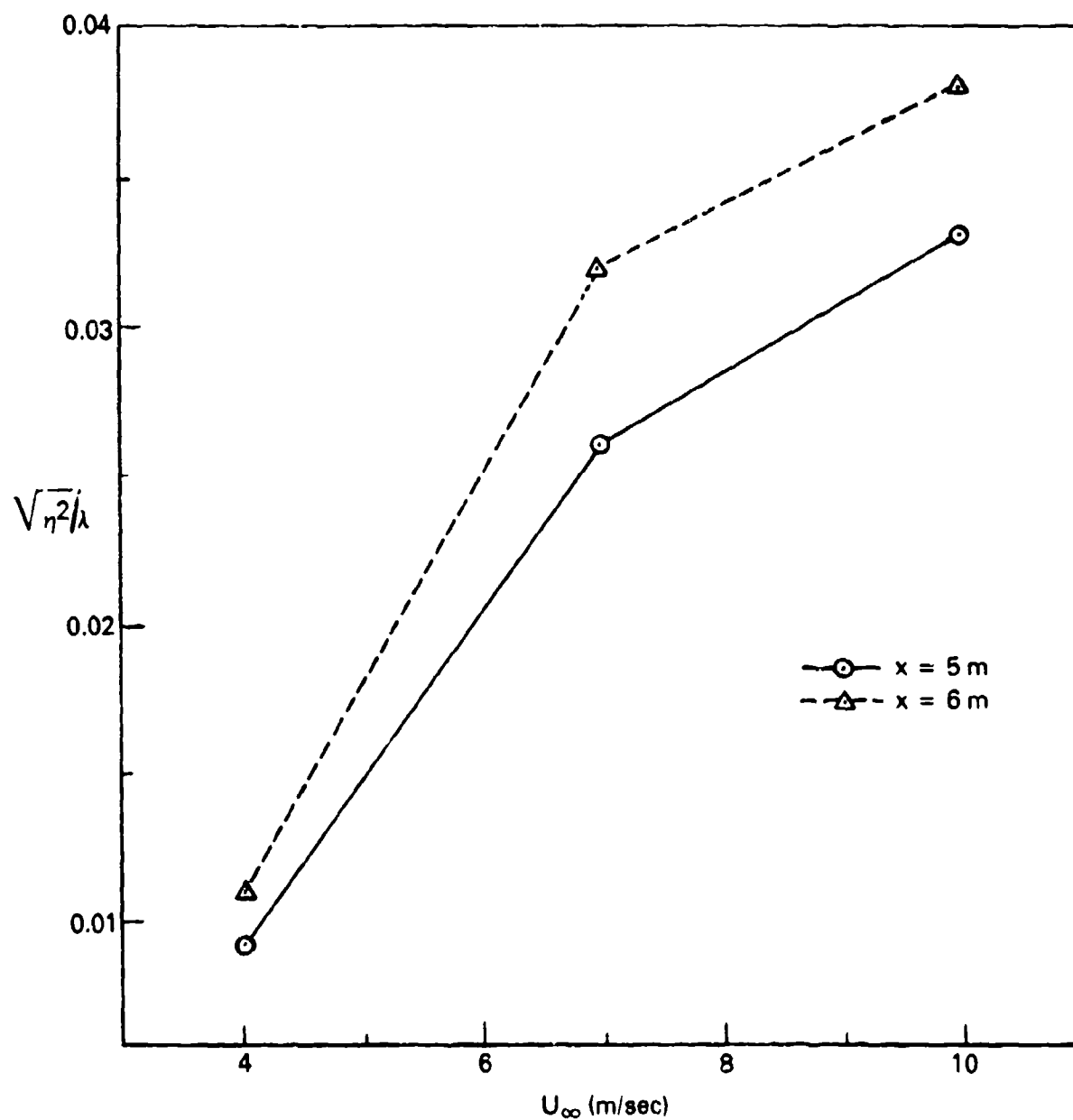


FIGURE 27. VARIATION OF DOMINANT WAVE SLOPE WITH WIND SPEED.

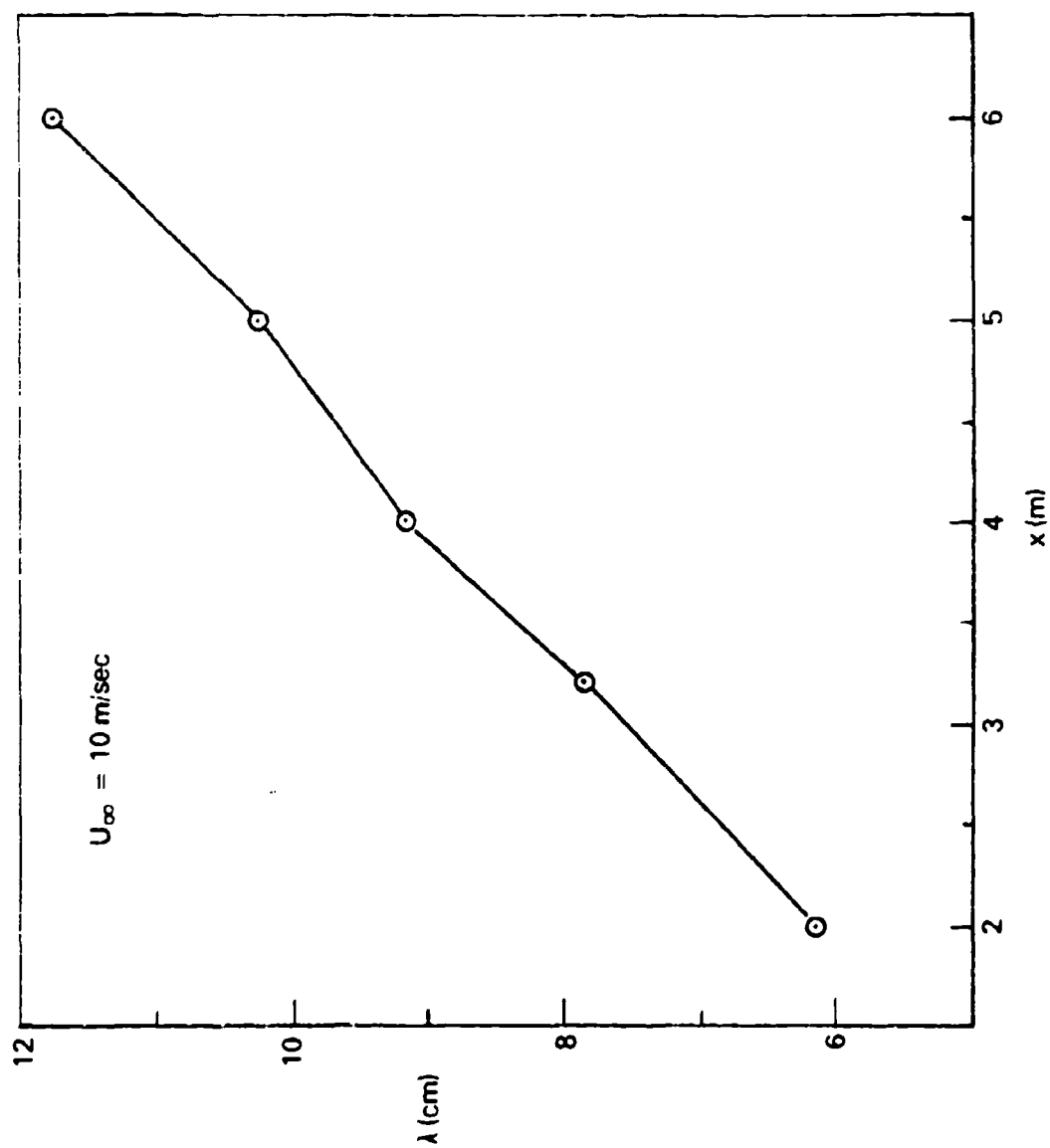


FIGURE 28. FETCH EFFECTS ON DOMINANT WAVE LENGTH.

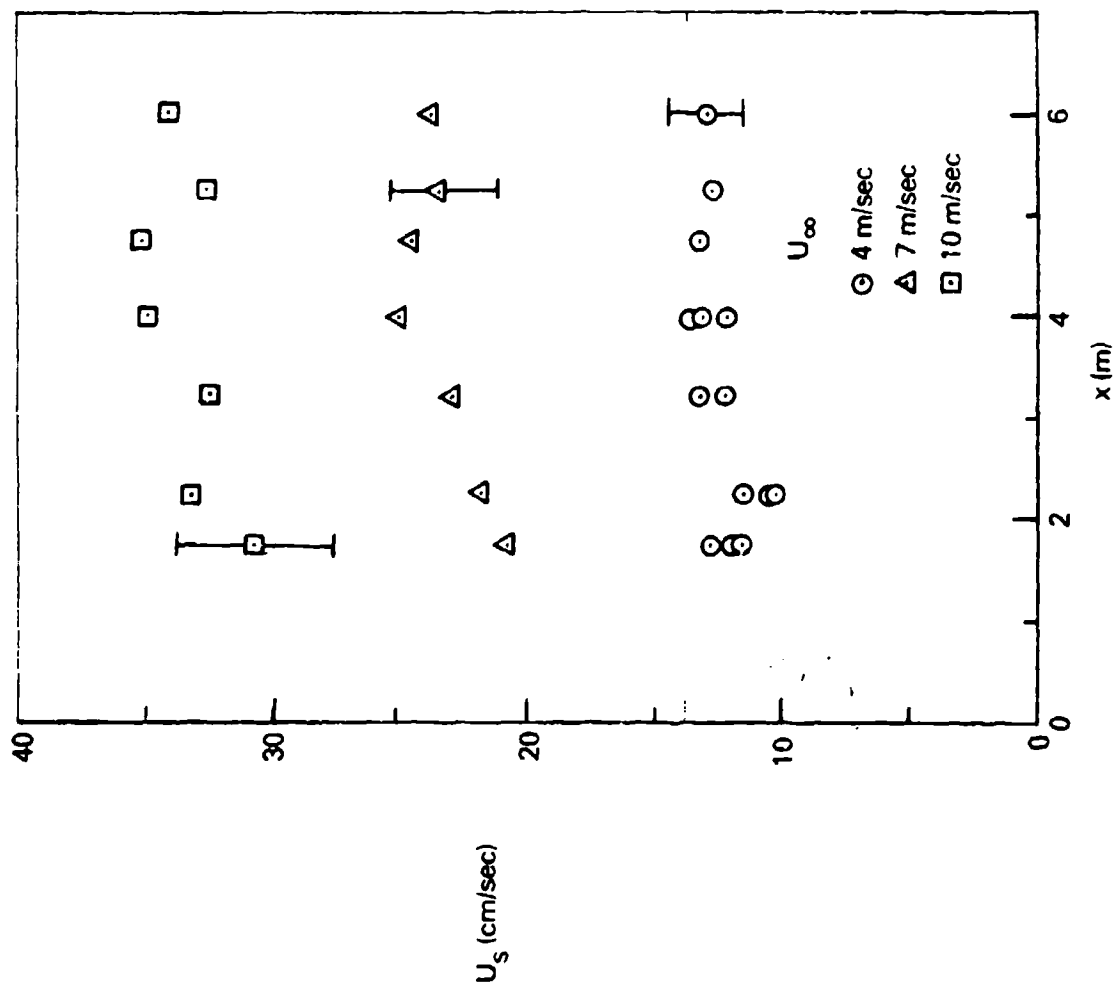
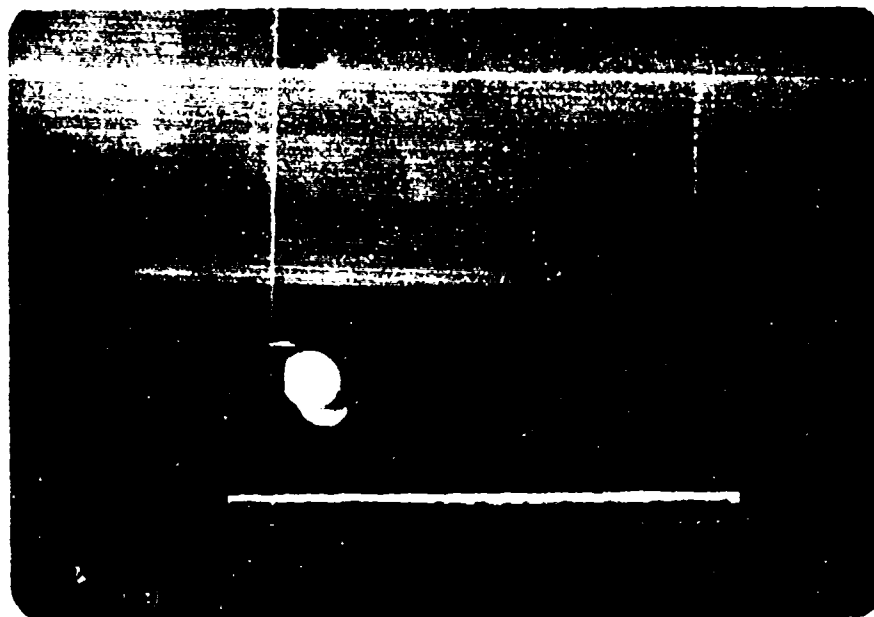
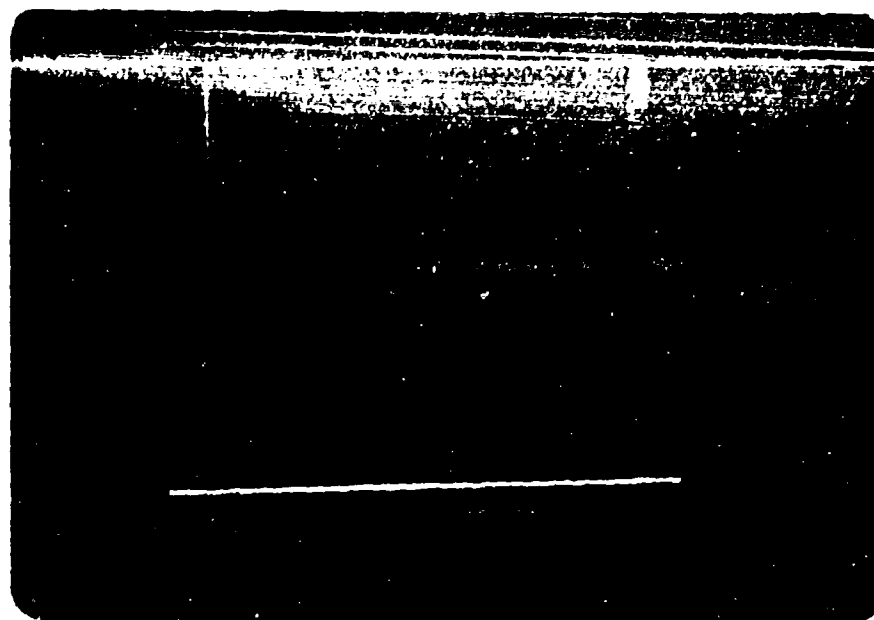


FIGURE 29. VARIATION OF SURFACE DRIFT VELOCITY WITH FETCH.



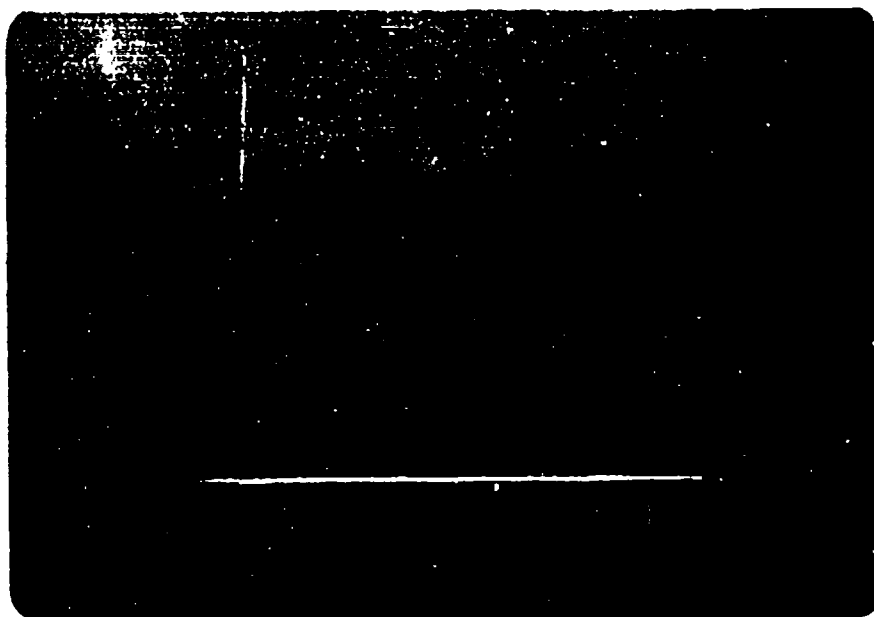
Water
Surface

(a) $U_{\infty} = 4 \text{ m/sec}$, $x = 1.7 \text{ m}$



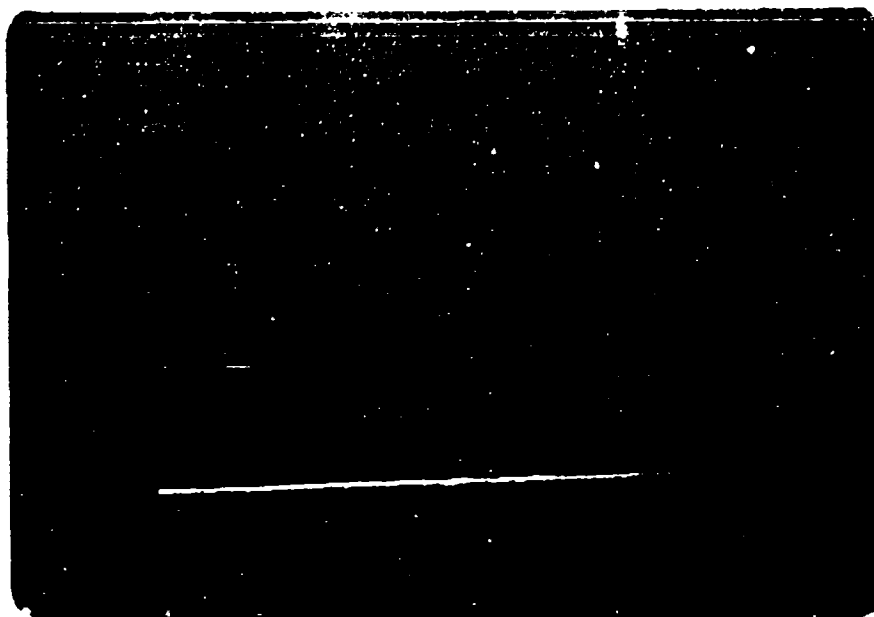
(b) $U_{\infty} = 4 \text{ m/sec}$, $x = 3.2 \text{ m}$

FIGURE 30. DYED WATER BOUNDARY-LAYER.



 Water
Surface

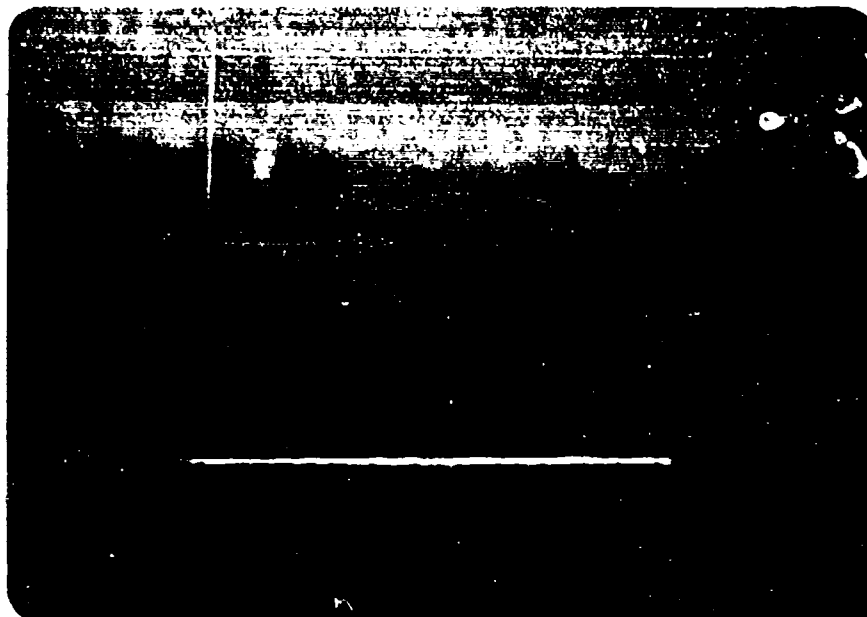
(c) $U_{\infty} = 7 \text{ m/sec}$, $x = 1.7 \text{ m}$






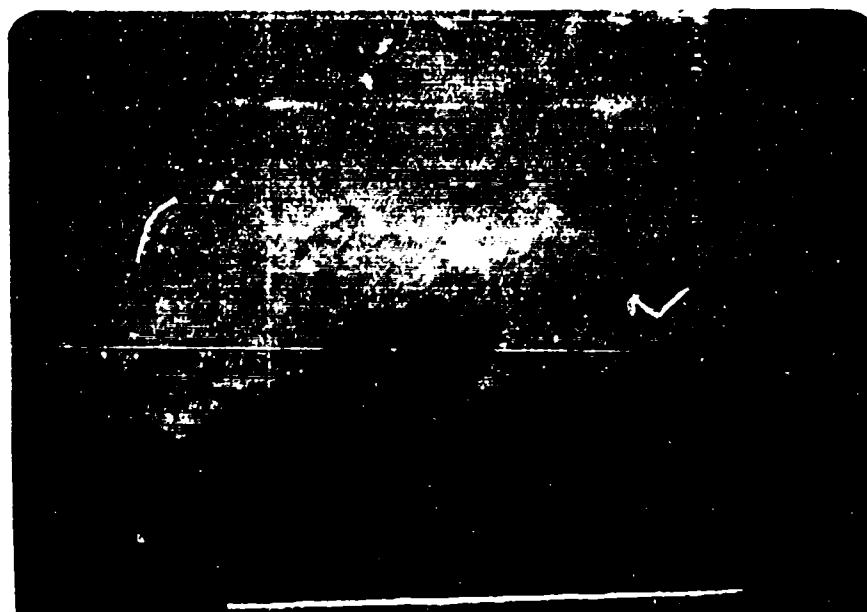
(d) $U_{\infty} = 7 \text{ m/sec}$, $x = 3.2 \text{ m}$

FIGURE 30. DYED WATER BOUNDARY-LAYER. (CONT.)




 Water
surface

(e) $U_{\infty} = 10 \text{ m/sec}$, $x = 1.7 \text{ m}$





(f) $U_{\infty} = 10 \text{ m/sec}$, $x = 3.2 \text{ m}$

FIGURE 30. DYED WATER BOUNDARY-LAYER. (CONT.)

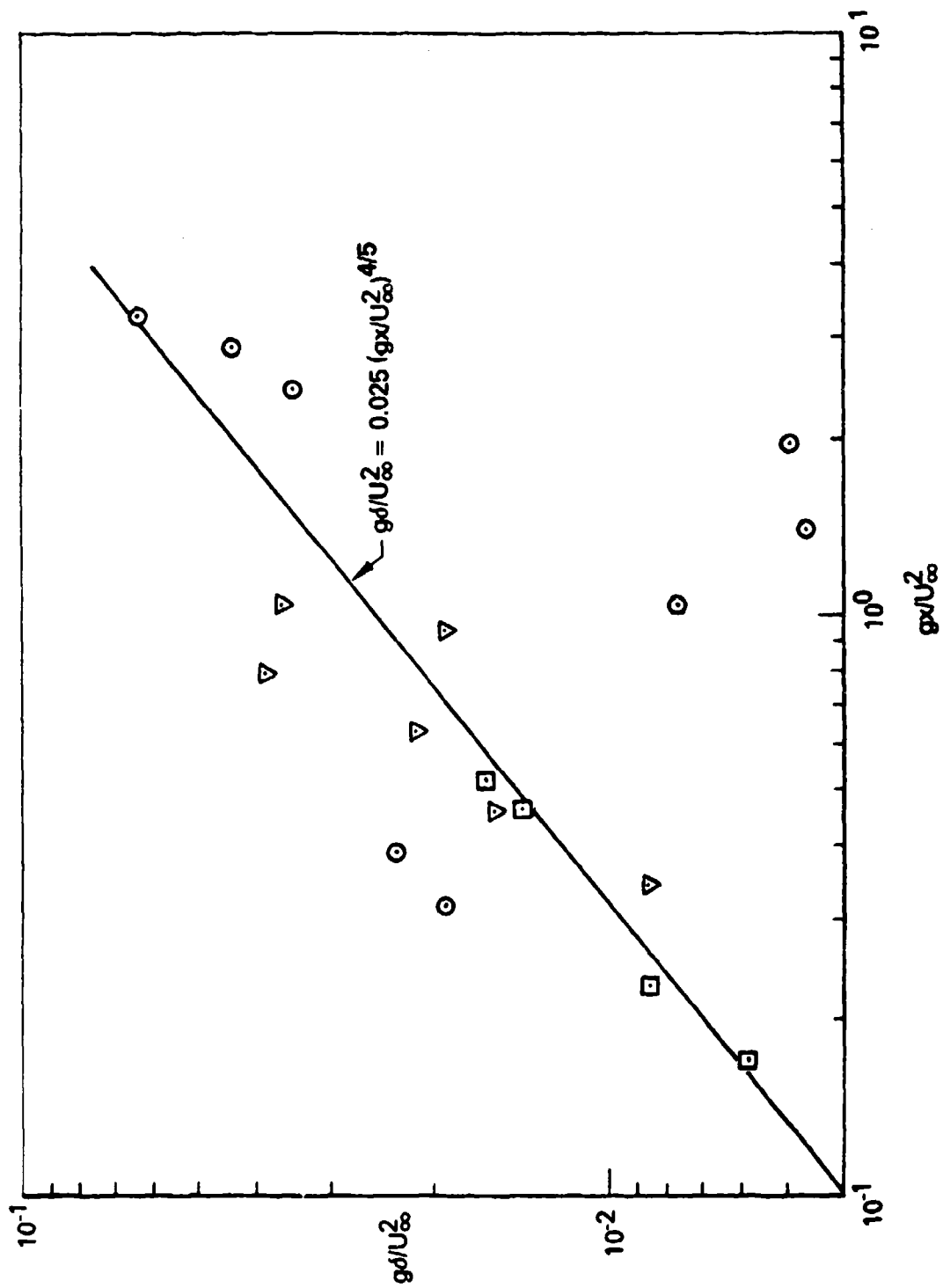


FIGURE 31. WATER BOUNDARY-LAYER THICKNESS.

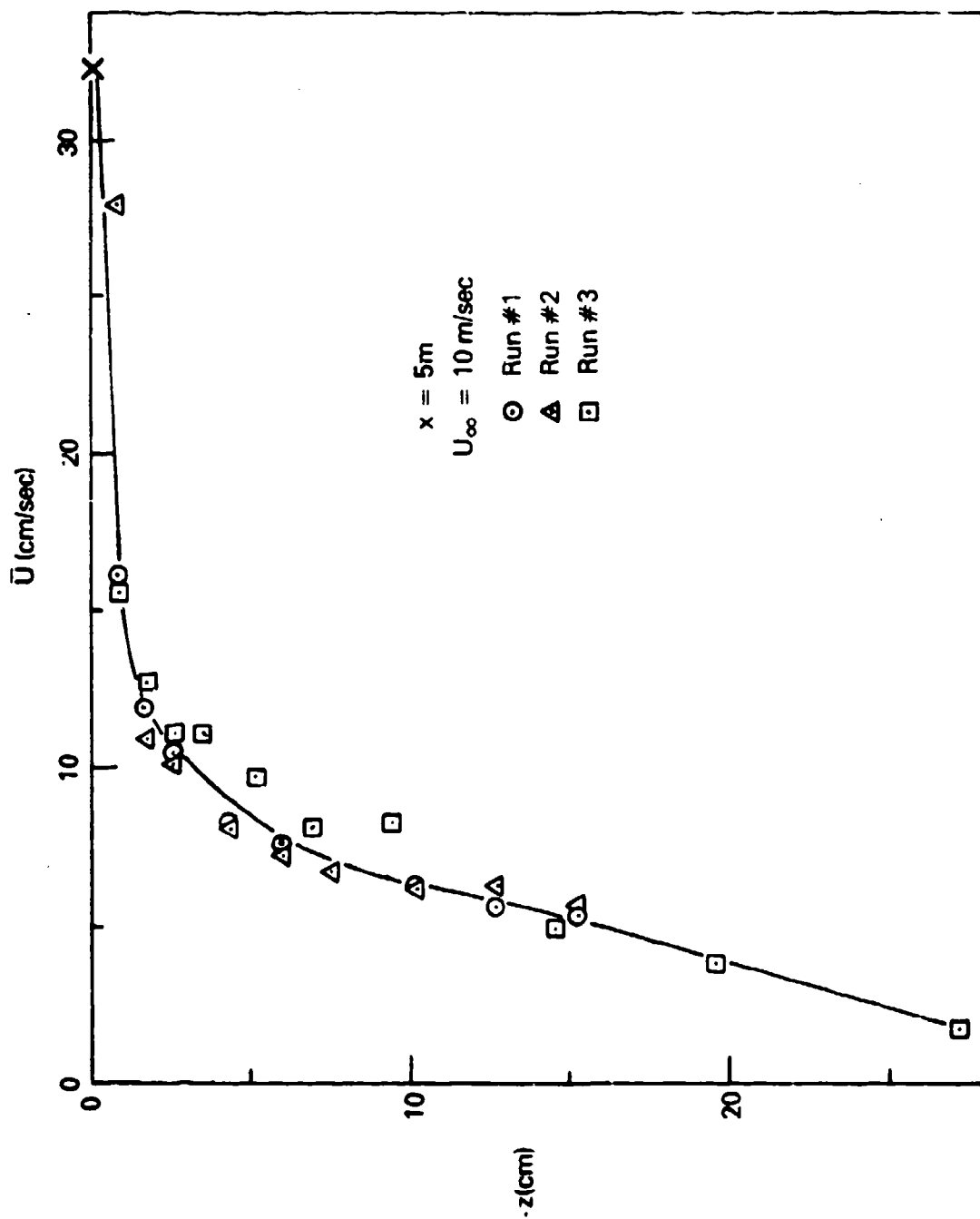


FIGURE 32. MEAN VELOCITY PROFILE IN WATER BOUNDARY-LAYER.

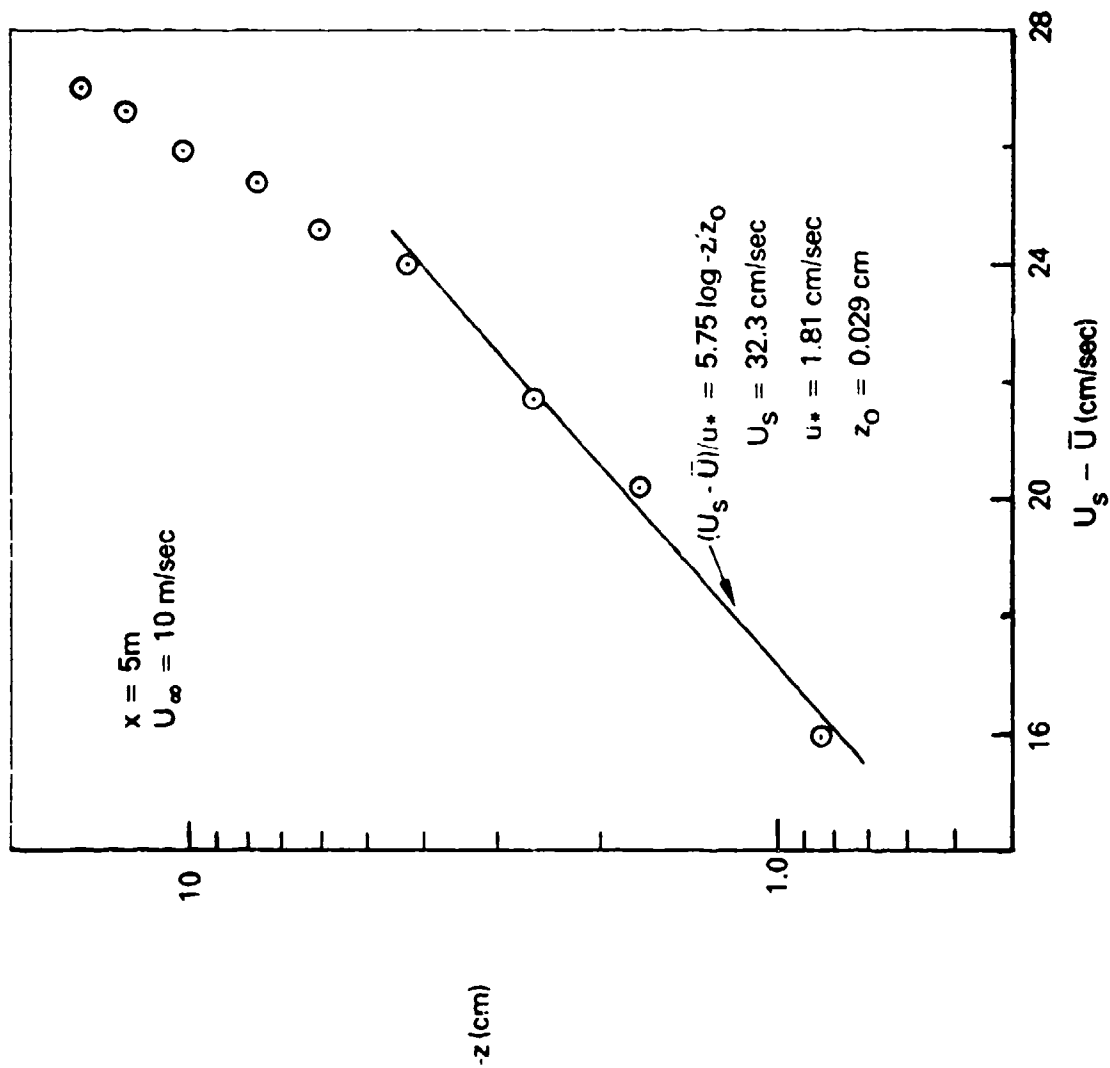


FIGURE 33. MEAN VELOCITY DEFECT PROFILE IN WATER BOUNDARY-LAYER

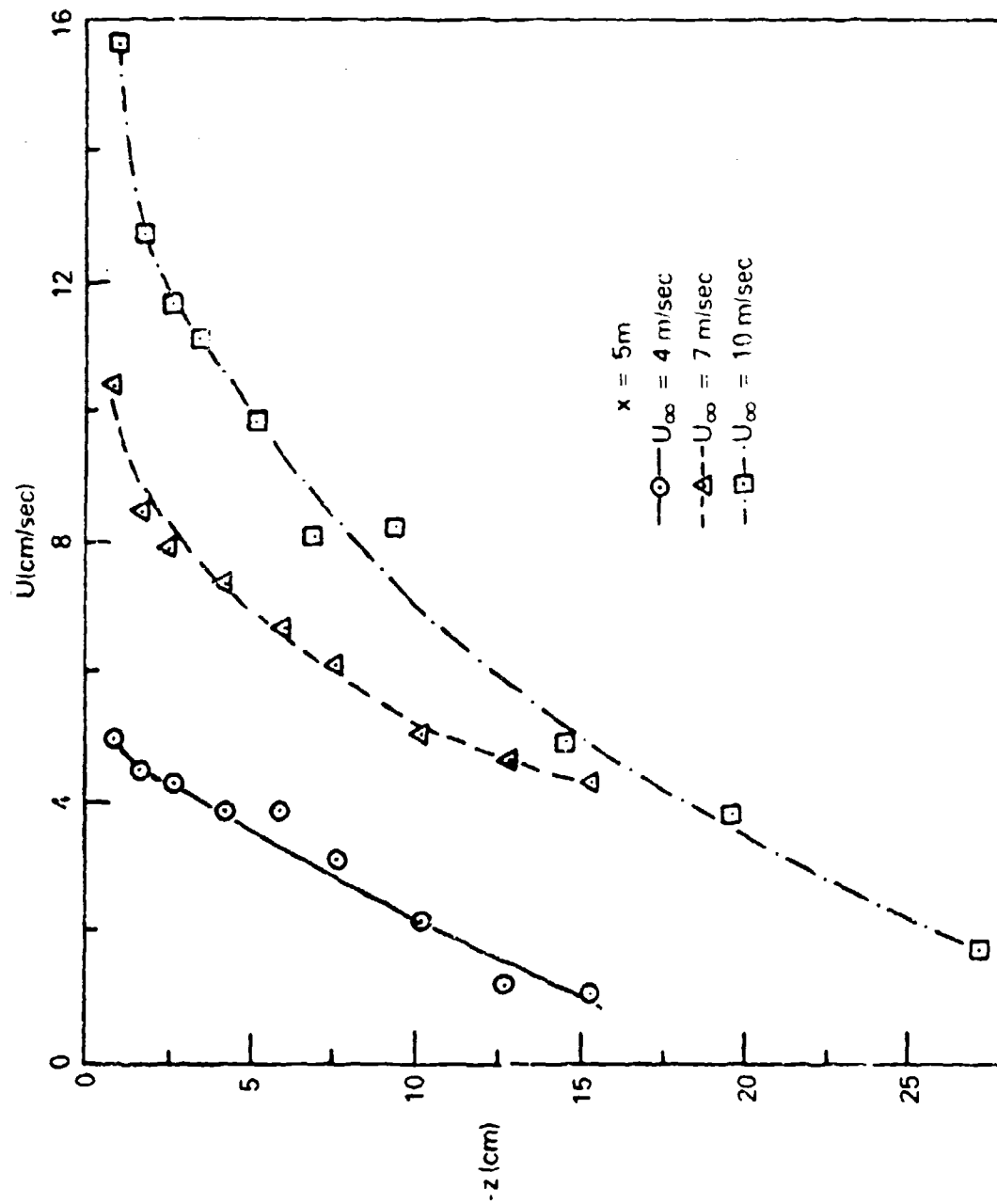


FIGURE 34. MEAN VELOCITY PROFILES IN WATER BOUNDARY-LAYER: EFFECTS OF WIND SPEED.

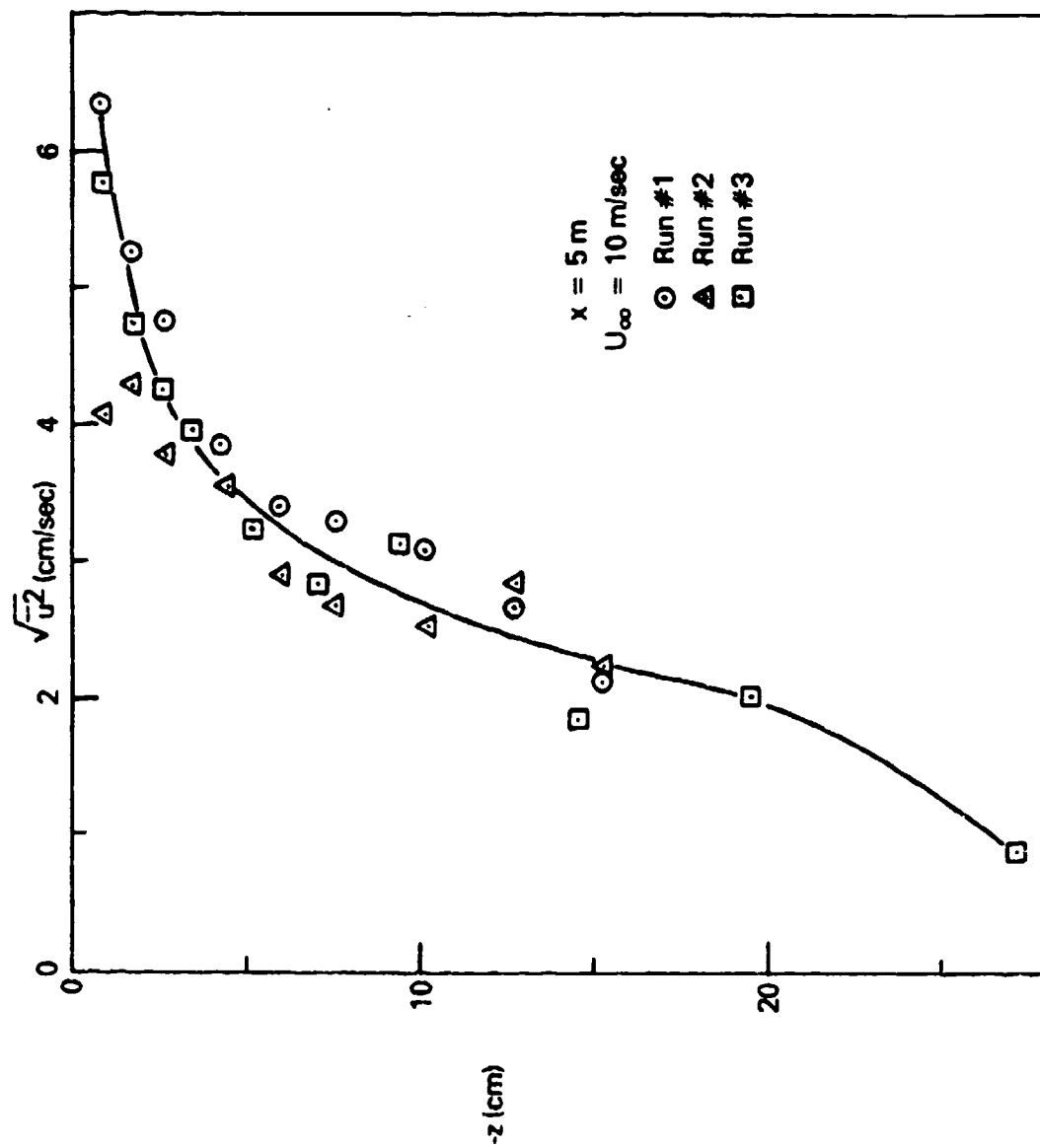


FIGURE 35. RMS OF LONGITUDINAL VELOCITY FLUCTUATIONS IN WATER BOUNDARY-LAYER.

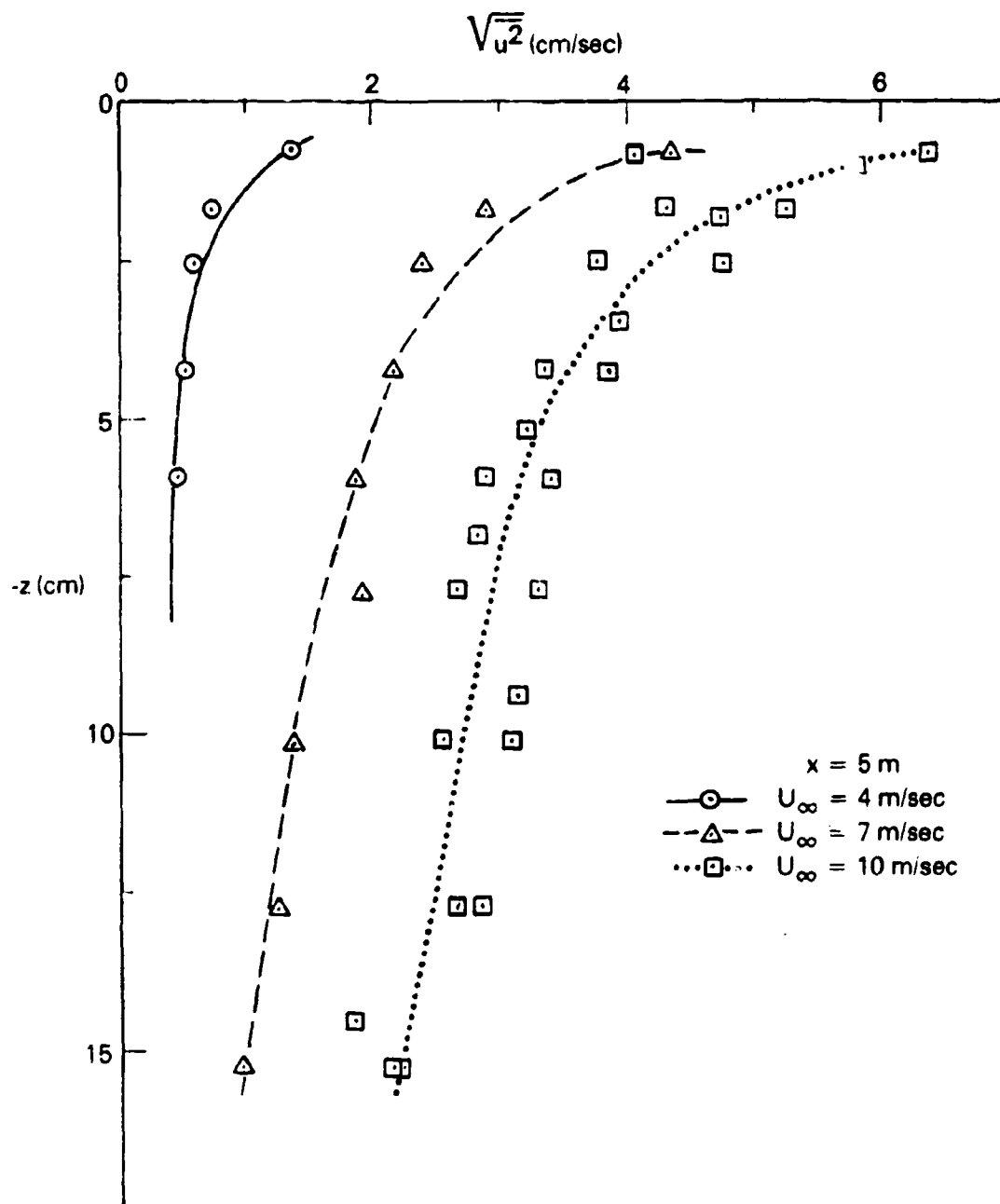


FIGURE 38. RMS OF LONGITUDINAL VELOCITY FLUCTUATIONS IN WATER BOUNDARY-LAYER.

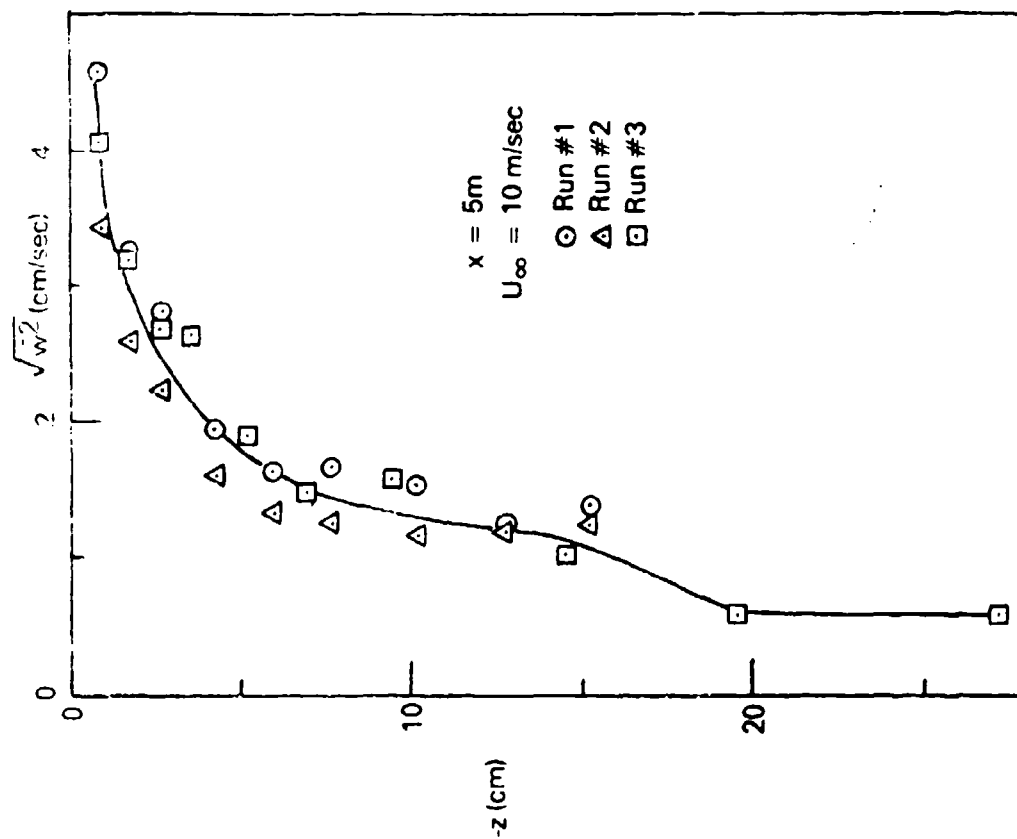


FIGURE 37. RMS OF VERTICAL VELOCITY FLUCTUATIONS IN WATER BOUNDARY LAYER.

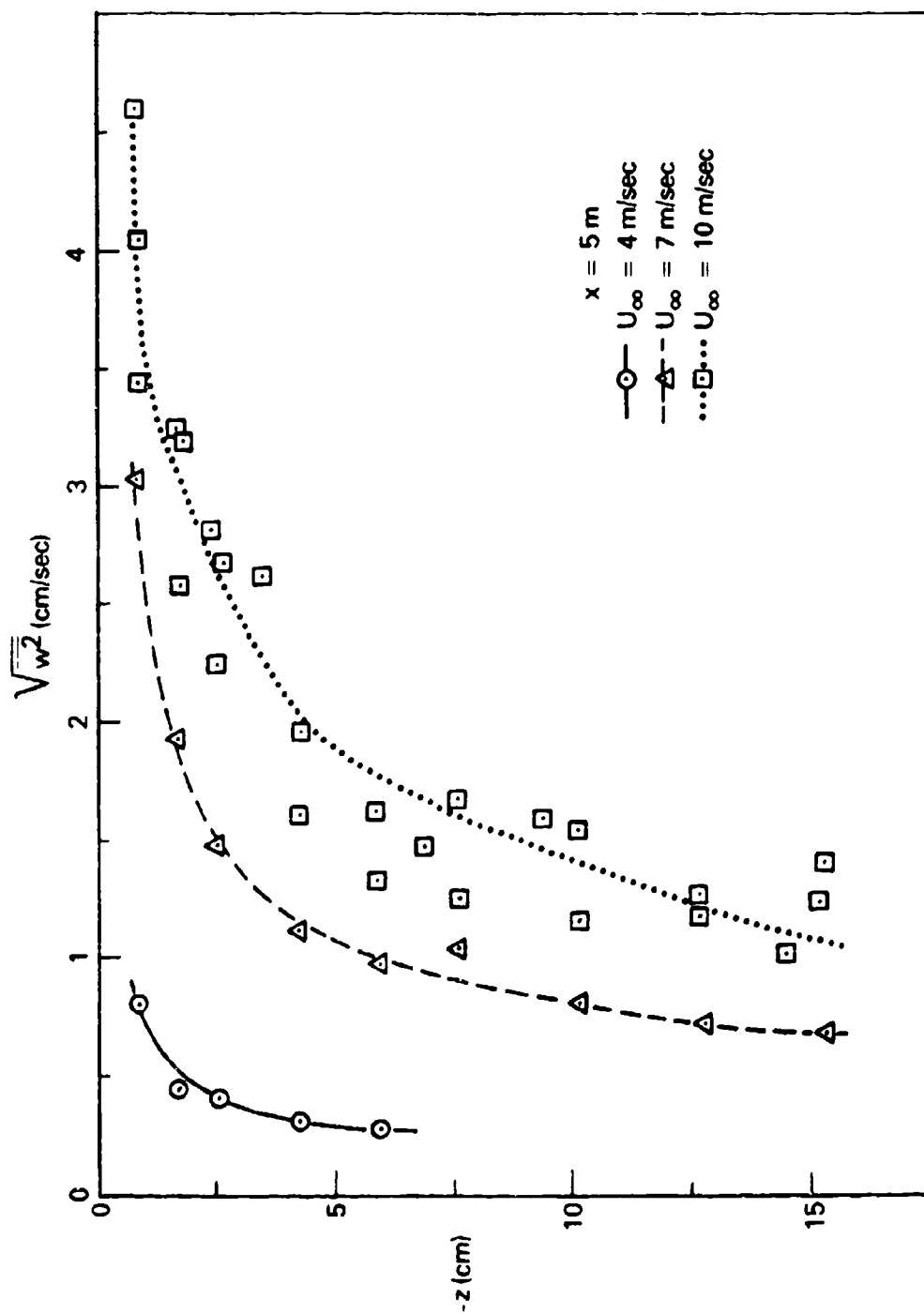


FIGURE 38. RMS OF VERTICAL VELOCITY FLUCTUATIONS IN WATER BOUNDARY-LAYER.

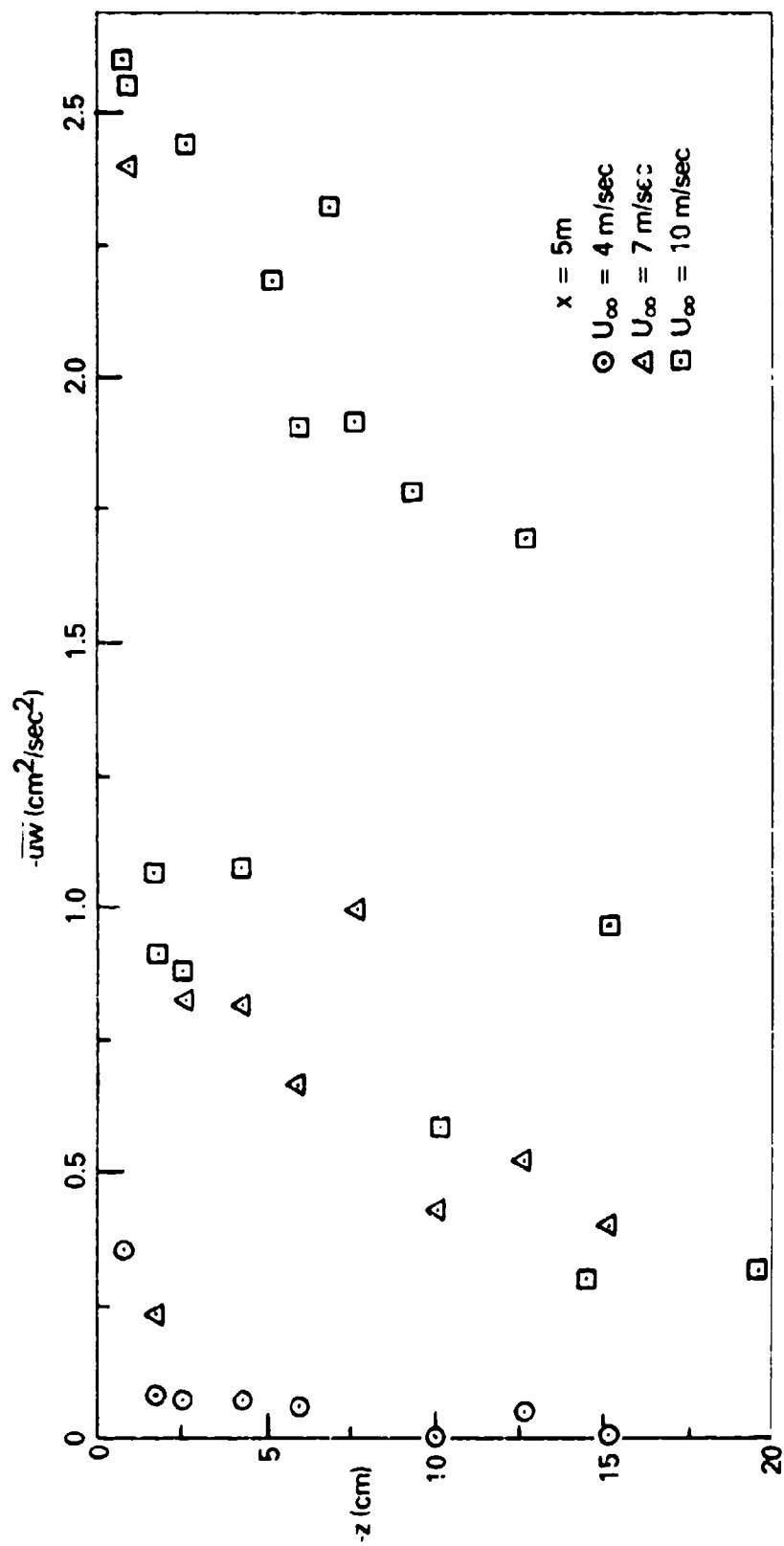


FIGURE 39. REYNOLDS STRESS PROFILES IN WATER BOUNDARY-LAYER.

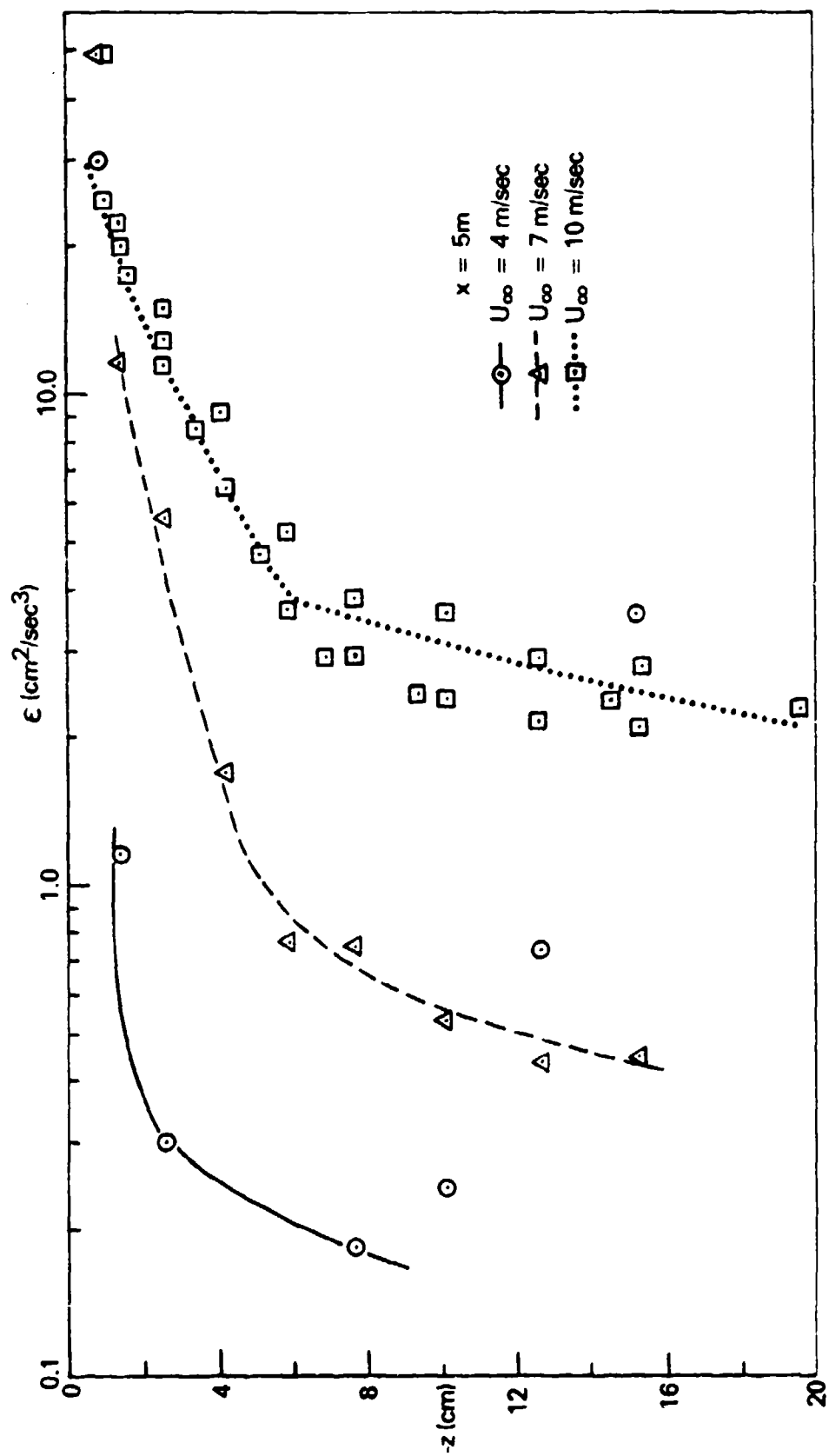


FIGURE 40. DISSIPATION RATE IN WATER BOUNDARY-LAYER.

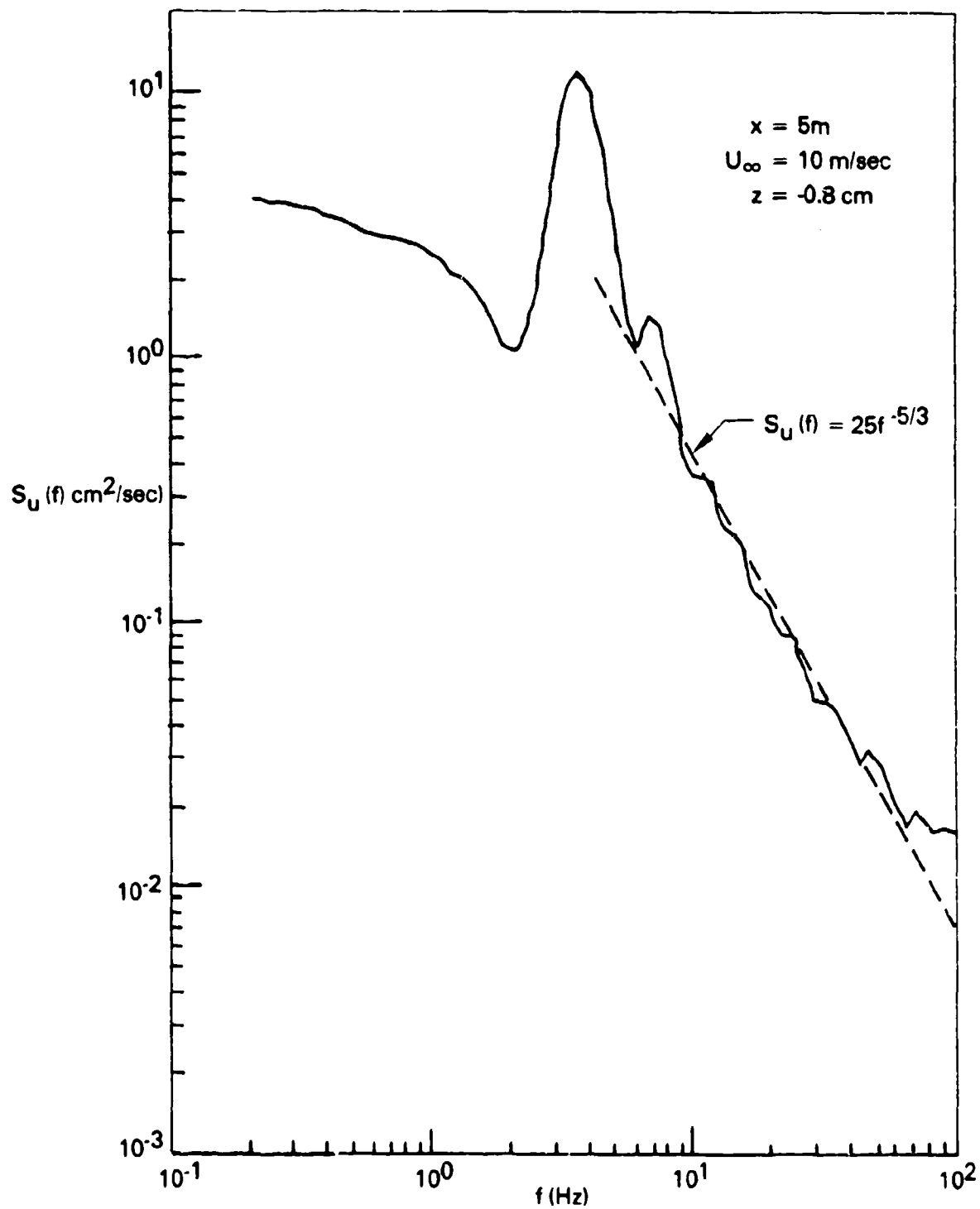


FIGURE 41. LONGITUDINAL VELOCITY SPECTRUM IN WATER BOUNDARY-LAYER.

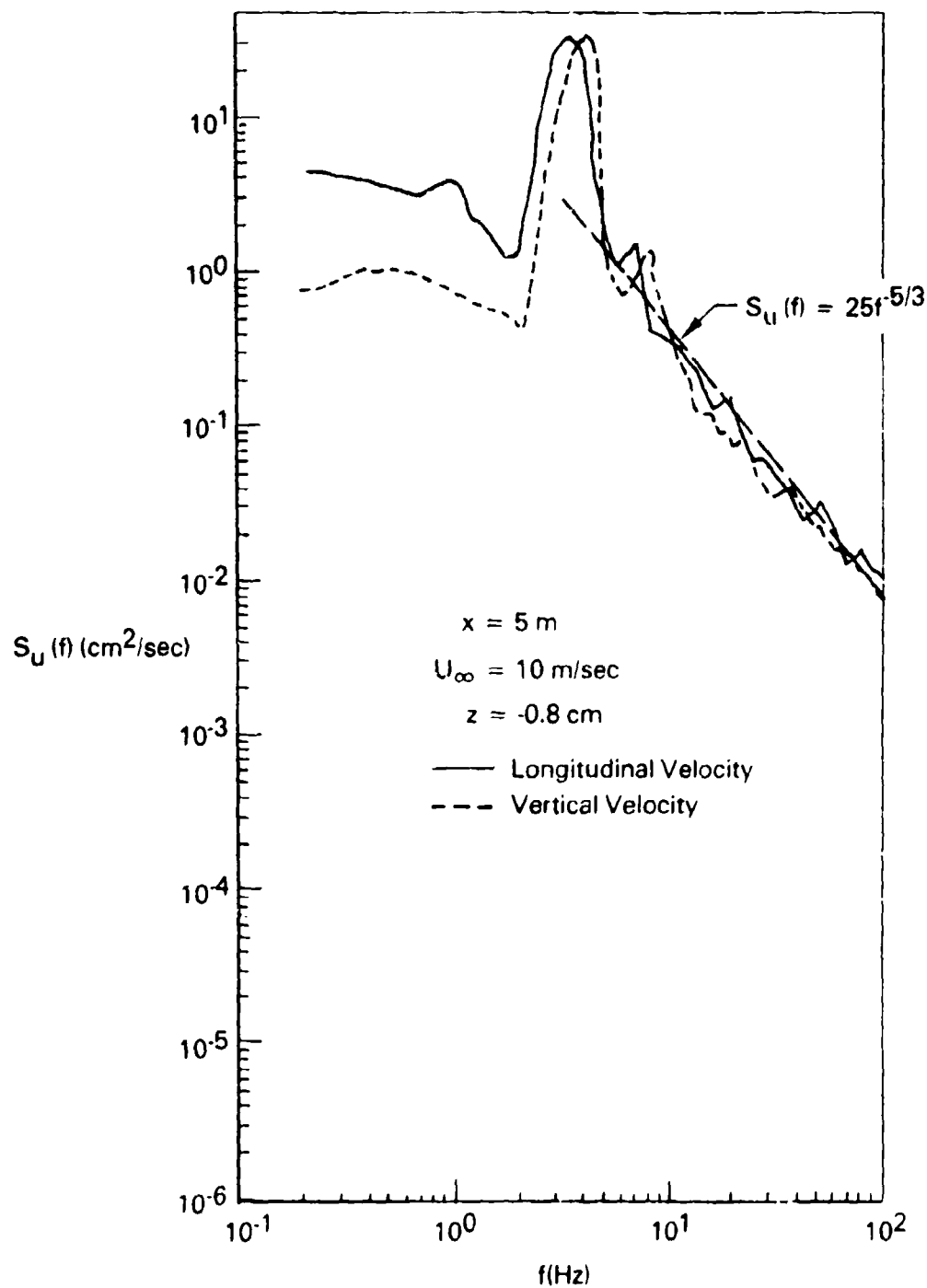


FIGURE 42. LONGITUDINAL VELOCITY SPECTRA IN WATER BOUNDARY-LAYER.

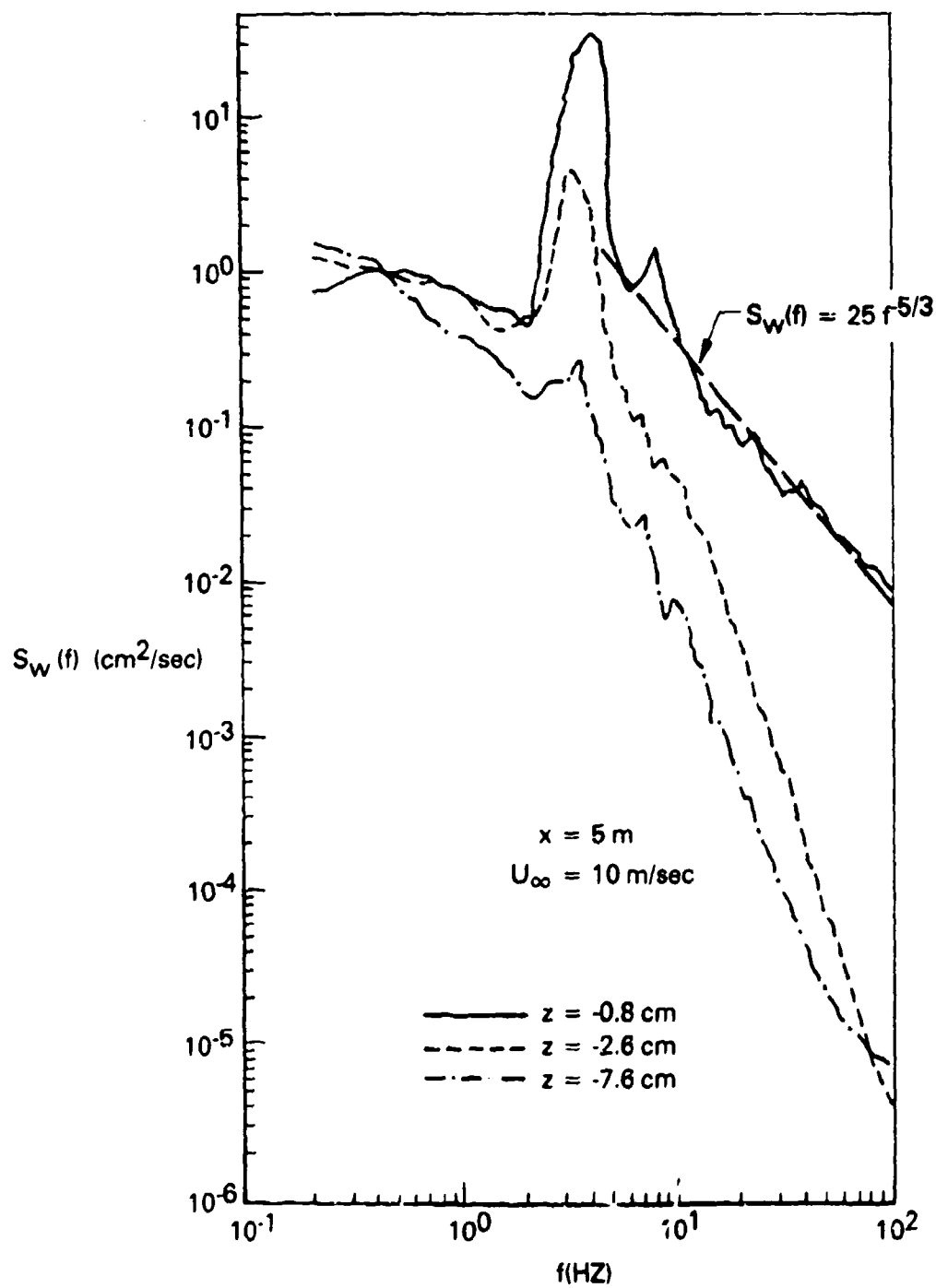


FIGURE 43. VERTICAL VELOCITY SPECTRA IN WATER BOUNDARY-LAYER.

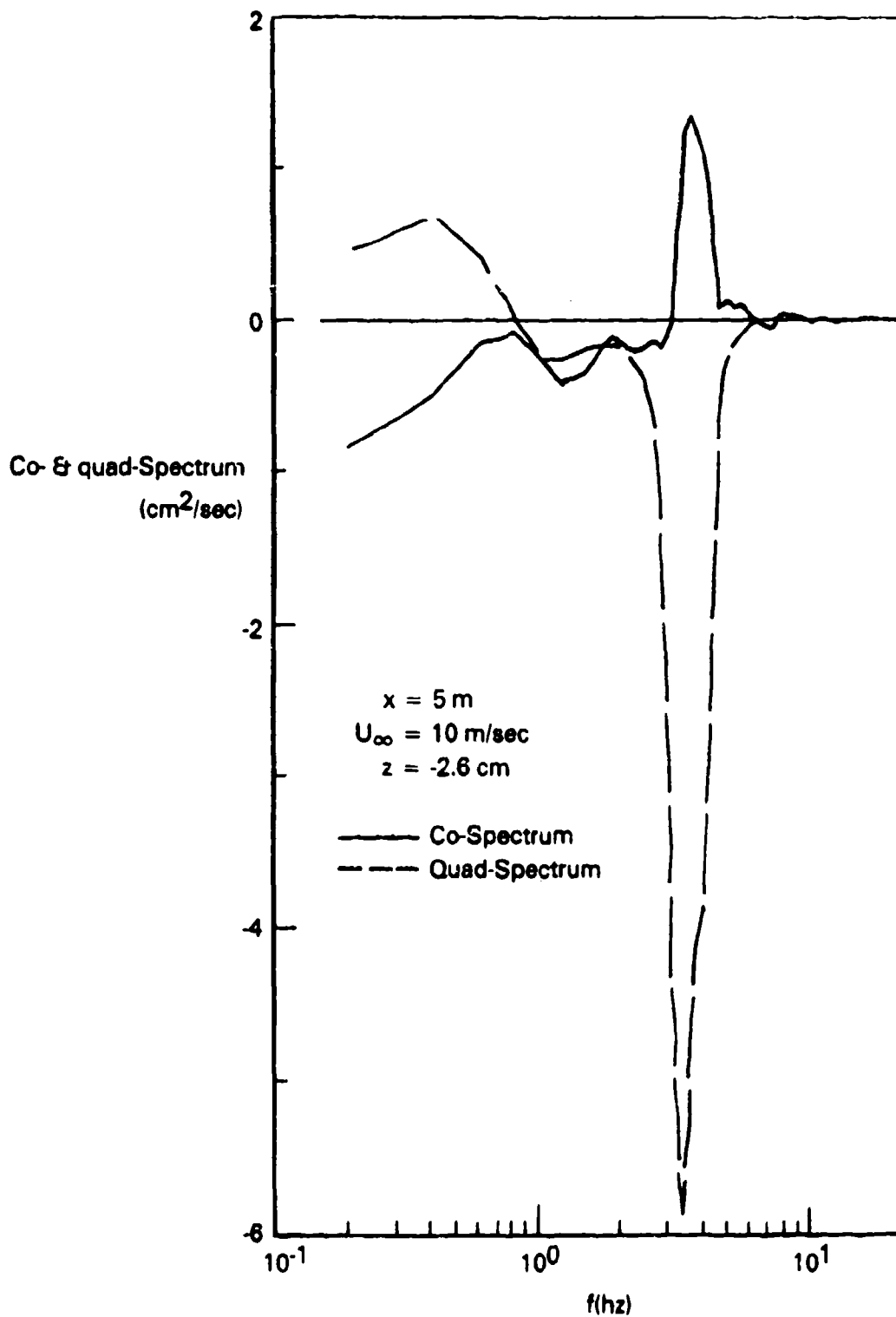


FIGURE 44. CO- AND QUAD-SPECTRUM OF LONGITUDINAL AND VERTICAL VELOCITIES IN WATER BOUNDARY-LAYER.

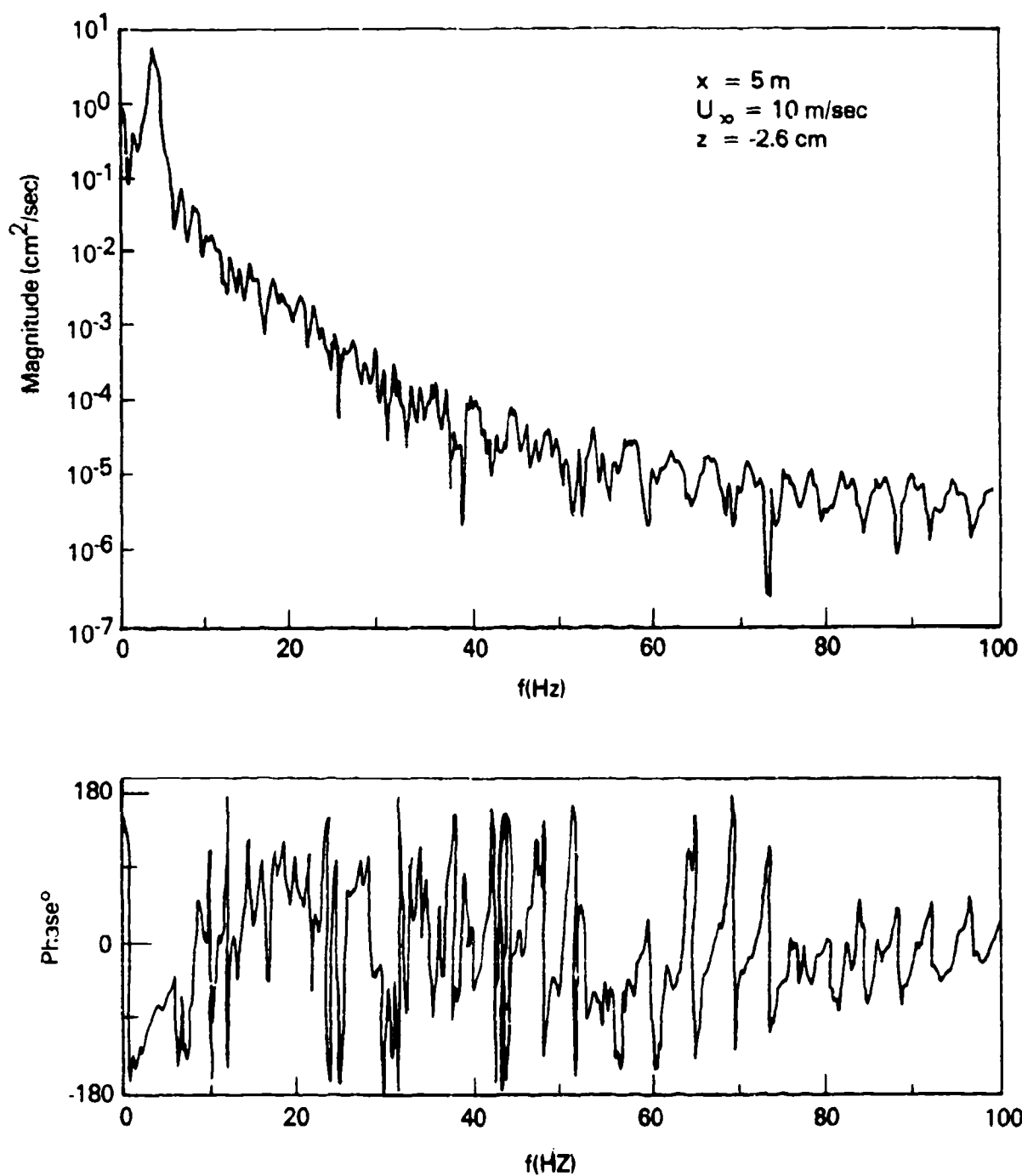


FIGURE 45. MAGNITUDE AND PHASE OF CROSS-SPECTRUM OF LONGITUDINAL AND VERTICAL VELOCITIES IN WATER.



(a) $H_0 = 0 \text{ cm}$, $U_\infty = 10 \text{ m/sec}$



(b) $H_0 = 2.54 \text{ cm}$, $U_\infty = 10 \text{ m/sec}$

FIGURE 46. WATER SURFACE PHOTOGRAPH. (CONT.)



(c) $H_0 = 5.08 \text{ cm}$, $U_\infty = 10 \text{ m/sec}$



(d) $H_0 = 7.62 \text{ cm}$, $U_\infty = 10 \text{ m/sec}$

FIGURE 46. WATER SURFACE PHOTOGRAPH.

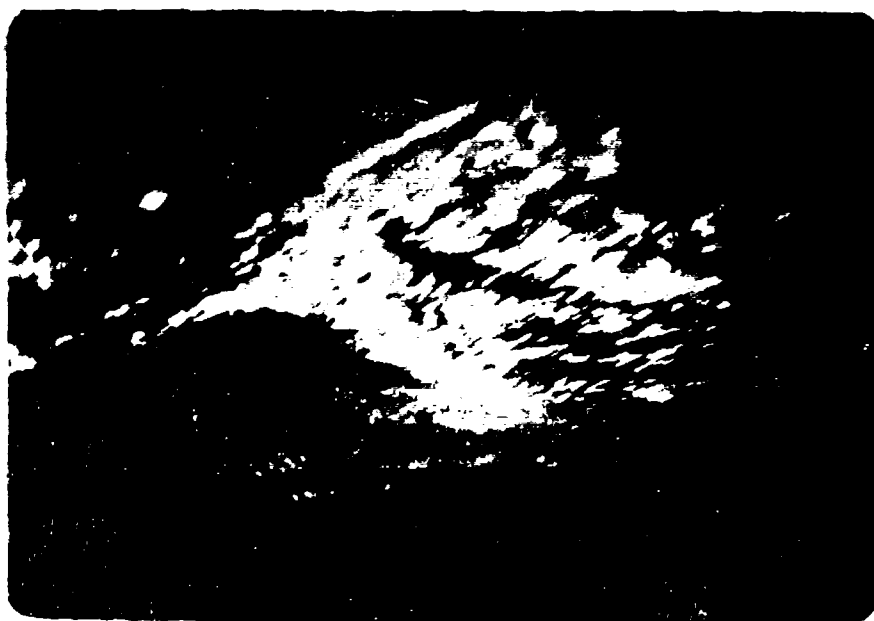


FIGURE 47. AIR BUBBLES ENTRAINED INTO WATER UNDER WAVE CREST.

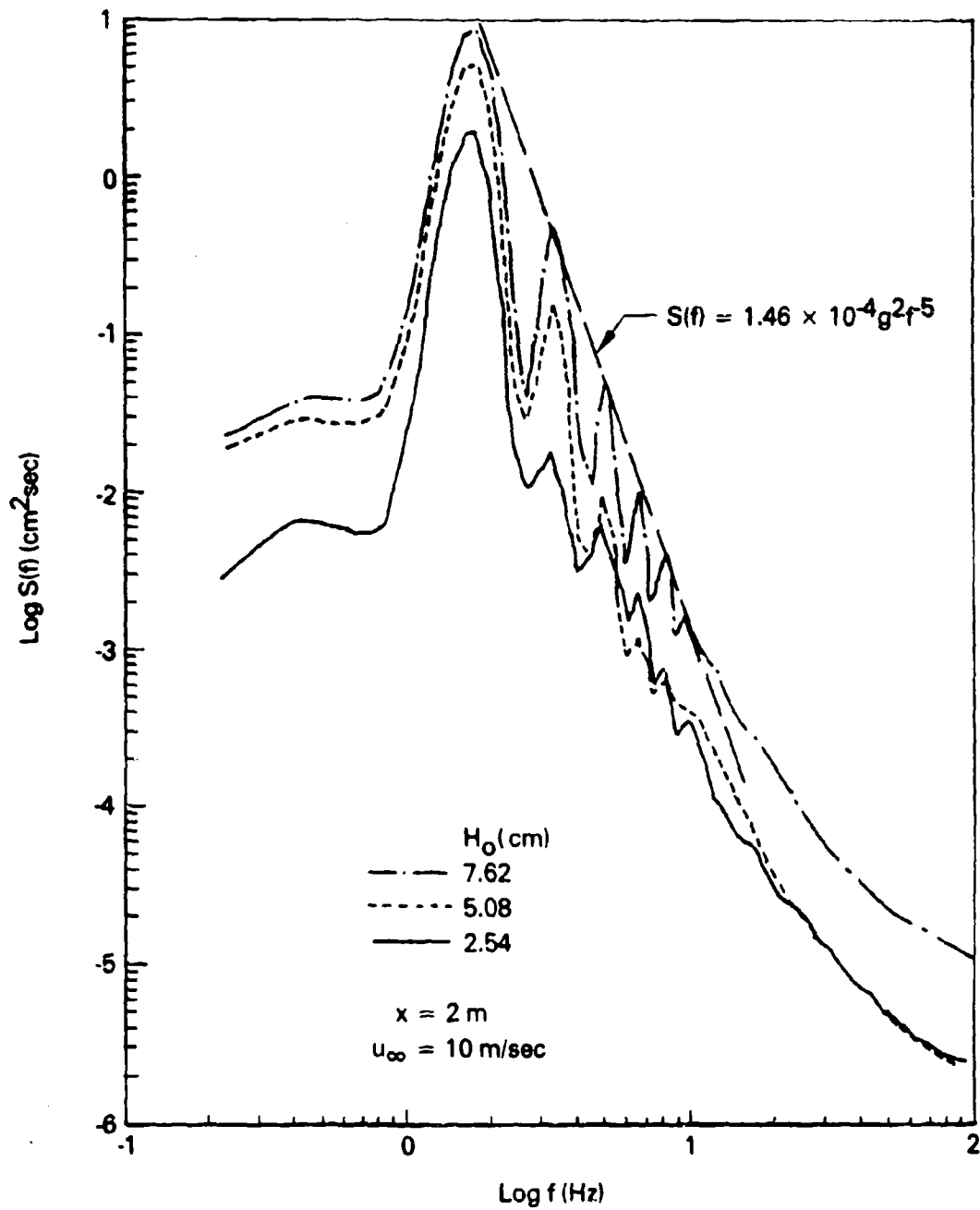


FIGURE 48. WAVE ENERGY SPECTRA (CAPACITANCE PROBE).

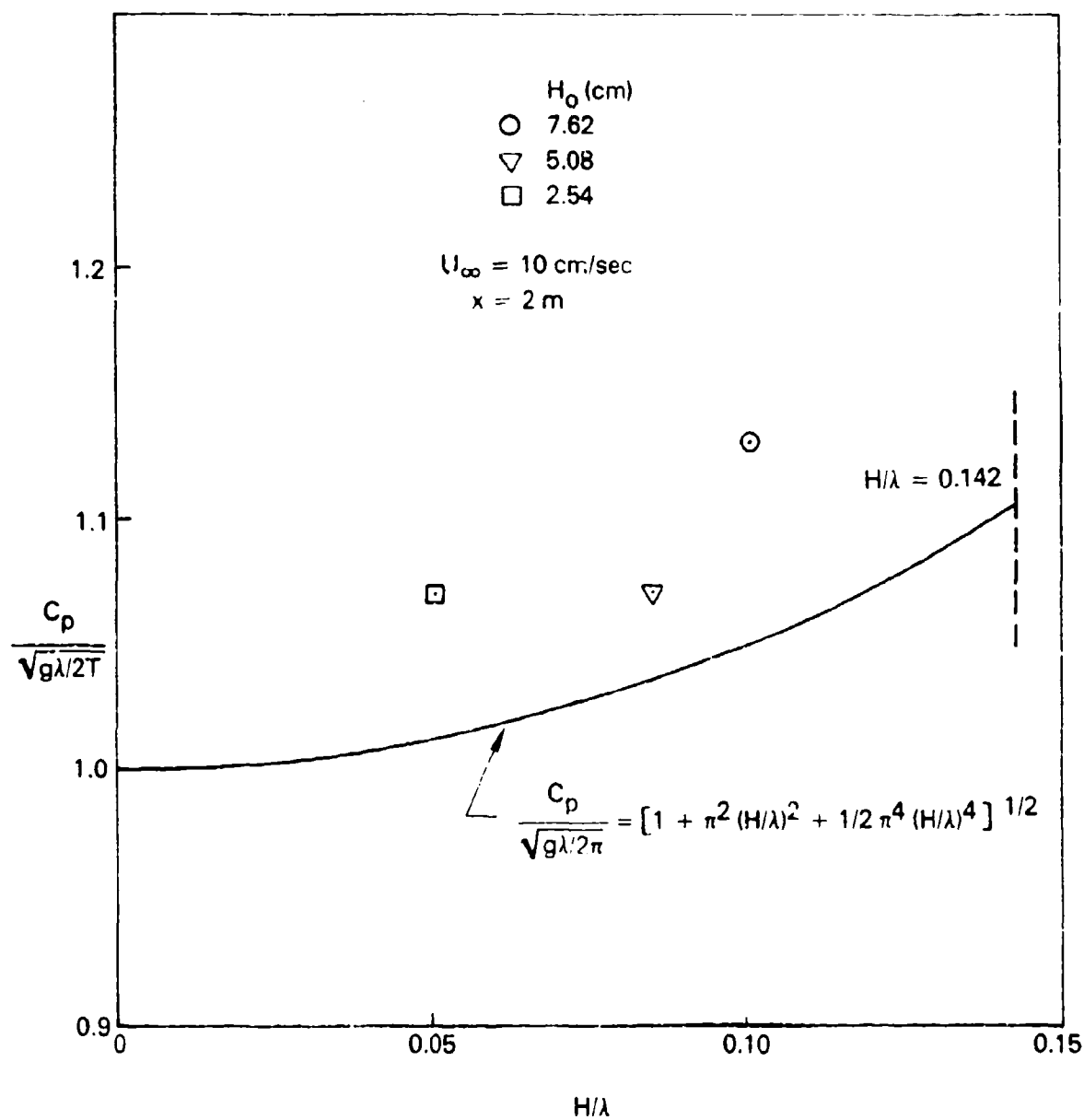


FIGURE 49. DOMINANT PHASE SPEED, C_p VERSUS WAVE STEEPNESS H/λ .

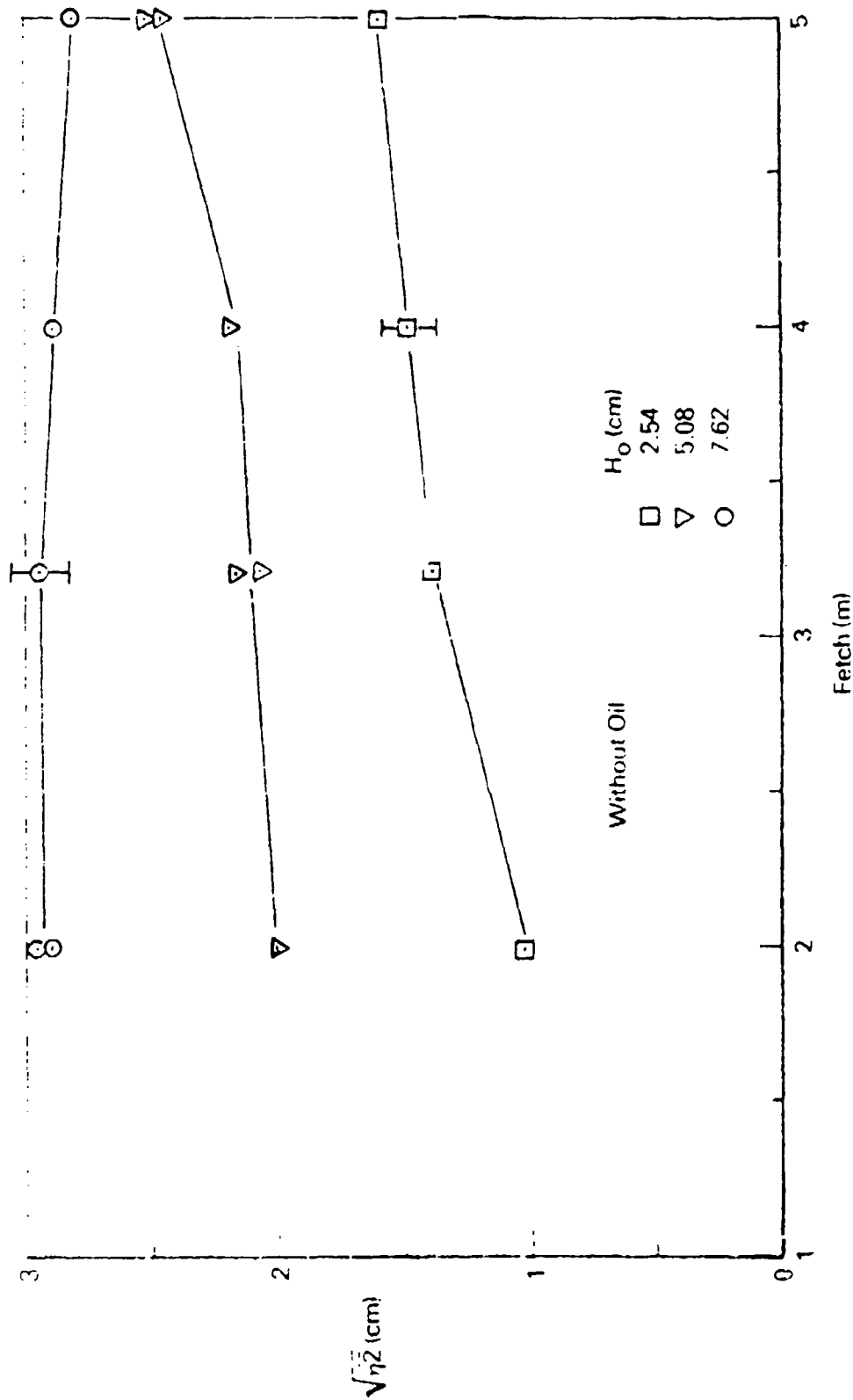


FIGURE 50. VARIATION OF WAVE AMPLITUDE WITH FETCH.

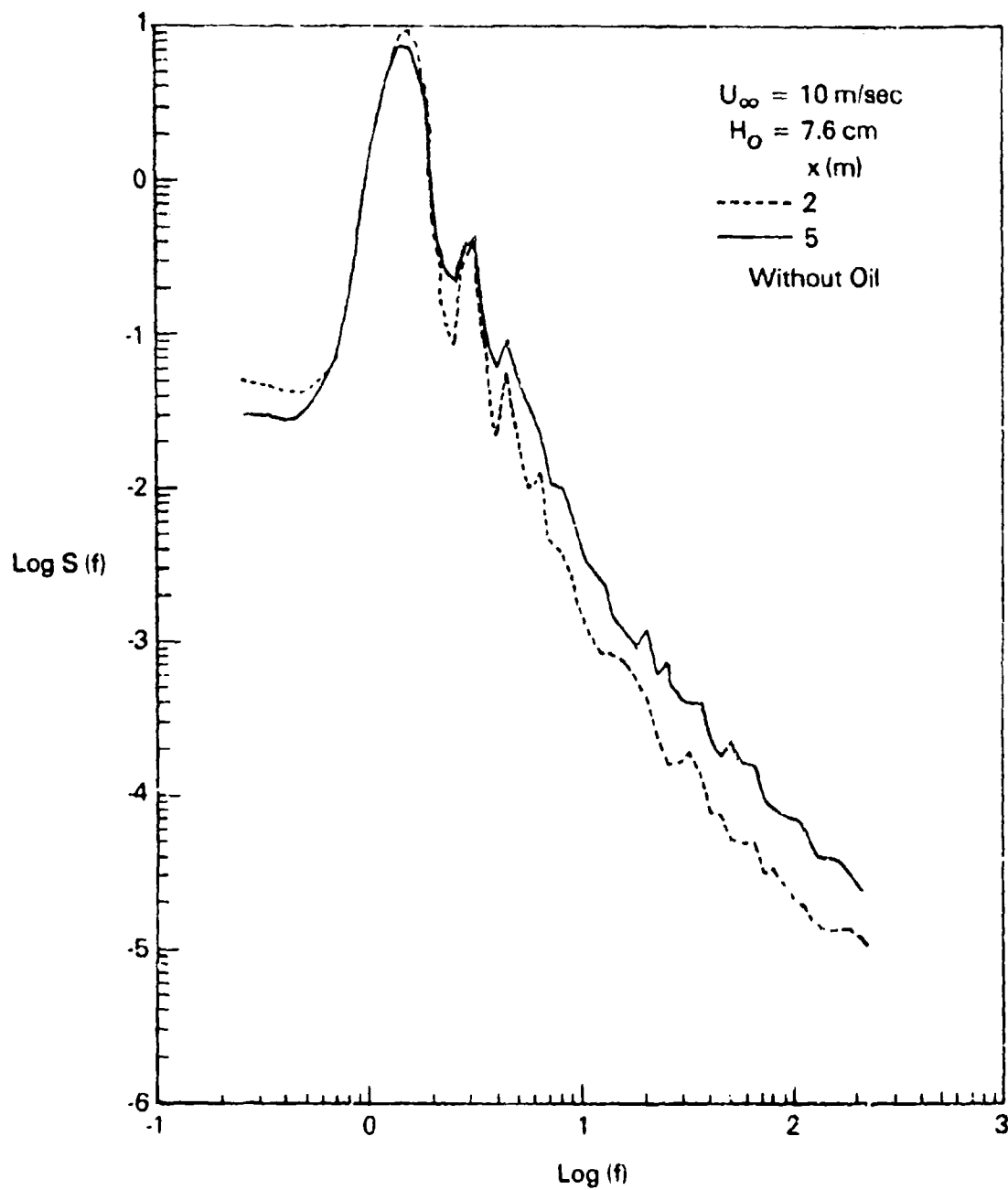


FIGURE 51. WAVE ENERGY SPECTRA AT TWO FETCHES.

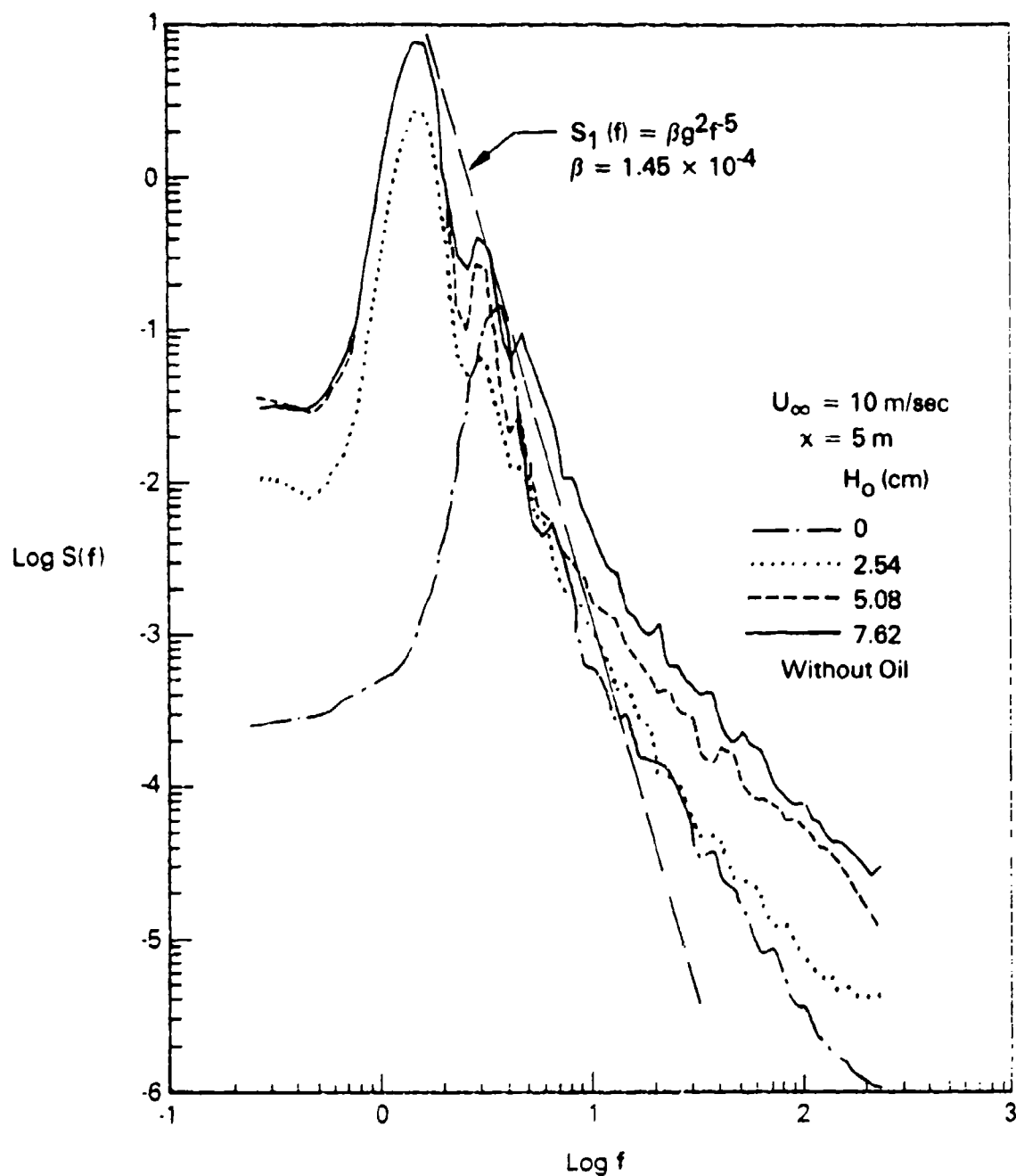


FIGURE 52. WAVE ENERGY SPECTRA WITH MECHANICALLY GENERATED WAVES.

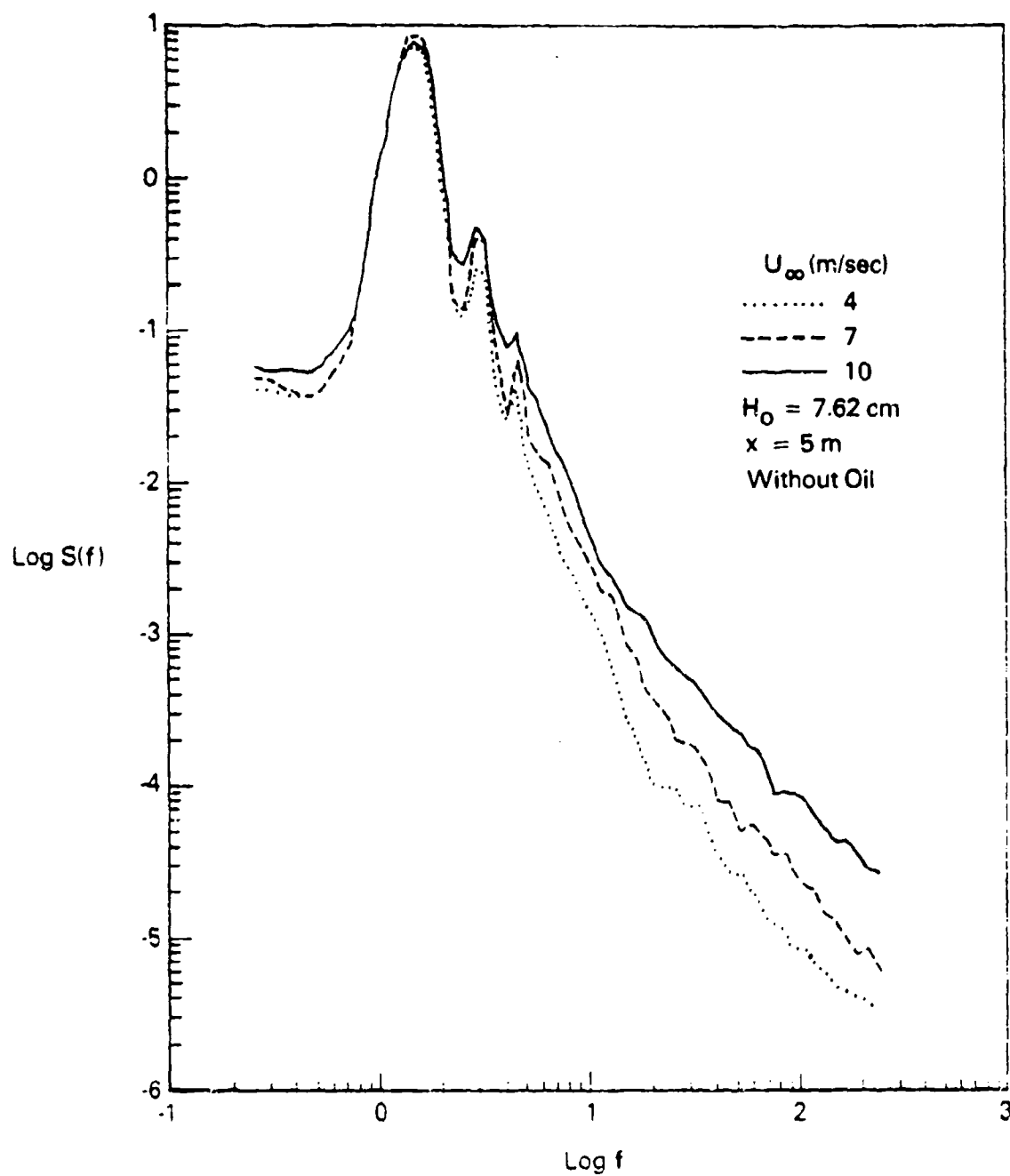


FIGURE 53. VARIATION OF WAVE ENERGY SPECTRUM WITH WIND SPEED.

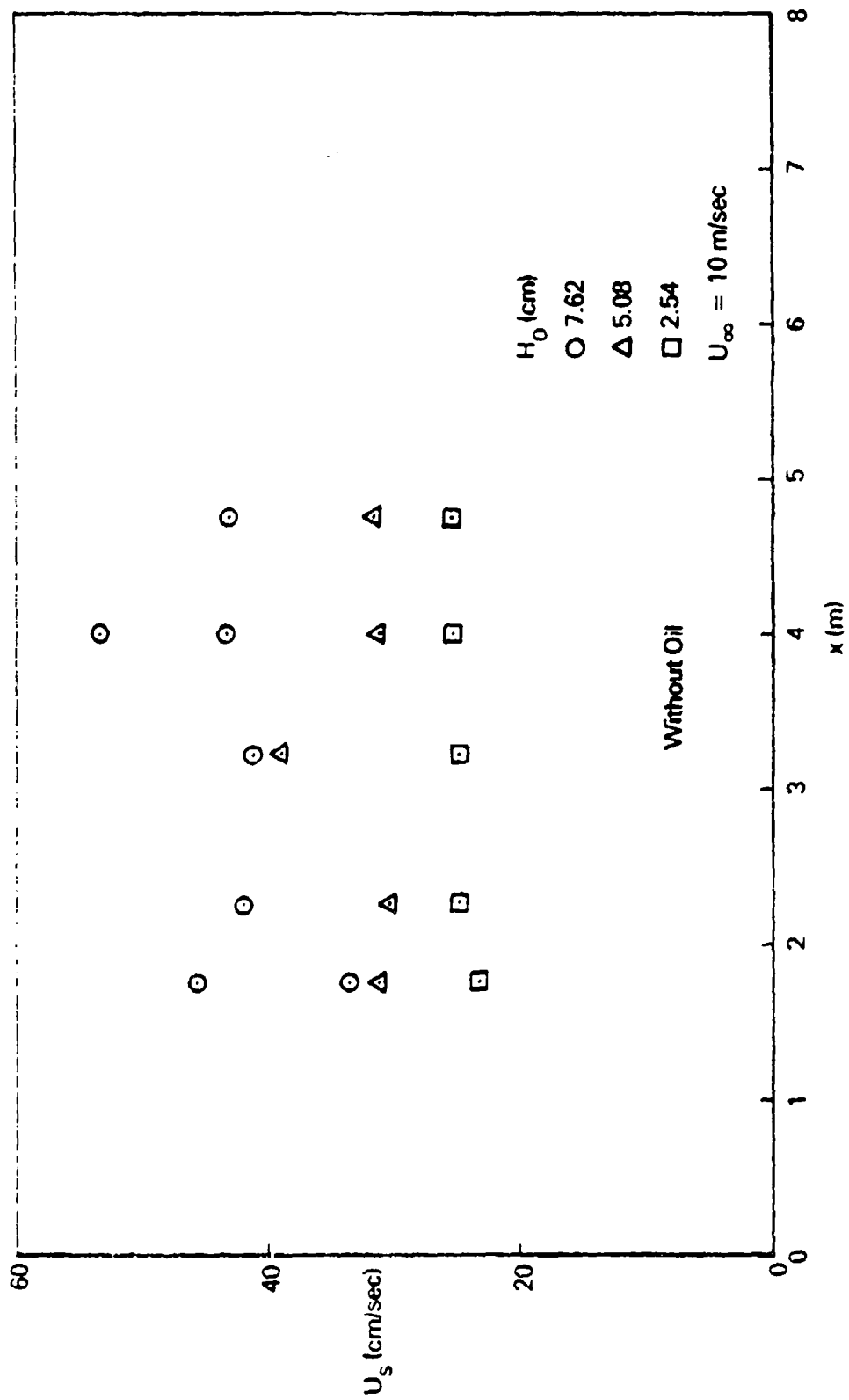


FIGURE 54. SURFACE DRIFT VELOCITY U_s VERSUS FETCH x .

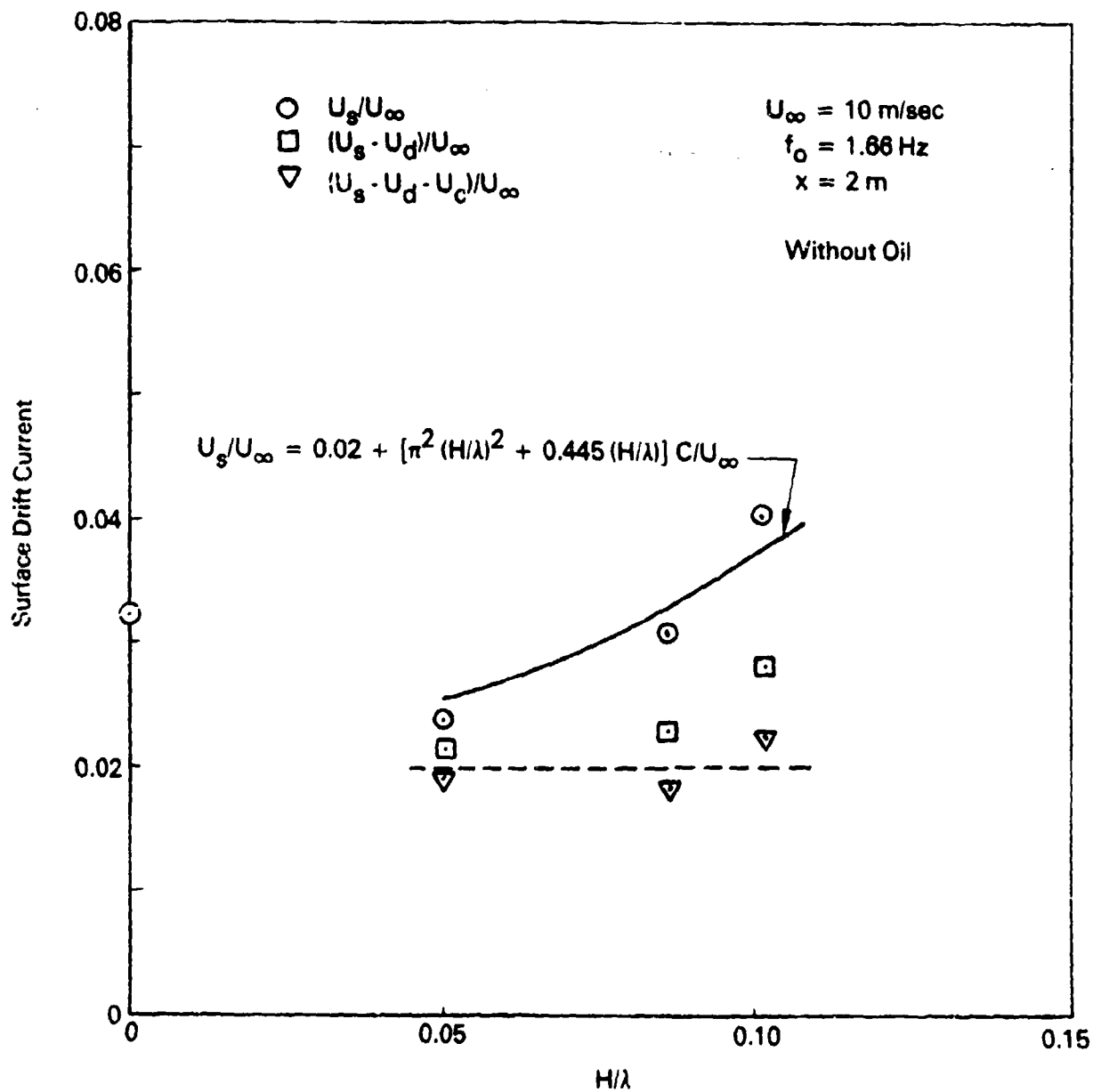


FIGURE 55. SURFACE DRIFT CURRENT U_s VERSUS WAVE STEEPNESS H/λ .



FIGURE 56. DYED WATER BOUNDARY, $H_0 = 7.62$ cm, $U_\infty = 10$ m/sec,
 $x = 4$ m.

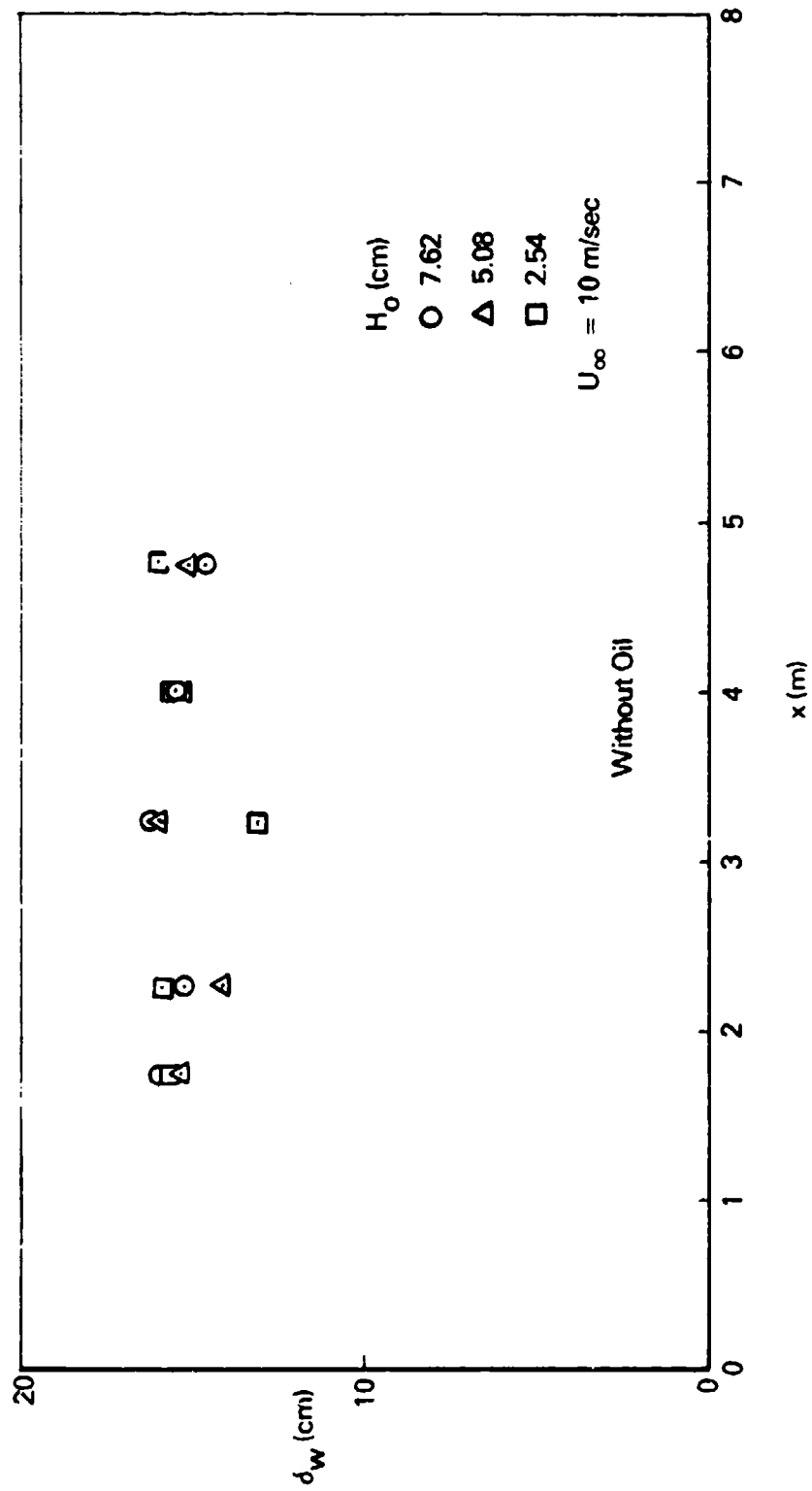


FIGURE 57. THICKNESS OF WATER BOUNDARY-LAYER δ_w VERSUS FETCH x .

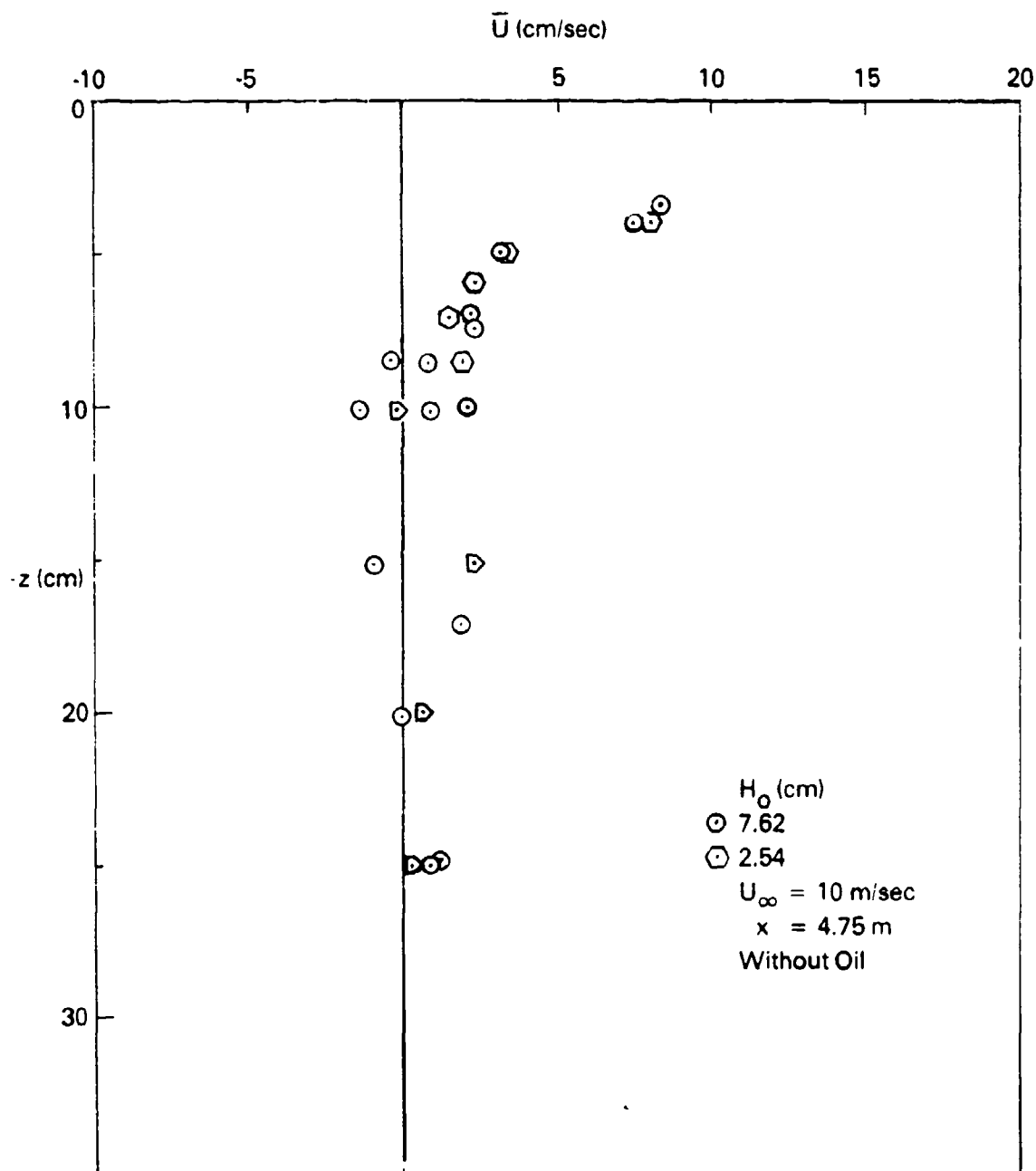


FIGURE 58. VERTICAL PROFILES OF LONGITUDINAL MEAN VELOCITY IN BREAKING AND NONBREAKING WAVES.

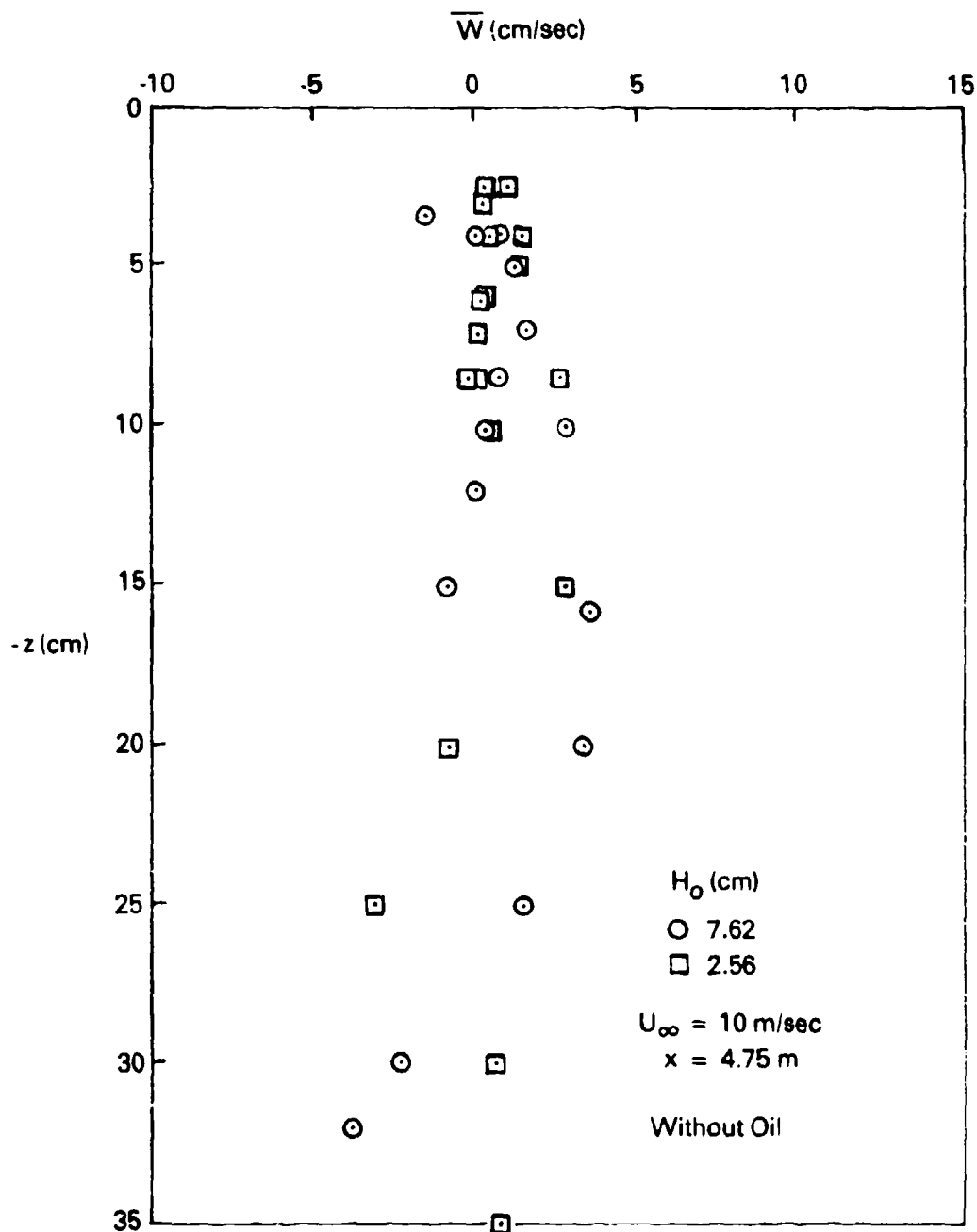


FIGURE 59. VERTICAL PROFILES OF VERTICAL MEAN VELOCITY IN BREAKING AND NONBREAKING WAVES.

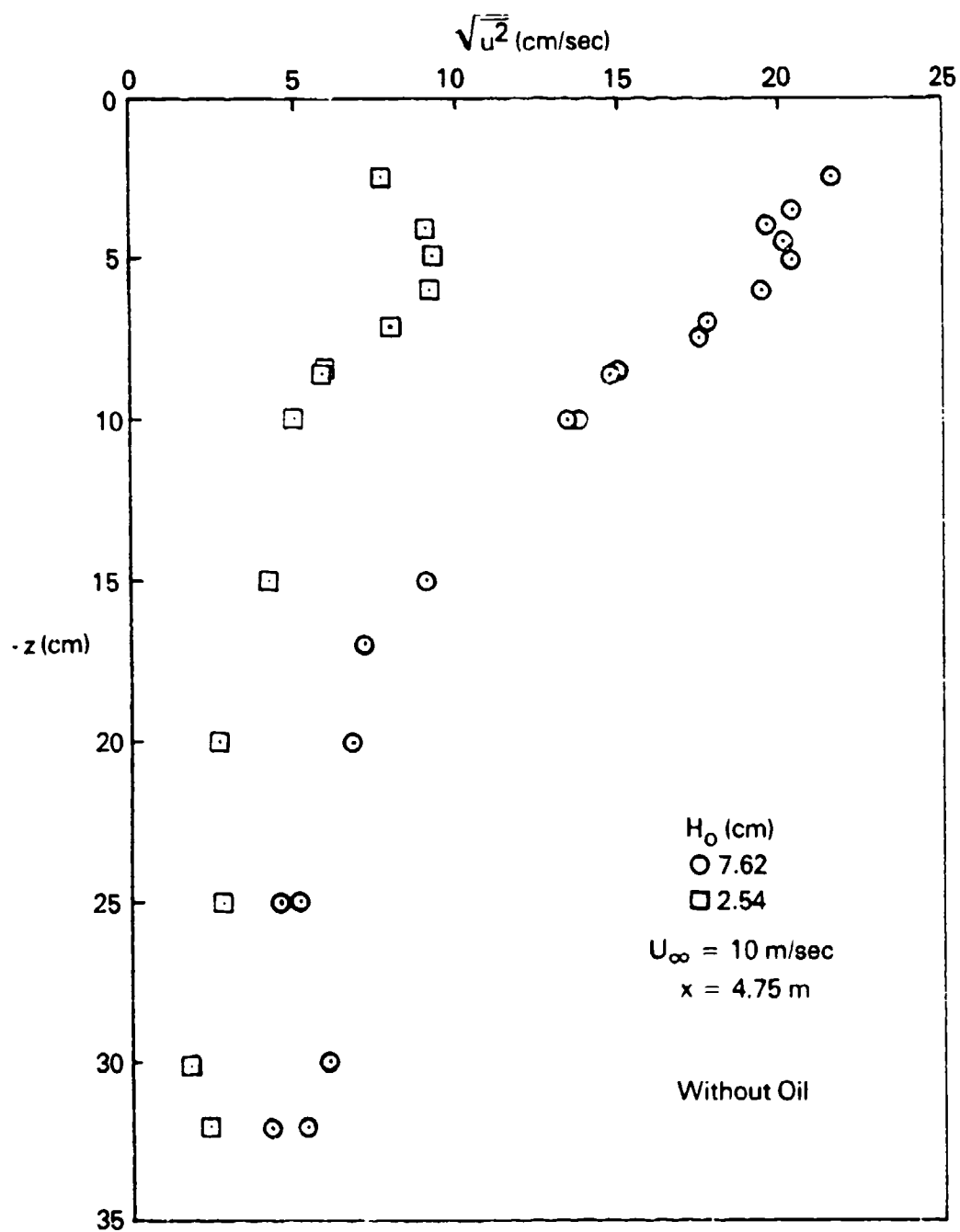


FIGURE 60. VERTICAL PROFILES OF RMS LONGITUDINAL VELOCITY IN BREAKING AND NONBREAKING WAVES.

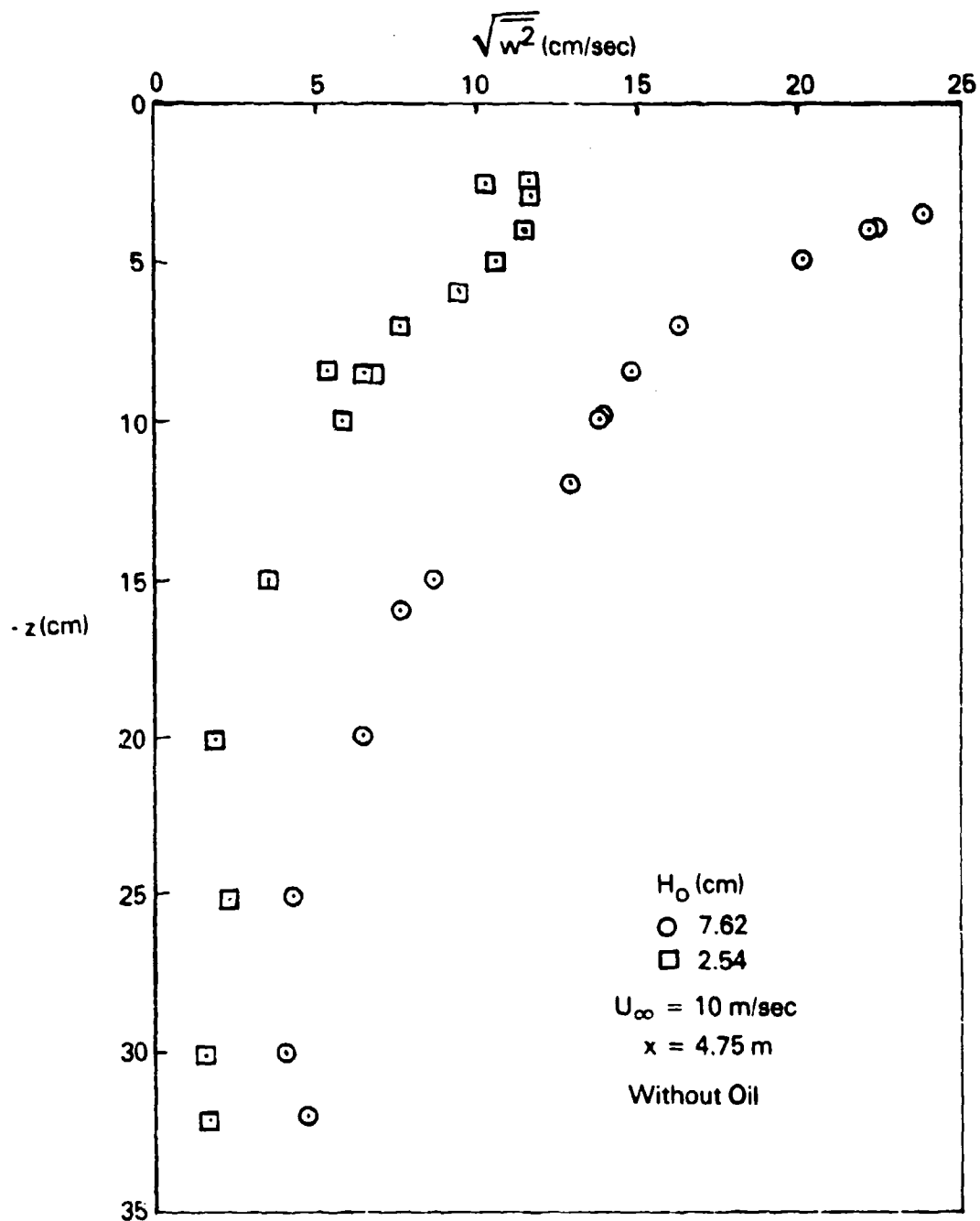


FIGURE G1. VERTICAL PROFILES OF RMS VERTICAL VELOCITY IN BREAKING AND NONBREAKING WAVES.

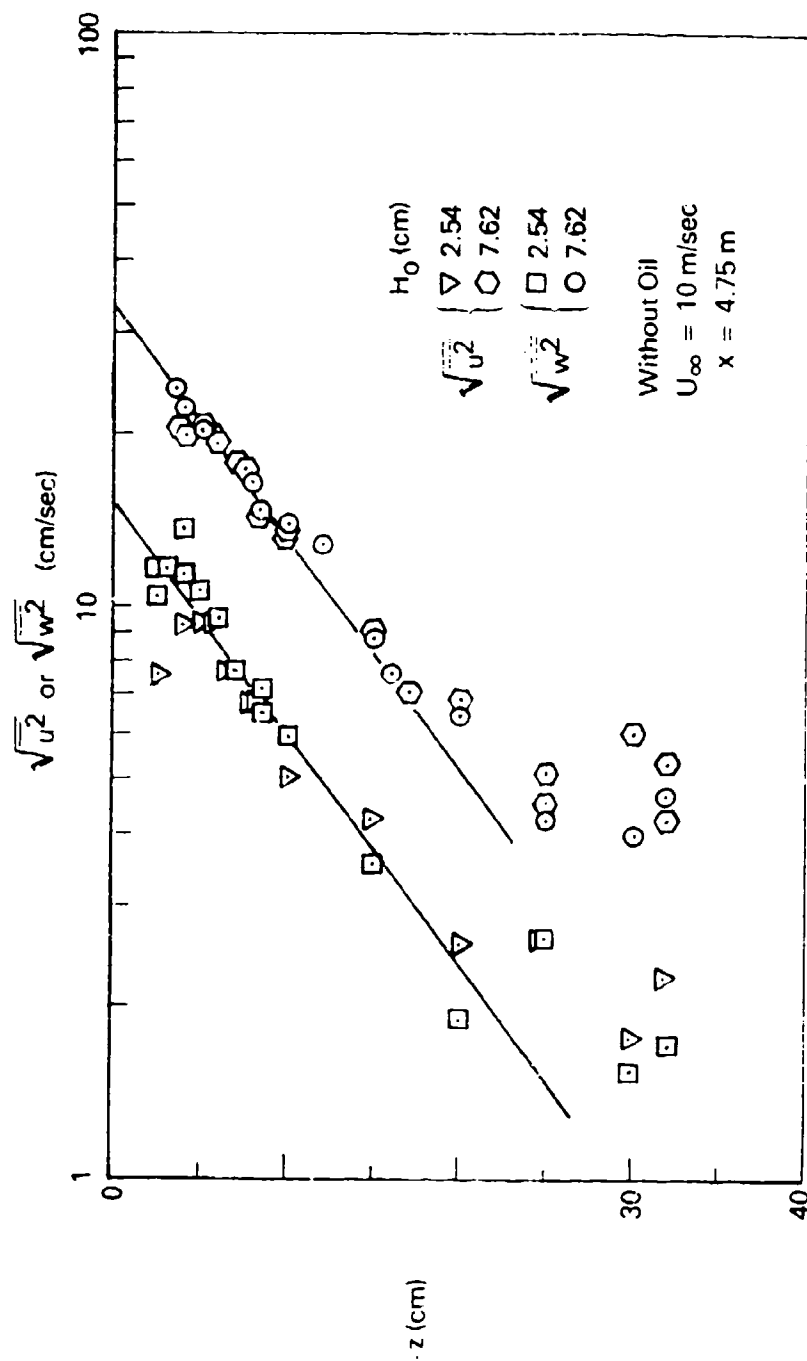


FIGURE 62. VERTICAL PROFILES OF RMS VELOCITY FLUCTUATIONS IN BREAKING AND NONBREAKING WAVES.

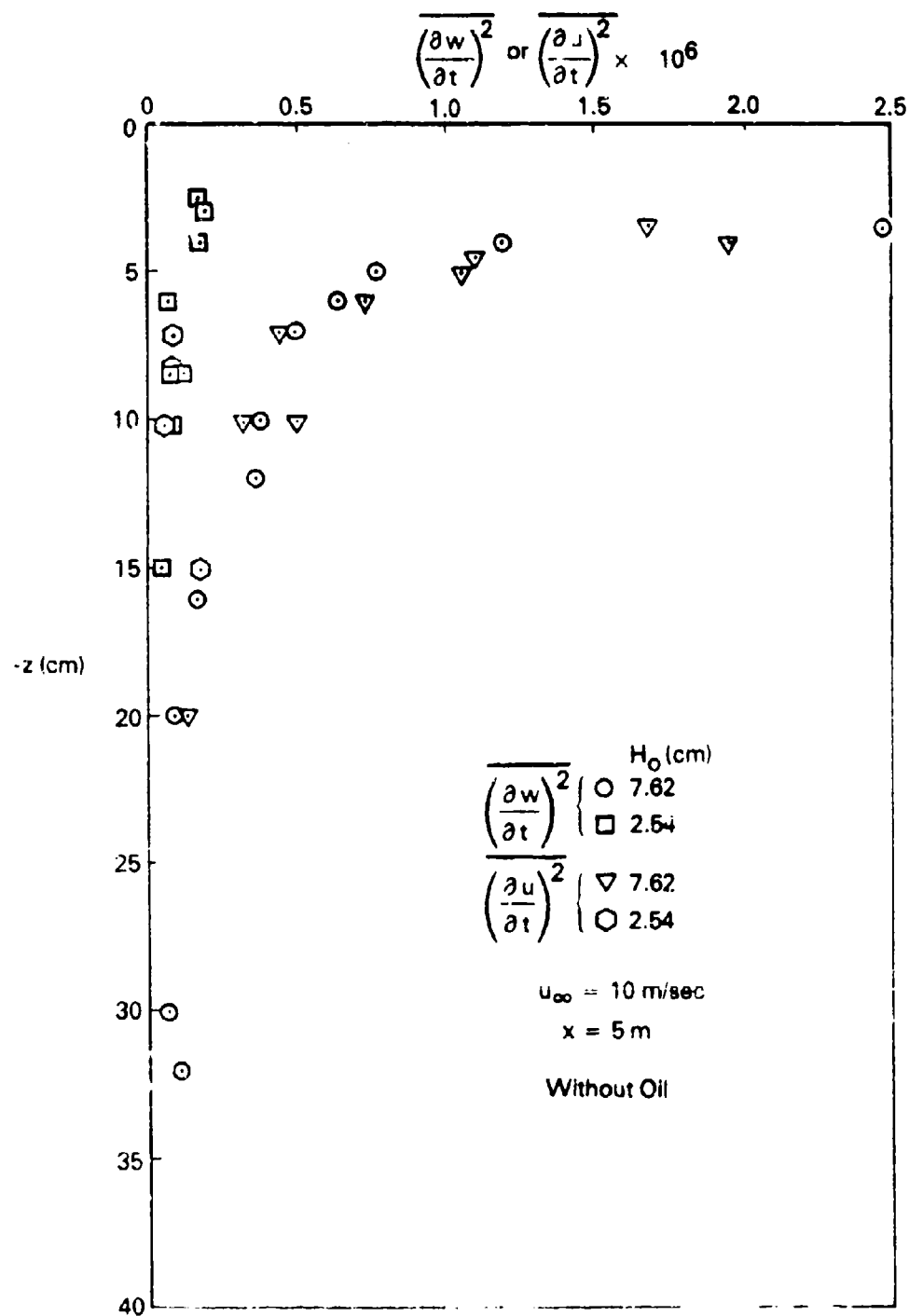


FIGURE 63. VERTICAL PROFILES OF MEAN SQUARE VELOCITY DERIVATIVES IN BREAKING AND NONBREAKING WAVES

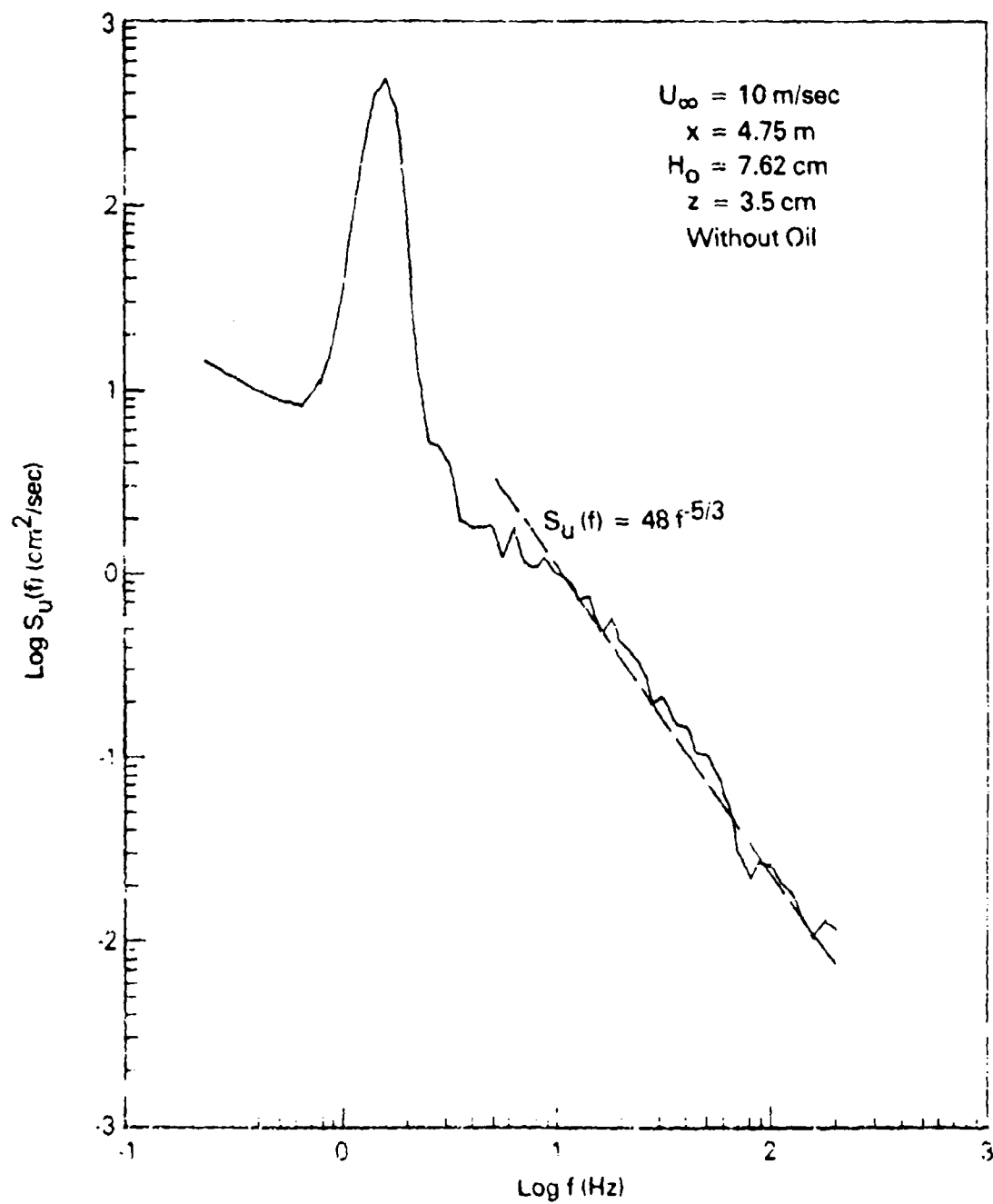


FIGURE 64. SPECTRUM OF LONGITUDINAL VELOCITY FLUCTUATIONS IN BREAKING WAVES.

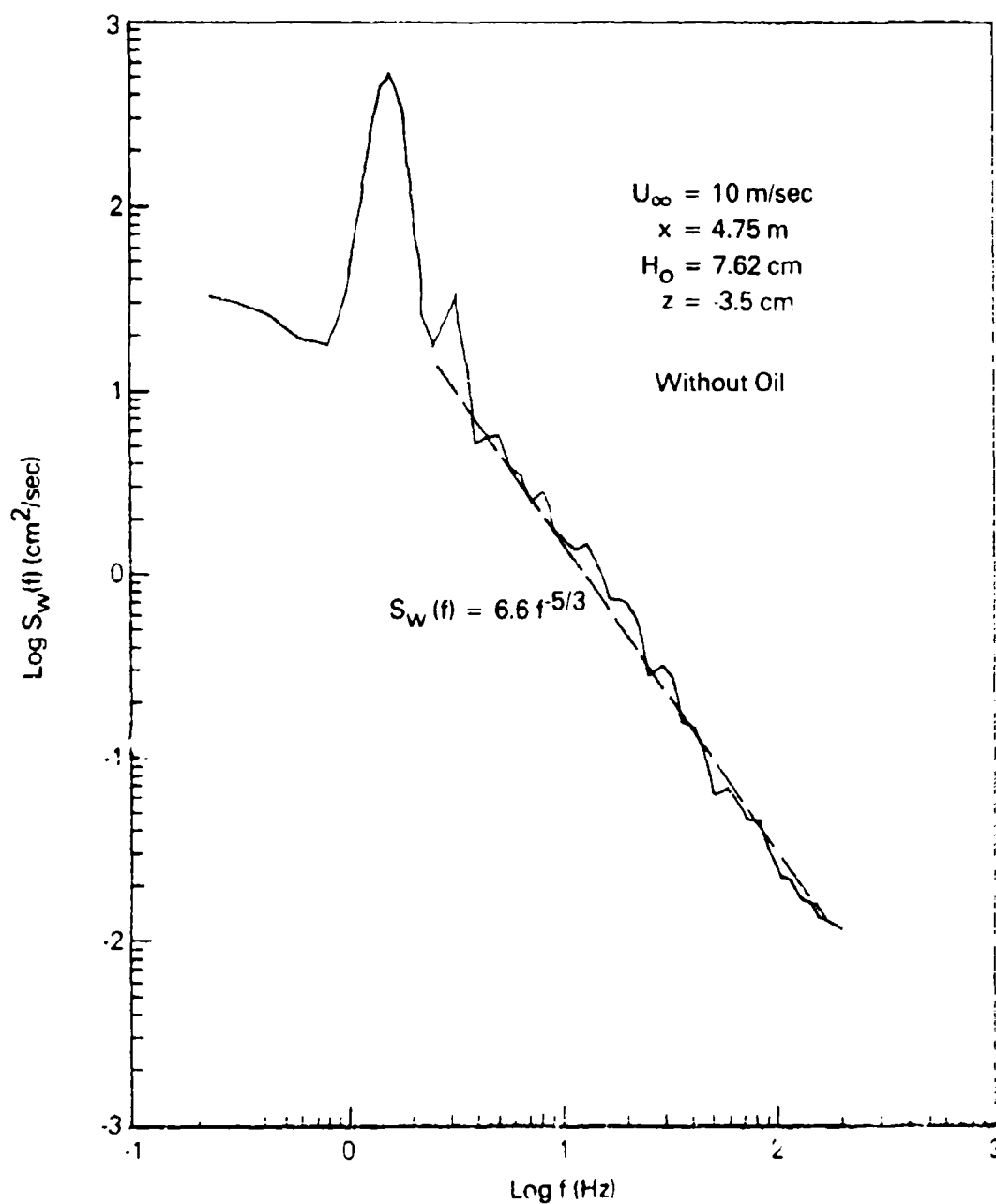


FIGURE 65. SPECTRUM OF VERTICAL VELOCITY FLUCTUATIONS IN BREAKING WAVES.

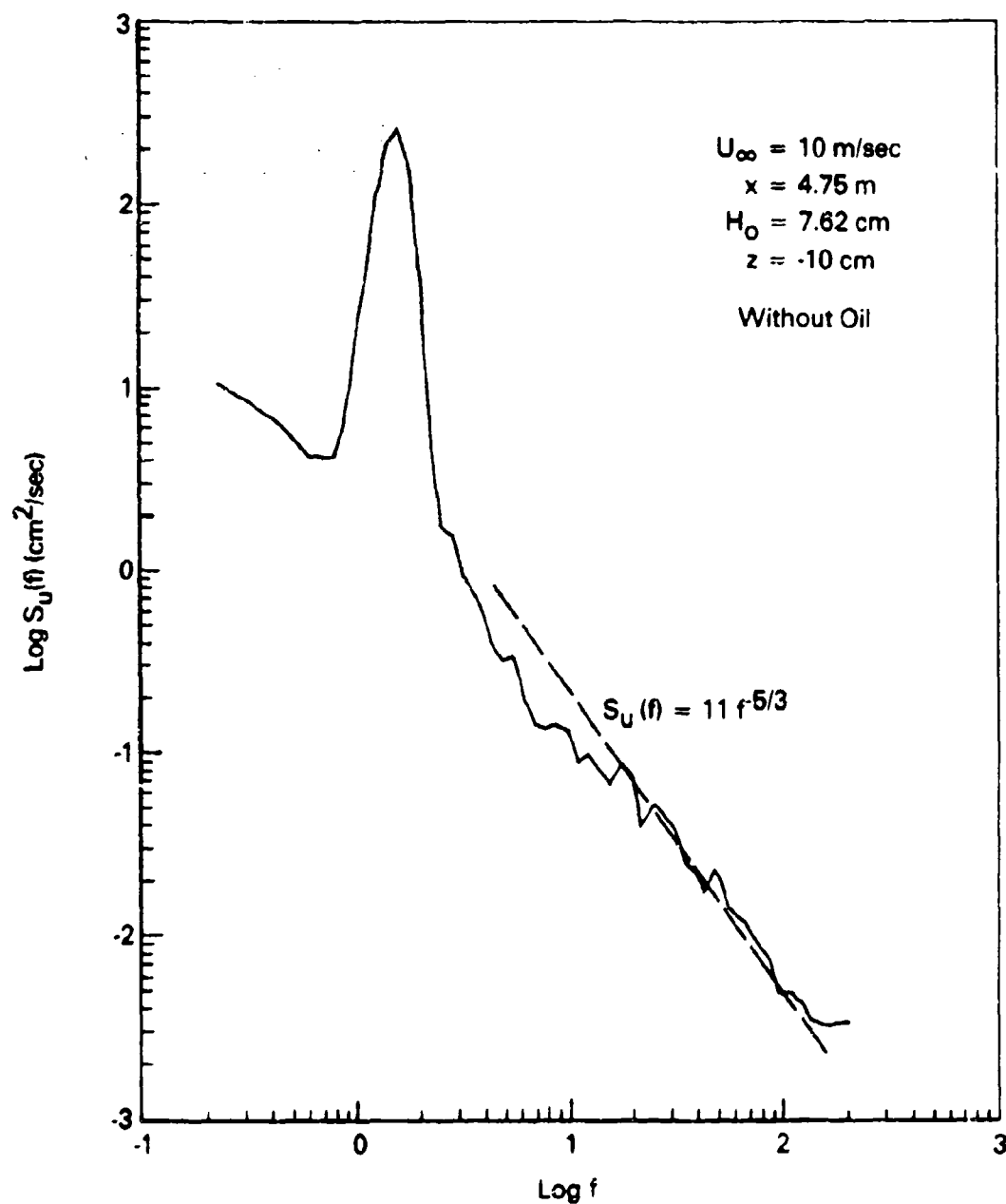


FIGURE 88. SPECTRUM OF LONGITUDINAL VELOCITY FLUCTUATIONS IN BREAKING WAVES.

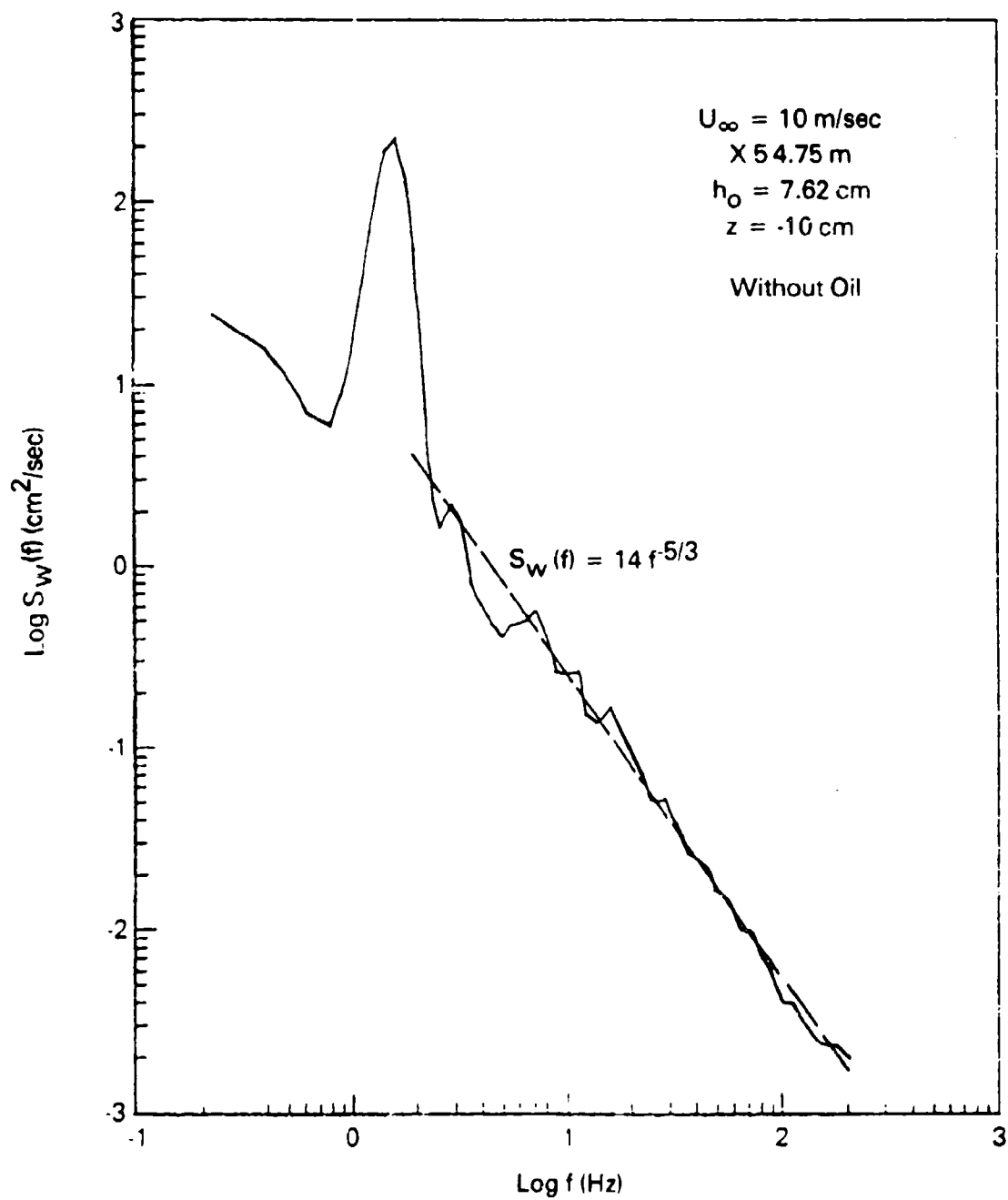


FIGURE 67. SPECTRUM OF VERTICAL VELOCITY FLUCTUATIONS IN BREAKING WAVES.

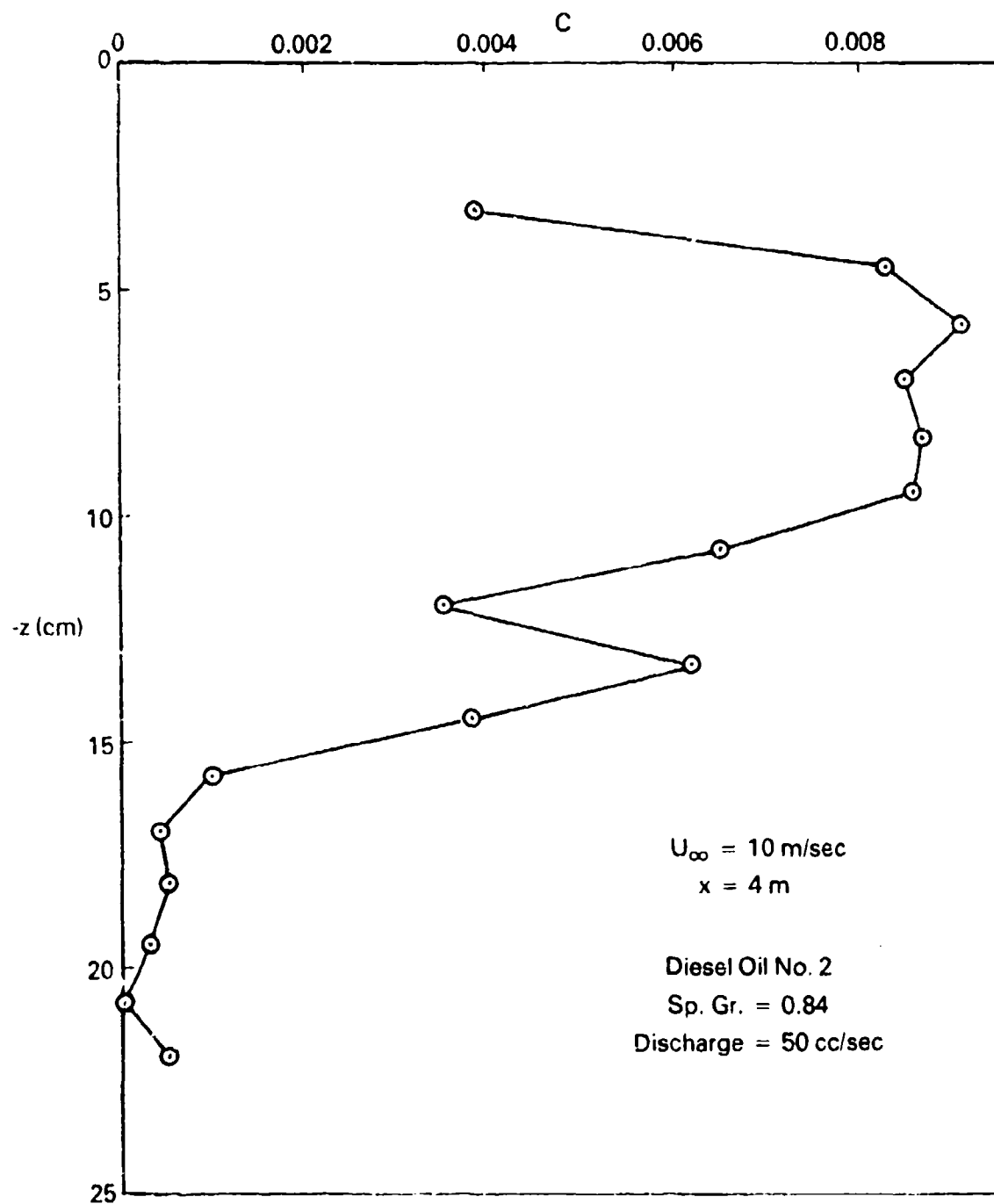


FIGURE 68. VERTICAL PROFILE OF INSTANTANEOUS OIL VOLUME CONCENTRATION.

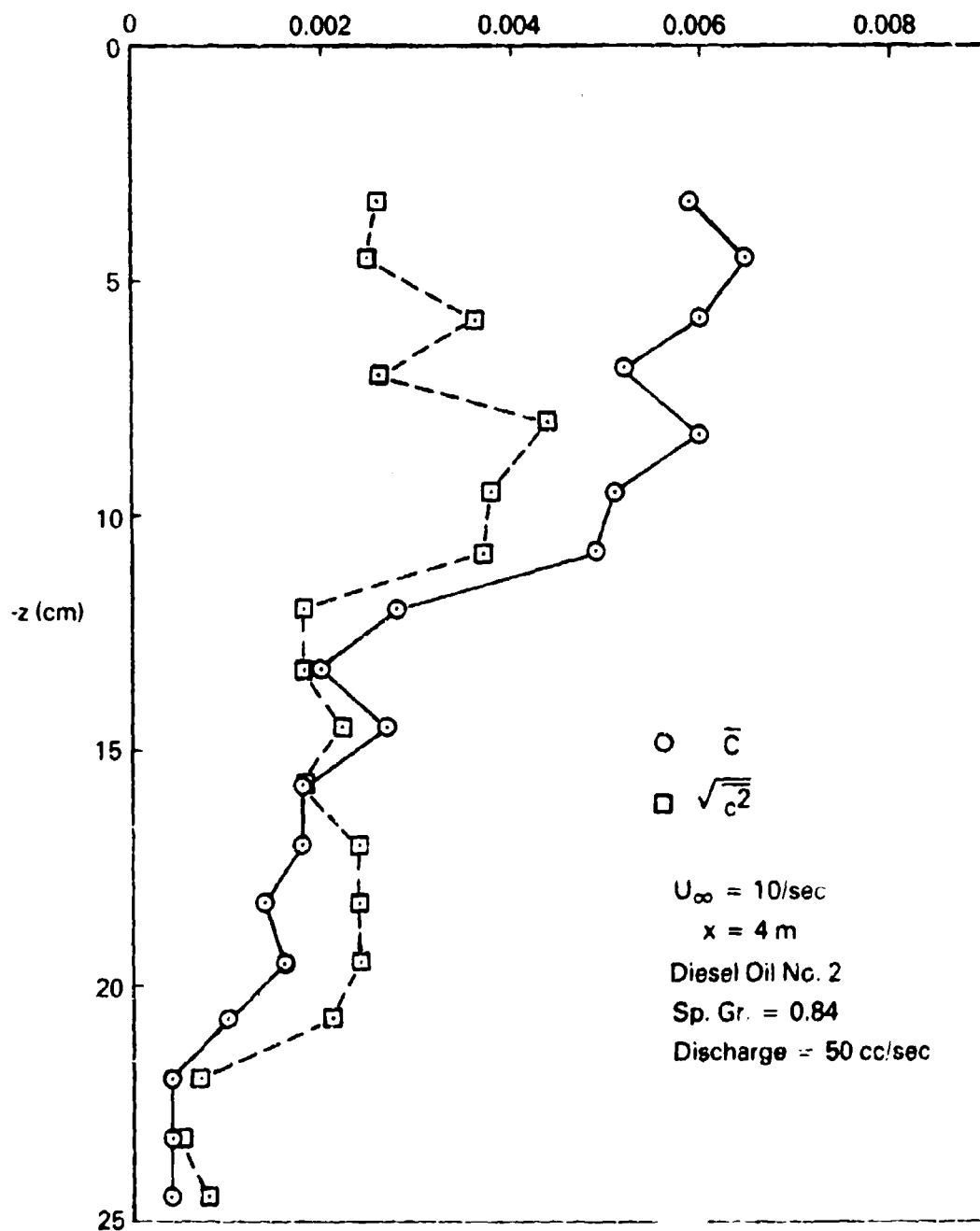


FIGURE 69. VERTICAL PROFILES OF MEAN AND RM^s OIL VOLUME CONCENTRATION.

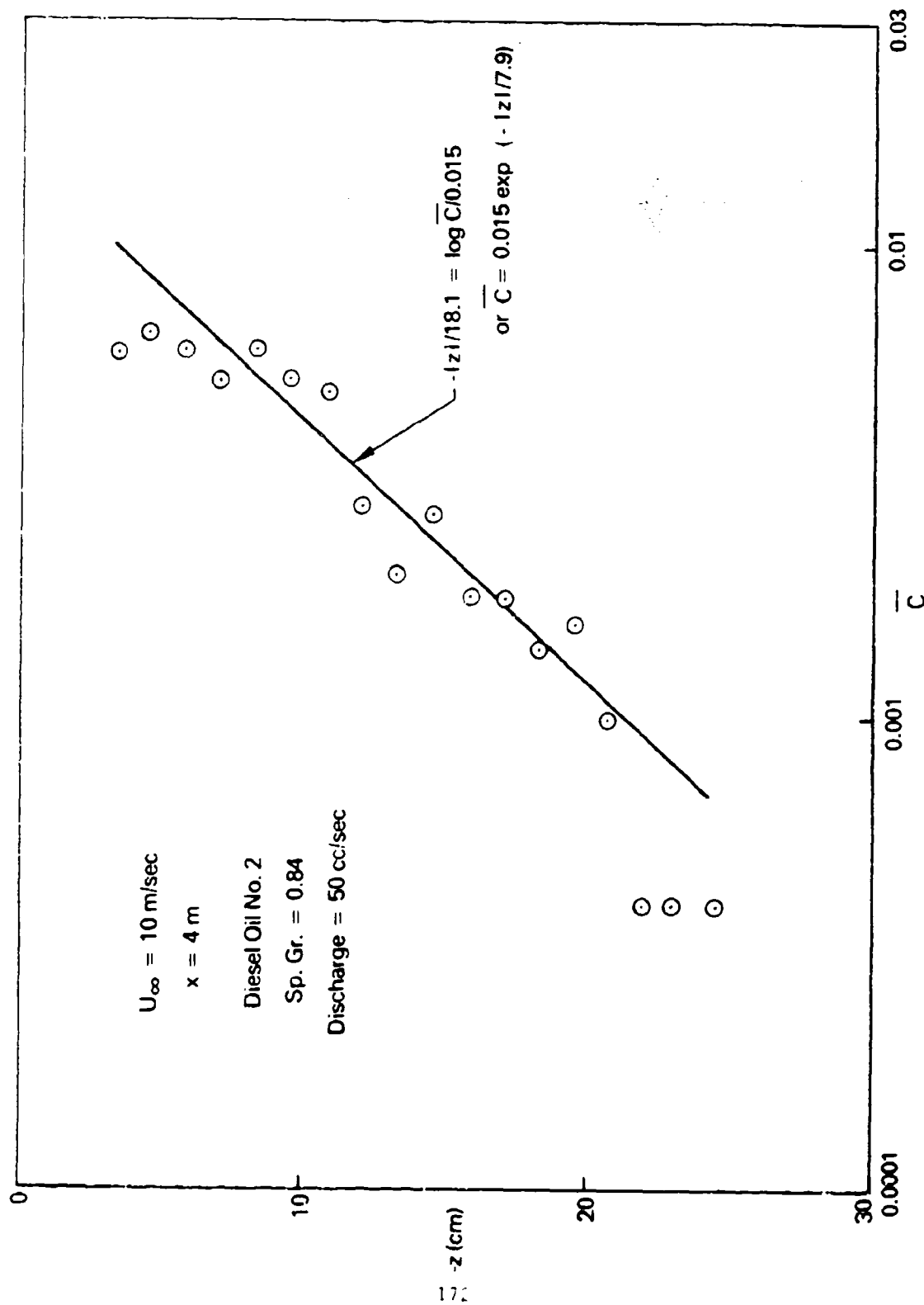


FIGURE 70. VERTICAL PROFILE OF MEAN OIL VOLUME CONCENTRATION.

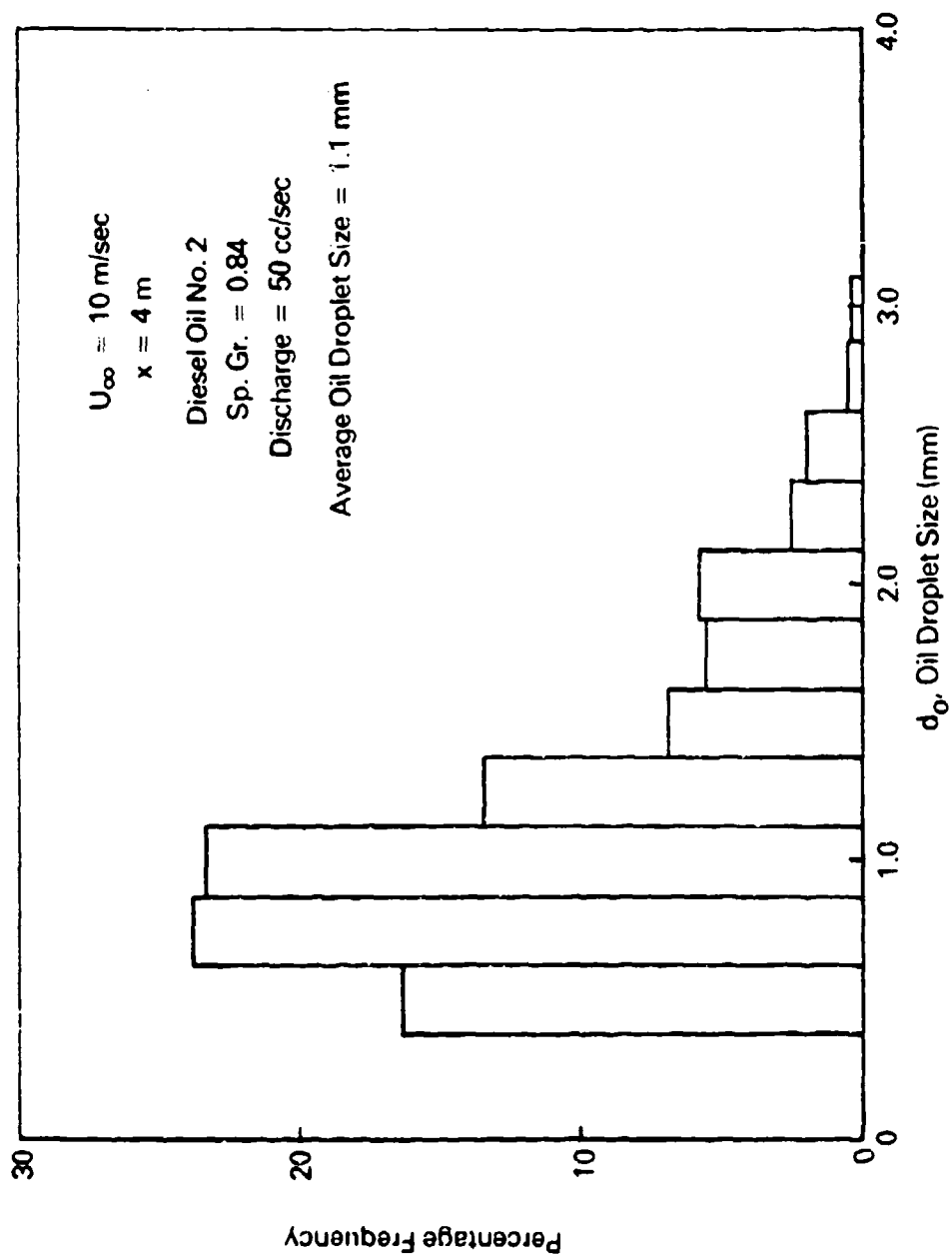


FIGURE 71. SIZE DISTRIBUTION OF OIL DROPLETS.

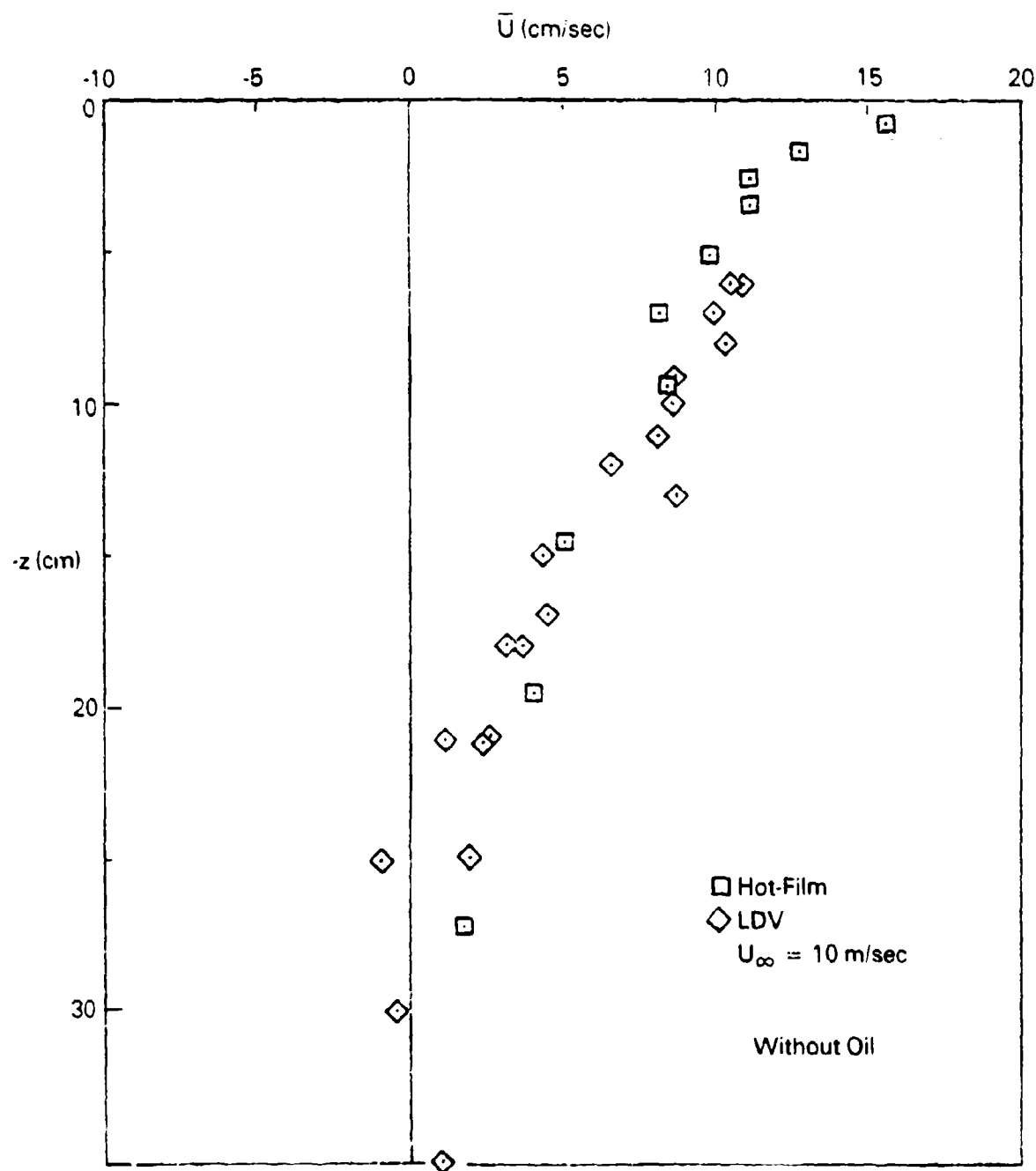


FIGURE 72. COMPARISON OF LONGITUDINAL MEAN VELOCITY PROFILE MEASURED IN WIND-WAVES BY LDV AND HOT-FILM PROBES.

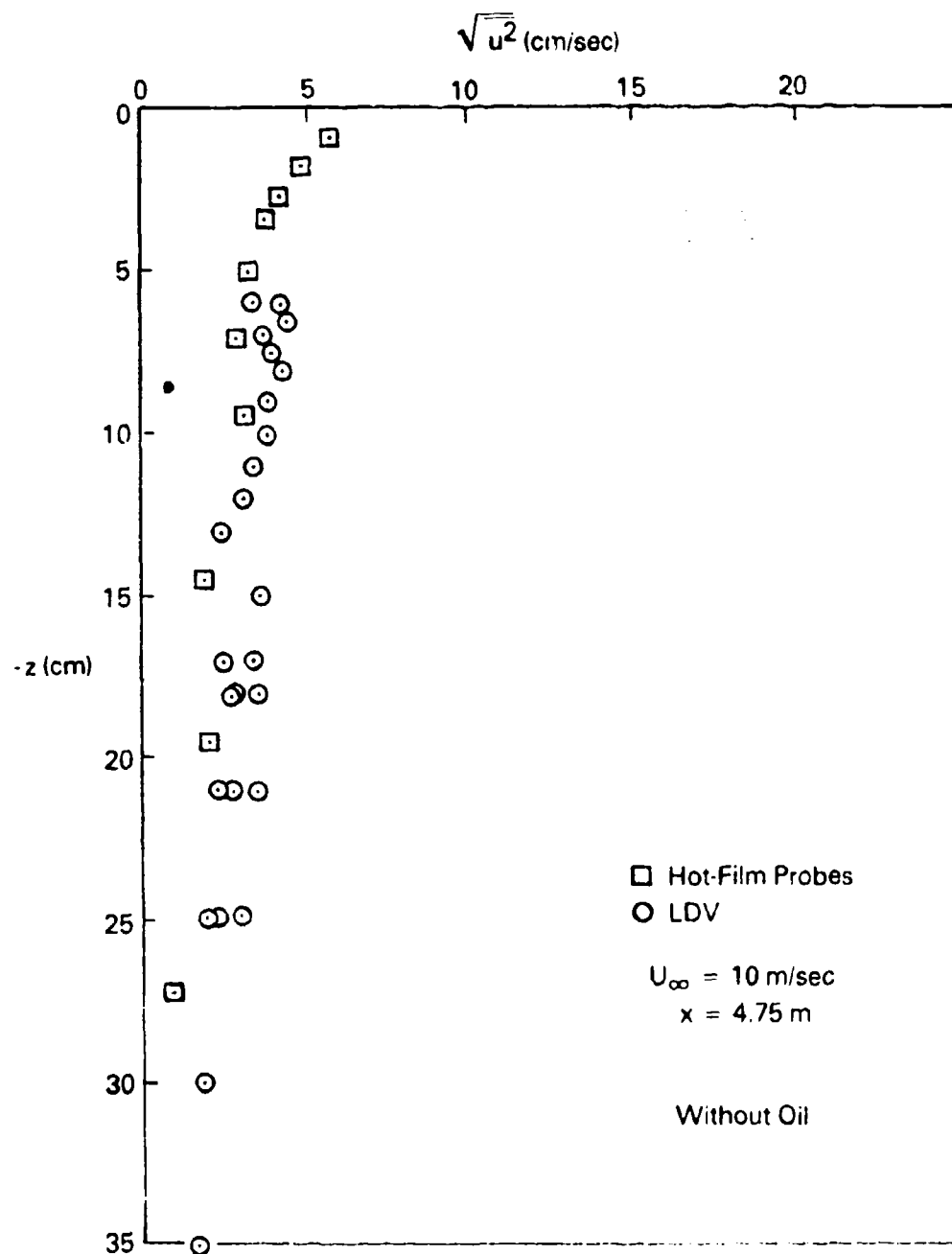


FIGURE 73. COMPARISON OF RMS LONGITUDINAL VELOCITY FLUCTUATIONS MEASURED IN WIND-WAVES BY LDV AND HOT-FILM PROBES.

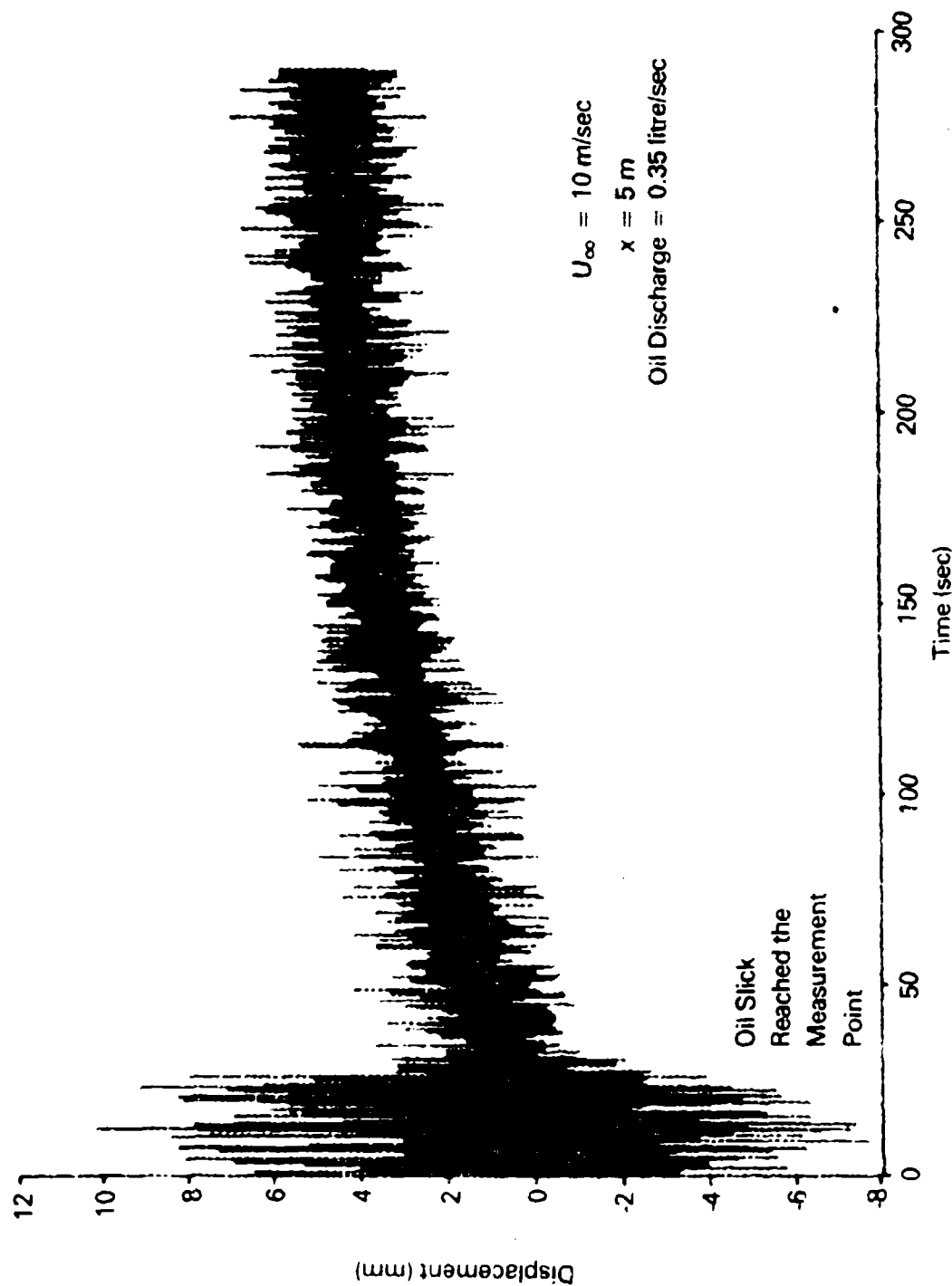


FIGURE 74. TRANSIENT PROFILES OF WIND WAVES IN RESPONSE TO OILSLICK.

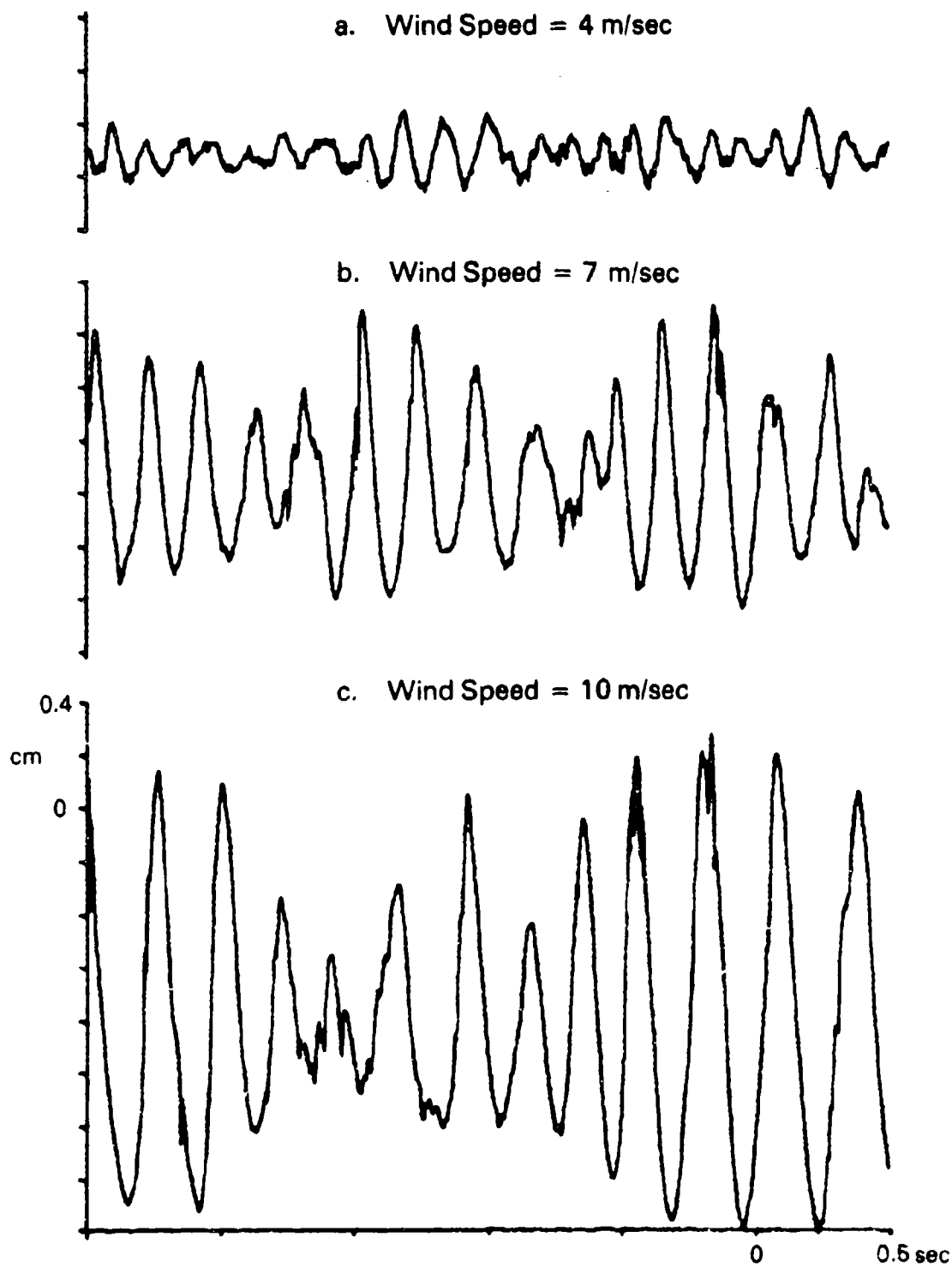


FIGURE 75. WIND-WAVE PROFILES WITHOUT OIL SLICK.

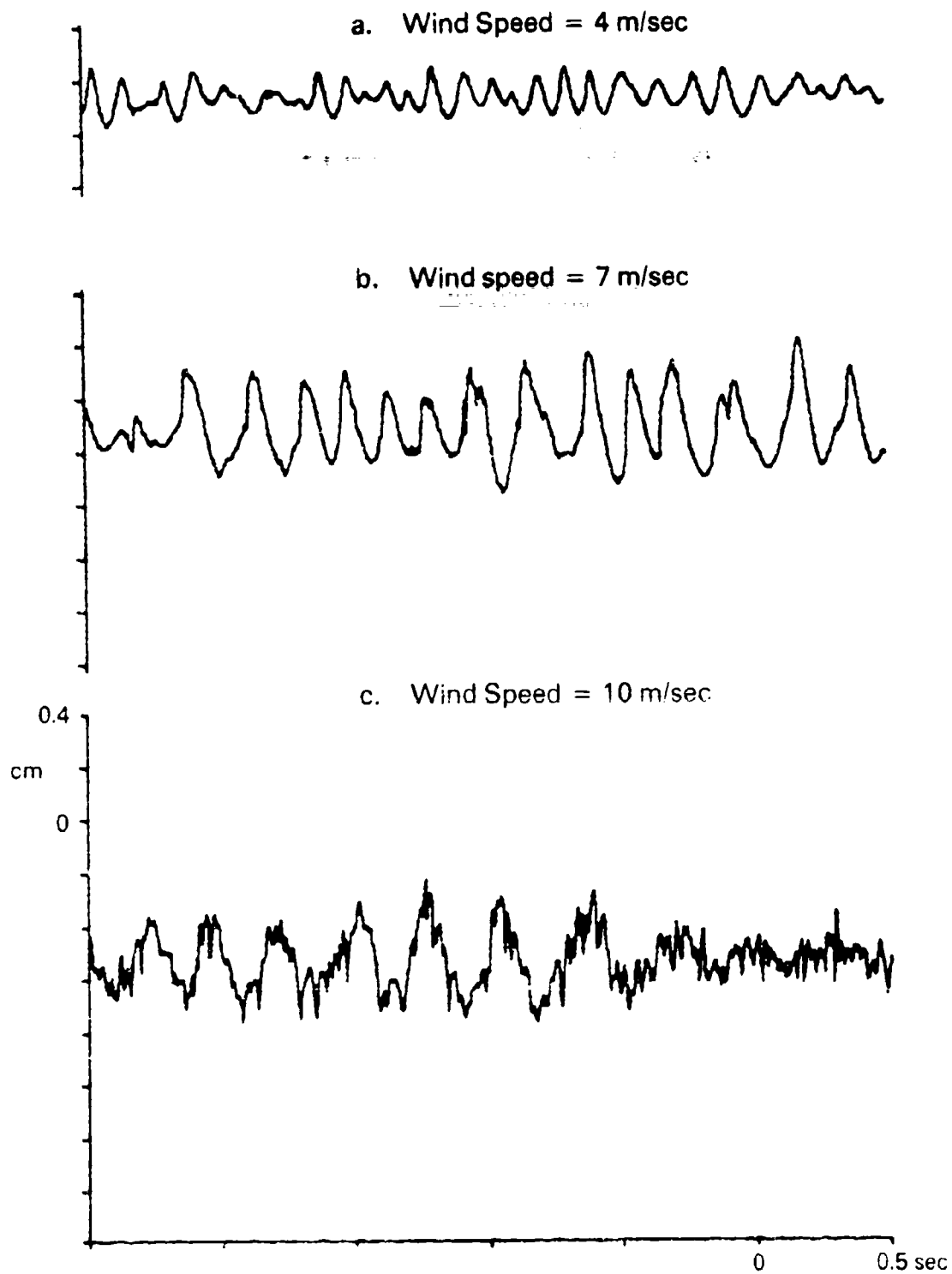


FIGURE 76. WIND-WAVE PROFILES WITH OIL SLICK.

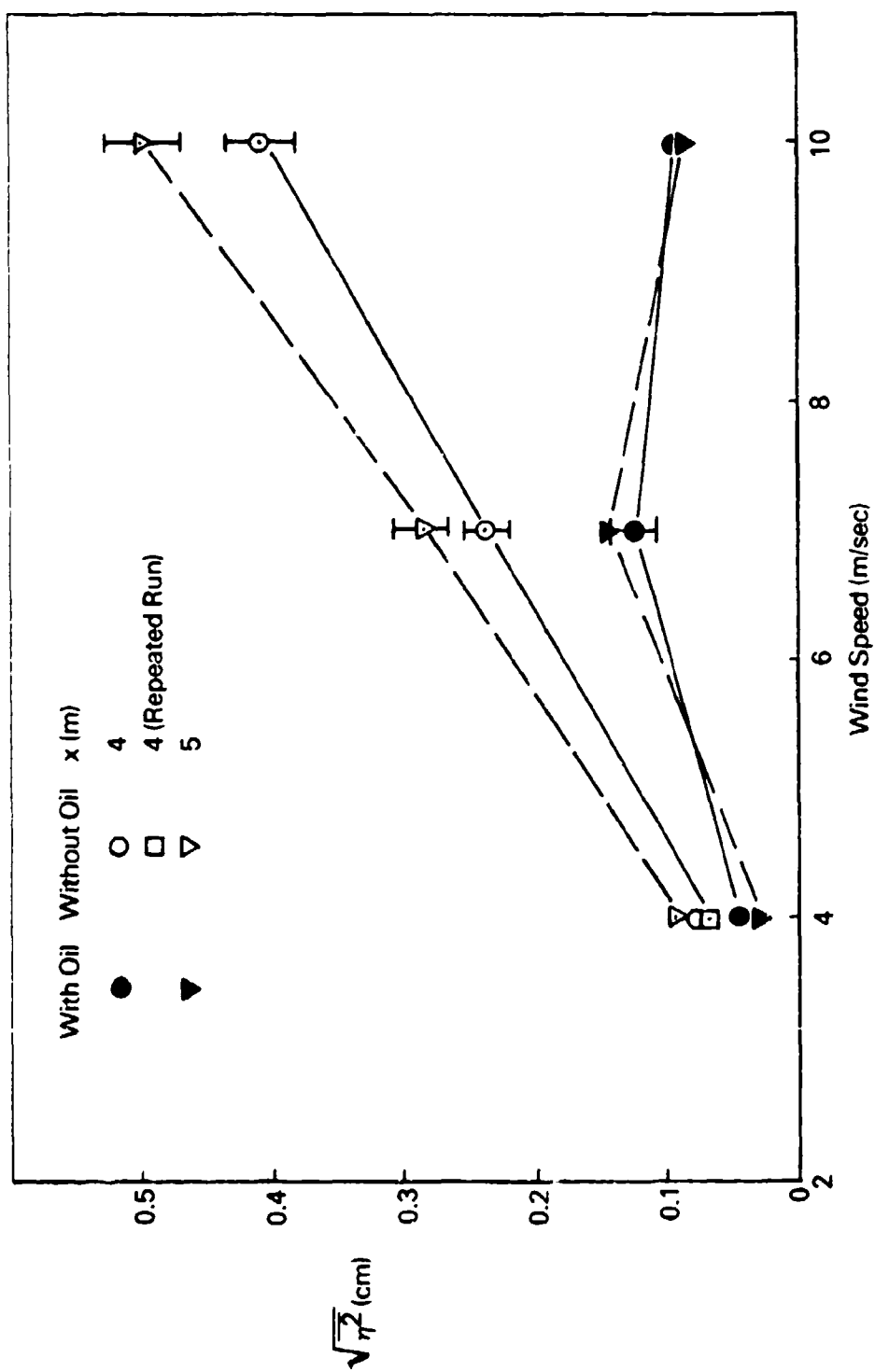


FIGURE 77. VARIATION OF RMS WAVE WEIGHT WITH WIND SPEED.

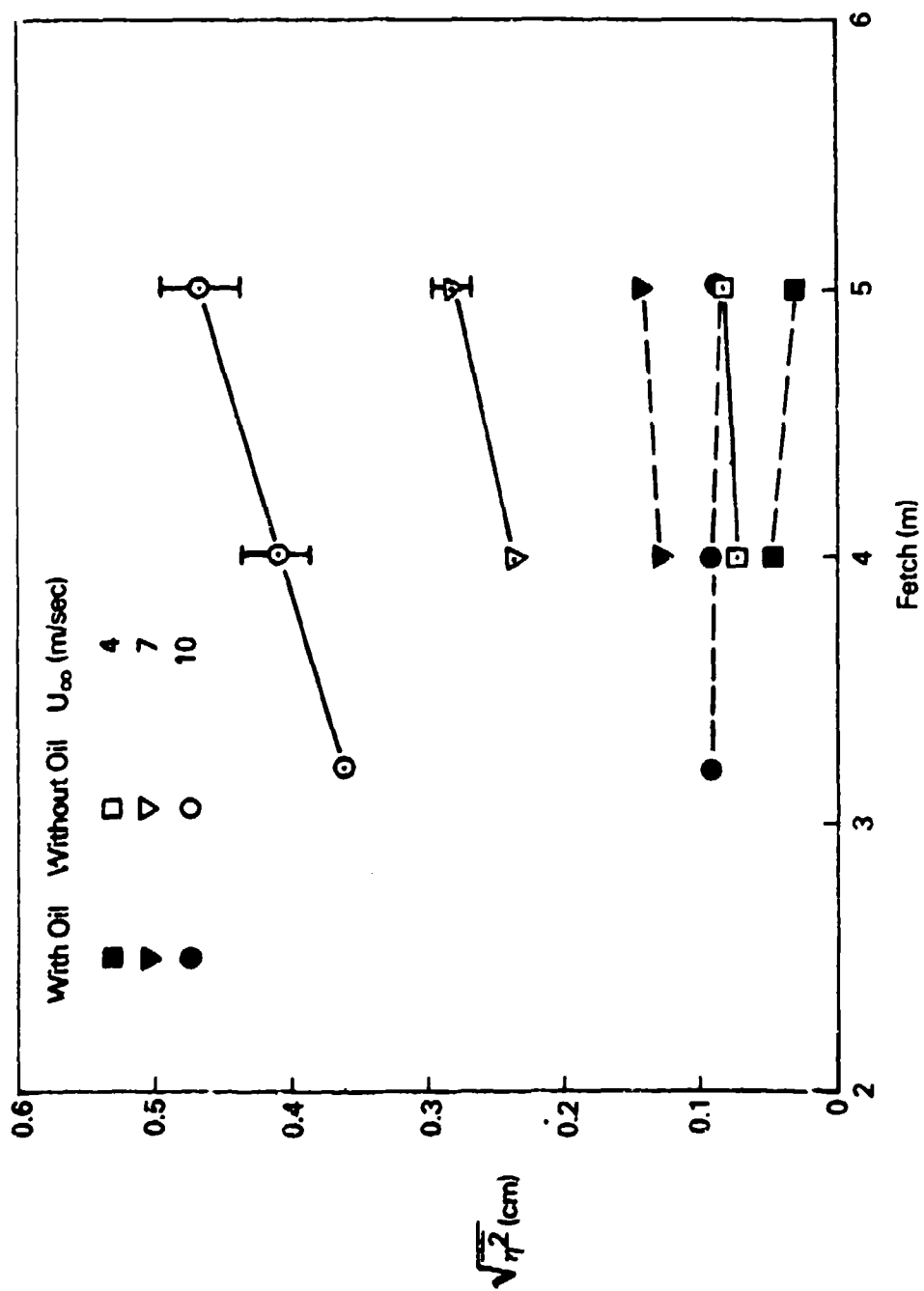


FIGURE 78. VARIATION OF RMS WAVE HEIGHT WITH FETCH.

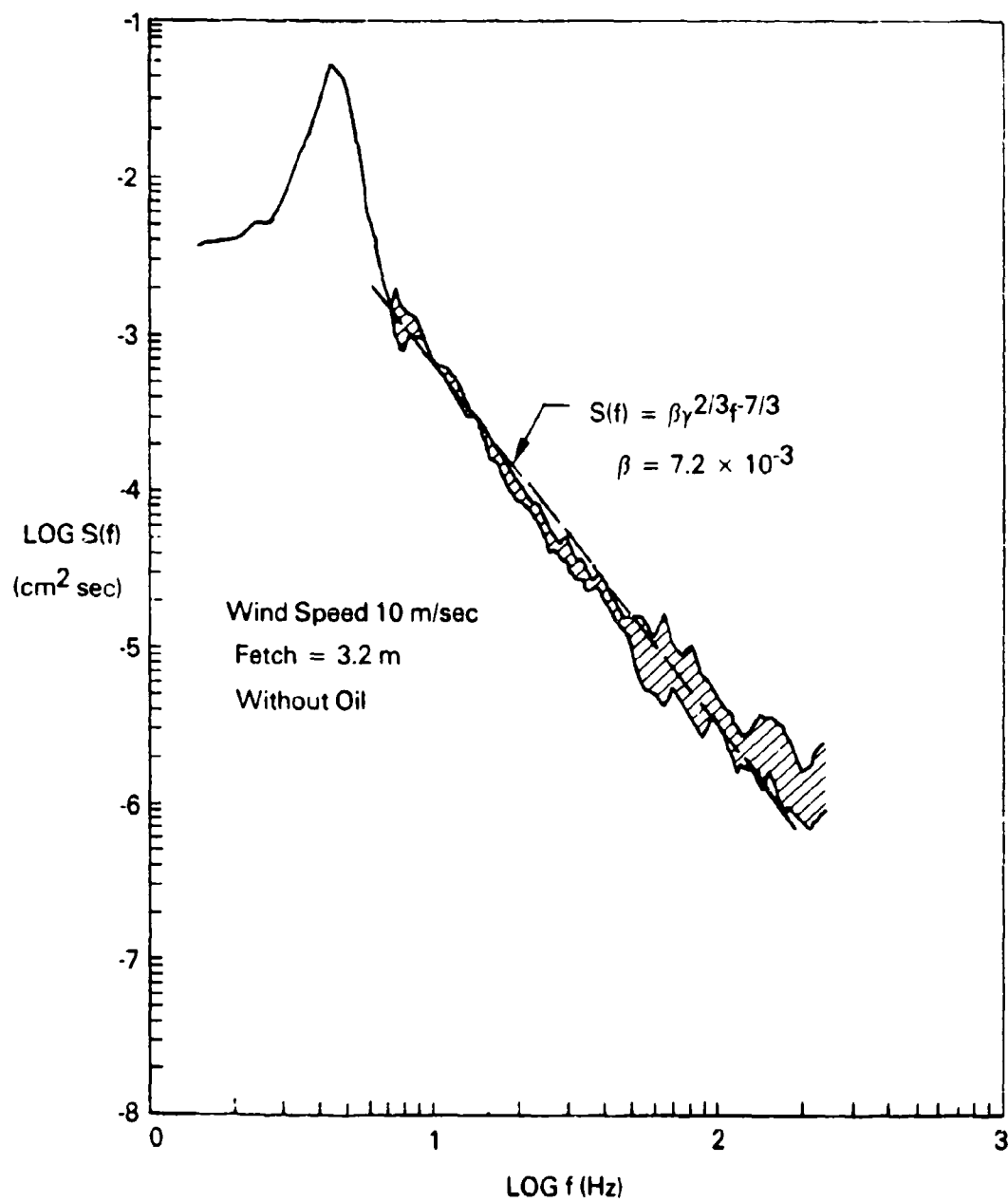


FIGURE 79. WAVE ENERGY SPECTRUM.

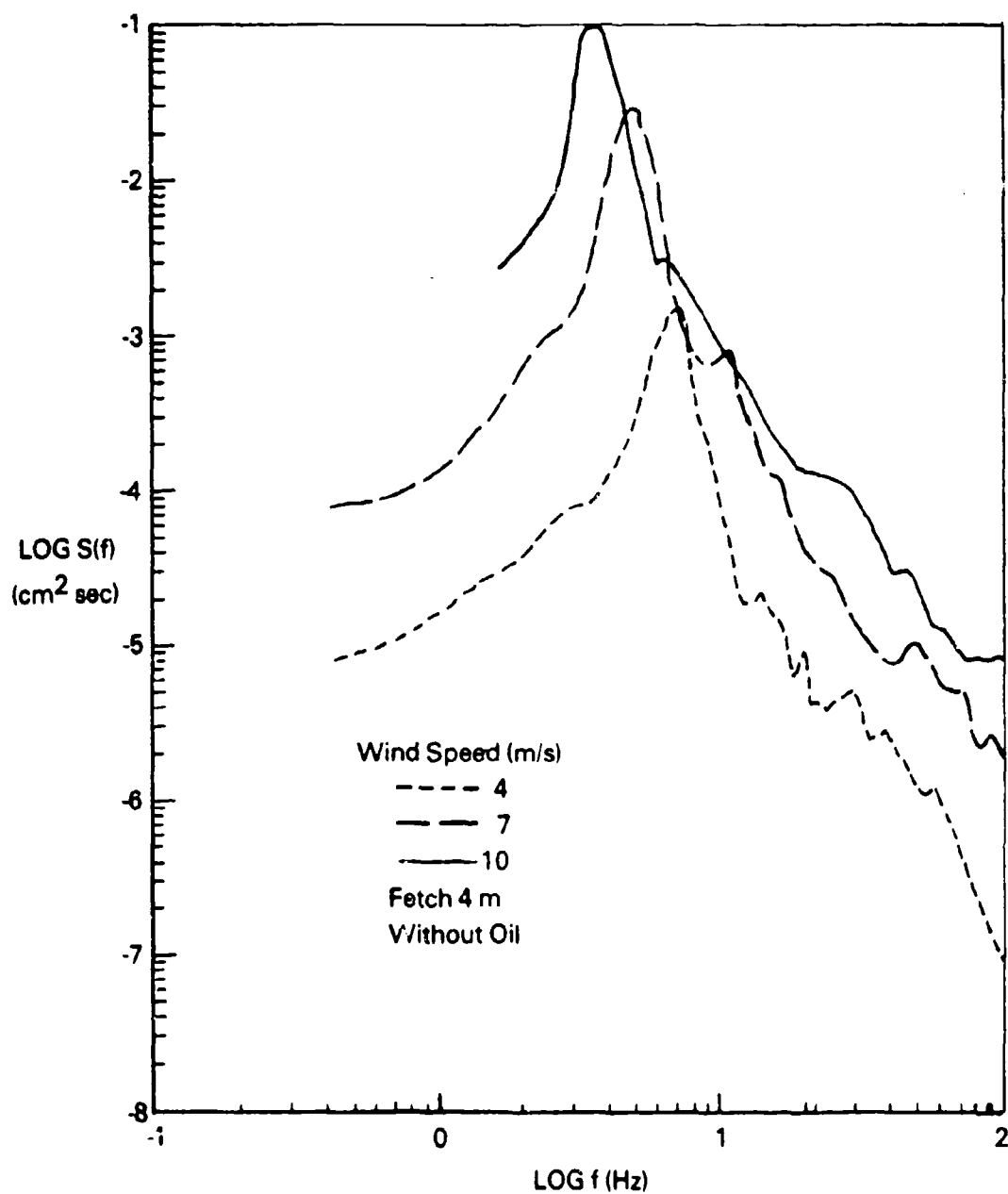


FIGURE 80. WAVE ENERGY SPECTRUM VARIATION WITH WIND SPEED.

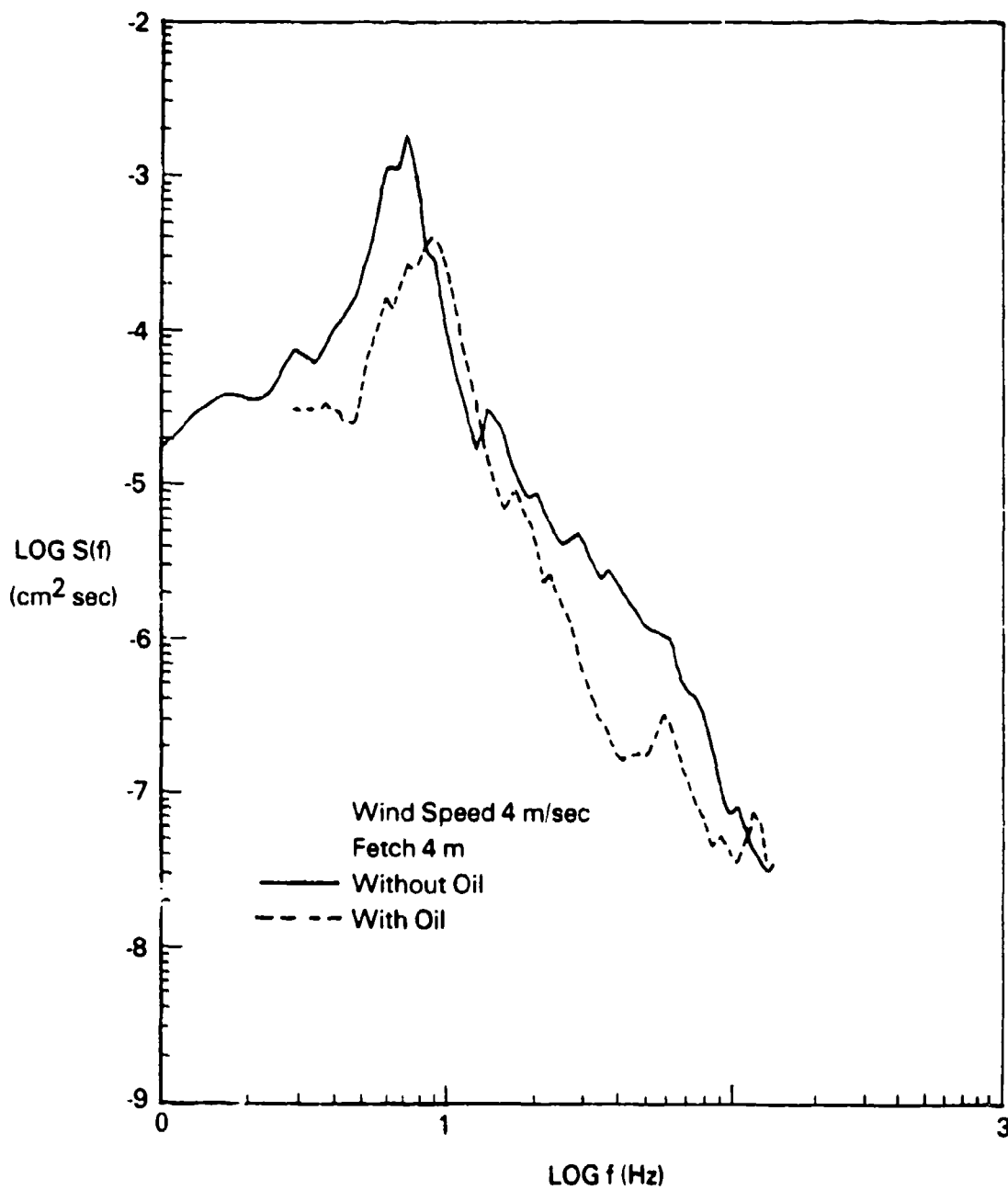


FIGURE 81. WAVE ENERGY SPECTRA MEASURED WITH AND WITHOUT OIL.

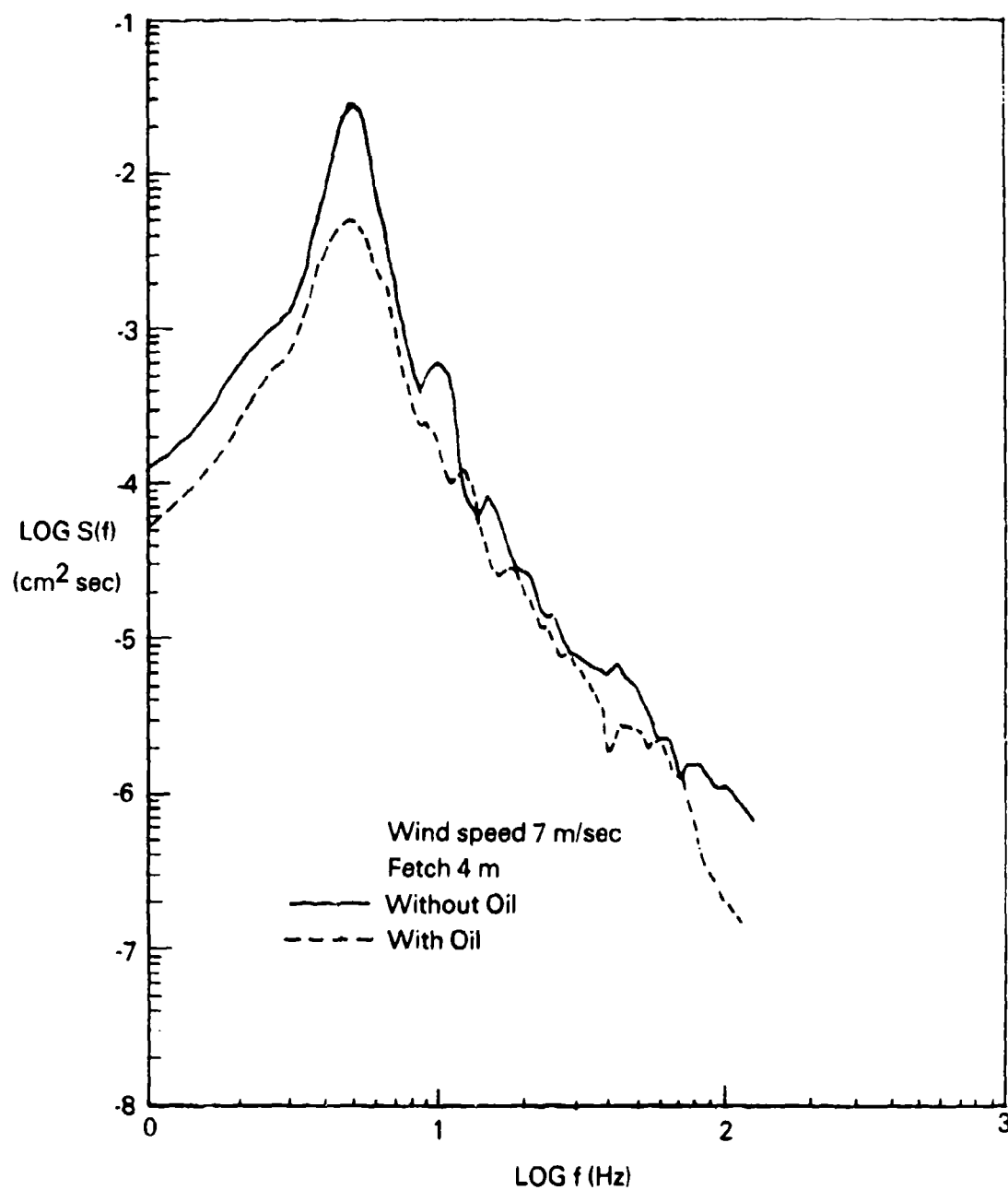


FIGURE 82. WAVE ENERGY SPECTRA MEASURED WITH AND WITHOUT OIL.

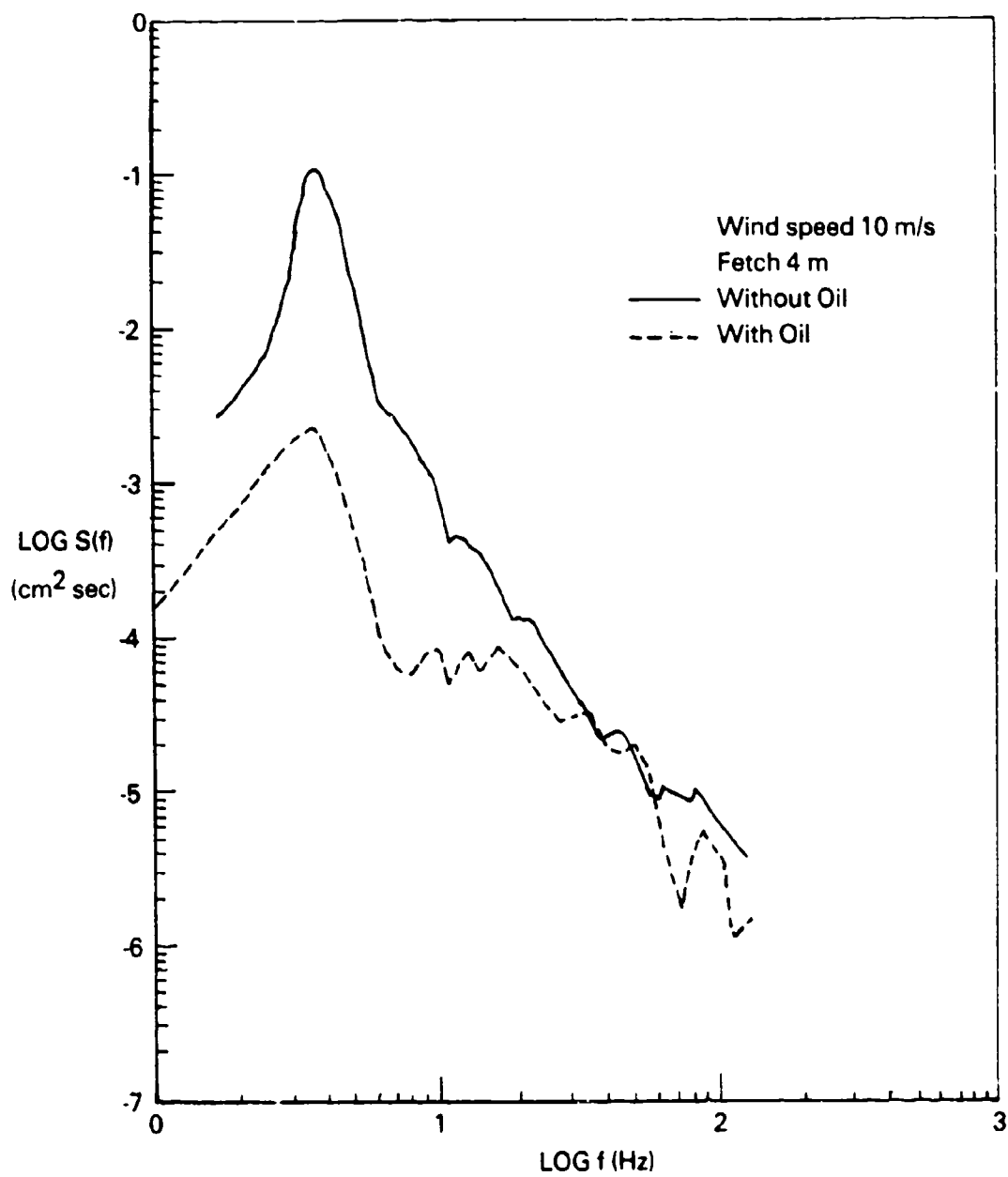


FIGURE 83. WAVE ENERGY SPECTRA MEASURED WITH AND WITHOUT OIL.

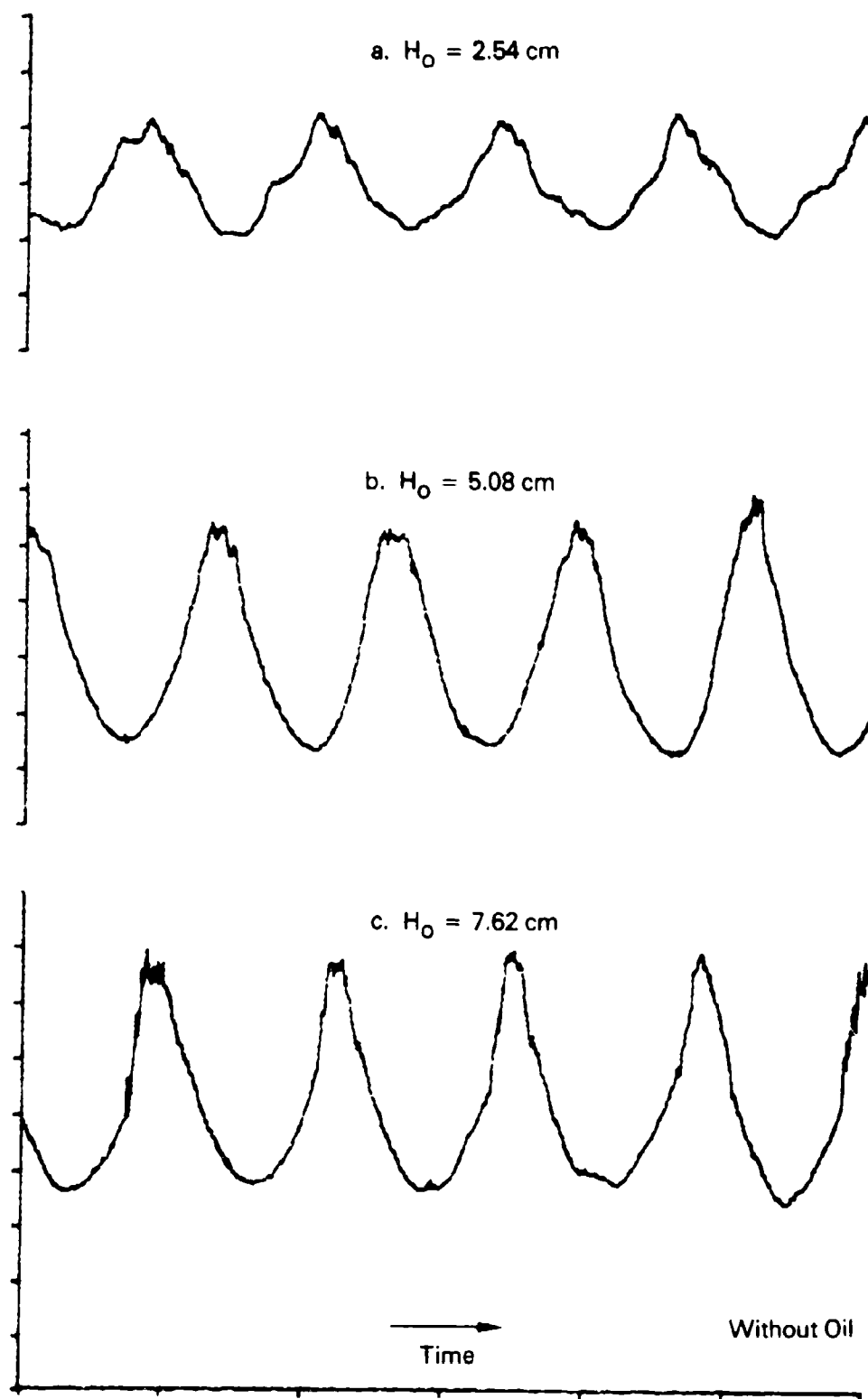


FIGURE 84. PROFILES OF MECHANICALLY GENERATED WAVES WITH WIND, VERTICAL SCALE = 2 cm/DIV., HORIZONTAL SCALE = 0.5 sec/div.

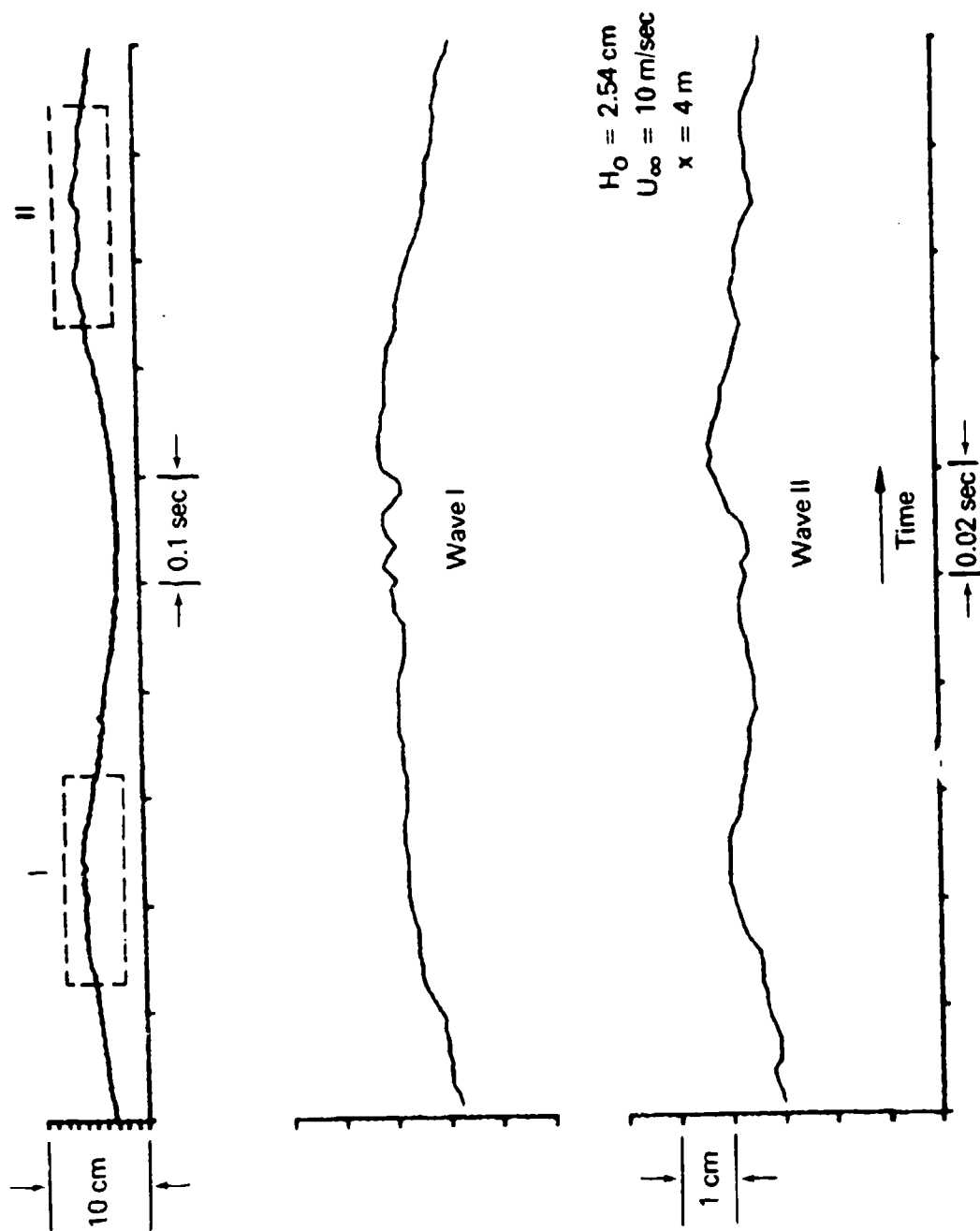


FIGURE 85. A TYPICAL PROFILE OF NONBREAKING WAVES WITHOUT OIL.

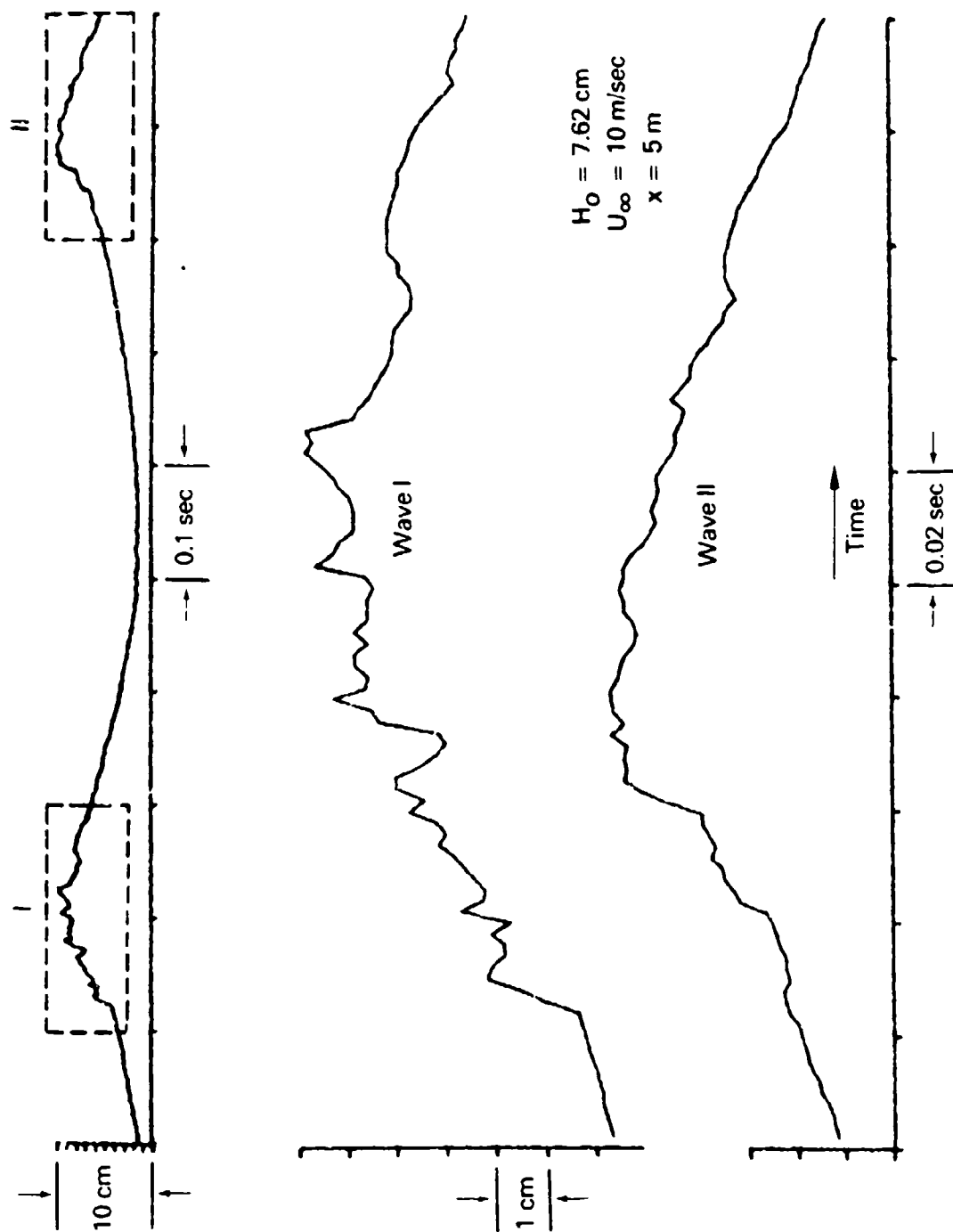


FIGURE 86. TYPICAL PROFILE OF BREAKING WAVES WITHOUT OIL.

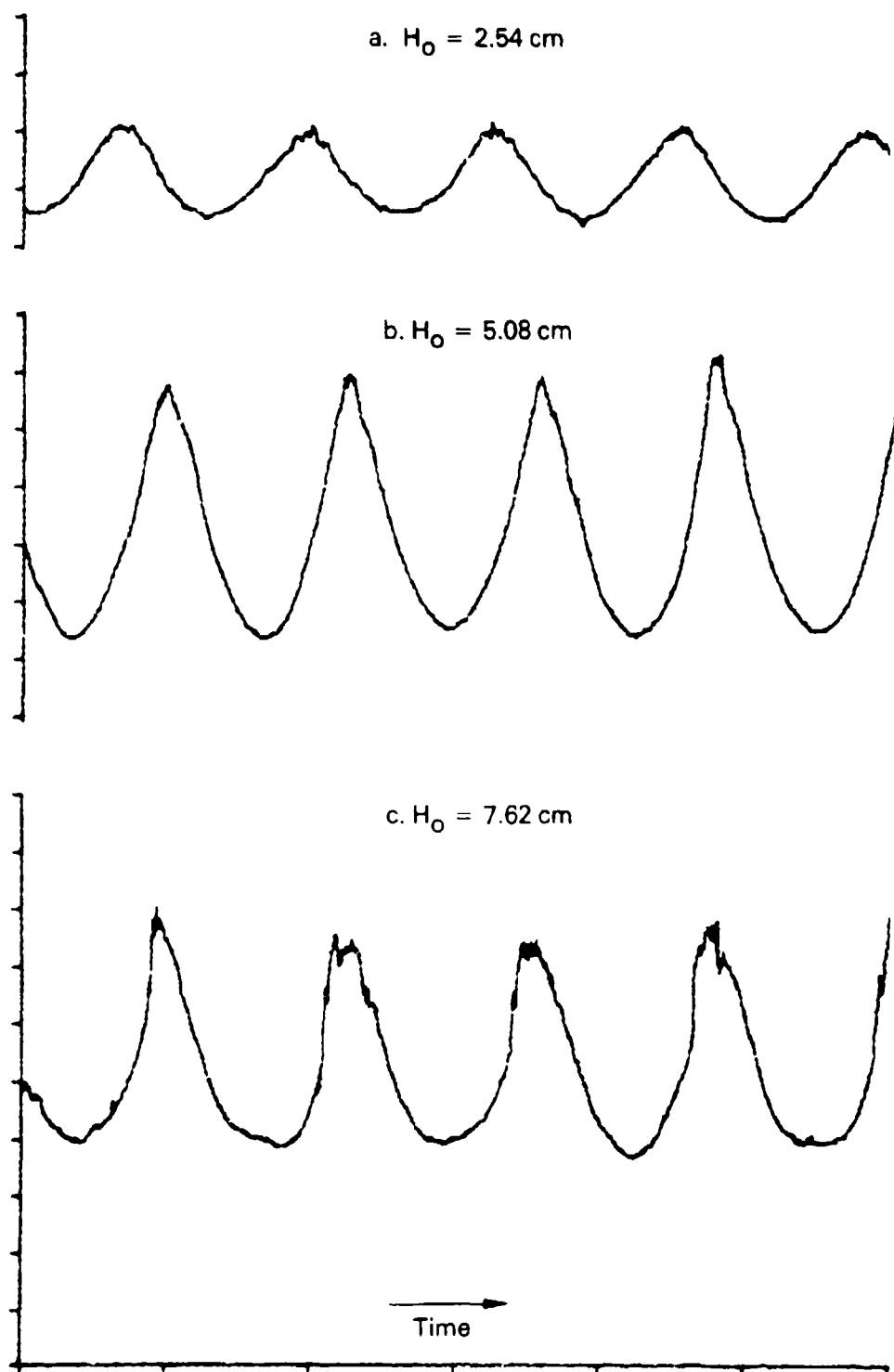


FIGURE 87. PROFILE OF MECHANICAL GENERATED WAVES WITH WIND AND OIL STICK. VERTICAL SCALE = 2 cm/div., HORIZONTAL SCALE = 0.5 sec/div.

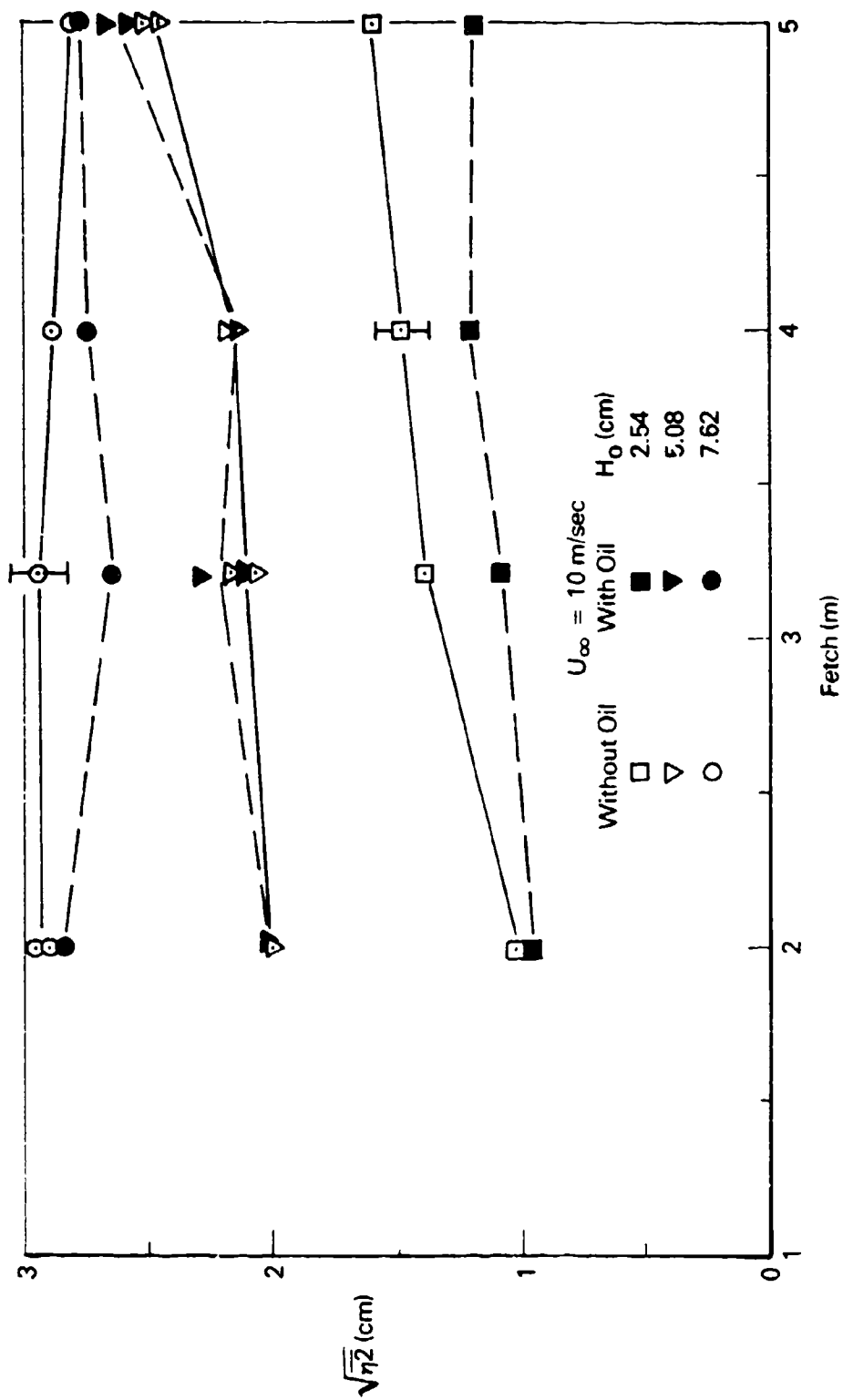


FIGURE 88. VARIATION OF WAVE HEIGHTS WITH FETCH.

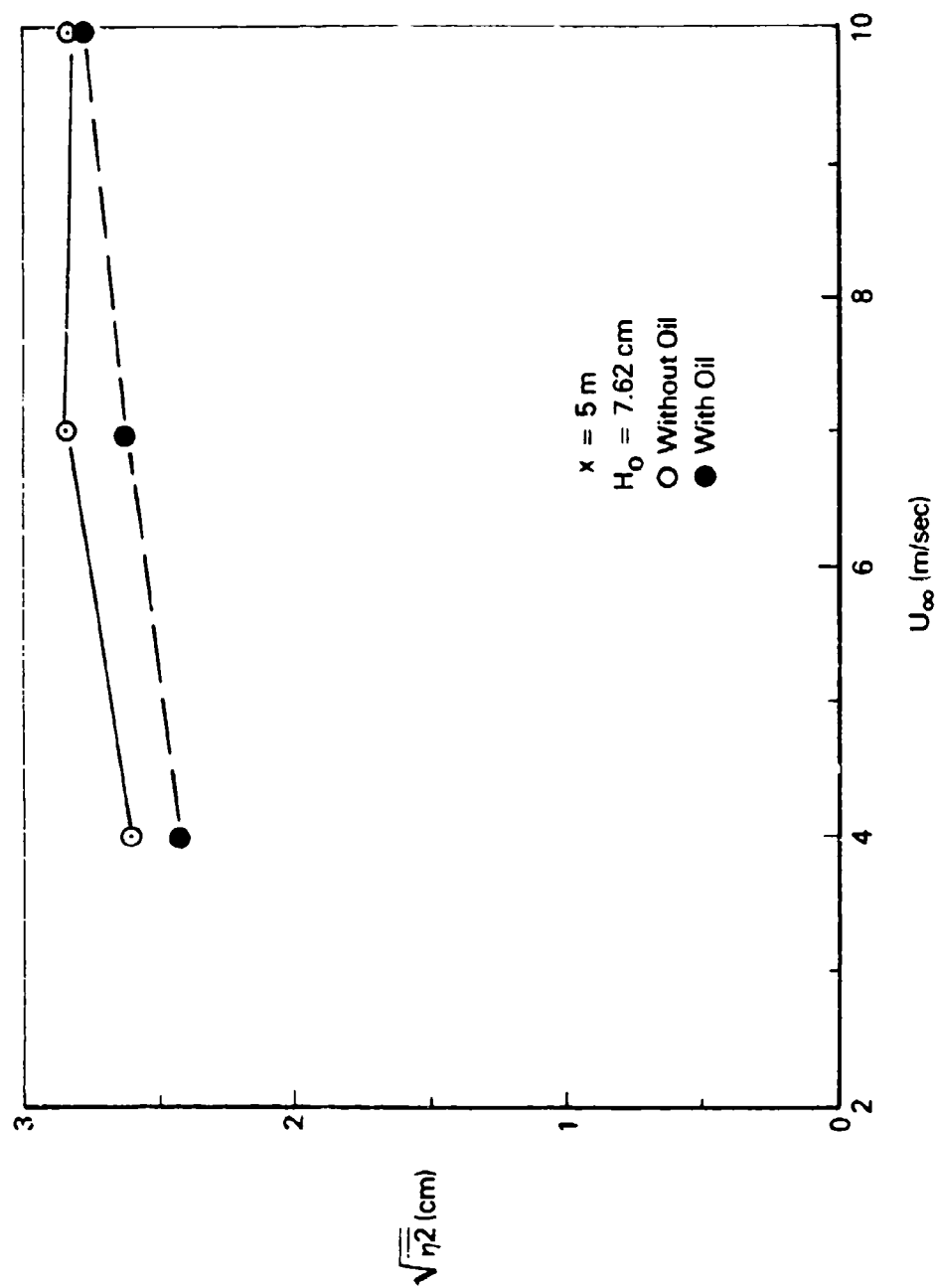


FIGURE 89. VARIATION OF RMS WAVE HEIGHTS WITH WIND SPEED.

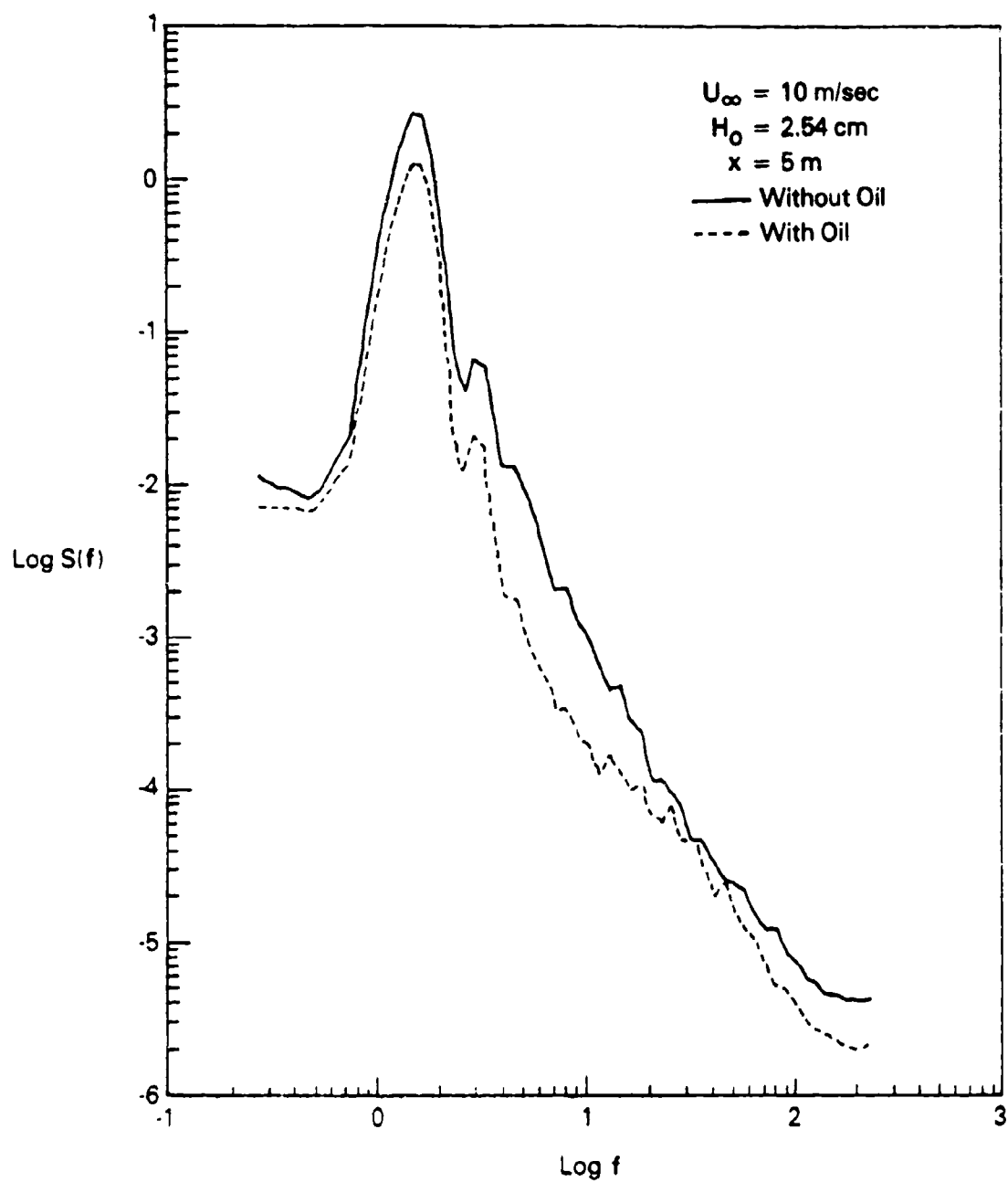


FIGURE 90. COMPARISON OF WAVE ENERGY SPECTRA, $H_0 = 2.54 \text{ cm}$.

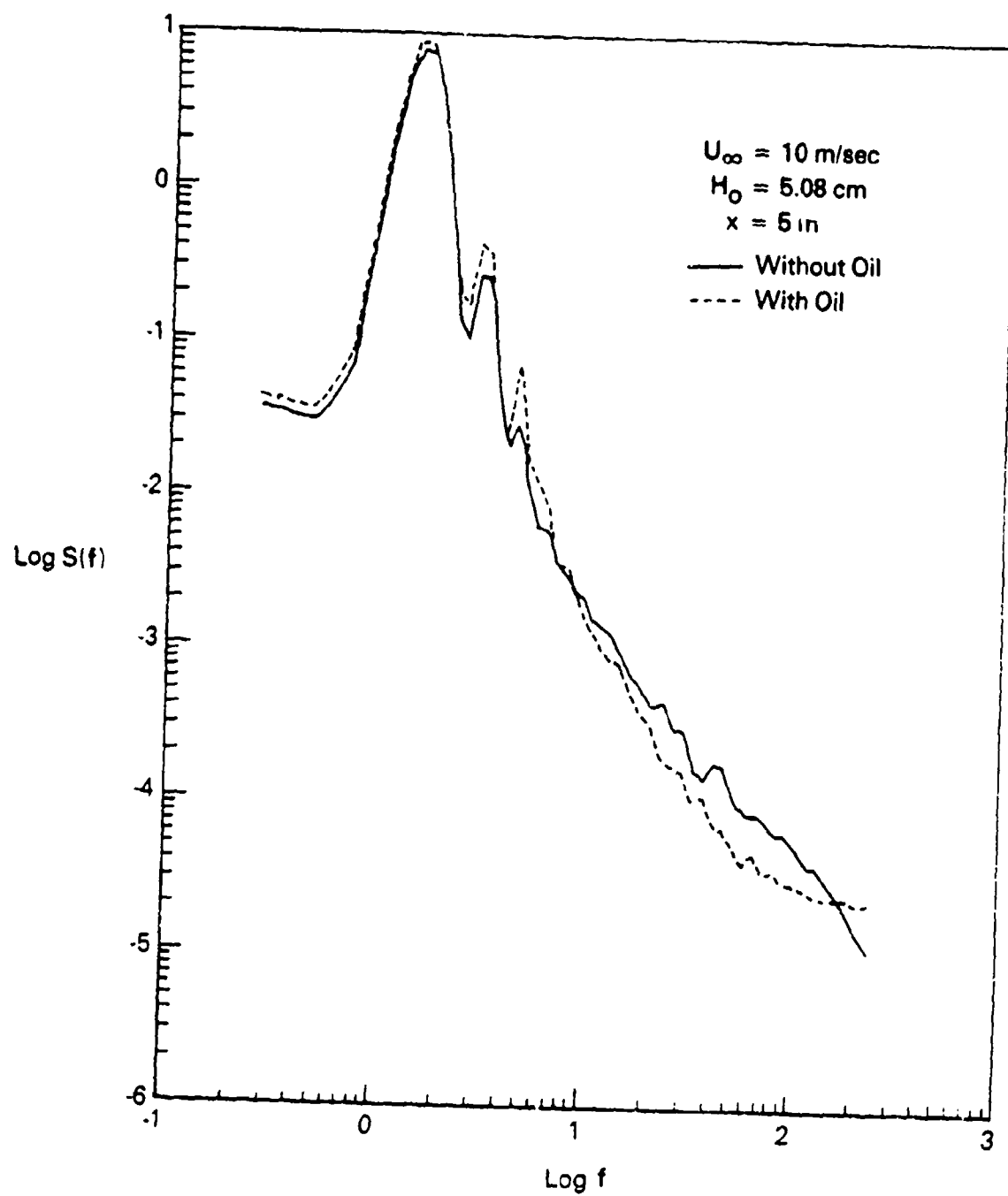


FIGURE 91. COMPARISON OF WAVE ENERGY SPECTRA
 $H_0 = 5.08 \text{ cm}$.

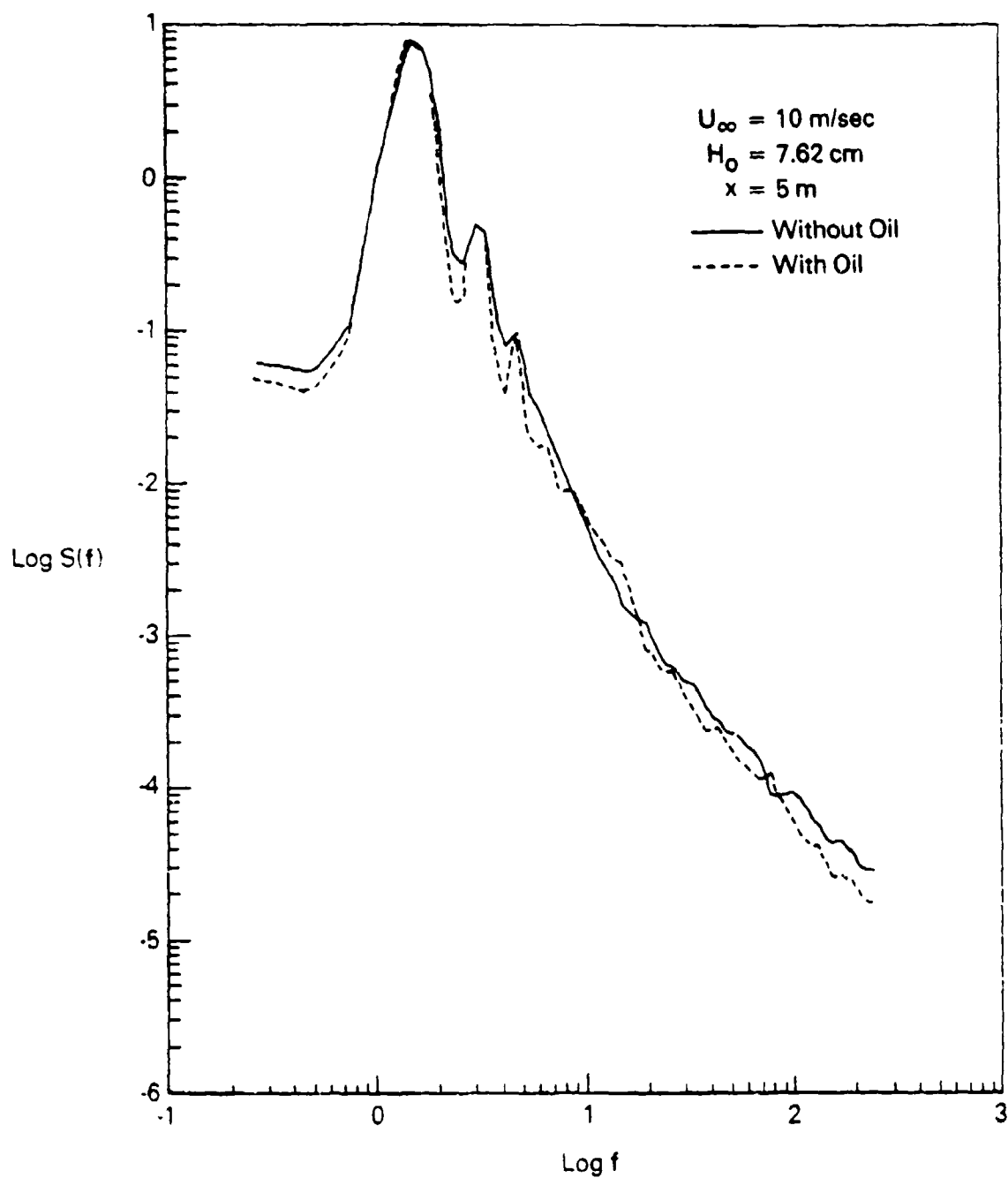


FIGURE 92. COMPARISON OF WAVE ENERGY SPECTRA WITH AND WITHOUT OIL SLICK.